Full field modeling of discontinuous dynamic recrystallization in a CPFEM context

David Alejandro Ruiz Sarrazola

PSL
UNIVERSITÉ PARIS

THÈSE DE DOCTORAT
DE L'UNIVERSITÉ PSL

Préparée à MINES ParisTech

Full field modeling of discontinuous dynamic recrystallization in a CPFEM context - Modélisation à champ complet pour la recristallisation dynamique discontinue dans un contexte CPFEM

Soutenue par

David Alejandro RUIZ SARRAZOLA

Le 07 12 2020

École doctorale n°364

ED SFA - Sciences Fondamentales et Appliquées

Spécialité

Mécanique numérique et Matériaux

Composition du jury :

Roland LOGÉ Professeur associé, École Polytechnique Fédérale de Lausanne	Président
Laurent DELANNAY Professeur, Université Catholique de Louvain	Rapporteur
Lukasz MADEJ Professeur, AGH University of Science and Technology	Rapporteur
Javier SIGNORELLI Professeur, Instituto de Física Rosario	Examinateur
Franz ROTERS Professeur, Max Planck Institute of Microstructure Physics	Examinateur
Aurore MONTOUCHET Responsable de laboratoire, Framatome	Examinateur
Daniel PINO MUÑOZ Maître de recherche, MINES ParisTech	Examinateur
Marc BERNACKI Professeur, MINES ParisTech	Directeur de thèse

MINES ParisTech | PSL

Acknowledgments

First I would like to express my deepest gratitude to my supervisors Prof. Marc Bernacki and Prof. Daniel Pino Muñoz, for giving me the opportunity to participate in this project, and for their guidance and support during my time in CEMEF, that made this time a very enriching experience. I also want to thank Prof. Nathalie Bozzolo for her contributions and enriching discussions that helped deepen my understanding of metallurgical phenomena.

My gratitude also goes to all the members of the jury for accepting and taking the time to read and evaluate my PhD thesis.

I also wish to thank the ANR and all the members of DIGIMU consortium for the support and funding that allowed the development of this project, along with all the personnel in CEMEF. I would specially like to mention and thank Sélim Kraria for all his help.

Finally my biggest thanks goes to my parents Sonia Sarrazola and Benhur Ruiz for all their support in everything I do and to my friends and family in Colombia, specially to Nataly Zapata for being there and making life more enjoyable.

General Introduction

After the industrial revolution metals took a central role in technology development and became one of the foundations of human society. They are present in electronics, transportation, communications, manufacture and productions industries. Thus, creating a constant need for the production of metallic materials with better properties, and to optimize the manufacturing processes.

Almost all of the properties of metallic materials (yield strength, conductivity, elastic limit, corrosion resistance, fatigue resistance) are influenced by the state of their microstructure. Subjecting a material metallic material to a forming operation (forging, rolling, extruding or drawing) causes its microstructure to evolve. This evolution depends on the material, its initial state and on the conditions of the forming process.

Understanding and controlling how the microstructure evolves depending on the applied conditions, can allow us to optimize the forming processes and to produce metallic materials with better properties. However, the microstructural evolution of metals is a complex subject that involves the interaction of many different phenomena [1].

One particular subject of interest, that is the main focus of this work, is materials subjected to hot forming operations (forging). When a metallic material with low stacking fault energy is deformed at high temperatures its microstructure evolves by a process denominated discontinuous dynamic recrystallization (DDRX). DDRX has been widely studied and comprehensive reports on the subject can be found in the literature [1, 2, 3]. This has lead to the development of several models that aim to predict This phenomenon.

In this context the DIGIMU project was created. The DIGIMU project is developed at CEMEF - Mines Paristech [4] with the support of the ANR and the companies that conform the DIGIMU industrial consortium: ArcelorMittal, Framatome, ASCOMETAL, AUBERT & DUVAL, CEA, SAFRAN, TIMET, CONSTELLIUM and TRANSVALOR. The aim of the DIGIMU project is to develop an innovative global framework for the simulation of microstructural changes during forming processes [5].

Due to the complexity of the processes involved and their interactions macroscopic models are not able to fully account for the local evolution of the microstructure. To account for this local evolution, full field models that describe the microstructure at a mesoscale are required. As part of the DIGIMU project, L. Maire [6] developed a full field model that was able to describe DDRX up to high deformation levels, which is a requirement to reproduce industrial forming processes.

However this model is based on a simplified description of plastic defor-

mation that does not account for the heterogeneity of the microstructure, the mechanical response nor the coupled effects of this heterogeneity on the other metallurgical mechanisms. To model and predict the evolution of the microstructure during a hot forming process it is necessary to fully consider the heterogeneous deformation, the mechanical response, the microstructural evolutions and their interactions. Among the models present in the literature, of which reviews can be found in [7, 8, 9], some make attempts to account for the heterogeneous plastic deformation and its impact, however these models are only able to describe low deformation levels.

In this PhD work, that is also part of the DIGIMU project, the model proposed by L. Maire [6] is enhanced by coupling it with a crystal plasticity finite element method (CPFEM). The CPFEM is able to describe the mechanical response and considers the heterogeneity of plastic deformation. The coupling between the models is performed in a way that interactions between the different mechanisms involved in DDRX are considered. The coupled model is also discussed comparatively to experimental measurements in order to evaluate its capability. This PhD work is divided into chapters as:

- Chapter 1: The first chapter is dedicated to a literature review of the different DRX models available in the literature. The focus is put on models that employ improved descriptions of plastic deformation, and identifying the coupling strategies and their limitations.

- Chapter 2: The second chapter presents the CP formulation used in this work. Then it describes the developed CP library with its code structure and numerical tools. The different polycrystal models are also described along with the FEM framework used. It finalizes presenting the validation tests performed.

- Chapter 3: The third chapter starts by describing the DDRX model based on level set (LS) finite element (FE) framework, along with the different phenomenological laws considered. The coupling algorithm is presented, along with the interpolation scheme that allows the interaction between the mechanisms. A sensitivity analysis is also performed to determine the optimal numerical parameters for the coupled models. Finally different tests of the coupled model features are presented.

- Chapter 4: In the fourth chapter the experimental data used to discuss the model are presented and analyzed. After, the calibration and validation procedure are presented along with the results. The model capabilities and limitations are analyzed and discussed. Finally a simplified version of the model is presented, and the model of Maire [6] is

compared with both the full version and the simplified version of the coupled model.

- Chapter 5: In the fifth chapter, some of initial attempts at perspective works are presented and discussed.

This PhD work has contributed to the following communications:

Written communications:

- Article - Ruiz Sarrazola, D. A., Maire, L., Moussa, C., Bozzolo, N., Pino Muñoz, D. & Bernacki, M. Full field modeling of Dynamic Recrystallization in a CPFEM context - Application to 304L steel. Computational Materials Science 184, 109892 (2020).

- Article - Ruiz Sarrazola, D. A., Pino Muñoz, D. & Bernacki, M. A new numerical framework for the full field modeling of dynamic recrystallization in a CPFEM context. Computational Materials Science 179, 109645 (2020).

- Article - Furstoss, J., Ruiz Sarrazola, D. A., Bernacki, M. & Pino Muñoz, D. Handling tensors using tensorial Kelvin bases : application to olivine polycrystal deformation modeling using elastically anisotropic CPFEM. Submitted to Computational Mechanics.

Oral communications:

- Poster - Ruiz Sarrazola, D. A., Pino Muñoz, D. & Bernacki, M. Full field modeling of Dynamic Recrystallization in a CPFEM context. REX&GG 2019 - 7th international conference on recrystallization and grain growth, Ghent (2019).

- Presentation - Bernacki M., Bozzolo N., Moussa C., Pino Muñoz D., De Micheli P., Maire L., Fausty J., Védie L., Florez S., Ruiz Sarraloza D.A., Murgas Portilla B., Alvarado K., Ouhiba S., Poitrault I., Montouchet A., Dumont C., Franchet J.M., Demurger J., Millet Y., Boissonnet L., De Rancourt V., Rigal E. Towards the full modeling of microstructure evolutions during metal forming industrial processes. REX&GG 2019 - 7th international conference on recrystallization and grain growth, Ghent (2019).

- Poster - Furstoss, J., Ruiz Sarrazola, D. A., Bernacki, M., Petita, C., Ganinoa, C., & Pino Muñoz, D. Accounting for elastic anisotropy in

crystal plasticity finite element method within the context of olivine plastic deformation. American Geological Union Fall Meeting, San Francisco, CA (2019).

Contents

Chapter 1

Literature review

The study of physical metallurgy, which is linked to the study of physical properties of metallic alloys is vast and complex. In this chapter, a brief overview of dynamic recrystallization mechanism is introduced. Moreover the terminology that is going to be used all along the manuscript is detailed

1.1 Introduction

In crystalline materials, the atoms are orderly arranged in a pattern that is repeated in three dimensions. The description of this arrangement is denominated the crystal structure, and is defined by the pattern minimal arrangement, denominated the unit cell, that repeats along the lattice. These unit cells come from the atomistic interactions and they minimize the free energy in the material.

However, materials contain defects : point defects, like vacancies; line defects, like dislocations; plane defects, like stacking faults. These defects modify the free energy in the material and the material properties. Additionally crystalline materials like metals are usually polycrystalline materials, composed of several crystal or grains, defined as zones of continuous lattice orientations. The zones that separate two grains are denominated grain boundaries (GB). Depending on the degree of misorientation grain boundaries are classified either as: high angle grain boundaries (HAGB), misorientation higher than $10 - 15°$; or low angle grain boundaries (LAGB), misorientation lower than $10 - 15°$, also denominated subgrain boundaries. Detailed descriptions of the crystal defects and the crystal structure can be found in [10].

In this work we mainly focus on dislocations as they are introduced during plastic deformation. According to their geometry dislocations can be

classified as: edge dislocations, extra or missing half-plane of atoms in the lattice; screw dislocations, relative displacement of one face of the crystal in reference to its adjacent face.

To define dislocations, the Burgers circuit and vector (b) are used. The burgers circuits is a closed atom to atom path defined anywhere in a crystal that contains a dislocation. If the same path is defined in the same part of a crystal without dislocations, the circuit does not close. The vector necessary to close the circuit is the Burgers vector. The Burgers vector of a single dislocation has fixed length and direction. Figure 1.1 illustrates the Burgers circuit and vector defined for a positive edge dislocation.

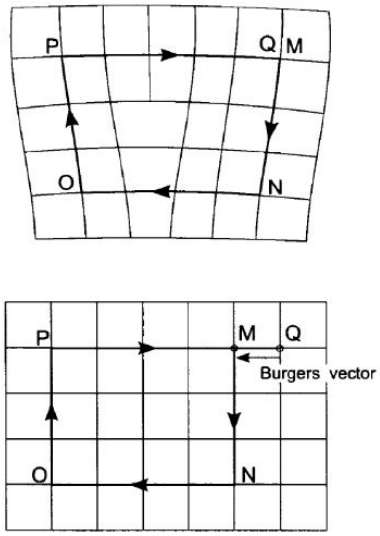

Figure 1.1: Schematic representation of a Burgers circuit with positive line sense into the paper, around an edge dislocation (Top). The same Burgers circuit in a perfect crystal and its Burgers vector, determined by the failure in closure (Bottom). Figure from [10].

Since the description and study of atomistic interactions is quite difficult, the microstructure of metals and its evolution is commonly studied at a polycrystal scale, referred in this work as the mesocale (dislocation dynamics and other studies at the dislocation or atomic scale are not within the scope of this work). Figure 1.2 illustrates a schematic representation of this scale.

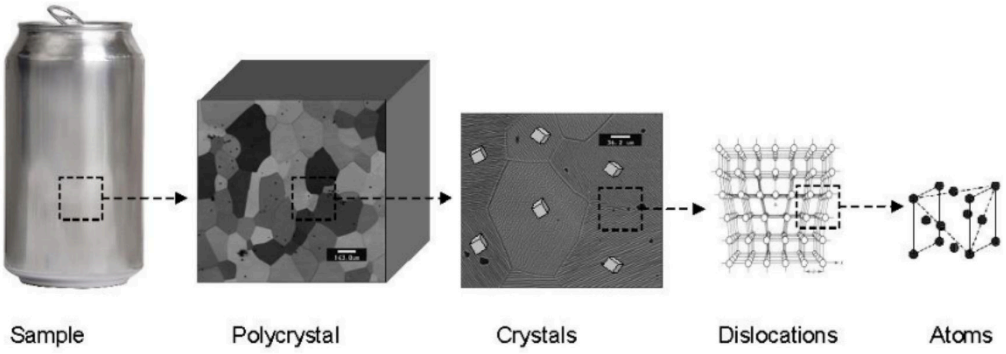

Figure 1.2: Schematic representation of metallic material form the macroscopic scale to the atomistic scale. Figure from [11].

At the mesoscale, dislocations are classically considered through the density of dislocations (ρ) in the material, a type of concentration. Dislocation density is measured by counting the number of dislocation lines that thread a unit area of surface; or in terms of the total dislocation length per unit volume [12].

When a metal is plastically deformed the free energy inside the material is raised by means of the accumulation of dislocations. This leads to a thermodynamically unstable state. However, at low temperatures the energy is not dissipated and the defects remain in the material. At high temperatures thermally activated mechanisms occur that can remove these defects or rearrange them in lower energy configurations.

These mechanisms include: recovery, by which dislocations are annihilated or rearranged inside the grains without usually affecting grains boundaries (denominated dynamic recovery when it happens along with plastic deformation); recrystallization (ReX), by which new dislocation free grains are formed (recrystallized grains form in zones with high stored energy and high misorientation); grain boundary migration (GBM), by which GB will migrate due to driving pressures. Detailed descriptions of these mechanisms can be found in [1]. Figure 1.3 shows an illustration of theses mechanisms at the mesocale, from a deformed microstructure (a) to: recovery (b), partially recrystallized (c) and fully recrystallized microstructure (d). GB are depicted as thick black lines and subgrain boundaries are depicted as thin black lines.

The recrystallization mechanisms can occur heterogeneously in the material, causing that at the mesoscale the recrystallization mechanisms has clear nucleation (appearance of recrystallized grains) and growth stages. Or they can occur uniformly, so that the microstructure evolves gradually with no nucleation and growth stages easily identifiable at the mesoscale. In the first

case they are denominated discontinuous and in the second case as continuous. This constitutes a phenomenological classification that only describes how they are perceived at the mesoscale and not the nature of the atomic mechanism themselves.

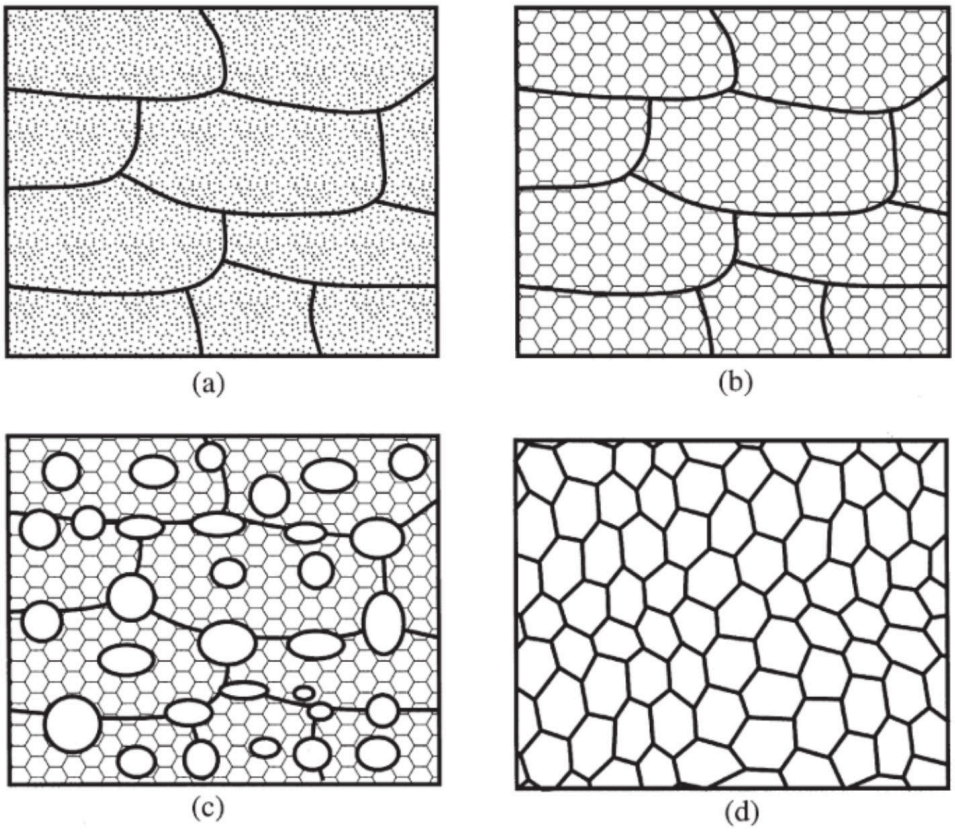

Figure 1.3: Schematic representation of a deformed microstructure (a) evolving by means of: recovery (b), partially recrystallized (c) and fully recrystallized (d). Figure from [1].

The microstructure of a metallic material subjected to hot forming operations will evolve by the combined action of all these mechanisms: plastic deformation, dynamic recovery, ReX and GBM. This is denominated dynamic recrystallization (DRX). On metallic materials with low staking fault energy this process is discontinuous, thus it is denominated discontinuous dynamic recrystallization (DDRX).

Metallic materials undergoing DDRX show the following common characteristics, that have been summarized several times in the literature [1, 7, 13]:

- The flow stress curve of the material shows a peak value, which is different from the steady state stress. Depending on the temperature and strain rate conditions, multiple peaks can be observed.

- In order for DDRX to start, the deformation in the material must reach first a critical strain value, this value is reached before the peak stress.

- Recrystallized grains usually appear at GB. However in cases of low strain rate and large initial grain sizes, the appearance of recrystallized grains inside existing grains becomes more significant.

- Recrystallization kinetics accelerate with the decrease in the initial grain size, with the decrease in strain rate and with the increase in temperature.

- The grain size tends to decrease comparatively to the initial value and converge toward a steady value.

Considering that DDRX includes the interactions of the different mechanisms previously introduced, they are further described next.

1.1.1 Plastic deformation

Plastic deformation in metals is an anisotropic mechanism, that results form the motion, generation and accumulation of dislocations. Due to the difficulty of modeling dislocation motion at the mesoscale, crystal plasticity theory [14] is used to model the behaviour of polycrystals. It provides a link to microscopic features by incorporating concepts of dislocation theory.

Crystal plasticity theory considers that the basic movement of dislocations is called glide. Glide occurs when a dislocation moves in the surface that contains its Burgers vector. The glide of several dislocations constitutes slip, it can be represent as the sliding of one plane of atoms over another. The motion of dislocations is not limited to glide, a description of the different types of dislocations motion can be found in [10].

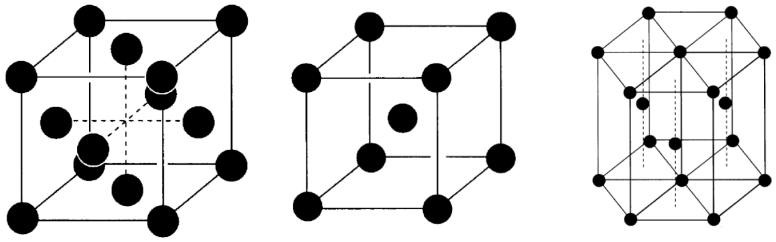

Figure 1.4: Common unit cells present in metallic materials. FCC (left side), BCC (center) and HCP (right side). Black dots represent an atom of the material. Image modified from [10].

Slip occurs on specific planes and directions denominated the slip plane and slip direction, the combination of the two constitutes a slip system. Slip planes are the most densely populated planes (contain greatest number of atoms per area), while slip directions are the directions with the most atoms per length. The number of slip systems in a crystal depend on the crystal structure unit cells. On metallic crystals the most common crystal structures are: FCC, BCC and HCP, (shown in figure 1.4) which contain 12, 24 and 3 slip systems respectively.

In order for slip to start a minimal stress is required. In figure 1.5, a cylindrical crystal sample subjected to a tensile force F, the tensile stress σ parallel to F is given by $\sigma = F/A$, with A the area of the surface where F is being applied. The acting force F has a component acting on the slip direction $F\cos\lambda$ with λ the angle between the slip direction and F. The component of F in the slip direction acts on an area $A/\cos\phi$ with ϕ the angle between F and the normal of the slip plane. Thus the shear stress τ acting on the slip system is defined as:

$$\tau = \frac{F}{A}\cos\lambda\cos\phi \quad , \tag{1.1}$$

τ is denominated the resolved shear stress. In order for plastic deformation to start, τ must reach a minimal value denominated the critical resolved shear stress (CRSS). The product of $\cos\lambda\cos\phi$ is the commonly known Schmid factor. Equation 1.1 can be extended to 3 dimensions and for a slip system α as:

$$\tau^{\alpha} = \boldsymbol{\sigma} : (\boldsymbol{m}^{\alpha} \otimes \boldsymbol{n}^{\alpha}) \quad , \tag{1.2}$$

with $\boldsymbol{\sigma}$ the Cauchy stress tensor and $(\boldsymbol{m}^{\alpha} \otimes \boldsymbol{n}^{\alpha})$ the Schmid tensor, with $\boldsymbol{m}^{\alpha}$ the vector defining the slip direction and $\boldsymbol{n}^{\alpha}$ the normal vector of the slip

plane. Eq. 1.2 known as the Schmid Law [15], shows that for a given applied stress $\boldsymbol{\sigma}$, the resulting shear stress causing plastic deformation depends on the crystal structure and its orientation.

The shear stress causes shearing in the material, while the volume remains constant. The material also deforms elastically, however elastic strains are comparatively smaller than plastic strains, and numerous crystal plasticity models neglect them. The stress acting on the material does not active only one slip system, but several of them, so the material plastic deformation is the result of the crystallographic slip on all active slip systems. Additionally the applied shear stress can also cause the crystal lattice to rotate. This rotation leads to changes in the material texture, defined as the sum of crystallographic orientations.

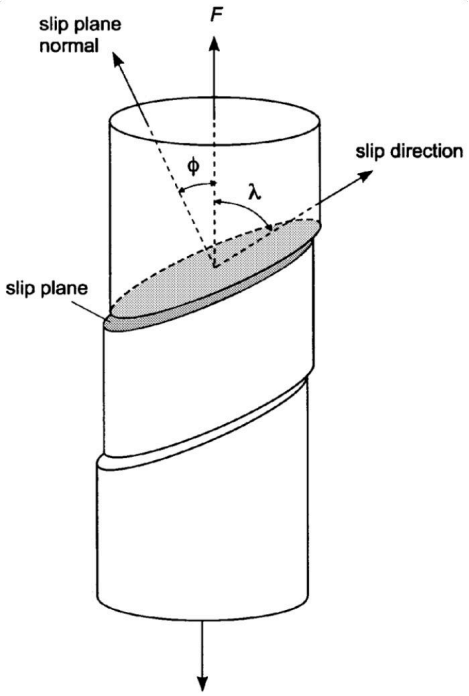

Figure 1.5: Schematic representation of the geometry of slip due to the application of a force F. Image modified from [10].

As the material deforms, additional dislocations are generated, when dislocations encounter obstacles like GB, they pile up . Dislocations can not move through grain boundaries, however the stress induced by the accumulation of dislocations in a GB can induce the motion of dislocations in the neighbour grain. The accumulation of dislocations around obstacles causes that subsequent motion of dislocations becomes more difficult and requires

higher stress. This translates into the material hardening.

These considerations are the basics concepts of the crystal plasticity theory. In general terms a single crystal plasticity model is defined by: a kinematic framework that describes the motion of the crystal and evolution laws for the state variables of the model. The evolution laws commonly refer to the flow rule (which defines the relation between the stress and the strain rate) and the hardening rule (which defines the hardening rate of the material). Some models include additional considerations regarding non local effects and special treatments for GB as the ones described in [16]. The single crystal model used in this work is described in chapter 2 along with different flow rules and hardening rules considered in the literature.

In crystal plasticity models dislocation density can be subdivided in types. According to the possibility of dislocations to move as mobile or immobile. According to their source as: dislocations generated due to multiplication mechanisms (well known as Statically Stored Dislocations - SSD) or dislocations generated due to strain gradient fields caused by geometrical constrains of the crystal lattice (well known as Geometrically Necessary Dislocations - GND).

A single crystal model describes the behaviour of individual crystals, however as mentioned earlier metals are polycrystal materials. In order to describe their behaviour a polycrystal model is then required. The polycrystal model describes the way that the macroscopic strain is partitioned between the grains and how the grains interact with each other. The main polycrystals models found in the literature are (detailed descriptions of these models and their variants can be found in [17]):

- The Sachs Model [18]: this model assumes that all grains in the polycrystal experience the same stress equal to the macroscopic stress, and that each crystal deforms by activating only one slip system. The slip system activated is the one subjected to highest resolved shear stress. The grains deform independently and grains interactions are not considered. This model leads to incompatibilities in the deformation between grain boundaries and does not consider heterogeneity in the deformation inside the grains.

- The Taylor model [19]: this model assumes that all grains in the polycrystal deform in the same way as the polycrystal. This condition ensures compatibility in the deformation between GB, by disregarding local stress equilibrium. Interaction between grains is also not considered in this model nor heterogeneity in the deformation inside the grain.

- The relaxed constrains Taylor model [20, 21, 22]: this model is derived from the Taylor model. It assumes an iso-strain condition. However this condition is relaxed in specific directions. For example the lath model relaxes the iso-strain condition in the rolling direction (RD) and in the normal direction (ND), while the pancake model relaxes the condition in the transverse direction (TD) and in the ND. This model is specially intended to model grains under specific deformation conditions, for example elongated grains produced in rolling as in the pancake model. Interaction between grains are also not considered in this model.

- N-site models [23, 24, 25]: this model considers the behaviour of more than one grain at the same time. The LAMEL model considers two grains and the GIA model considers the behaviour of cluster of 8 grains. The deformation of the group of grains must be equal to the macroscopic deformation, however the constrains are relaxed inside the cluster. This allows to, consider at some degree, the interaction between neighbouring grains. However long range interactions are not considered, nor heterogeneity in the deformation inside the grain.

- The viscoplastic self-consistent model (VPSC) [14, 26, 27, 28]: this model is based on the work of Eshelby [29], each grain is considered as an ellipsoidal inclusion in an homogeneous matrix. The stress and strain of the polycrystal (matrix) are defined by the average behaviour of all the grains. Long range interactions are considered as the behaviour of each grain is affected by the behaviour of the average. However neighbour interactions are not considered, all grains with the same initial orientation behave in the same way and heterogeneity inside the grains are not considered.

- Crystal plasticity finite element method (CPFEM) [30, 31, 32, 33]: this framework couples the finite element method with crystal plasticity by using a single crystal plasticity model to describe the stress-strain relation. The CPFEM ensures compatibility at the local level, equilibrium is also full filled in a weak sense. Both short range and long range interactions are considered, so no additional assumptions are required. If grains are discretized with more than one element, heterogeneity inside the grains are considered. Its main limitation remains its high computational cost.

- Crystal plasticity spectral method [34, 35, 36]: An alternative to the CPFEM method consist to use the fast Fourier transformation (CPFFT)

to solve the equilibrium equations instead of FEM. This method has been shown to be computationally largely more efficient than the FEM method. However it requires a regular grid and periodicity in the domain, limiting its application when very large deformations have to be considered as in conventional metal forming operations.

1.1.2 Grain boundary energy (GBE)

As mentioned earlier GB are usually classified according to their misorientation between HAGB or LAGB. This classification can also provide a general description of their properties. The properties and structure of LAGB are caliscally considered as a function of misorientation, while the properties and structure of HAGB generally considered as being independent of their misorientation. However, this is only a general description as there are numerous types of high angle grain boundaries that do not adhere to it [1]. Following this classification a common way to define the grain boundary energy (γ_{GB}) as a function of the misorientation (θ) is using Read-Shockley type equations [37] as:

$$\gamma_{GB}(\theta) = \begin{cases} \gamma_{GB}^{max}\left(\frac{\theta}{\theta_{max}}\right)\left(1-\ln\left(\frac{\theta}{\theta_{max}}\right)\right) & \text{for} \quad \theta < \theta_{max} \quad , \\ \gamma_{GB}^{max} & \text{for} \quad \theta \geq \theta_{max} \quad , \end{cases} \tag{1.3}$$

with γ_{GB}^{max} the maximal grain boundary energy and θ_{max} the threshold angle used to define the type of GB. In DDRX models LAGB are classically not considered and γ_{GB} is defined as an isotropic constant value. It must be highlighted that this topic (description of γ_{GB} in full field Rex modeling) is an active research topic in the community, mainly to take into account misorientation dependence (as in the Read-Shockley model) but also for the inclination dependence (torque terms) [38, 39]. This aspect will not be considered in this work, γ_{GB} will be mostly assumed as a constant only dependant of the considered material.

1.1.3 Grain boundary mobility

GB migrate as a result of several atomistic mechanisms happening near the boundary, these mechanisms depend on the structure of the boundary. However they are very difficult to study as they happen at high temperatures, high velocity and in non equilibrium conditions. Thus, the determination of the GB mobility is also very difficult [1]. Considering that the migration of a GB is due to an acting pressure (P_{GB}), it is generally considered that the

velocity of the grain boundary (V_{GB}) is proportional to P_{GB}. In this relation, the constant of proportionality is the grain boundary mobility (M_{GB}). M_{GB} is dependant of the temperature and is commonly defined according to an Arrhenius type law as:

$$M_{GB} = M^0_{GB} \exp\left(\frac{-Q_m}{RT}\right) \quad , \tag{1.4}$$

with M^0_{GB} the mobility pre-exponential factor, Q_m the activation energy for GBM, R the universal gas constant, and T the absolute temperature. This description of the mobility is classical in hot metal forming and prevails in the current modelling of ReX at the mesoscale. However, as for γ_{GB}, this question is largely studied in the state of the art due to misfits between some experimental works and this picture of the mobility or the reduced mobility (product of M_{GB} and γ_{GB}, $M_{GB} * \gamma_{GB}$) [40, 41]. Recent advances concern the introduction of tensorial mobility or disconnection models used at the GB scale [42, 43]. However, in this work the classical definition of the GB mobility, Eq. 1.4, will be used.

1.1.4 Recovery

Recovery refers to the mechanism that allows the material to partially restore its properties by reducing the number of dislocations [1]. The number of dislocations is reduced by the annihilation of dislocations and rearrangement of dislocations into lower energy configurations like lower angle grain boundaries and the formation of subgrains. These processes are the result of: dislocations glide (described previously), dislocations cross-slip (defined as dislocations switching from one plane to another) and dislocations climb (defined as dislocations moving out of their slip plane to another plane of atoms).

As mentioned earlier, DDRX models do not usually consider LAGB i.e., subgrains. Since recovery is considered to not affect HAGB, it is usually included as part of phenomenological laws that describe the evolution of dislocation density with strain. For example Eq. 1.5 describes the law used in the works of Montheillet et al. [44]:

$$\frac{\partial \rho}{\partial \epsilon} = K_1 \rho^{\xi} - K_2 \rho \quad , \tag{1.5}$$

with K_1 the parameter describing the increase in dislocations due to plastic deformation, and K_2 the parameter describing the annihilation of dislocations due to dynamic recovery. This law can represent the well known Yoshie-

Laasroui-Jonas equation [45] when $\xi = 0$, and the Kocks-Mecking equation [46, 47] when $\xi = 1/2$.

1.1.5 Grain boundary migration (GBM)

As described before, GBM is caused by atomistic mechanics acting in zones near the boundaries that depend on the structure of the boundary. As already detailed in the mobility discussion section, the classical kinetic equation describing GBM is [1, 48, 49]:

$$\boldsymbol{V}_{GB} = M_{GB} P_{GB} \boldsymbol{n} \quad , \tag{1.6}$$

with $\boldsymbol{n}$ the outside unitary vector normal to GB. In context of metal forming, two main driving pressures are considered: the capillarity pressure (P^C_{GB}), due to the minimization of the interface energy and the stored energy pressure (P^E_{GB}), due to the minimization of the energy stored by plastic deformation. P^C_{GB} is classically defined as $P^C_{GB} = -\gamma_{GB} K$, with K the GB curvature (trace of the curvature tensor in 3D). At the mesoscale P^E_{GB} is directly linked to the dislocation density and often homogenized per grain. Then the following equation is used:

$$P^E_{GB} = \tau_E[\rho] \quad , \tag{1.7}$$

with τ_E the dislocation line energy estimated as $\tau_E = \mu b^2/2$, with b the magnitude of the Burgers vector and μ the shear modulus. $[\rho]$ corresponds to the jump of stored energy across the GB in terms of dislocation density. Finally $\boldsymbol{V}_{GB}$ can be approximated by the following equation:

$$\boldsymbol{V}_{GB} = M_{GB} \left(\tau_E[\rho] - \gamma_{GB} K \right) \boldsymbol{n} \quad . \tag{1.8}$$

1.1.6 Nucleation

The DDRX mechanism, can be divided into two main submechanisms: nucleation, i.e., the formation of dislocation free grains and their subsequent growth, driven by Eq. 1.8. However the term nucleation is ambiguously used in ReX. Nucleation refers to the classical nucleation theory of phase transformation [49], that considers random atomic fluctuations leading to the formation of a crystallite (microscopic crystal) separated by a HAGB (nucleus), which is subsequently able to overcome the interfacial energy. Using the same definition, nucleation theory calculations show that, for the case of ReX, the radius required for the nucleus to grow (critical radius) will be so big that the rate of appearance of nucleus will be negligible [50]. In fact, it is

well-known today that in ReX, new grains originate from small-volumes that pre-exist in the deformed microstructure [1]. So a preferable term would be probably to discuss the appearance of ReX grains rather than nuclei, even if this questionable terminology persist in the literature.

The appearance of recrystallized grains is assumed to occur at high temperatures in zones with high stored energy (high dislocation density) or zones with high misorientation (zones with high misorientation have high stored energy because of the GND required to accommodate the misorientation). The main mechanism identified in the literature for the appearance of recrystallized grains, during DDRX, is strain induced boundary migration (SIBM). In SIBM, part of an existing grain boundary will bulge and migrate towards the interior of a high strained grain, leaving a zone with low dislocation density behind. This mechanism often leads to the formation of necklaces structures, characterized by the presence of several small recrystallized grains along grain boundaries.

The newly formed recrystallized grain will disappear unless its driving force due to the stored energy is higher than the capillarity effect. This condition is classically approximated according to the Bailey-Hirsch criterion, which defines the critical grain size as:

$$r_{cr} = \frac{2\gamma_{GB}}{\tau_E[\rho]} \quad . \tag{1.9}$$

Further detail of this mechanism can be found in [1]. The appearance of recrystallized grains during DDRX is typically modelled by the introduction of dislocation free grains in the microstructure. Classical models [51, 52, 53, 54, 55] describe a critical dislocation density (ρ_{cr}) required for the appearance of recrystallized grains defined as:

$$\rho_{cr} = \left(\frac{20\gamma_{GB}\dot{\epsilon}_P^{eff}}{3blM_{GB}\tau_E^2} \right)^{\frac{1}{3}} \quad , \tag{1.10}$$

with l the dislocation mean free path and $\dot{\epsilon}_P^{eff}$ the effective plastic strain rate. The number of recrystallized grains introduced follows a nucleation rate law:

$$\dot{n} = C\dot{\epsilon}_P^{eff} \exp\left(\frac{Q_n}{RT}\right) \ , \tag{1.11}$$

with C a constant and Q_n the activation energy for nucleation.

1.1.7 Summary

Considering the interaction of all the mechanisms, the effects of DDRX on the microstructure during hot deformation can be summarized as [56]:

- The heterogeneous deformation of grains causes a non-uniform distribution of the stored energy, that determines where recrystallized grains appear and in which direction they grow.
- The morphology change and orientation rotation of the deformed grains also affects the appearance of recrystallized grain and GBM. Subsequently, the evolution of the grains alters the final microstructure and texture.
- The appearance of recrystallized grains, GBM and dynamic recovery also cause reduction in the slip resistance by eliminating dislocations and consequently gives rise to significant changes in the mechanical properties.
- The changes in the mechanical properties and microstructure alter the subsequent plastic deformation behavior of the metal in a non-negligible manner.

The general terminology and scope has been clarified along with the general introduction of DDRX. In the next section, we present the main models that have been proposed in the literature to model DDRX which is the main focus of this work.

1.2 Modeling of DDRX

Different types of models have been proposed in the literature to describe DDRX. These models are generally classified as (detailed reviews can be found in [7, 8, 9]):

- Phenomenological models: these models consist to describe the evolution of the global recrystallization fraction (X) and mean grain size ($\bar{R}$) as a function of the strain and temperature [57, 58, 59], based on the well known JMAK models [60, 61, 62]. These models only describe average behaviors by fitting phenomenological laws to experimental data.
- Mean field models: in these approaches the microstructure is described as set of n-number of grains. The evolution of each grain follows physical-based laws comparing its state against the average of all grains [44, 63, 64] or specific sets of grains [55, 65, 66].

- Full field models: in this context the microstructure topology is explicitly described at the polycrystal scale. These approaches allow to consider local phenomena and interactions between neighbouring grains. Several types of full field models exist in the literature:
  - Models derived from the Potts model [67] like: Monte-carlo models [68, 69] and cellular automata models [56, 70, 71, 72, 73].
  - Deterministic models like: vertex models [74, 75], level-set models [76, 77, 78, 79] and phase-field models [80, 81, 82, 83].

One common limitation of the mentioned numerical strategies is that they use simplified descriptions of plastic deformation: the Yoshie-Laasroui-Jonas equation or the Kocks-Mecking equation (Eq. 1.5) [44, 55, 65, 66, 79], simplified plasticity models [63, 64] or macroscopic plasticity models [68]. These simplifications do not take into account the crystal structure nor the grains orientation, which leads to an uniform behaviour of all the grains and subsequently affect the kinetics of recrystallization. On the other hand models that incorporate CP formulations [56, 69, 70, 71, 72, 73, 75], provide better descriptions of plastic deformation but present limitations in: the description of heterogeneous deformation, the coupling between the CP model and the GBM model, or are not able to describe high levels of plastic deformation (common in metal forming operations).

In the next section a detailed description of the mentioned DDRX models is presented, we focus on models that use enhanced descriptions of plastic deformation and their coupling strategies. Phenomenological models are not included. Even tough they are widely used, specially in industrial context, due to their simplicity and low computational cost, they rely on significant simplifications of the physical phenomena and thus only describe specific parameters of the DDRX mechanisms. A discussion regarding phenomenological models can be found in [6].

1.2.1 Mean field models

Mean field recrystallization models follow a common structure: the microstructure is described implicitly as a set of grains with specific shape (usually spherical). Each grain is associated to state variables, dislocation density, size, orientation. Each grain usually represents not a single grain but a fraction of grains which share the same initial state (as a bin of a multi-dimensional distribution), and will evolve equally. Figure 1.6 illustrates this representation, each spherical grain has an associated size (D_i), orientation (M_i) represented by the Taylor factor, and dislocation density (ρ_i).

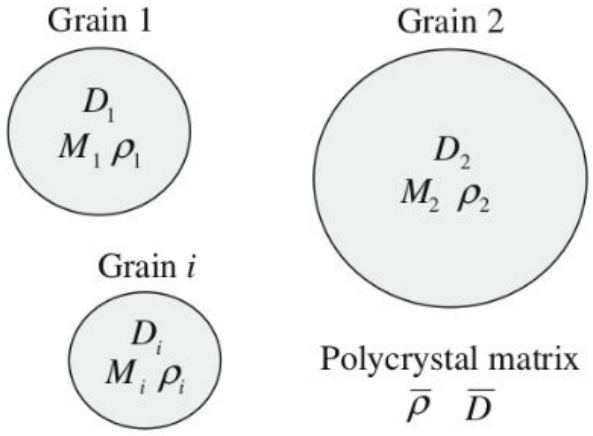

Figure 1.6: Schematic of the microstructure representation as considered in the mean field model model of Cram et al [63]. Figure from [63].

The physical phenomena are described by individual laws. The grains interact either with the medium, represented by the average behaviour of all the grains like in the model of [44], or with specific set of grains like in the models of [55, 65, 66]. For example in the model proposed by Cram et al. [63, 64], when considering GBM due to difference in stored energy, the dislocation density of each grain is compared against the average dislocation density of the medium ($\bar{\rho}_i$):

$$\bar{\rho}_i = \frac{\sum D_i^2 \rho_i}{\sum D_i^2} \quad . \tag{1.12}$$

This means that the interaction between a grain and its neighbours is replaced by the interaction of each grain with the medium. Figure 1.7 shows a schematic representation of this simplification for the dislocation density gradient calculation.

A similar representation of the microstructure is used in the VPSC model. In the VPSC model the microstructure is represented by a set of elliptical grains embedded in a medium. Each grain or grain class is associated to state variables and the state of the medium is described by the average behaviour of all the grains. This common representation of the microstructure between DDRX mean field models and the VPSC model facilitates their coupling, which has been proposed in the literature.

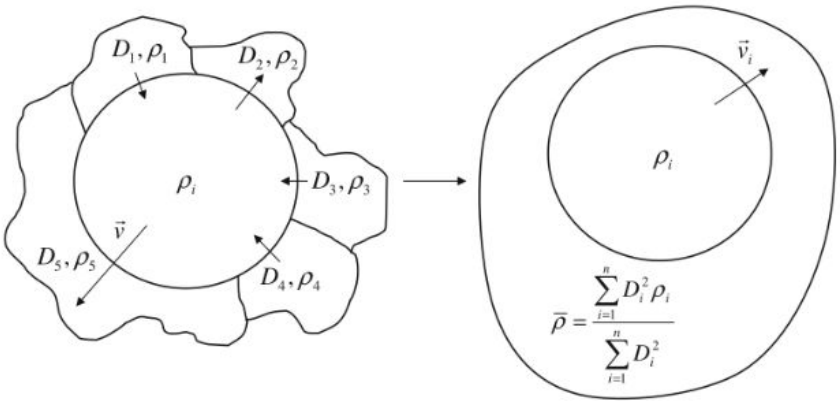

Figure 1.7: Schematic representation of the interaction between neighbouring grains replaced by the interaction with the medium for the dislocation density gradient calculation. Figure from [63].

We can cite the DDRX model proposed by Cram et al [63, 64], which uses the plasticity model of [84] that imposes a condition of iso-work allowing individual grains to be deformed differently. The model of Zhou et al [85, 86, 87], in which the iso-work model is replaced by the VPSC formulation in the DDRX model of Cram et al [63, 64].

In the model proposed by Cram et al. [63, 64], the plastic deformation is calculated according to the model of [84] which imposes a condition of iso-work for all the grains. This condition is used to distribute the imposed macroscopic stress ($d\epsilon_{mac}$), among the individual grains:

$$d\epsilon_i = \frac{K}{\sigma_i} \quad , \tag{1.13}$$

$$d\epsilon_{mac} = \frac{\sum V_i d\epsilon_i}{\sum V_i} \quad , \tag{1.14}$$

with K the work performed, $d\epsilon_i$ the strain of each individual grain i, σ_i the stress of each individual grain i and V_i the volume of each individual grain i. Next, the strain hardening is defined as:

$$\frac{d\sigma_i}{d\epsilon_i} = \Theta_{II}\left(1 - \frac{\sigma_i}{\sigma_{s,i}}\right) \quad , \tag{1.15}$$

with $\sigma_{s,i}$ the steady state stress of each grain i and Θ_{II} the stage II work-hardening rate. Finally, the relation between the stress and the dislocation density is defined as:

$$\sigma_i = \alpha M_i \mu b \sqrt{\rho_i} \left(\frac{\dot{\epsilon}_i}{\dot{\epsilon}_{ref}} \right)^m \quad , \tag{1.16}$$

with α a numerical constant, μ the shear modulus, b the magnitude of the Burgers vector, ρ_i the dislocation density of the grain i and m a strain rate sensitivity exponent.

In this model the general calculation procedure for each time step is as follow: first, plastic deformation is calculated according to the described plasticity model; second, recrystallized grains are introduced following a nucleation rate law; finally, the GBM is performed. This model only considers the driving force due to stored energy in the GBM calculation. Nonetheless, Even if the plasticity model allows grains to deform differently from each other and the Taylor factor considers the grain orientation to some degree, this approach remains a significant simplification of plastic deformation in metals.

In the model of Zhou et al. [85, 86, 87], by taking advantage that the VPSC considers the evolution of the grains orientation, an additional term is included in the nucleation rate law. This term is a function of the grain rotation from its initial orientation. It is introduced following the idea that grains with a higher rotation will have a higher internal misorientation, thus higher formation of subgrain boundaries so their probability to nucleate will be higher. This illustrates the possibility of modifying classical nucleation laws with the additional information provided by CP formulations.

One difficulty in the coupling between the VPSC model and this DDRX mean field model is that in the VPSC model grains are considered as ellipsoids, represented by the 3 major axis of the ellipsoid and their volume weight in the aggregate; while in the DDRX model grains are considered as spheres. To couple the two models the authors use a dual representation. In the VPSC calculation a grain is considered as an ellipsoid and on the DDRX model the same grain is considered as a sphere. The two representations are related through the volume weight, however this procedure is not explained in detail in their work. The calculation procedure of each time step is as follow: the VPSC calculation is performed, if the dislocation density does not reach the critical value required for nucleation, the next step of VPSC calculation is performed; if the dislocation density reaches the critical value, recrystallized grains are introduced. After the introduction of ReX grains the GBM calculation is performed. Finally the volume weights of all the grains are normalized.

By coupling VPSC model with a the described DDRX mean field model, the authors obtain a better description of the DDRX mechanism. This includes a better description of the dislocation density evolution, that considers

the initial orientation of grains, the ability of the model to predict texture evolution (VPSC) and the possibility to include to some degree the effect of misorientation in nucleation laws. Also, since the computational cost of both the mean field DDRX model and the VPSC-CP models is not high, the resulting coupled model has low computational cost when compared with full field approaches.

However this approach is still limited: first, even if the coupling takes advantage of the similar representation of the microstructure used in both models, the differences in the grain shapes are not clearly resolved; second, heterogeneous deformation of grains is not considered, nor gradients inside grains; third, local neighbour interactions between the grains can not be considered in mean field models nor in the VPSC model.

1.2.2 Full field Potts models

Full field Potts models are based on the widely known Potts model [67], they include both the Monte Carlo (MC) and the Cellular Automata (CA) models. In these approaches the microstructure is described explicitly by using a regular grid of cells or sites as shown in figure 1.8. In the context of DDRX simulations the use of regulars grids makes it difficult to consider deformation, as it causes distortions in the regular grid. Different techniques proposed in the literature to deal with this problem will be mentioned in the following.

Monte Carlo model

In the MC model the total energy of the domain E is classically defined as:

$$E = \sum_{i=1}^{N} \left(\sum_{j=1}^{n_i} \frac{1}{2} \gamma_{GB}(s_i, s_j) + E_\rho(s_i) \right) \quad , \tag{1.17}$$

with N the number of sites, n_i the number of neighbour sites j of a site i, E_ρ the stored energy (related to dislocation density), $\gamma_{GB}(s_i, s_j)$ is the grain boundary energy between the site and its neighbour.

The evolution of the sites is calculated using a sampling algorithm: sites are chosen at random, a possible change in the state of the site is proposed (change of orientation). The change in energy $\triangle E$ caused by the possible change in the site is calculated. The change is accepted according to a probability function that depends on $\triangle E$. In each MC step N random sites are chosen, since the sites are chosen at random not all sites are changed during

each MC step, the MC time step is not equivalent to a physical time step. A common form of $p(\triangle E)$ is a symmetric function:

$$p(\triangle E) = \frac{1}{2} w_0 \left[1 - \tanh\left(\frac{\triangle E}{2kT_s} \right) \right] \quad , \tag{1.18}$$

with w_0 the reduced mobility between the sites, k the Boltzmann constant, T_s a simulation temperature which is not the physical temperature.

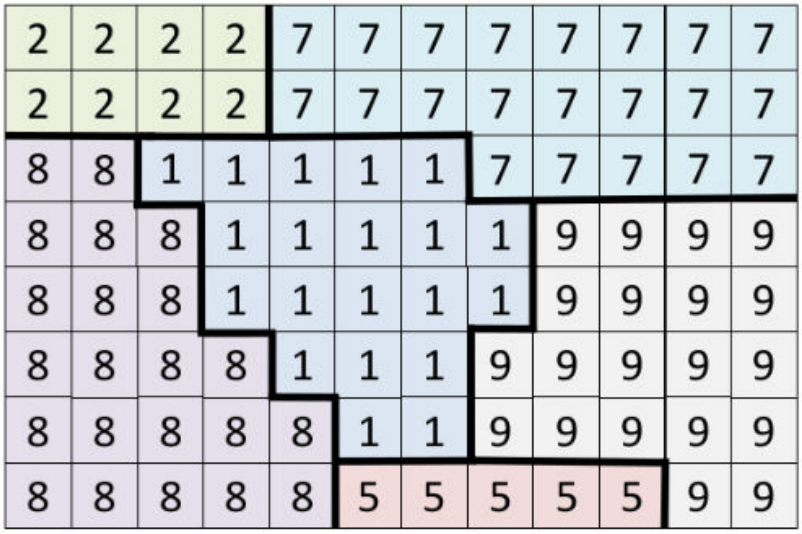

Figure 1.8: Representation of grains (Ids) and their boundaries (Bold lines) in a regular grid of square cells. Figure from [6].

One of the limitations of the MC model is that the morphology of the grains are affected by the mapping into the lattice, and can influence the kinetics of recrystallization. Moreover the MC time step can not be directly related to physical time step, although alternatives have been proposed in the literature [88, 89]. On the other hand the main advantage of the MC model its the simplicity of its implementation even in parallelize calculation context which allows to perform large simulations.

To the knowledge of the author few DDRX MC models have been proposed [90, 91, 68]. The most recent was proposed by Tutcuoglu et al [69], where the authors have proposed a coupled CPFFT/MC formulation. To couple the two approaches, the authors use a regular square grid that is used for both the CPFFT and the MC calculations. During each time step of the simulation a CPFFT calculation is performed and the state variables are updated accordingly. After, the MC model is used to evaluate the possibility of state switch. If a state switch is accepted, the related internal state

variables are not updated immediately, but they are updated gradually over several time steps. This gradual updated is used by the authors to prevent convergence problems in the next time step during the following CPFFT calculation. In this work the authors do not mention how the deformation of the domain and its effects are considered. Plus, simulations are presented only up to 2.5% deformation, and the results are not compared with experimental data nor with other models.

Cellular Automata Model

In the CA model, similarly to the MC model, the domain is partitioned into a regular grid, each cell is associated with a series of state variables, and the states are switched according to switching rules. However, in the CA model each simulation step can be regarded as a time step since all the cells are evaluated, and during each time step the states of the cells are only updated at the end of the step, when all evaluations have been performed. A common switching rule considers the probability of updating the state of a cell as:

$$P(\text{switch}) = \frac{v_{GB}}{v_{GB}^{max}} \quad , \tag{1.19}$$

with v_{GB} the local grain boundary velocity and v_{GB}^{max} the maximum grain boundary velocity calculated in the domain for the specific time step. If the switch occurs the state of the neighbour cell is consumed, different switch rules are discussed in [92]. When evaluating the state switch of a cell, a local neighbourhood is considered. Different types of neighbours can be defined for the cells, as shown in figure 1.9. The type of neighbourhood used can be adapted for different cells and different time steps. One important advantage of CA model over the MC model is the consideration of a local velocity, that describes the propagation rate between sites. However, it presents a similar difficult to the MC approach in the description of the grain curvature, since GB are represented by square cells.

As in the previously described models, the appearance of recrystallized grains is modelled according to phenomenological laws, and is represented by modifying the state variables of the cells. In order to account for plastic deformation in CA DDRX simulations, several approaches have been proposed:

Chen et al. [70, 93] proposed a topology transformation technique to account for deformation in 2D CA DDRX simulations. Two coordinate system are defined, one material coordinate system that is deformed according to a specific deformation mode, and one CA coordinate system that is kept constant.

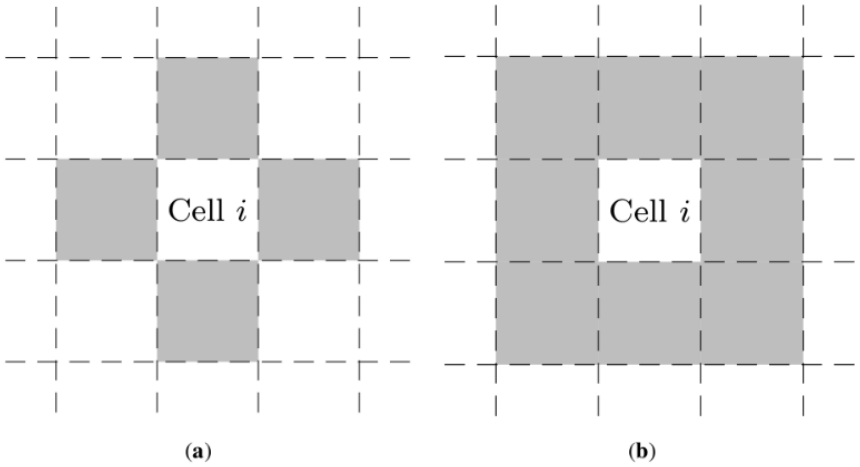

Figure 1.9: Different types of neighbours considered in CA or MC models. (a) von Neumann neighboorhood, (b) Moore neighborhood. Figure from [9].

The GB are transferred from one space to another. The calculation follows the following steps: The evolution of the dislocation density is calculated, according to a phenomenological law, on the material coordinate system which is deformed. When the dislocation reaches the critical value, the GB are mapped to the CA coordinate system. In the CA system the ReX grains are introduced and the GBM calculations are performed by means of the CA model. The CA model considers capillarity effects and the driving force due to energy gradients in the GBM calculations. However, the capillarity effect is considered by assuming that grains are always spherical, so the grains deformation is not considered nor their curvature. The size of the grains is estimated from the area of the cells.

For recrystallized grains, a critical size is not considered. Each recrystallized grain is represented by one cell, and a random orientation is assigned to it when introduced. The initial dislocation density of recrystallized grains is set to zero. A dislocation density density value of zero greatly favors the growth of recrystallized grains, but remains a rough approximation. When the CA calculations are finished, the grains are transferred back to the material system. Figure 1.10 shows an schematic representation of the transformations.

Following the work of Chen et al, Chuan et al [71] extended the previously described approach, and proposed a 2D model that coupled CPFEM with CA to model DDRX. This model also used two grid spaces, one for the CPFEM calculations and the other for the CA calculations. The two grid spaces used

represent the same domain, however they are not equal in resolution. One square cell is used for the CPFEM grid and an assembly of ten by ten cells is used for the CA grid.

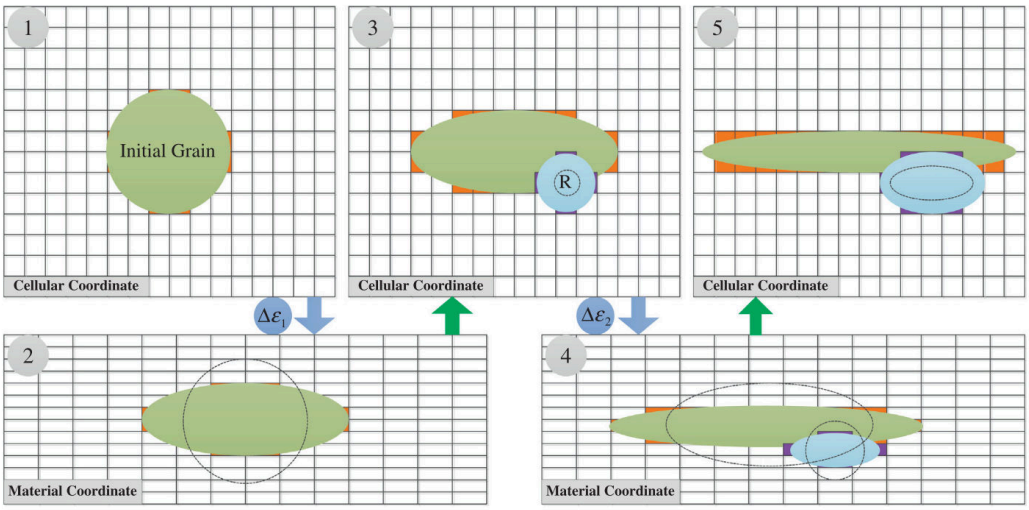

Figure 1.10: Flowchart of the topology transformation technique proposed by Chen et al. [70, 93]. Figure from [70].

In this model, the mapping between the two grids was performed by considering all cells in the CA assembly to respect the same value that the corresponding cell in the CPFEM grid. One of the main limitations of this approach is that the CA model did not affect the CPFEM model, the mapping procedure only includes the strain gradients and orientations mapped from the CPFEM to the CA model. Additionally after deformation, the grids in the CPFEM model, which were deformed, did not correspond correctly to the undeformed CA grids, causing errors in the mapping procedure.

To address these mapping issues Popova et al [72] proposed a 2D model that coupled CPFEM with a CA DDRX model in which only one square grid was used for both the CPFEM calculations and the CA calculations. Since the two models use the same cells, no mapping is required. However, using the same grid for the two models also causes that after deformation, the CA calculations are performed on a deformed grid. The effect of the deformation of the grid on the CA calculations was not considered in this model. In this work the maximal deformation reached was 35%.

The model of Popova et al was further extended to 3D by Li et al [56], this approach is denominated CACPFE. The CACPFE approach addresses the issue of the deformation of the grid and its effect on the CA calculations, illustrated in figure 1.11, by adding a distance criteria to the CA switching

rules: the higher the distance between a cell and its neighbour, the lower the probability that this cell will be consumed.

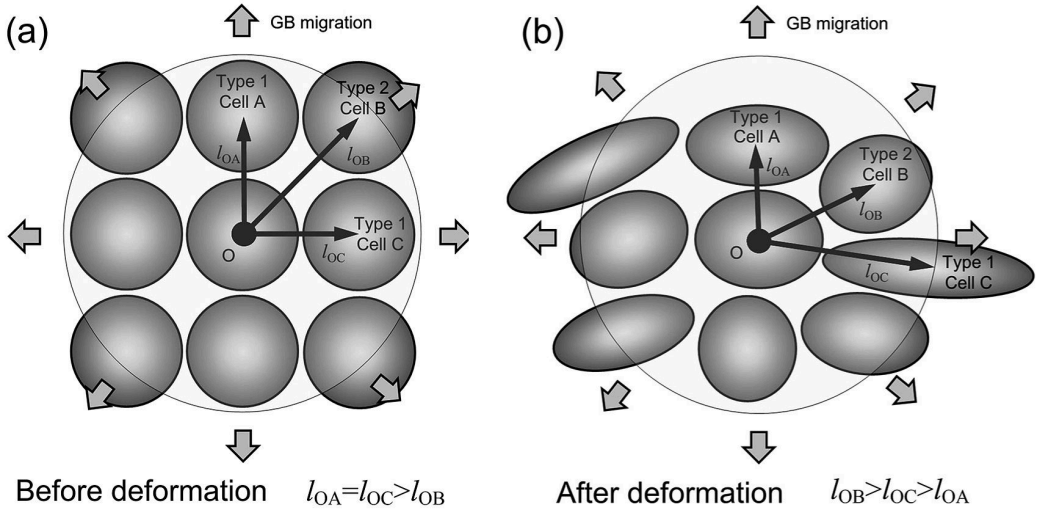

Figure 1.11: Schematic representation of the changes between the cell distances due to plastic deformation in the model of Li et al. [56]. Figure from [56].

Additionally, in order to prevent the number of neighbours of border cells to be reduced, destroying the continuity, a periodic boundary condition is imposed. One additional improvement of this model is that the CPFEM and CA calculations are actually coupled, the variables used in the CPFEM calculation are affected by CA calculations. However, even with the described improvements the maximal deformation reached in this work was 40%.

As an alternative, Madej et al. [94, 95, 73] proposed the coupling of CPFEM with a random CA (RCA) model. The RCA model does not use a regular grid, which means that the traditional definition of neighbours used in CA models can not be used. Instead neighbours are chosen according to a radius criteria, that selects among the connected cells as shown in figure 1.12.

In this model, two grids are generated at the beginning of the simulation, each integration point in the CPFEM grid corresponds to one cell in the RCA grid. After each CPFEM calculation the position of the points are updated on both grids equally. Thus the two grids keep the same shape and deform equally during the simulation. So far the authors publications have addressed mostly the computational developments required to implemented this approach which seems very promising. One particular limitation of this approach is that the value of the radius criteria used has an effect on the

simulation results and on the computational time. Small radius values can reduce the computational cost but also block the evolution of the ReX, since a cell can end with very few or no neighbours. Additionally, following the schematic shown in figure 1.12, in some configurations a cell can interact with neighbours grouped in one specific direction.

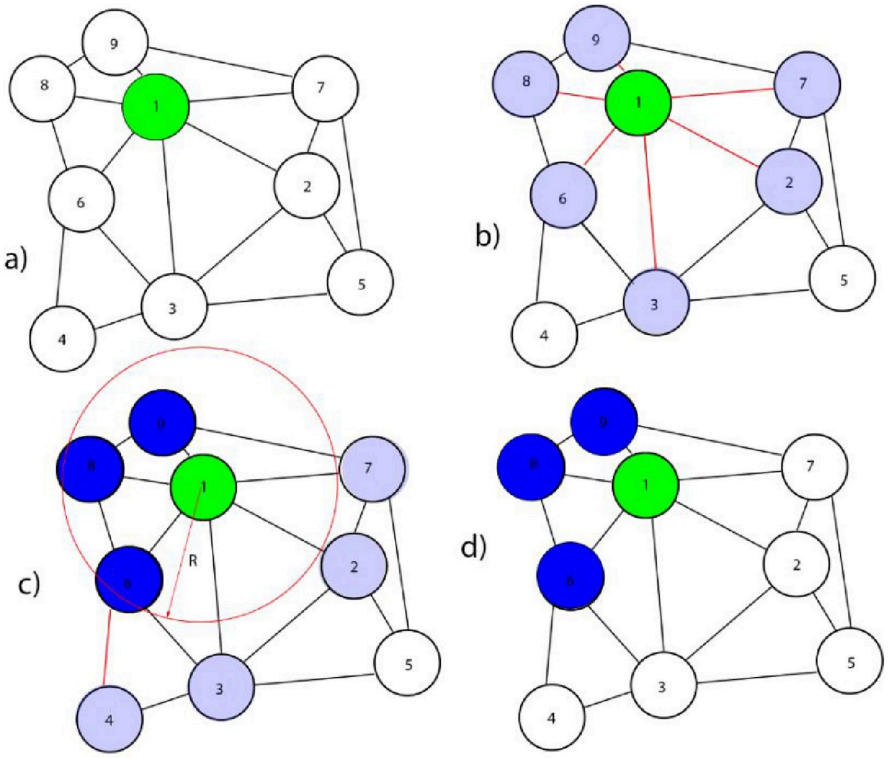

Figure 1.12: Example of a neighbor selection of a green CA cell in the model of Madej et al [94, 95, 73]. Figure from [73].

To summarize, the coupling of MC and CA models to CPFEM simulations remains difficult due to the requirement of an uniform structured grid (with the notable exception of the RCA model). The approaches described to tackle this issue, even though they allow to consider deformation to some degree, cause distortions in the neighbour definition which can lead to non-physically results. Also, since grains are represented by squares cells they present limitations in the description of the grains curvature, so the grains are considered to be always spherical. Finally the models presented so far are not able to reach very large deformations, which are classically encountered in hot metal forming context.

1.2.3 Full field vertex model

In the 2D vertex model [96, 97, 98] the microstructure is represented by only considering the grains boundaries. The grain boundaries are described by a series of line segments connected by nodes, located on the multiple junctions, and virtual nodes located along the grain boundaries, used to describe the curvature, as shown in figure 1.13.

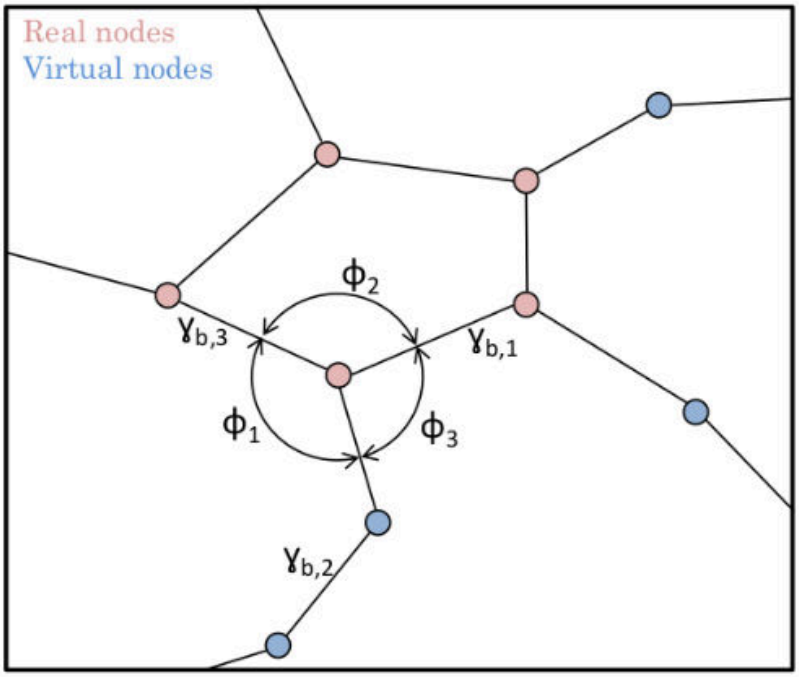

Figure 1.13: Example of the grain boundary representation in the vertex model. Figure from [6].

GBM is calculated by considering the grain boundary energy C on a line segment a and the dissipation rate R, defined as:

$$C(x) = \int_a \gamma_{GB} da \quad , \tag{1.20}$$

$$R(x, v) = \int_a \frac{v_{GB}^2}{M_{GB}} da \quad , \tag{1.21}$$

The motion of single segment k is calculated by solving the equation:

$$\frac{\partial C}{\partial x_k} + \frac{\partial R}{\partial v_{GB\,K}} = 0 \quad . \tag{1.22}$$

After the calculation of v_{GB}, the position of the nodes for a time step is updated as:

$$x(t + \triangle t) = x_k + v_{GB\,k}(t)\triangle t \quad . \tag{1.23}$$

The changes in the topology of the microstructure are considered by applying a series of topological operations, as described in [99]. In 3D, a grain is represented by surfaces, discretized by triangular facets, which describe its boundaries. This increases the difficulty and computational cost of the topological operations required [100]. Most vertex models have been proposed to only model GBM [101, 100, 74], few have been proposed to model DDRX, specially in 3D.

Mellbin et al [102, 103, 75] proposed a 2D DDRX model, that couples a CP Taylor model with a 2D vertex model, along with nucleation laws. The model uses two meshes. One mesh is used to perform the calculations of the vertex model, only nodes on the triple junctions are considered. The GBM calculations include a term related to the stored energy. The second mesh is generated on top of the vertex mesh, placing one node inside of all the grains considered in the vertex mesh. The CP calculations are performed on each node of the second mesh. Figure 1.14 shows the two meshes used. During deformation the two meshes are updated simultaneously during all the simulation.

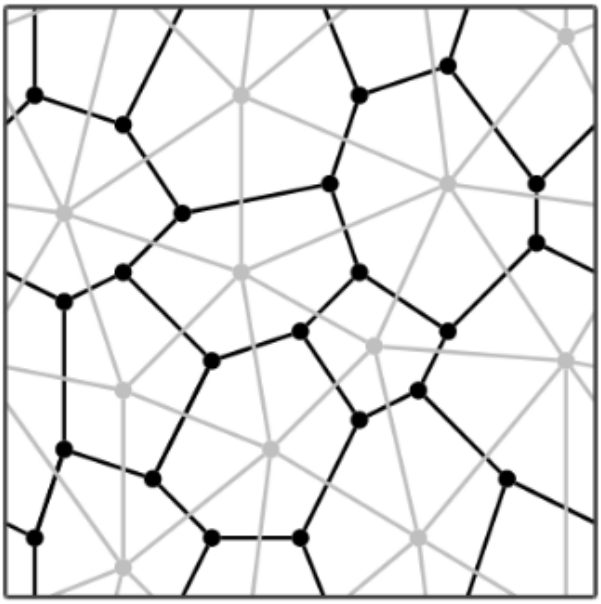

Figure 1.14: Representation of the two meshes used in the model proposed by Melbin et al [102, 103, 75]. Figure from [102].

The coupling algorithm uses a staggered approach, in which several CP time steps are calculated for each vertex time step. This is done since the CP time step depends on the strain rate and is smaller than the time step in the vertex model, that is defined according to the segments lengths and the nodes velocities. One limitation of the current approach is that the CP Taylor model used, does not consider heterogeneous deformation nor grains interactions. Additionally in a 2D formulation the ways that the crystal can deform and rotate to accommodate plastic deformation are reduced. This increases the deformation and rotation in the available directions, leading to over predictions.

1.2.4 Phase field model

Phase field (PF) models described the microstructure by PF variables. PF variables are continuous functions in space and time, that represent a local structure. Inside each grain, the PF variables keeps a constant value (classically 1 inside the grain and 0 outside). The GB are represented as diffuse interfaces through the PF variable. Thanks to this diffuse interface formulation, there is no need to explicitly track the location of the interfaces as in sharp interface models (e.g., vertex models). Figure 1.15 illustrates a PF variable along an interface.

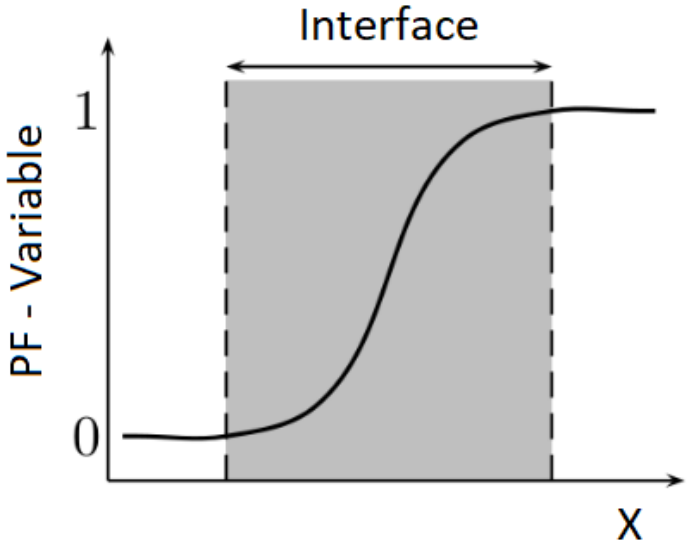

Figure 1.15: PF variable along an interface, diffuse interface representation.

Considering that the driving force for ReX is the minimization of energy, in the PF framework the free energy of the system, described as a functional of the PF variables and their gradients, is minimized. The energy functional of multiphase system composed of k PF variables (η_k) under constant temperature can be described as [104, 105, 106]:

$$F = \int_V \left[f(n_k) + \sum_{k=1}^{N} \frac{K_k}{2} (\nabla \eta_k)^2 \right] dV \quad , \tag{1.24}$$

with V the total volume, f the local energy density function, K_k a gradient energy coefficient that controls the gradients influence. This parameter is related to the diffuseness and thus to the width of the interface (numerical width which differs generally from the physical one). The evolution laws are defined from f as:

$$\dot{\eta}_k = -L_k \frac{\delta F}{\delta n_k} \quad , \tag{1.25}$$

with L_k a kinetic coefficient related to the grain boundary mobility. The evolution law is then solved using finite differences, finite elements or spectral algorithms (FFT). In order to correctly solve the behaviour at the interfaces, a fine grid is generally required. This results in high computational cost which is one of the main limitations of this numerical approach, specially for domains considering a high number of grains.

Coupling CP calculations with PF-DDRX calculations implies a significant increase of computational cost, in a method that is already limited by its own computational cost. Thus, most of the models found in the literature performing this coupling use spectral algorithms, so they require structured meshes and periodic boundary conditions.

Among the models found in the literature we can cite: the model by Zhao et al [107, 82] that couples the CPFFT model proposed by [108] with the PF-FFT model for recrystallization proposed by [109]. In the model coupling, two different grids are used, one for the CPFFT calculations and one for the PF calculations. The PF grid is constructed by dividing the CPFFT grid into smaller cells. The values of the variables from the CPFFT calculations are linearly interpolated to the PF grid, except the orientation values which uses a nearest neighbour interpolation. In the coupling algorithm the PF calculations are only performed once a nucleation event occurs.

To define when nucleation occurs, a probability function, which defines the occurrence of a nucleation event, is associated with the dislocation density field from the CPFFT calculations. Since nucleation events occur at a smaller scale than the CPFFT grid, the effect of nucleation only reduces partially

the dislocation density according to a softening parameter that is calibrated. After the dislocation density is updated, the stress fields are recalculated by using the same strain field in order to prevent convergence problems before performing the next CPFFT calculation. In this work the maximal plastic deformation reached was 50%, however the authors do not clarify how they deal with the distortion of the grid, to reach this deformation levels.

The model by Kujirai et al. [83], couples the CPFEM model of [110] with a PF model based on the works of [111] in 2D. The PF equations in this work are solved using a finite difference scheme. In this work two grids are used, the CPFEM model uses a triangular mesh, while PF calculations are performed on a square grid.

The general coupling procedure is similar to previously described procedures. First, the CPFEM calculation is performed and the state variables are updated. After, the dislocation density is evaluated and recrystallized grains are introduced where the dislocation density reaches a critical value (defined according to a phenomenological law). When a recrystallized grain is introduced, it is assigned a minimal dislocation density, a random orientation and its accumulated deformation is set to zero. Once the recrystallized grains have been introduced, the state variables are interpolated to the PF grid. The interpolation is done by assigning the value of the element in the FE mesh, to all the points of the PF grid located inside the element. The PF calculation is then performed. In this work, the grid used for the PF calculations has a higher resolution than the FE mesh. However, from the article it is not clear how the PF grid is deformed and the tests presented do not describe deformation levels higher than $\epsilon = 0.30$ during simple shear.

1.2.5 Full field level-set method

The level-set (LS) method used in this work, describes grains by using distance functions that measure the euclidean distance to the grain interface, the method is described in detail in chapter 3. In this work we extend the DRX model of Maire [79, 6] that models DRX by coupling a LS framework, based on works of [77, 78, 112], with phenomenological laws. One of the advantages of this model compared to the models found in the literature is its ability to model DRX up to very large deformation levels. However it is currently limited by the phenomenological description of plastic deformation.

1.3 Summary and Discussion

In this chapter we have reviewed the different approaches proposed in the literature to model DDRX, and the different approaches used to describe plastic deformation in the context of DDRX modeling. The reviewed works showed that:

- DDRX models are generally coupled with simplified plasticity or deformation models. A natural perspective is to go toward a coupling with CP formulations, since CP formulations provide a better description of dislocation density evolution during plastic deformation.
- Mean field DDRX models have the advantage of having low computational cost when compared with full field models, however they are not able to describe heterogeneous deformation, intragranular heterogeneity nor local neighbour interactions.
- Due to the complexity of the mechanism involved in DRX, there are no formulations that fully couple and solve a system of equations considering appearance of recrystallized grains, GBM and plastic deformation. Instead a staggered approach is classically used in which for each DDRX time step the different mechanisms (plastic deformation, GBM, appearance of recrystallized grains) are considered as acting one after another in sequence.
- The use of a staggered approach requires the implementation of an appropriate interpolation framework. One common limitation encountered is that the effects of GBM are not considered in the CP calculations.
- The sequence usually used in staggered approaches is defined as: first compute plastic deformation, next insert recrystallized grains, and last calculate GBM.
- The time step required to solve correctly the equations describing CP is usually smaller than the time step required to solve the equations describing GBM. So, several models use different time steps for the two steps, meaning that the GBM calculation is not performed at every mechanical time step. In several models, this step is only performed when recrystallized grains are introduced.
- Considering deformation and most significant heterogeneous deformation is not easily considered in DDRX models, since assumptions around

grain shape or requirements of uniform structured grids are part of numerous DDRX models.

- Computational cost is an important limitation in coupling full field DDRX models with CP formulations, this aspect has drastically limited the number of 3D full field coupled models available in the literature. One common approach used to minimize the computational cost, specially in PF formulations, is the use of FFT instead of FEM. However the requirements of structured grids limits drastically their ability to consider heterogeneous plastic deformation up to high levels, as encountered in classical hot metal forming simulations.

From this review, none of the proposed models is able to simulate DDRX up to high deformation levels in 3D considering heterogeneous plastic deformation. This is the main perspective of these works. The first step is the development of our CP model which will be presented in the next chapter.

1.4 Résumé en Français

Dans ce chapitre, nous avons passé en revue les différentes approches proposées dans la littérature permettant de décrire l'évolution des densités de dislocation due à la déformation plastique en recristallisation dynamique discontinue (DDRX). Les travaux examinés ont montré que:

- Les modèles en DDRX sont généralement associés à des modèles de plasticité ou de déformation simplifiés. Une perspective naturelle est d'aller vers un couplage avec les formulations CP, car les formulations CP fournissent une meilleure description de l'évolution de la densité de dislocation lors de la déformation plastique.

- En raison de la complexité des mécanismes impliqués en DDRX, il n'y a pas de formulations qui couplent et résolvent complètement un système d'équations considérant l'apparition de grains recristallisés, le migration des joints de grains (GBM) et la déformation plastique. Au contraire, une approche échelonnée est classiquement utilisée dans laquelle pour chaque pas de temps en DDRX, les différents mécanismes (déformation plastique, GBM, apparition de grains recristallisés) sont considérés comme agissant les uns après les autres de maniere sequentielle.

- L'utilisation d'une approche échelonnée nécessite que les différents champs variables qui décrivent la microstructure soient affectés par tous les calculs (déformation plastique, GBM, apparition de grains recristallisés). Cela nécessite la mise en œuvre d'un cadre d'interpolation approprié.

- La séquence est généralement définie comme suit: calcul de la déformation plastique, insertion des grains recristallisés, puis GBM.

- Le pas de temps requis pour résoudre correctement les équations décrivant la plasticité cristalline est généralement plus petit que le pas de temps requis pour résoudre les équations liées à la GBM. Ainsi, en général des pas de temps différents sont utilisés pour les deux étapes. Dans certains modèles, l'étape de GBM n'est effectuée que lorsque des grains recristallisés sont introduits.

- La prise en compte de la déformation et de la déformation hétérogène n'est pas facilement prise en compte dans les modèles DRX car les hypothèses concernant la forme des grains ou les exigences de grilles structurées uniformes font partie des hypothèses récurrentes dans l'état de l'art.

- Le coût de calcul est une limitation importante dans le couplage de modèles DDRX en champ complet avec des formulations CP. Cet aspect limite considérablement le nombre de modèles couplés 3D en champ complet disponibles dans la litérature. Une approche utilisée pour minimiser le coût de calcul, en particulier dans les formulations champ de phases réside à utiliser des résolutions de type transformée de Fourier rapide sur grilles régulières. Cependant, l'utilisation des grilles structurées limite considérablement la capacité à prendre en compte la déformation plastique hétérogène jusqu'à des niveaux élevés, comme rencontre classiquement dans les conditions thermomécaniques de mise en forme à chaud.

Afin de répondre à ces besoins et aux limites existantes, une approche de type CPFEM dans un contexte level-set est envisagé et développé dans la suite.

Chapter 2

Crystal plasticity library

2.1 Introduction

The first numerical step of this work concerns the development of a crystal plasticity library, that provides a precise description of the mechanical behaviour of polycrystal aggregates. This chapter is dedicate to the description of the developed CP library and includes the descriptions of: the single crystal model formulation, the numerical implementation procedure, the polycrystal models and the tests used to validate these developments.

2.2 Single crystal model kinematics

The single crystal model used follows the work of [113] and is based on an elasto-viscoplastic formulation. The elasto-viscoplastic formulation is an extended version of the viscoplastic formulation to include elastic effects. Considering the generalized Schmidt law:

$$\tau^{\alpha} = \boldsymbol{\sigma} : (\boldsymbol{m}^{\alpha} \otimes \boldsymbol{n}^{\alpha}) \quad , \tag{2.1}$$

for slip occurrence on a slip system α, τ^{α} must be higher than the slip system strength, represented by its critical resolved shear stress (CRSS) (τ_C^{α}). For multiple slip the Taylor-Bishop-Hill model [19, 114] considers that a crystal can accommodate any plastic deformation by activating only five slip systems. In the Taylor model [19], the slip systems activated are the ones that minimize the energy dissipated during slip. This approach considers that all slip systems have the same initial τ_C^{α} and that they harden at the same rate.

Bishop and Hill [114] proposed an alternative approach that considers the problem in terms of stress. In this approach, the goal is to find the stress state that allows for multiple slip. The stress state chosen is the one

that maximizes the plastic work. The Bishop-Hill approach is equivalent to the Taylor approach if the τ_C^α and their evolution (hardening) are considered equal for all slip systems. However, one limitation of the Taylor-Bishop-Hill is that it requires robust numerical procedures to determine the set of slip systems activated and to prevent the appearance of singular matrices because of the non-uniqueness of the sets of slip systems.

To avoid the problems derived from determining the active slip systems, the viscoplastic formulation [115] considers that all slip systems are active in the crystal. Thus, all slip systems contribute to accommodate plastic deformation. In the viscoplastic formulation the flow rules that determine the slip rate ($\dot{\gamma}^\alpha$) of a slip system due to the acting τ^α, are generally exponential laws. So, instead of describing $\dot{\gamma}^\alpha$ with a heaviside type function, that jumps from zero to a defined value when τ^α reaches τ_C^α, $\dot{\gamma}^\alpha$ is described by continuous function with a sharp increasing slope around τ_C^α. When τ^α is smaller than τ_C^α, the value of $\dot{\gamma}^\alpha$ is very close to zero. Viscoplastic flow rules are further discussed in section 2.3.

Considering slip as the principal deformation mechanism, the single crystal kinematic are described based on the multiplicative decomposition of the deformation gradient tensor $\mathbf{F}$ into: An elastic part $\mathbf{F}_e$ and a plastic part $\mathbf{F}_p$. The elastic deformation gradient is further decomposed into the left elastic stretch tensor $\mathbf{V}_e$ and the elastic rotation tensor $\mathbf{R}_e$.

$$\mathbf{F} = \mathbf{F}_e\mathbf{F}_p = \mathbf{V}_e\mathbf{R}_e\mathbf{F}_p \quad . \tag{2.2}$$

The plastic deformation gradient leads the body from the initial configuration B_0, to the intermediate configuration $\bar{B}$, lattice orientation does not change. The elastic rotation leads the body to an additional intermediate configuration $\tilde{B}$, the lattice orientation changes. Finally the elastic stretch leads the body to the final configuration B. Figure 2.1 illustrates the mentioned transformations.

The configuration B_0 describes the crystal in a local coordinate system. In a global coordinate system B_0 is reached by rotating the crystal according to its initial orientation described by its initial texture. The configuration $\tilde{B}$, used to write the constitutive equations in this work, can be obtained by elastically unloading the crystal form the current configuration, through $\boldsymbol{V}_e^{-1}$.

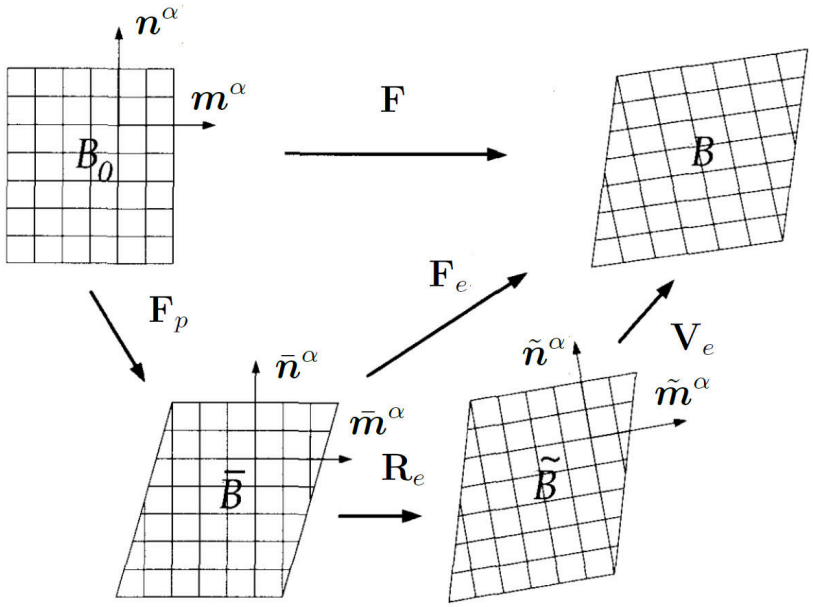

Figure 2.1: Multiplicative decomposition of the deformation gradient tensor **F**. Image modified from [113].

So, following the kinematic decomposition described in Eq. 2.2, the velocity gradient ($\boldsymbol{l}$) is defined as:

$$\begin{aligned} \boldsymbol{l} &= \dot{\boldsymbol{F}}\boldsymbol{F}^{-1} = \dot{\boldsymbol{V}}_e\boldsymbol{V}_e^{-1} + \boldsymbol{V}_e\tilde{\boldsymbol{L}}^*\boldsymbol{V}_e^{-1} \quad , \\ \tilde{\boldsymbol{L}}^* &= \dot{\boldsymbol{R}}_e\boldsymbol{R}_e^T + \boldsymbol{R}_e\bar{\boldsymbol{L}}_p\boldsymbol{R}_e^T \quad . \end{aligned} \tag{2.3}$$

Since in the viscoplastic formulation all slip systems are considered to be active, the plastic velocity gradient $\bar{\boldsymbol{L}}_p$ in $\tilde{B}$ is:

$$\bar{\boldsymbol{L}}_p = \sum_{\alpha=1}^{N} \dot{\gamma}^\alpha \left(\bar{\boldsymbol{m}}^\alpha \otimes \bar{\boldsymbol{n}}^\alpha\right) \quad , \tag{2.4}$$

with N the number of slip systems in the crystal. The orientation of the slip systems is defined by $\bar{\boldsymbol{Z}}^\alpha = \bar{\boldsymbol{m}}^\alpha \otimes \bar{\boldsymbol{n}}^\alpha$, the Schmidt tensor.

The velocity gradient is further decomposed into its symmetric and skew-symmetric parts as: $\boldsymbol{l} = \boldsymbol{d} + \boldsymbol{w}$, with $\boldsymbol{d} = \text{sym}(\boldsymbol{l})$ and $\boldsymbol{w} = \text{skew}(\boldsymbol{l})$. For a tensor $\mathbf{A}$, the skew operation is defined as $\text{skew}(\mathbf{A}) = 1/2(\mathbf{A} - \mathbf{A}^\mathbf{T})$ and the sym operation is defined as $\text{sym}(\mathbf{A}) = 1/2(\mathbf{A} + \mathbf{A}^\mathbf{T})$. This decomposition leads to:

$$\tilde{\boldsymbol{D}} = \dot{\tilde{\boldsymbol{E}}}_e + \tilde{\boldsymbol{D}}^* \quad , \tag{2.5}$$

$$\tilde{\boldsymbol{D}}^* = \text{sym}(\tilde{\boldsymbol{C}}_e\tilde{\boldsymbol{\Omega}}_e) + \sum_{\alpha=1}^{N}\dot{\gamma}^\alpha \text{sym}(\tilde{\boldsymbol{C}}_e\tilde{\boldsymbol{Z}}^\alpha) \quad , \tag{2.6}$$

$$\tilde{\boldsymbol{D}} = \text{skew}(\boldsymbol{V}_e^T\dot{\boldsymbol{V}}_e) + \tilde{\boldsymbol{W}}^* \quad , \tag{2.7}$$

$$\tilde{\boldsymbol{W}}^* = \text{skew}(\tilde{\boldsymbol{C}}_e\tilde{\boldsymbol{\Omega}}_e) + \sum_{\alpha=1}^{N}\dot{\gamma}^\alpha \text{skew}(\tilde{\boldsymbol{C}}_e\tilde{\boldsymbol{Z}}^\alpha) \quad , \tag{2.8}$$

with $\tilde{\boldsymbol{\Omega}}_e = \dot{\mathbf{R}}_e\mathbf{R}_e^T$ the spin of the lattice, $\tilde{\boldsymbol{Z}}^\alpha = \tilde{\mathbf{m}}^\alpha \otimes \tilde{\mathbf{b}}^\alpha$ the rotated Schmidt tensor, $\tilde{\mathbf{m}}^\alpha = \mathbf{R}_e\mathbf{m}^\alpha$ the rotated vector in the slip plane direction, $\tilde{\mathbf{n}}^\alpha = \mathbf{R}_e\mathbf{n}^\alpha$ the rotated vector normal to the slip plane, $\tilde{\boldsymbol{C}}_e = \boldsymbol{V}_e^T\boldsymbol{V}_e$ the elastic right Cauchy-Green tensor and $\tilde{\boldsymbol{E}}_e = 1/2(\tilde{\boldsymbol{C}}_e - 1)$ the elastic strain tensor. The work conjugate of $\tilde{\boldsymbol{E}}_e$ is the second Piola-Kirchhof stress $\tilde{\S}$, and the elastic relationship is given by:

$$\tilde{\S} = \tilde{\mathscr{C}}_e : \tilde{\boldsymbol{E}}_e \quad , \tag{2.9}$$

with $\tilde{\mathscr{C}}_e$ the elasticity tensor, rotated to the lattice current orientation. Considering that the elastic strains are orders of magnitude lower than the plastic strains, the infinitesimal strain assumption is introduced:

$$\mathbf{V}_e = \mathbf{1} + \boldsymbol{\epsilon}_e \quad \text{with} \quad \|\boldsymbol{\epsilon}_e\| << 1 \quad , \tag{2.10}$$

with $\boldsymbol{\epsilon}_e$ the infinitesimal elastic deformation tensor. This causes that the configurations B and $\tilde{B}$ differ only by an infinitesimal amount, thus $\dot{\boldsymbol{V}}_e = \dot{\boldsymbol{\epsilon}}_e$ and the following approximations can be introduced: $\tilde{\boldsymbol{D}} \approx \boldsymbol{d}$, $\tilde{\boldsymbol{W}} \approx \boldsymbol{w}$, $\text{skew}(\tilde{\boldsymbol{V}}_e^T\dot{\boldsymbol{V}}_e) \approx \text{skew}(\dot{\boldsymbol{\epsilon}}_e\boldsymbol{\epsilon}_e)$, $\tilde{\boldsymbol{C}}_e \approx 1$, $\tilde{\boldsymbol{E}}_e \approx \boldsymbol{\epsilon}_e$, $\tilde{\S} \approx \boldsymbol{\tau}$, with $\boldsymbol{\tau}$ the Kirchhoff stress related to the Cauchy stress $\boldsymbol{\sigma}$ by $\boldsymbol{\tau} = \det(\boldsymbol{F})\boldsymbol{\sigma}$, with $\det(\boldsymbol{F}) \approx \det(\mathbf{1}+\boldsymbol{\epsilon_e})$. These approximations plus:

$$\tilde{\boldsymbol{D}}^* \approx 2\text{sym}(\boldsymbol{\epsilon}_e\tilde{\boldsymbol{\Omega}}_e) + \sum_{\alpha=1}^{N}\dot{\gamma}^\alpha \text{sym}(\tilde{\boldsymbol{Z}}^\alpha) \quad , \tag{2.11}$$

$$\tilde{\boldsymbol{W}}^* \approx \tilde{\boldsymbol{\Omega}}_e + \sum_{\alpha=1}^{N}\dot{\gamma}^\alpha \text{skew}(\tilde{\boldsymbol{Z}}^\alpha) \quad , \tag{2.12}$$

allow to reduce the single crystal model kinematics to:

Kinematics

$$\mathbf{d} = \dot{\boldsymbol{\epsilon}}_e + \boldsymbol{\epsilon}_e \tilde{\boldsymbol{\Omega}}_e - \tilde{\boldsymbol{\Omega}}_e \boldsymbol{\epsilon}_e + \tilde{\mathbf{D}}_p \quad , \tag{2.13}$$

$$\mathbf{w} = -skew\left(\dot{\boldsymbol{\epsilon}}_e \boldsymbol{\epsilon}_e\right) + \tilde{\boldsymbol{\Omega}}_e + \tilde{\mathbf{W}}_p \quad , \tag{2.14}$$

Elasticity

$$\boldsymbol{\tau} = \tilde{\mathscr{C}}_e : \boldsymbol{\epsilon}_e \quad , \tag{2.15}$$

Plasticity

$$\tilde{\mathbf{D}}_p = \sum_{\alpha=1}^{n} \dot{\gamma}^\alpha sym\left(\tilde{\mathbf{Z}}^\alpha\right) \quad , \tag{2.16}$$

$$\tilde{\mathbf{W}}_p = \sum_{\alpha=1}^{n} \dot{\gamma}^\alpha skew\left(\tilde{\mathbf{Z}}^\alpha\right) \quad , \tag{2.17}$$

Schmid law

$$\tau^\alpha = \boldsymbol{\tau} : sym\left(\tilde{\mathbf{Z}}^\alpha\right) \quad . \tag{2.18}$$

Flow and hardening rules

$$\dot{\gamma}^\alpha = f\left(\tau^\alpha, \tau_C^\alpha\right) \quad , \tag{2.19}$$

$$\dot{\tau}_c^\alpha = \dot{g}\left(\tau_C^\alpha, \dot{\gamma}\right) \quad . \tag{2.20}$$

The single crystal model is completed by defining the flow rule f and the hardening rule $\dot{g}$. Several flow rules and hardening rules are available in the literature, some of them will be described in the following.

2.3 Crystal flow rules and hardening rules

As mentioned above flow rules and hardening rules define the magnitude of the slip rates $\dot{\gamma}^\alpha$ caused by applied stress and the material strength and its evolution. Following the work of [16] they can be classified into phenomenological models or dislocation based models, depending on weather or not they consider the evolution of dislocations densities (ρ) explicitly (dislocation based).

2.3.1 Phenomenological models

Phenomenological flow rules

In general, viscoplastic phenomenological models define the slip rates $\dot{\gamma}^\alpha$ as function of τ^α and τ_C^α:

$$\dot{\gamma}^\alpha = f\left(\tau^\alpha, \tau_C^\alpha\right) , \tag{2.21}$$

the most common functions found in the literature are power laws of the form [116, 117, 30, 118, 119]:

$$\dot{\gamma}^\alpha = \dot{\gamma}_0^\alpha \left| \frac{\tau^\alpha}{\tau_C^\alpha} \right|^{\frac{1}{m}} \mathrm{sing}(\tau^\alpha) , \tag{2.22}$$

with m a material parameter, and $\dot{\gamma}_0^\alpha$ the reference slip rate. Or extended ones [113]:

$$\dot{\gamma}^\alpha = \dot{\gamma}_0 \exp\left\{ -\frac{F_0}{k\theta} \left[1 - \left(\frac{|\tau^\alpha| - \tau_C^\alpha}{\tau_C^\alpha} \right)^p \right]^q \right\} sign(\tau^\alpha) , \tag{2.23}$$

with F_0 the Helmholtz free energy of activation p, q material parameters, k the Boltzmann constant and θ the absolute temperature. As mentioned before, one important characteristic of theses type of flow rules is that any stress will induce strain rate. However low values of τ^α will induce negligible strain rates. One limitation of this type of description is that the high gradient described around the value τ_C^α, can lead to convergence issues when τ^α is much higher than τ_C^α.

Phenomenological hardening rules

The evolution of the material resistance is defined by the evolution of the CRSS τ_C^α defined as:

$$\dot{\tau}_{CRSS}^\alpha = \dot{g}\left(\tau_c^\alpha, \dot{\gamma}\right) . \tag{2.24}$$

The most common functions found in the literature include functions of the form [116, 117, 30, 118]:

$$\dot{\tau}_c^\alpha = \sum_{\beta=1}^{n} h_{\alpha\beta} \left| \dot{\gamma}^\beta \right| , \tag{2.25}$$

with $h_{\alpha\beta}$ the interaction matrix, defined as:

$$h_{\alpha\beta} = q_{\alpha\beta}\left[h_0\left(1 - \frac{\tau_C^\beta}{\tau_s}\right)^a\right], \tag{2.26}$$

with h_0, a, and τ_s material hardening parameters. The parameters $q_{\alpha\beta}$ which takes the value of 1 for co-planar slip systems and the value of 1.4 for non co-planar slip systems, describe latent hardening. Latent hardening describes how the accumulation of dislocations in one slip system affects the other slip systems. Thus, it depends on the relations between the slip systems.

One simplification that can be introduced, following the Taylor model [19], is that all slips systems will have same initial τ_C^α and will harden equally. This simplification reduces the number of variables that need to be considered when solving the system, by considering only one τ_C instead of N (number of slip systems). By reducing the number of variables, the numerical solution of the equations is simplified and convergence is more easily achieved. However, depending of the material, it could be a strong assumption. One example, are Voce type saturation laws [113, 119]:

$$\dot{\tau}_c = H_0\left(\frac{\tau_{sat} - \tau_C}{\tau_{sat} - \tau_0}\right)\sum_\beta \left|\dot{\gamma}^\beta\right|, \tag{2.27}$$

with τ_{sat} the saturation value and τ_0 a reference value. Since only one value of τ_C is considered, latent hardening and any other interaction between the slip systems are neglected. Other phenomenological models use the Taylor hypothesis to defined τ_C as [120, 121]:

$$\tau_C = \tau_0 + \psi\mu b\sqrt{\rho}\,, \tag{2.28}$$

with $\tau_0 = \sigma_0/M$ the initial microscopic yield stress of the material, σ_0 the macroscopic yield stress of the material, ψ a material dependent parameter, b the burger's vector magnitude, M the Taylor factor, and ρ the dislocation density. The evolution of τ_C is determined by the evolution of the dislocation defined by laws of the form of [44]:

$$\frac{\partial\rho}{\partial\epsilon} = K_1\rho^\xi - K_2\rho\,. \tag{2.29}$$

As introduced in chapter 1 this law can represent the well known Yoshie-Laasroui-Jonas equation [45] when $\xi = 0$, and the Kocks-Mecking equation [46, 47] when $\xi = 1/2$. The parameter K_1 describes the accumulation of dislocations due to plastic strain, and the parameter K_2 describes the effect of dynamic recovery. However, even if these type of laws includes the dislocation density as a parameter, they are not regarded as dislocation based

laws. Because, no physical mechanism related to the dislocation motion are explicitly considered when describing the evolution of the dislocation density.

2.3.2 Dislocation based models

Dislocation based models define the slip rates magnitude $\dot{\gamma}^\alpha$ as function of the movement of dislocations, and the hardening rule is defined as the evolution of dislocations densities. Thus, concepts regarding the physical mechanism of dislocation motion are explicitly considered. Among the models found in the literature, we can cite:

Model proposed by Arsenlis et al [32, 122]

In this model four types of dislocations are considered: Edge (e) and screw dislocations (s) divided by their polarity ($+, -$)), the flow rule is defined in terms of the dislocations fluxes:

$$\dot{\gamma}^\alpha = \left(\rho^\alpha_{e+} v^\alpha_{e+} + \rho^\alpha_{e-} v^\alpha_{e-} + \rho^\alpha_{s+} v^\alpha_{s+} + \rho^\alpha_{s-} v^\alpha_{s-}\right) |b^\alpha| \,, \tag{2.30}$$

with v the average velocity of the dislocation density and b the burgers vector. The product of the dislocation density and it's velocity is the dislocation flux.

The hardening rule is modeled by the evolution of each type of dislocation density, for a dislocation of type $\xi \in \{e+, e-, s+, s-\}$. The evolution equation considers generation, annihilation and accumulation/loss by dislocation flux such as:

$$\dot{\rho}^\xi = \dot{\rho}^\xi_{gen} + \dot{\rho}^\xi_{ann} + \dot{\rho}^\xi_{flux} \,. \tag{2.31}$$

Model proposed by Cheong and Busso [123]

The model considers a flow rule similar to equation 2.23:

$$\dot{\gamma}^\alpha = \dot{\gamma}_0 \exp\left\{-\frac{F_0}{k\theta}\left[1 - \left(\frac{|\tau^\alpha| - S^\alpha_T}{\hat{\tau}}\right)^p\right]^q\right\} \mathrm{sign}(\tau^\alpha) \,, \tag{2.32}$$

with S^α_T the total athermal slip resistance to dislocation motion and $\hat{\tau}$ a function of the shear modulus μ:

$$\hat{\tau} = \hat{\tau}_0 \frac{\mu(\theta)}{\mu} \,, \tag{2.33}$$

with $\hat{\tau}_0$ and μ_0 the reference values at a temperature of 0 K.

The hardening rule is defined as the evolution of S_T^α, as a function of edge p_e^α and screw p_s^α dislocations densities:

$$S_T^\alpha = \lambda \mu b^\alpha \sqrt{\sum_{\beta=1}^{N_{slip}} \left[h^{\alpha\beta} \left(\rho_e^\beta + \rho_s^\beta \right) \right]}, \tag{2.34}$$

with λ a statistical coefficient that accounts for the deviation from the regular spatial arrangements of the dislocation, b^α the magnitude of the Burgers vector and $h^{\alpha\beta}$ the dislocation interaction matrix defined as:

$$h^{\alpha\beta} = \omega_1 + (1 - \omega_2)\, \delta^{\alpha\beta}, \tag{2.35}$$

with $\omega_{1,2}$ the interaction coefficients and $\delta^{\alpha\beta}$ the Kronecker function. The model is completed by defining the rates of generation and annihilation for the types of dislocations considered.

Model proposed by Ma et al [124, 125, 126]

This model considers that in order for dislocation to glide, they must overcome the stress field generated by dislocations located on planes parallel to their slip plane (parallel dislocations ρ_p), and move across dislocations located on planes perpendicular to their slip plane (forest dislocations ρ_f). The density of parallel and forest dislocations are calculated as the projected summation over all the slip systems of statistical stored dislocation density (SSD) ρ_{SSD}^α:

$$\rho_F^\alpha = \sum_{\beta=1}^{N} X^{\alpha\beta} \rho_{SSD}^\beta \left| cos\left(\boldsymbol{n}^\alpha, \boldsymbol{m}^\beta \right) \right|, \tag{2.36}$$

$$\rho_P^\alpha = \sum_{\beta=1}^{N} X^{\alpha\beta} \rho_{SSD}^\beta \left| sin\left(\boldsymbol{n}^\alpha, \boldsymbol{m}^\beta \right) \right|, \tag{2.37}$$

with $X^{\alpha\beta}$ the interaction strength between slip systems. The flow rule is defined by the Orowan equation as:

$$\dot{\gamma}^\alpha = \rho_m^\alpha b v^\alpha, \tag{2.38}$$

with b the magnitude of the burgers vector, v^α the average mobile dislocation velocity, and ρ_m^α the mobile dislocation density calculated as:

$$\rho_m^\alpha = BT \sqrt{\rho_P^\alpha \rho_F^\alpha}, \tag{2.39}$$

with B a combination of physical and numerical parameters. The mobile dislocation velocity is calculated assuming the cutting of forest dislocations as the velocity determining mechanism:

$$v^{\alpha} = \lambda^{\alpha} v_{attack} \exp\left(-\frac{Q_{slip}}{k_B T}\right) \sinh\left(\frac{\tau_{eff}^{\alpha} V^{\alpha}}{k_B T}\right) \text{sign}\left(\tau^{\alpha}\right) , \tag{2.40}$$

with λ^{α} the jump width, v_{attack} the attack frequency, Q_{slip} the activation energy for dislocation glide, V^{α} the effective volume and k_B the Boltzmann constant. The effective shear stress τ_{eff}^{α} is calculated as function of the RSS, CRSS and the forest and parallel dislocation densities. This value is 0 when $\left|\tau_{eff}^{\alpha}\right| \leq \tau_c^{\alpha}$.

The hardening rule is calculated as the rate of change of SSD and takes into consideration mechanism of lock formation, dipole formation, athermal annihilation and thermal annihilation.

2.3.3 Discussion concerning the crystal flow rules and hardening rules

Phenomenological models define the flow rule and hardening rule only in terms of material parameters. Since these parameters do not represent physical quantities, a limited range of temperatures and strain rates in which they are valid exist. However their implementation is relatively easy and have low computational cost compared with the dislocation based models. They are the most used models in the literature and have been shown to be able to model correctly the behaviour of FCC metals.

Dislocation based models try to take into account the nature of dislocation densities and their interaction. Then, once the corresponding parameters are identified, these models can be usable for a wide range of strain rates and temperatures. However they tend to include a higher number of parameters that need to be identified (with generally complex experimental setup), additionally their implementation is more complex and they have higher computational cost than phenomenological models, due to the additional equations introduced. The choice of one model is then dependent on the intended application, material of interest, available material data and computational resources.

2.4 Constitutive Integration procedure

The set of equations that describe the single crystal model constitutes a coupled system of first order ordinary differential equations for $(\boldsymbol{\tau}, \mathbf{R}_e, \tau_C^\alpha)$. Knowing the configuration of the body at a time t_n this system of differential equations must be integrated in order to calculate the configuration at the time $t_{n+1} = t_n + \triangle t$. So, given the configuration at a time time t_n $(\boldsymbol{\tau}_n, \mathbf{R}_{e,n}, \tau_{C,n}^\alpha)$, the loading $\mathbf{d}_{n+1}$ and $\mathbf{w}_{n+1}$, the initial orientation and the material properties, the results of the integration procedure is the configuration at t_{n+1}, $(\boldsymbol{\tau}_{n+1}, \mathbf{R}_{e,n+1}, \tau_{C,n+1}^\alpha)$.

One important remark is that the integration procedure is performed on the sample (fixed) coordinate system. Since the elastic compliance tensor and the Schmidt tensor are defined on a local coordinate system aligned with the lattice, they must be transformed. The transformation is done using a rotation tensor $\mathbf{C}_0$. $\mathbf{C}_0$ is defined according the crystal initial texture, described by means of its Euler angles $(\varphi_1, \phi, \varphi_2)$ (Cocks convention [14]):

$$\mathbf{C}_0 = \begin{bmatrix} \cos\varphi_1\cos\varphi_2 - \sin\varphi_1\cos\phi\sin\varphi_2 & -\cos\varphi_1\cos\varphi_2 - \sin\varphi_1\cos\phi\sin\varphi_2 & \sin\varphi_1\sin\phi \\ \sin\varphi_1\cos\varphi_2 + \cos\varphi_1\cos\phi\sin\varphi_2 & -\sin\varphi_1\sin\varphi_2 + \cos\varphi_1\cos\phi\cos\varphi_2 & -\cos\varphi_1\sin\phi \\ \sin\varphi_2\cos\phi & \cos\varphi_2\sin\phi & \cos\phi \end{bmatrix} . \quad (2.41)$$

Additionally, during deformation the orientation evolves and must be updated according to the lattice rotation. So, for a time t_n, the rotation tensor considering $\mathbf{R}_{e,n}$ is defined as:

$$\mathbf{C}_n = \mathbf{R}_{e,n}\mathbf{C}_0 \quad , \quad (2.42)$$

$\mathbf{C}_n$ is used to update the orientation of the elastic tensor and the Schmidt tensor:

$$\tilde{\mathscr{C}}_{d,n} = (\mathbf{C}_n \otimes \mathbf{C}_n) : \mathscr{C}_e : (\mathbf{C}_n \otimes \mathbf{C}_n)^T \quad , \quad (2.43)$$

$$\tilde{\mathbf{Z}}_n^\alpha = \mathbf{C}_n\mathbf{m}^\alpha \otimes \mathbf{C}_n\mathbf{n}^\alpha \quad . \quad (2.44)$$

For the particular case of materials with linear elastic isotropic behavior $\tilde{\mathscr{C}}_{d,n+1} = \mathscr{C}_e$, so there is no need to update the orientation of the elastic tensor. With that consideration, to integrate the system of equations (Eq. 2.13 to 2.20), the first step is to rewrite Eq. 2.13 as:

$$\dot{\boldsymbol{\epsilon}}_e + \boldsymbol{\epsilon}_e\dot{\mathbf{R}}_e\mathbf{R}_e^T - \dot{\mathbf{R}}_e\mathbf{R}_e^T\boldsymbol{\epsilon}_e = \boldsymbol{R}_e\left[\frac{\partial}{\partial t}(\boldsymbol{R}_e^T\boldsymbol{\epsilon}_e\boldsymbol{R}_e)\right]\boldsymbol{R}_e^T = \mathbf{d} - \tilde{\mathbf{D}}_p \quad , \quad (2.45)$$

from this equation we can write:

$$\frac{\partial}{\partial t}(\boldsymbol{R}_e^T \boldsymbol{\epsilon}_e \boldsymbol{R}_e) = \boldsymbol{R}_e^T(\mathbf{d} - \tilde{\mathbf{D}}_p)\boldsymbol{R}_e \quad , \tag{2.46}$$

next, we integrate using backward Euler scheme:

$$\begin{aligned}\boldsymbol{R}_{e,n+1}^T \boldsymbol{\epsilon}_{e,n+1} \boldsymbol{R}_{e,n+1} = \\ \boldsymbol{R}_{e,n}^T \boldsymbol{\epsilon}_{e,n} \boldsymbol{R}_{e,n} + (\triangle t)\boldsymbol{R}_{e,n+1}^T(\mathbf{d}_{n+1} - \tilde{\mathbf{D}}_{p,n+1})\boldsymbol{R}_{e,n+1} \quad ,\end{aligned} \tag{2.47}$$

and by reorganizing the terms we get:

$$\boldsymbol{\epsilon}_{e,n+1} = \boldsymbol{R}_{e,n+1}\boldsymbol{R}_{e,n}^T \boldsymbol{\epsilon}_{e,n} \boldsymbol{R}_{e,n}\boldsymbol{R}_{e,n+1}^T + (\triangle t)(\mathbf{d}_{n+1} - \tilde{\mathbf{D}}_{p,n+1}) \quad . \tag{2.48}$$

The term $\boldsymbol{R}_{e,n+1}\boldsymbol{R}_{e,n}^T$ describes the increase in the elastic rotation tensor and can be grouped as $\triangle \mathbf{R}_e = \boldsymbol{R}_{e,n+1}\boldsymbol{R}_{e,n}^T$, with its transpose defined as $\triangle \mathbf{R}_e^T = \boldsymbol{R}_{e,n}\boldsymbol{R}_{e,n+1}^T$. Next, considering Eq. 2.16, $\tilde{\mathbf{D}}_{p,n+1}$ can be expressed as:

$$\tilde{\mathbf{D}}_{p,n+1} = \sum_{\alpha=1}^{n} \dot{\gamma}_{n+1}^{\alpha} sym\left(\tilde{\mathbf{Z}}_{n+1}^{\alpha}\right) \quad . \tag{2.49}$$

According to Eq. 2.19, $\dot{\gamma}_{n+1}^{\alpha} = f\left(\tau_{n+1}^{\alpha}, \tau_{C,n+1}^{\alpha}\right)$ (it is defined according to the flow rule). The term $\tilde{\mathbf{Z}}_{n+1}^{\alpha}$ is the Schmidt tensor in the current orientation, defined with the rotation tensor as $\tilde{\mathbf{Z}}_{n+1}^{\alpha} = \mathbf{C}_{n+1}\mathbf{s}^{\alpha} \otimes \mathbf{C}_{n+1}\mathbf{m}^{\alpha}$. From this $\boldsymbol{\epsilon}_{e,n+1}$ can be written as:

$$\boldsymbol{\epsilon}_{e,n+1} = \triangle \mathbf{R}_e \boldsymbol{\epsilon}_{e,n} \triangle \mathbf{R}_e^T + \triangle t \mathbf{d}_{n+1} - \triangle t \sum_{\alpha=1}^{n} \dot{\gamma}_{n+1}^{\alpha} sym\left(\tilde{\mathbf{Z}}_{n+1}^{\alpha}\right) \quad . \tag{2.50}$$

For simplicity, in the following we will use $\boldsymbol{\epsilon}_{e,n+1}^{*} = \triangle \mathbf{R}_e \boldsymbol{\epsilon}_{e,n} \triangle \mathbf{R}_e^T + \triangle t \mathbf{d}_{n+1}$ and $\tilde{\mathbf{P}}_{n+1}^{\alpha} = sym\left(\tilde{\mathbf{Z}}_{n+1}^{\alpha}\right)$. So, we can define:

$$\boldsymbol{\epsilon}_{e,n+1} = \boldsymbol{\epsilon}_{e,n+1}^{*} - \triangle t \sum_{\alpha=1}^{n} \dot{\gamma}_{n+1}^{\alpha} \tilde{\mathbf{P}}_{n+1}^{\alpha} \quad . \tag{2.51}$$

From this equation the deviatoric and isochoric parts of $\boldsymbol{\epsilon}_{e,n+1}$ can be separated. The deviatoric part is:

$$\mathrm{dev}\boldsymbol{\epsilon}_{e,n+1} = \mathrm{dev}\boldsymbol{\epsilon}_{e,n+1}^{*} - \triangle t \sum_{\alpha=1}^{n} \dot{\gamma}_{n+1}^{\alpha} \tilde{\mathbf{P}}_{n+1}^{\alpha} \quad . \tag{2.52}$$

Applying the same treatment to Eq. 2.15, the hydro-static part of $\boldsymbol{\tau}$ is not considered since it does not induce plastic deformation in metals, we get:

$$\text{dev}\boldsymbol{\tau}_{n+1} = \tilde{\mathscr{C}}_{d,n+1} : \text{dev}\boldsymbol{\epsilon}_{e,n+1} \quad , \tag{2.53}$$

with $\tilde{\mathscr{C}}_{d,n+1}$ the rotated fourth order deviatoric elastic tensor. Finally combining Eq. 2.52 and Eq. 2.53, the equation for the evolution of $\boldsymbol{\tau}_n$ is defined as:

$$\tilde{\mathscr{C}}^{-1}_{d,n+1} : \text{dev}\boldsymbol{\tau}_{n+1} = \text{dev}\boldsymbol{\epsilon}^{*}_{e,n+1} - \triangle t \sum_{\alpha=1}^{n} \dot{\gamma}^{\alpha}_{n+1} \tilde{\mathbf{P}}^{\alpha}_{n+1} \quad . \tag{2.54}$$

Next, we consider the evolution of τ^{α}_{C} defined by the hardening rule, Eq. 2.20. The details of the integration procedure depends on the type of hardening rule used. But, in general a backward Euler scheme can be used to obtain the evolution equation:

$$\tau^{\alpha}_{C,n+1} = \tau^{\alpha}_{C,n} + (\triangle t)\dot{g}\left(\tau^{\alpha}_{C,n+1}, \dot{\gamma}^{\alpha}_{n+1}\right) \ , \tag{2.55}$$

For simplified hardening rules, that consider only one τ_{CRSS} for all the slip systems, a forward Euler scheme can also be used to integrate Eq. 2.20:

$$\tau^{\alpha}_{c,n+1} = \tau^{\alpha}_{c,n} + (\triangle t)\dot{g}\left(\tau^{\alpha}_{c,n}, \dot{\gamma}^{\alpha}_{n}\right) \ . \tag{2.56}$$

Finally, to obtain an equation for the evolution of $\boldsymbol{R}_e$, from Eq. 2.14 and Eq. 2.17, the spin of the lattice is defined as:

$$\tilde{\boldsymbol{\Omega}}_{e,n+1} = \mathbf{w}_{n+1} - \sum_{\alpha=1}^{N} \dot{\gamma}^{\alpha}_{n+1} \tilde{\mathbf{Q}}^{\alpha}_{n+1} \ , \tag{2.57}$$

with $\tilde{\mathbf{Q}}^{\alpha}_{n+1}$ the antisymmetric part of $\tilde{\mathbf{Z}}^{\alpha}_{n+1}$. The term $skew\left(\dot{\boldsymbol{\epsilon}}_e \boldsymbol{\epsilon}_e\right)$ is not considered since it is usually small [127]. The integration is then performed using the exponential map [128]:

$$\mathbf{R}_{e,n+1} = exp\left[\left(\tilde{\boldsymbol{\Omega}}_{e,n+1}\right) \triangle t\right] \mathbf{R}_{e,n} \ , \tag{2.58}$$

with the exponential map defined in Einstein notation as:

$$\exp(\Omega_{ik}) = \delta_{ik} + \frac{\sin w}{w}\Omega_{ij} + \frac{1-\cos w}{w^2}\Omega_{il}\Omega_{lk} \ , \tag{2.59}$$

with $w^2 = (1/2)\Omega_{mn}\Omega_{mn}$.

Equations 2.54, 2.55 and 2.58 are a set of coupled nonlinear algebraic equations that can be written in terms of residuals. A classic N-R (Newton

- Raphson strategy) could be used to solve the system of equations, however such a choice would be complex because of the number of variables involved in the calculation. To simplify this step a staggering scheme is used. The staggering scheme is a two levels iterative procedure that allows to solve each equation independently from the others.

In the first level: First Eq. 2.54 is solved using N-R considering only $\text{dev}\boldsymbol{\tau}_{n+1}$ as a variable, the values of $\tau^{\alpha}_{c,n+1}$ and $\mathbf{R}_{e,n+1}$ are kept constant at their best available estimate. To do this, Eq. 2.54 is linearized with respect to $\text{dev}\boldsymbol{\tau}_{n+1}$. This leads to an algebraic system that is solved iteratively for $\triangle\text{dev}\boldsymbol{\tau} = \text{dev}\boldsymbol{\tau}_{n+1} - \text{dev}\boldsymbol{\tau}_{n}$, as described by Eqs. 2.60 and 2.61:

$$R_1 = \tilde{\mathscr{C}}^{-1}_{d,n+1} : \text{dev}\boldsymbol{\tau}_{n+1} - \text{dev}\boldsymbol{\epsilon}^{*}_{e,n+1} + \triangle t \sum_{\alpha=1}^{n} \dot{\gamma}^{\alpha}_{n+1} \tilde{\mathbf{P}}^{\alpha}_{n+1} = 0 \quad , \tag{2.60}$$

$$\left(\tilde{\mathscr{C}}^{-1}_{d,n+1} + \sum_{\alpha=1}^{N} \triangle t \frac{\partial \dot{\gamma}_{n+1}}{\partial \tau^{\alpha}_{n+1}} \left(\tilde{\mathbf{P}}^{\alpha}_{n+1} \otimes \tilde{\mathbf{P}}^{\alpha}_{n+1} \right) \right) : \triangle\text{dev}\boldsymbol{\tau} = - \text{dev}\boldsymbol{\epsilon}_{e,n+1} + \text{dev}\boldsymbol{\epsilon}^{*}_{e,n+1} - \triangle t \sum_{\alpha=1}^{n} \dot{\gamma}^{\alpha}_{n+1} \tilde{\mathbf{P}}^{\alpha}_{n+1} \quad , \tag{2.61}$$

the iterations are performed until the residual R_1 is smaller than a defined tolerance.

In the second step of the first level, Eq. 2.55 is solved considering only $\tau^{\alpha}_{c,n+1}$ as a variable and keeping $\text{dev}\boldsymbol{\tau}_{n+1}$ and $\mathbf{R}_{e,n+1}$ at their best available estimates. If the hardening rule considers different values of τ^{α}_{c} per slip system, a N-R procedure similar to the previously described one is used. If considering only one τ^{α}_{c} for all slip systems, the value of $\tau_{c,n+1}$ can simply be updated using the explicit Euler scheme.

In the third step of the first level, the value of $\mathbf{R}_{e,n+1}$ is updated according to Eq. 2.58. On the second level of the staggered scheme, all the steps of the first level are repeated until the norms of both $\triangle\boldsymbol{\tau}$ and $\triangle\tau^{\alpha}_{c}$ are lower than a tolerance. The steps of the staggered integration scheme are detailed next:

1. Given:
   - The loading $(\mathbf{d}_{n+1}, \mathbf{w}_{n+1})$.
   - The initial orientation $\mathbf{C}_0$.
   - The crystal structure $\mathbf{Z}^{\alpha} = \mathbf{s}^{\alpha} \otimes \mathbf{m}^{\alpha}$.
   - The material properties $\mathscr{C}_e$.

- The initial state $(\boldsymbol{\tau}_n, \mathbf{R}_{e,n}, \tau^{\alpha}_{c,n})$.

2. Calculate the rotation matrix $\mathbf{C}_n = \mathbf{R}_{e,n}\mathbf{C}_0$.
3. Rotate $(\mathbf{Z}^{\alpha}, \mathscr{C}_e)$ to the current orientation:
   - $\tilde{\mathscr{C}}_{e,n+1} = (\mathbf{C}_n \otimes \mathbf{C}_n) : \mathscr{C}_e : (\mathbf{C}_n \otimes \mathbf{C}_n)^T$.
   - $\tilde{\mathbf{Z}}^{\alpha}_{n+1} = \mathbf{C}_n\mathbf{s}^{\alpha} \otimes \mathbf{C}_n\mathbf{m}^{\alpha}$.
   - $\triangle\mathbf{R}_e = \mathbf{R}_{e,n}\mathbf{R}^T_{e,n} = \mathbf{I}$.
4. Solve for $\boldsymbol{\tau}_{n+1}$:
   - $\tilde{\mathscr{C}}^{-1}_{d,n+1} : dev\left(\boldsymbol{\tau}_{n+1}\right) = dev\left(\boldsymbol{\epsilon}^{*}_{e,n+1}\right) - \triangle t \sum_{\alpha=1}^{N} \dot{\gamma}^{\alpha}_{n+1}\tilde{\mathbf{P}}^{\alpha}_{n+1}$.
5. Solve for $\tau^{\alpha}_{c,n+1}$:
   - $\tau^{\alpha}_{c,n+1} = \tau^{\alpha}_{c,n} + (\triangle t)\dot{g}\left(\tau^{\alpha}_{c,n+1}, \dot{\gamma}^{\alpha}_{n+1}\right)$.
6. Update $\mathbf{R}_{e,n+1}$:
   - $\mathbf{R}_{e,n+1} = exp\left[\left(\mathbf{w}_{n+1} - \sum_{\alpha=1}^{N} \dot{\gamma}^{\alpha}_{n+1}\tilde{\mathbf{Q}}^{\alpha}_{n+1}\right)\triangle t\right]\mathbf{R}_{e,n}$.
7. Two levels iteration scheme:
   (a) Calculate the rotation matrix $\mathbf{C}_{n+1} = \mathbf{R}_{e,n+1}\mathbf{C}_0$.
   (b) Rotate $(\mathbf{Z}^{\alpha}, \mathscr{C}_0)$ to the current orientation:
      - $\tilde{\mathscr{C}}_{d,n+1} = (\mathbf{C}_{n+1} \otimes \mathbf{C}_{n+1}) : \mathscr{C} : (\mathbf{C}_{n+1} \otimes \mathbf{C}_{n+1})^T$.
      - $\tilde{\mathbf{Z}}^{\alpha}_{n+1} = \mathbf{C}_{n+1}\mathbf{s}^{\alpha}_0 \otimes \mathbf{C}_{n+1}\mathbf{m}^{\alpha}_0$.
      - $\triangle\mathbf{R}_e = \mathbf{R}_{e,n+1}\mathbf{R}^T_{e,n}$.
   (c) Solve for $\boldsymbol{\tau}_{n+1}$:
      - $\tilde{\mathscr{C}}^{-1}_{d,n+1} : dev\left(\boldsymbol{\tau}_{n+1}\right) = dev\left(\boldsymbol{\epsilon}^{*}_{e,n+1}\right) - \triangle t \sum_{\alpha=1}^{N} \dot{\gamma}^{\alpha}_{n+1}\tilde{\mathbf{P}}^{\alpha}_{n+1}$.
      - the NR algorithm uses a sub stepping procedure to improve convergence velocity.
   (d) Solve for $\tau^{\alpha}_{c,n+1}$:
      - $\tau^{\alpha}_{c,n+1} = \tau^{\alpha}_{c,n} + (\triangle t)\dot{g}\left(\tau^{\alpha}_{c,n+1}, \dot{\gamma}^{\alpha}_{n+1}\right)$.
   (e) Update $\mathbf{R}_{e,n+1}$:
      - $\mathbf{R}_{e,n+1} = exp\left[\left(\mathbf{w}_{n+1} - \sum_{\alpha=1}^{N} \dot{\gamma}^{\alpha}_{n+1}\tilde{\mathbf{Q}}^{\alpha}_{n+1}\right)\triangle t\right]\mathbf{R}_{e,n}$.
   (f) Check convergence $||\triangle\boldsymbol{\tau}|| < \text{tol}$ and $||\triangle\tau^{\alpha}_{c}|| < \text{tol}$, if not, return to step (a), if convergence continue.

8. If required, calculate material tangent module $\tilde{\mathscr{C}}_{P,(n+1)}$.

The material tangent module is required when performing crystal plasticity calculations coupled with the FEM, in this framework the deviatoric tangent module is given by:

$$\tilde{\mathscr{C}}_{P,(n+1)} = J_{n+1}^{e-1}\left(\tilde{\mathscr{C}}_{d,n+1}^{-1} + \sum_{\alpha=1}^{N} \triangle t \frac{\partial \dot{\gamma}_{n+1}}{\partial \tau_{n+1}^{\alpha}} \left(\tilde{\mathbf{P}}_{n+1}^{\alpha} \otimes \tilde{\mathbf{P}}_{n+1}^{\alpha}\right)\right)^{-1} \quad , \tag{2.62}$$

with $J_{n+1}^{e} = det\left(1 + \boldsymbol{\epsilon}_{e,n+1}\right)$.

2.5 Numerical implementation

The implementation of the described crystal plasticity formulation is not straightforward. In this section, techniques that facilitate the implementation are described.

2.5.1 Tensor base

One difficulty of the numerical implementation of the crystal plasticity library is the manipulation and operations of fourth order tensors, such as the elastic constants matrix ($\mathscr{C}$). In particular, the calculation of the inverse can be complicated and numerically expensive. Because of this, it can be useful to rewrite those tensors in a form that facilitates their operation.

The Voigt notation, for example, is frequently used to reduce the fourth and second order tensors to 6 dimensional matrices and vectors respectively. However, it does not preserve the tensorial properties of second and fourth order tensors. For example considering Hooke's law and the compliance tensor ($\mathscr{S}_{ijkl}$):

$$\epsilon_{ij} = \mathscr{S}_{ijkl}\sigma_{kl} \quad , \quad \text{with } \mathscr{S}_{ijkl} = (\mathscr{C}_{ijkl})^{-1}, \tag{2.63}$$

and in Voigt notation:

$$\epsilon_{I}^{V} = \mathscr{S}_{IJ}^{V}\sigma_{J}^{V} \quad , \quad \text{with } \mathscr{S}_{IJ}^{V} = (\mathscr{C}_{IJ}^{V})^{-1}, \tag{2.64}$$

with the indexes $I, J = 1...6$. If $\mathcal{F}_{V}^{4th}$ is the operator that transforms a fourth order tensor to the Voigt notation, the problem encountered is that:

$$\mathscr{S}_{IJ}^{V} \neq \mathcal{F}_{V}^{4th}(\mathscr{S}_{ijkl}) \quad . \tag{2.65}$$

This problem can be solved by performing careful corrections, specially for terms derived from calculations that include the inverse of the compliance and elastic stiffness tensors. However it can easily lead to errors, for example in the calculation of the material tangent module in the crystal plasticity formulation.

Alternatives notations like the Mandel notation [129] or the notation proposed by [127] are also found in the literature. One can also use averaging procedures to express twice symmetric fourth rank order tensors (e.g. elastic constants tensor) in an other tensor possessing the same geometrical properties [130].

Particular tensor bases can also be used to express fourth order and second order tensors. These approaches have the advantage to preserve the tensorial structure. So, for the elastic relation, the inverse of the elastic constants tensor expressed in these bases correspond to the compliance tensor. The approach used in this work follows the work of [14, 131].

The second order tensors ($\boldsymbol{T}^{(\lambda)} = T_{ij}^{(\lambda)}$) that compose these bases should be orthonormal and symmetric, presented here using Einstein's notation for clarity:

$$T_{ij}^{(\lambda)} = T_{ji}^{(\lambda)} \ , \tag{2.66}$$

$$T_{ij}^{(\lambda)} T_{ji}^{(\lambda')} = \delta_{\lambda\lambda'} \ , \tag{2.67}$$

with $\{\lambda, \lambda'\} \in \{1, .., 6\}$. Fourth order and second order tensors with symmetry under index permutation, (e.g. $(\mathscr{C} = \mathscr{C}_{ijkl} = \mathscr{C}_{jikl} = \mathscr{C}_{ijlk} = \mathscr{C}_{klij})$ and $(\boldsymbol{\sigma} = \sigma_{ij} = \sigma_{ji})$), can be expressed into this base as:

$$\mathscr{C}_{ijkl} = \sum_{\lambda=1}^{6} C_{\lambda\lambda'} T_{ij}^{(\lambda)} T_{kl}^{(\lambda')} \ , \tag{2.68}$$

$$\sigma_{ij} = \sum_{\lambda=1}^{6} \sigma_{\lambda} T_{ij}^{(\lambda)} \ . \tag{2.69}$$

The coefficients $C_{\lambda\lambda'}$ and σ_{λ} are defined by the products:

$$C_{\lambda\lambda'} = T_{ij}^{(\lambda)} \mathscr{C}_{ijkl} T_{kl}^{(\lambda')} \ , \tag{2.70}$$

$$\sigma_{\lambda} = \sigma_{ij} T_{ij}^{(\lambda)} \ . \tag{2.71}$$

One advantage of this base is that the results of the tensor operations: addition, contraction and inversion, can be obtained by the corresponding

operations performed in the base. For example the elastic relation $\sigma_{ij} = \mathscr{C}_{ijkl}\epsilon_{kl}$ becomes:

$$\sigma_\lambda = C_{\lambda\lambda'}\epsilon_\lambda \ . \tag{2.72}$$

Furthermore a particular base formed by the eigentensors $\boldsymbol{T}^{(\lambda)}$ that diagonalizes $C_{\lambda\lambda'}$ can be found. The eigentensors are defined as:

$$\mathscr{C}_{ijkl}T^{(\lambda)}_{kl} = C^\lambda T^{(\lambda)}_{ij} \ . \tag{2.73}$$

The elastic compliance tensor computation can be performed directly in the base, as the inverse of C^λ:

$$\mathscr{S}_{ijkl} = \sum_{\lambda=1}^{6} [C^\lambda]^{-1} T^{(\lambda)}_{ij} T^{(\lambda)}_{kl} \ . \tag{2.74}$$

For crystal plasticity calculations, the stiffness tensor is equal to the elastic stiffness tensor only in the elastic regime. In the plastic regime the elasto plastic stiffness tensor is no longer diagonal when expressed in the tensorial base. Nevertheless , this methodology permits both to get simple scalar equations for the elastic regime and reduce fourth rank tensors as second order matrices when plastic deformation is active.

2.5.2 Isotropic case

For the particular case of isotropic symmetry (which will be mostly the case considered in this work), the elastic matrix can be expressed as :

$$\mathscr{C}_{ijkl} = \mu(\delta_{ik}\delta_{jl} + \delta_{il}\delta_{jk}) + \lambda\delta ij\delta_{kl} \ , \tag{2.75}$$

where, μ and λ are the shear modulus and the Lamé parameter, respectively. The eigentensors $\boldsymbol{T}^{(\lambda)}$ for this symmetry are:

$$\boldsymbol{T}^{(1)} = \begin{pmatrix} -\frac{1}{\sqrt{6}} & 0 & 0 \\ 0 & -\frac{1}{\sqrt{6}} & 0 \\ 0 & 0 & \frac{2}{\sqrt{6}} \end{pmatrix} \ , \tag{2.76}$$

$$\boldsymbol{T}^{(2)} = \begin{pmatrix} -\frac{1}{\sqrt{2}} & 0 & 0 \\ 0 & \frac{1}{\sqrt{2}} & 0 \\ 0 & 0 & 0 \end{pmatrix} \ , \tag{2.77}$$

$$\boldsymbol{T}^{(3)} = \begin{pmatrix} 0 & 0 & 0 \\ 0 & 0 & \frac{1}{\sqrt{2}} \\ 0 & \frac{1}{\sqrt{2}} & 0 \end{pmatrix} \ , \tag{2.78}$$

$$\boldsymbol{T}^{(4)} = \begin{pmatrix} 0 & 0 & \frac{1}{\sqrt{2}} \\ 0 & 0 & 0 \\ \frac{1}{\sqrt{2}} & 0 & 0 \end{pmatrix} , \tag{2.79}$$

$$\boldsymbol{T}^{(5)} = \begin{pmatrix} 0 & \frac{1}{\sqrt{2}} & 0 \\ \frac{1}{\sqrt{2}} & 0 & 0 \\ 0 & 0 & 0 \end{pmatrix} , \tag{2.80}$$

$$\boldsymbol{T}^{(6)} = \begin{pmatrix} \frac{1}{\sqrt{3}} & 0 & 0 \\ 0 & \frac{1}{\sqrt{3}} & 0 \\ 0 & 0 & \frac{1}{\sqrt{3}} \end{pmatrix} . \tag{2.81}$$

The first five eigentensors are deviatoric and are associated with shears, and the eigenvalues associated with them are equal and worth 2μ. The last eigentensor is associated with dilatation strains and its eigenvalue is the elastic compressibility module $3X = 2\mu + 3\lambda$.

Thanks to the characteristics of its eigentensors, in the case of isotropic elasticity, this base is specially advantageous for the crystal plasticity framework which only considers the deviatoric stresses. Because, only the first five eigentensors need to be considered in the calculations, simplifying them even more.

2.5.3 Code structure

The crystal plasticity library was implemented in C++. One of the main considerations in the implementation was that: depending on the application of interest different flow rules, hardening rules, crystal structures, and material constitutive laws, might be required, as described in section 2.3. So, the code structure was designed to facilitate the implementation of different laws. This was done by taking advantage of the C++ classes, objects and class templates, as described in the following.

The structure of the code consists of several classes and class templates that define the elements required to perform the crystal plasticity calculation. These are: crystal plasticity class template, which defines the integration algorithm; the flow rule class template, which describes the calculation of the strain rate as a function of the stress; the constitutive law class, which describes the elastic relation; the Crystal class, which describes the crystal structure (slip systems) and the hardening law class, which describes the CRSS and their evolution.

The crystal plasticity class template has members that are objects of the flow rule class template and of the constitutive law class. The flow rule class

template has members that are objects of crystal class and the hardening law class. Figure 2.2 shows a schematic representation of this structure. To perform a calculation a crystal plasticity object needs to be defined. The definition of the crystal plasticity object, requires the definition of a flow rule object, and a constitutive class object. Subsequently, the definition of a flow rule object requires the definition of a crystal object and a hardening rule object.

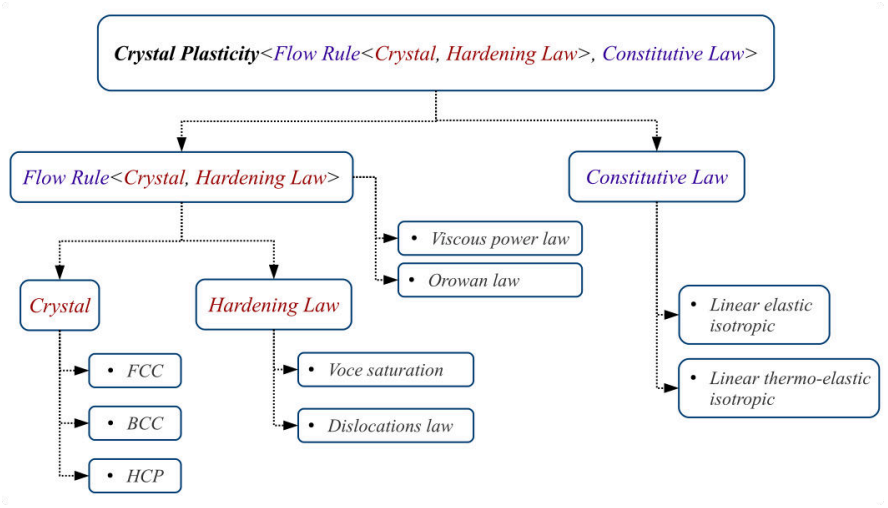

Figure 2.2: Schematic representation of the code structure, showing the classes templates, classes and objects.

Thanks to the implemented structure, when defining a crystal plasticity object any flow rule object can used. Following the example on figure 2.2, the crystal plasticity object can be defined with either viscous power law or an Orowan law. In the same way the viscous power law object can be defined with either a Voce saturation law or with a dislocations based law.

To achieve this, in the classes and class templates virtual methods are defined. In this definition only the required parameters to perform a calculation are specified. For example the flow rule class template includes a method that takes the stress to update the plastic slip rates. This method is called in the crystal plasticity class when required. However, the specific procedure to calculate the slip rates is only implemented in each specific flow rule. Since, all objects of the flow rule class share the same general method to calculate the slip rates, the call to this method done in the integration procedure is the same for all the implemented flow rules. So, when implementing a new flow rule no modifications need be made to the other classes. The described methodology was used in the definition of all the classes that compose the

code.

Additionally, to facilitate the passing of parameters and variables, the integration with external solvers and to reduce the consumption of memory, the parameters and variables required for the calculations are defined externally (memory allocation). When a calculation is going to be performed, the pointers to all the variables and parameters needed in the calculation are passed to the crystal plasticity object. The crystal plasticity object subsequently sets the pointers that it requires and passes them to its members. The members of the crystal plasticity object repeat the procedure and pass the pointers to their respective members.

2.6 Polycrystal models

The single crystal model described so far, models the response of individual crystals subjected to deformation conditions. However, to model the behaviour of polycrystals, composed of several crystals, an additional assumption must be introduced. This assumption links the macroscopic stress and strains applied at the polycrystal level to the local strains and stress in each crystal. Several polycrystal models are presented in the literature [17], here we will describe the CPFEM used in this work (additionally the VPSC model is also detailed in chapter 5).

2.6.1 Crystal plasticity finite element method

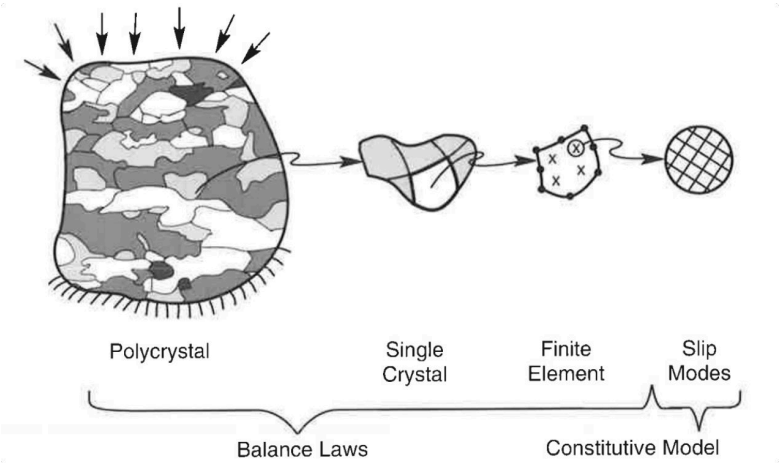

Figure 2.3: Schematic representation of CPFEM applied to model the behaviour of polycrystals. Figure from [14].

The Crystal plasticity finite element method (CPFEM) [31, 32, 33, 132] couples the finite element method with crystal plasticity. In the FEM formulation, the stress - strain response of each element will be determined by the single crystal model. By using FEM, stress equilibrium are ensured at least in a weak sense as well as compatibility along grain boundaries, grain interactions are also considered and intragranular strain heterogeneity can be calculated. Figure 2.3 shows a schematic representation of CPFEM applied to model the behaviour of polycrystals. The main limitation of CPFEM is it high computational cost, which limits its application to microscale simulations.

FEM formulation used in this work

In order to simulate the mechanical behaviour of a polycrystalline sample, a FE framework based on a P1+/P1 mixed velocity pressure (v, P) formulation, is used. Considering the momentum conservation equation, in Einstein notation, written in terms of its deviatoric and spherical components, we obtain:

$$\begin{aligned} \rho\frac{\partial v_i}{\partial t} - S_{ij,j} + P_{,i} - b_i = 0 \ , \\ K v_{i,i} + \dot{P} = 0 \ , \end{aligned} \tag{2.82}$$

with ρ the material density, S_{ij} the deviatoric stress, b_i the body forces and K the bulk modulus. The weak formulation is obtained by integrating over the domain Ω and multiplying by the test functions w_i and q:

$$\begin{aligned} \int_\Omega \rho\frac{\partial v_i}{\partial t} w_i dV - \int_\Omega S_{ij,j} w_i dV + \int_\Omega P_{,i} w_i dV - \int_\Omega b_i w_i dV = 0 \ , \\ - \int_\Omega v_{i,i} q dV - - \int_\Omega \frac{1}{K}\dot{P} q dV = 0 \ , \end{aligned} \tag{2.83}$$

Considering that:

$$\begin{aligned} - \int_\Omega S_{ij,j} w_i dV + \int_\Omega P_{,i} w_i dV = \\ = - \int_\Omega \left(S_{ij} w_i\right)_j dV + \int_\Omega \left(P w_i\right)_i dV + \int_\Omega S_{ij}\epsilon_{ij}(w_i) dV - \int_\Omega P w_{i,i} dV \\ = - \int_\Omega \left((S_{ij} - P\delta_{ij}) w_i\right)_j dV + \int_\Omega S_{ij}\epsilon_{ij}(w_i) dV - \int_\Omega P w_{i,i} dV \\ = - \int_{\Gamma_t} t_i w_i dS + \int_\Omega S_{ij}\epsilon_{ij}(w_i) dV - \int_\Omega P w_{i,i} dV \end{aligned} \tag{2.84}$$

with Γ_t the boundary of Ω where a traction t_i is applied. Equations 2.83 can be rewritten as:

$$\begin{aligned} R_1 = &\int_\Omega \rho \frac{v_i}{\triangle t} w_i dV - \int_\Omega \rho \frac{v_i^t}{\triangle t} w_i dV + \int_\Omega S_{ij}\epsilon_{ij}(w_i) dV \\ &- \int_\Omega P w_{i,i} dV - \int_{\Gamma_t} t_i w_i dS - \int_\Omega b_i w_i dV = 0 \ , \\ R_2 = &- \int_\Omega v_{i,i} q dV - \int_\Omega \frac{1}{K}\frac{P}{\triangle t} q dV + \int_\Omega \frac{1}{K}\frac{P^t}{\triangle t} q dV = 0 \ , \end{aligned} \tag{2.85}$$

The term S_{ij} can be linearized as:

$$\begin{aligned} S_{ij} &\approx S_{ij}^t + \frac{\partial S_{ij}}{\partial \delta\epsilon_{kl}} \delta\dot{\epsilon}_{kl} \triangle t \\ &\approx S_{ij}^t + C_{ijkl}^{dev} \delta\dot{\epsilon}_{kl} \triangle t \ , \end{aligned} \tag{2.86}$$

with C_{ijkl}^{dev} the material tangent module provided by the constitutive model, in this case the single crystal model. In order to solve the system, a N-R algorithm is used:

$$\begin{aligned} \frac{\partial R_1}{\partial v_i} = \int_\Omega \rho \frac{\delta v_i}{\triangle t} w_i dV + \int_\Omega C_{ijkl}^{dev} \delta\dot{\epsilon}_{kl} \epsilon_{ij}(w_i) \triangle t dV \ , \\ \frac{\partial R_1}{\partial P} = - \int_\Omega \delta P w_{i,i} dV \ , \\ \frac{\partial R_2}{\partial v_i} = - \int_\Omega \delta v_{i,i} q dV \ , \\ \frac{\partial R_2}{\partial P} = - \int_\Omega \frac{1}{K\triangle t} \delta P q dV \ , \end{aligned} \tag{2.87}$$

which written in matrix notation is:

$$\begin{bmatrix} K_{vv} & K_{vp} \\ K_{vv}^T & K_{pp} \end{bmatrix} \begin{bmatrix} \delta v_i \\ \delta P \end{bmatrix} = - \begin{bmatrix} R_1 \\ R_2 \end{bmatrix} \quad . \tag{2.88}$$

To ensure the stability condition of the formulation, the well known mini-element (P1+/P1) [133] is used. Adding an additional internal degree of freedom to the velocity ensures the existence and uniqueness of the solution. In the cases considered in this work, we will consider isothermal, quasi-static deformation of polycrystals, without considering body forces.

Also, in order to model large deformation, an updated Lagrangian framework is used. After each time step the configuration of the body is updated, by updating the nodes position (x) as:

$$x_{t+\triangle t} = x_t + v_t \triangle t \tag{2.89}$$

2.6.2 Remeshing

In the Lagrangian framework, the continuous update of the nodes position causes distortion in the elements, reducing the mesh quality. Having a low quality mesh can cause serious convergence problems in the FE solution. So, when performing CPFEM simulations considering large deformations remeshing operations must be performed to ensure a good mesh quality.

The remeshing procedure in this work is done using MTC. MTC is a P1 automatic remesher based on elements topology improvement developed for Lagrangian simulations under large strains [134]. MTC allows the creation of isotropic and anisotropic meshes with variable element size. In addition to MTC a body fitting remesher (FITZ) was also developed in CEMEF [135] that in the context of polycrystal simulations allows to fit nodes to the LS functions 0 isovalue (The 0 isovalue of the LS functions in polycrystal simulations describes the GB, this is further detailed in chapter 3).

However, remeshing operations in $3D$ have a high computational cost and can introduce interpolation errors . So, to ensure an adequate mesh quality during the CPFEM simulations and limit the computational cost, a priori in this work remeshing operations will be performed at fixed deformation intervals of 25%. An isotropic remeshing strategy with uniform element size will be used (illustrated in figure 2.4), since we are interest in describing heterogeneous intragranular deformation. The meshing and remeshing strategies will be further discussed in chapter 3.

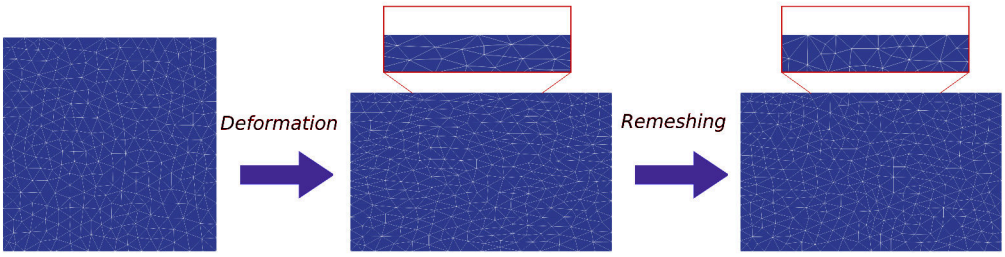

Figure 2.4: Isotropic remeshing strategy with uniform element size used in CPFEM simulations.

2.7 Validation of the crystal plasticity library

To validate the developed library simulations, cases from the literature were performed and the results compared with the values reported.

2.7.1 Material point simulations

The first test cases considered were material point simulations as presented in [113]. These cases describe the deformation of a AL7050 polycrystal composed of 256 grains with random initial orientations subjected to different deformation conditions. For these simulations, the Taylor model was used as the polycrystal model (the same strain rate is imposed on all grains equal to the macroscopic strain rate) and the flow rule and hardening rule used were:

$$\dot{\gamma}^{\alpha} = \dot{\gamma}_0^{\alpha} \left| \frac{\tau^{\alpha}}{\tau_C^{\alpha}} \right|^{\frac{1}{m}} \text{sing}(\tau^{\alpha}) \ , \tag{2.90}$$

$$\dot{\tau}_c = H_0 \left(\frac{\tau_{sat} - \tau_C}{\tau_{sat} - \tau_{C0}} \right) \sum_{\beta} \left| \dot{\gamma}^{\beta} \right| \ , \tag{2.91}$$

$$\tau_{sat} = \tau_{sat,0} \left[\frac{\sum_{\beta} \left| \dot{\gamma}^{\beta} \right|}{\dot{\gamma}_{S0}} \right] \ . \tag{2.92}$$

The material parameters for AL7050 are presented in table 2.1.

m	$\dot{\gamma}_0$	H_0	τ_{C0}
0.02	1.0 (s^{-1})	240 (MPa)	205 (MPa)
$\tau_{sat,0}$	m'	$\dot{\gamma}_{S0}$	[–]
290 (MPa)	0	$5.0 * 10^{10}$ (s^{-1})	[–]

Table 2.1: Flow rule and hardening rule parameters values considered for material points simulations of AL7050 [113].

For the first case considered, the polycrystal is subjected to plain compression defined by the velocity gradient ($\boldsymbol{l}$) as $\boldsymbol{l} = [\ 1.0\ 0\ 0\ ,\ 0\ 0\ 0\ ,\ 0\ 0\ -1.0\ ]$, and for the second case, the polycrystal is subjected to simple shear defined by the velocity gradient as $\boldsymbol{l} = [\ 0\ 0\ 2.0\ ,\ 0\ 0\ 0\ ,\ 0\ 0\ 0\ ]$. In both cases, the polycrystal response is studied in terms of its texture evolution (pole figures) and its stress response (described by normalized average equivalent stress $\sigma_{eq,N}$) at different strain levels (described by the average equivalent strain ϵ_{eq}).

$$\sigma_{eq,N} = \frac{1}{k_{S,0}} \sum_{i=1}^{N} \sqrt{\frac{3}{2}(\boldsymbol{\sigma}_i : \boldsymbol{\sigma}_i)} \,, \qquad \epsilon_{eq} = \sum_{i=1}^{N} \sqrt{\frac{2}{3}(\boldsymbol{\epsilon}_i : \boldsymbol{\epsilon}_i)} \,. \tag{2.93}$$

The results in both cases were compared to the results published in [113], and with the expected behaviour of a polycrystal for these deformations conditions presented in the literature [14]. For the first case (compression), the results in terms of stress response are presented in figure 2.5, the results are plotted along with the results from [113] digitalized from the published data. Additionally, the poles figures at the deformation levels of $\epsilon_{eq} = 0.5$, $\epsilon_{eq} = 1.0$ and $\epsilon_{eq} = 1.5$, are presented in figure 2.6 and as a reference for comparison, the corresponding pole figures published in [113] are shown in figure 2.7.

In this case, the simulation results in terms of both stress evolution and texture evolution show excellent agreement with the results presented by Marin [113]. The texture evolution also shows qualitative agreement with the expected texture evolution of a polycrystal subjected to plain compression as described in [14].

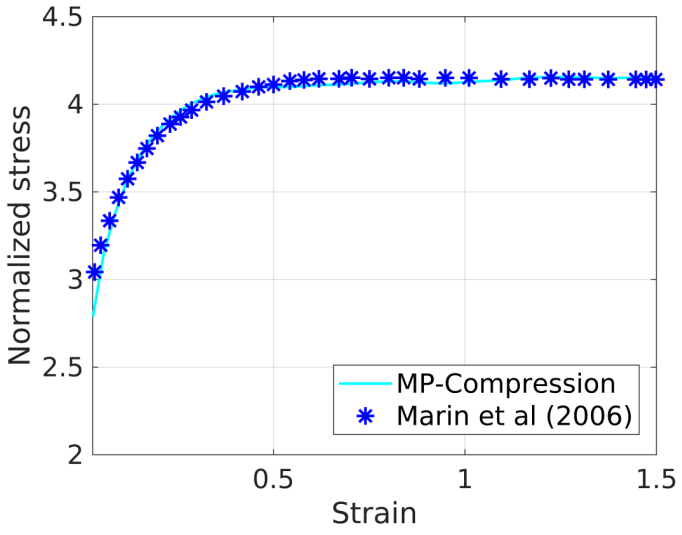

Figure 2.5: Stress response of the deformation of an aggregate of 256 FCC crystals subjected to plane strain compression, material point (MP) simulations. Data from [113] was obtained by digitalizing the published data.

For the second case (simple shear), the results in terms of stress response are presented in figure 2.8, as in the previous case the results are plotted along with the results from [113] digitalized from the published data. For this case, the poles figures are presented at the deformation levels of $\gamma_{eq} = 0.87$, $\gamma_{eq} = 1.73$ and $\gamma_{eq} = 2.60$ in figure 2.9, and the corresponding poles figures published in [113] are shown in figure 2.10.

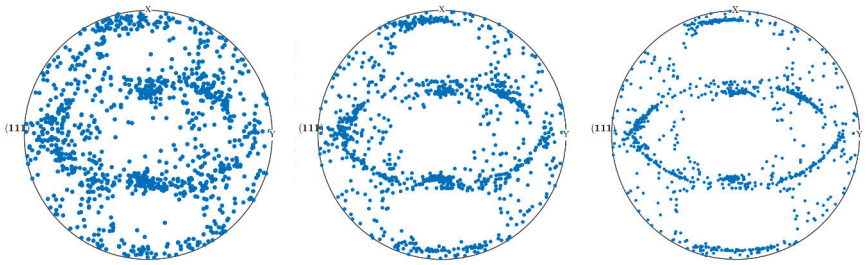

Figure 2.6: $\langle 111 \rangle$ pole figures of the deformation of an aggregate of 256 FCC crystals subjected to plane strain compression. Model simulation results. $\epsilon_{eq} = 0.5$ (left side), $\epsilon_{eq} = 1.0$ (center), $\epsilon_{eq} = 1.5$ (right side).

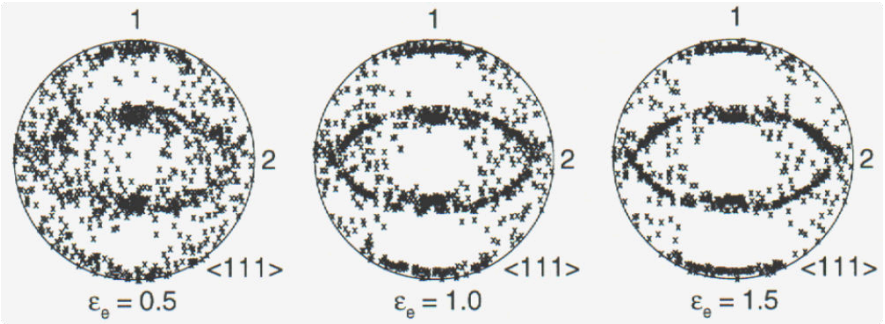

Figure 2.7: $\langle 111 \rangle$ pole figures of the deformation of an aggregate of 256 FCC crystals subjected to plane strain compression. Results from [113]. $\epsilon_{eq} = 0.5$ (left side), $\epsilon_{eq} = 1.0$ (center), $\epsilon_{eq} = 1.5$ (right side).

For the second case, the stress response shows slight differences between the simulated results and the results presented by Marin [113] at the beginning of the curves. These differences can be attributed to differences in the constitutive law. In the model of [113], the elastic behaviour is described by an anisotropic elastic law, while in this work an isotropic elastic law is used. The differences only appear in the second case because of the loading configuration. On the other hand the texture evolution shows good agreement

with the results of Marin [113]. The texture evolution also shows qualitative agreement with the expected texture evolution of a polycrystal subjected to simple shear as described by [14].

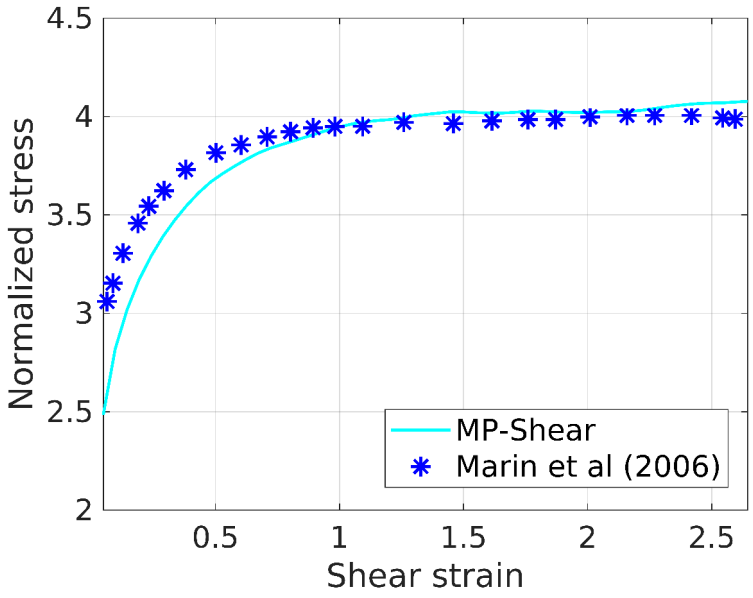

Figure 2.8: Stress response of the deformation of an aggregate of 256 FCC crystals subjected to simple shear. Data from [113] was obtained by digitalizing the published data.

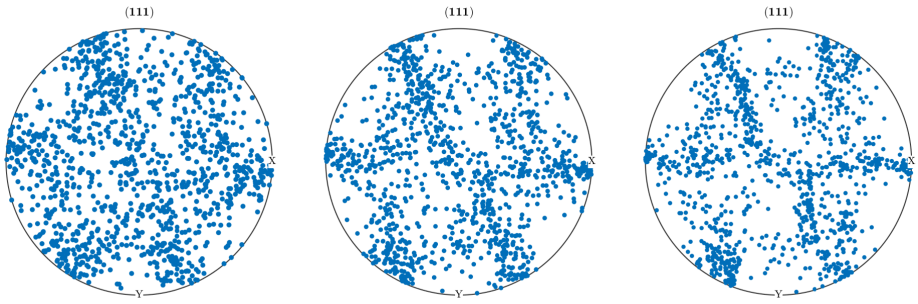

Figure 2.9: $\langle 111 \rangle$ pole figures of the deformation of an aggregate of 256 FCC crystals subjected to simple shear. Model simulation results. $\gamma_{eq} = 0.87$ (left side), $\gamma_{eq} = 1.73$ (center), $\gamma_{eq} = 2.60$ (right side).

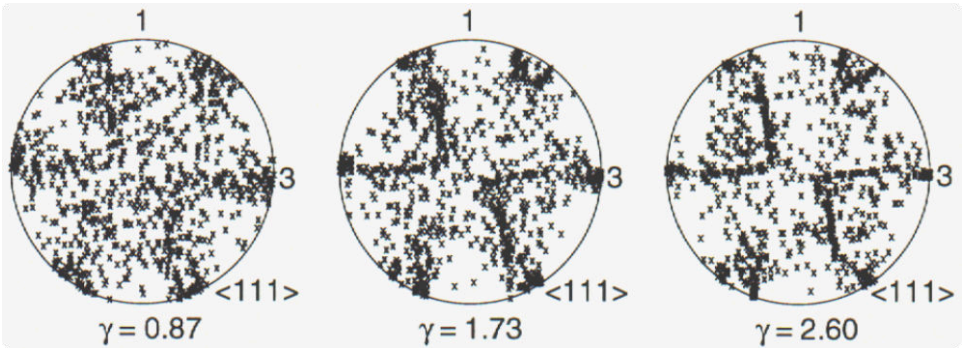

Figure 2.10: $\langle 111 \rangle$ pole figures of the deformation of an aggregate of 256 FCC crystals subjected to simple shear. Results from [113]. $\gamma_{eq} = 0.87$ (left side), $\gamma_{eq} = 1.73$ (center), $\gamma_{eq} = 2.60$ (right side).

2.7.2 CPFEM simulations

To test the crystal plasticity library coupled with FEM, the case of plain compression of 304L steel polycrystal presented in [121] was reproduced. The simulations consist of a channel die compression of a $0.5 * 0.5 * 0.5$ mm polycrystal composed of 100 grains.

The flow rule considered is the same power law considered in the material point test cases. While, the hardening rule used is the Yoshie-Laasroui-Jonas dislocation law, coupled with the Taylor hypothesis. Two type of dislocations are considered: ρ_{SSD} and ρ_{GND}. The evolution of ρ_{GND} is calculated as a function of the gradient of $\boldsymbol{F}_P$ following the classical definition of [136]. With the inclusion of ρ_{GND}, the set of equations describing the hardening behaviour is given by:

$$\tau_C = \tau_0 + \psi \mu b \sqrt{\rho_{Total}} \ , \tag{2.94}$$

$$\rho_{Total} = \rho_{SSD} + \rho_{GND} \ , \tag{2.95}$$

$$\dot{\rho_{SSD}} = K_1 - K_2 \rho_{SSD} \ , \tag{2.96}$$

$$\dot{\rho}^{\alpha}_{GND} = \frac{1}{b} \nabla \left(\dot{\gamma}^{\alpha} \boldsymbol{m}^{\alpha} \boldsymbol{F}_P \right) \ , \tag{2.97}$$

$$\dot{\rho}_{GND} = \sum_{\alpha} \text{norm}[\dot{\rho}^{\alpha}_{GND}] \ . \tag{2.98}$$

The boundary conditions imposed are shown in figure 2.11. The velocity imposed is calculated as the nodes position multiplied by the strain rate in the specified direction. Additionally, zero velocity in the boundary normal direction boundary conditions are also imposed to prevent the polycrystal from collapsing unto himself, at high deformation levels. If the zero velocity boundary conditions are not imposed, deformation levels higher than 40% are very difficult to reach, due to the small number of grains considered in the domain. The material parameters considered for the simulations are presented in table 2.2.

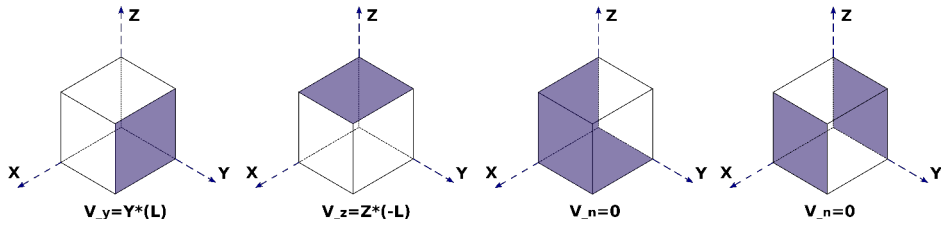

Figure 2.11: Schematic of the boundary conditions imposed for the channel die compression.

E	ν	$\dot{\gamma}_0$	b	M
150 (GPA)	0.3	0.001 (s^{-1})	$2.5 * 10^{-7}$ (mm)	3.3
$K0$	$K1$	$K2$	m	ψ
16.06 (MPa)	$1.1 * 10^{9}$ $(mm^{-}2)$	9.57	0.05	0.15

Table 2.2: Flow rule and hardening rule parameters values considered for CPFEM simulations of 304L steel [121].

The obtained simulation results in term of average stress response were compared to the experimental measurements reported in [121] and are presented in figure 2.12. Additionally figure 2.13 shows the simulated dislocation density distribution. For this case, the results in terms of stress evolution showed very good agreement with the experimental measurements. Additionally, when observing the dislocation density distribution in the domain, the results agree with the results presented in [121] and with the expected behaviour, with higher accumulation of dislocations around the grain boundaries where the plastic deformation gradient is higher.

The good agreement observed between the simulation results and the reference data in the tests performed, material point simulations and CPFEM simulations, served to validate the developments presented in this chapter and

to illustrate the versatility of the developed library in performing different types of simulations and including different behaviour laws.

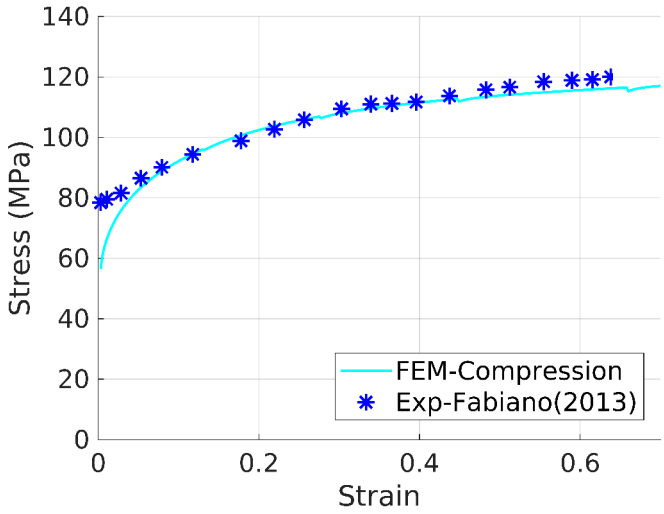

Figure 2.12: Average stress response compared with experimental measurements for channel die compression of 304L steel. Experimental measurements digitalized from [121].

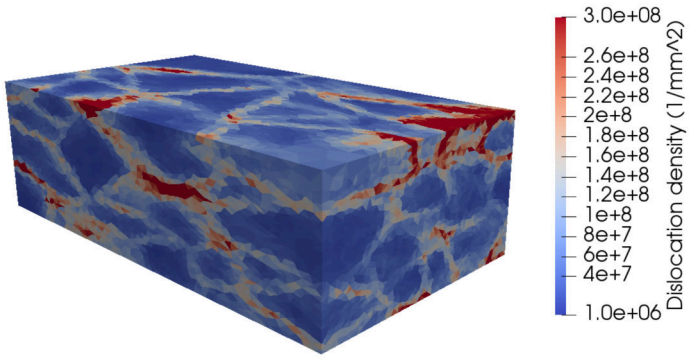

Figure 2.13: Simulation results in terms of dislocation density distribution in the polycrystal.

2.8 Summary and Discussion

In this chapter, the new crystal plasticity library developed to have a better description of the plastic deformation in metals was presented. The library

is based on the formulation of [113].

The library was developed in C++ as an external library and is compatible with several solvers. By taking advantage of some C++ features like, classes templates and pointers, the library was developed with a modular structure. This structure facilitates the implementation of new features with minimal modifications to the rest of the code. This aspect ensures that the library is versatile and easy to update. This is required as depending on the material and application of interest, different laws are needed.

In order to perform the numerical integration, a two levels N-R algorithm, that uses a double criteria to define convergence was implemented. The proposed algorithm was optimized to minimize the computational cost and to limit numerical errors introduced during the calculation. In this regard, a tensorial base was used to represent second and fourth order tensors. The use of the described based simplifies the numerical handling of tensors and operations over them.

The developed library was tested by reproducing cases found in the literature. The results were compared to both simulation results and experimental measurements. The results showed good agreement when compared with the reference data. The tested cases included the use of different polycrystal models, flow rules and hardening rules, thus showing the versatility of the developments.

In the next chapter the developed library is coupled with a LS framework to model DDRX up to high deformations. As described in chapter 1, the main advantages of the LS framework when compared to other DDRX models, are its ability to model complex geometries and to be capable to reach high deformation levels thanks to remeshing techniques as was illustrated in [6].

2.9 Résumé en Français

Dans ce chapitre, la nouvelle bibliothèque de plasticité cristalline développée est présentée. La bibliothèque est basée sur une formulation existante développée par Marin [113].

La bibliothèque a été développée en C ++ comme une bibliothèque externe et se veut générique. En tirant parti de certaines fonctionnalités C ++ comme les modèles de classes et les pointeurs, la bibliothèque a été développée avec une structure modulaire. Cette structure facilite la mise en œuvre de nouvelles fonctionnalités avec des modifications minimales du reste du code. Cet aspect garantit que la bibliothèque est polyvalente et facile à mettre à jour. Cela est nécessaire car en fonction des matériaux d'intérêt et de l'application visée, differentes lois peuvent etre necessaires.

Afin de réaliser l'intégration numérique, un algorithme de Newton-Raphson à deux niveaux, qui utilise un double critère pour définir la convergence, a été implémenté. L'algorithme proposé a été optimisé pour minimiser le coût de calcul et pour limiter les erreurs numériques introduites lors de la résolution. À cet égard, une base tensorielle particulière a été utilisée pour représenter des tenseurs de deuxième et quatrième ordre. L'utilisation de la base décrite simplifie la manipulation numérique des tenseurs et les opérations tensoriels.

La bibliothèque développée a été testée en reproduisant des cas issus de la littérature. Les résultats ont été comparés aux résultats de simulation et aux mesures expérimentales. Les résultats ont montré une bonne concordance par rapport aux données de référence. Les cas testés incluent l'utilisation de différents modèles polycristallins et de différentes règles d'écoulement et de durcissement, montrant ainsi la polyvalence des développements.

Dans le chapitre suivant, la bibliothèque développée est couplée à un cadre level-set pour modéliser la DDRX jusqu'à des déformations élevées. Les principaux avantages de l'approche LS sont sa capacité à modéliser des géométries complexes et à atteindre des niveaux de déformation élevés grâce à des techniques de remaillage [6].

Chapter 3

Full field model for DDRX

3.1 Introduction

In this chapter the CPFEM presented in chapter 2 is coupled with the level set finite element method (LS-FEM) and phenomenological laws to model DDRX. First the LS-FEM framework is presented, followed by the phenomenological models that are used to describe nucleation. Following the coupling algorithm is described, along with a sensitivity analysis of the model numerical parameters. Finally, tests of the coupled model are performed.

3.2 The level set method for grain boundary migration

The LS method was initially developed by Osher and Sethian [137] to trace the spatial and temporal evolution of evolving interfaces. This front-capturing approach, usable in FFT/FE context, enables to manage easily complex topological events such as appearance or disappearance of the modeled interfaces. This aspect explains its interest to describe GBM. First applications were proposed by Merriman [76] and Zhao [138] for few multiple junctions and by Bernacki et al. for polycrystal computations in context of ReX modeling [77, 78, 139, 140, 141].

3.2.1 Grain representation

In the context of microstructure modeling, a grain is classically described thanks to a LS function ψ defined over a domain Ω as the signed distance to the grain boundary [77, 78]. So, a GB is defined by the 0 isovalue of the LS function.

$$\psi(x,t) = \pm d(x,\Gamma(t)) \ \ , \forall x \in \Omega \ , \tag{3.1}$$

$$\Gamma(t) = \{x \in \Omega, \ \ \psi(x) = 0\} \ , \tag{3.2}$$

with d the minimum euclidean distance from the point x to the interface $\Gamma(t)$. A general adopted convention considers $\psi > 0$ inside the grain and $\psi < 0$ outside the grain. This is an arbitrary convention that does not have influence in the results, but needs to be keep constant once defined. In practice and in context of a FE strategy and linear interpolation, the LS function is estimated in each node of the FE mesh.

A microstructure can be generated and immersed in a FE mesh as LS functions by using Voronoi tessellation or a Laguerre-Voronoi tessellation techniques [142]. These generation procedures can lead to the creation of vacuum regions, nodes with no positive level set value. To correct these vacuum regions, the LS functions are corrected according to the following procedure [143]:

$$\psi_i(x) = \frac{1}{2}\left(\psi_i(x) - \max_{i \neq j}\left(\psi_j(x)\right)\right) \tag{3.3}$$

Additionally, to reduce the number of LS functions required to describe the microstructure, coloring techniques are used. These coloring techniques allow to define more than one grain per LS function. Grains defined inside the same LS function are separated by a minimal defined distance. Once the grains are generated they can be redistributed into different LS functions using a swapping procedure in order to avoid numerical coalescence [112]. Of course, it is also possible to immerse EBSD or SEM images to generate representative polycrystals in FE-LS context [144].

3.2.2 Grain boundary migration (GBM)

In the LS framework, GBM is described by solving a transport equation for a given velocity $\mathbf{v}_{GB}$ field:

$$\frac{\partial \psi(x,t)}{\partial t} + \mathbf{v}_{GB} \cdot \nabla \psi(x,t) = 0 \ , \tag{3.4}$$

with ∇ the gradient operator. The velocity field is calculated by considering capillarity ($\mathbf{v_c}$) effects and energy gradients ($\mathbf{v_e}$) effects. The GB velocity due to the capillarity effect requires the calculation of the normal to the grain boundary $\boldsymbol{n}$ and the grain curvature $\boldsymbol{k}$ (trace of the curvature tensor in 3D), these terms can be estimated through the following equations:

$$\boldsymbol{n} = -\nabla\psi \quad , \tag{3.5}$$

$$\boldsymbol{k} = \nabla \cdot \boldsymbol{n} = -\triangle\psi \quad . \tag{3.6}$$

This estimation requires that the LS functions remain signed distance functions $||\nabla\psi|| = 1$, at least around the GB interfaces. In this condition, Eq. 3.4 can be rewritten as a convective-diffusive equation:

$$\frac{\partial\psi(x,t)}{\partial t} - M_{GB}\gamma_{GB}\triangle\psi + M_{GB}\tau_{GB}\left[\rho\right]\nabla\psi = 0 \, , \tag{3.7}$$

with M_{GB} the mobility of the GB estimated with an Arrhenius type law as described in chapter 1, γ_{GB} the grain boundary energy, τ_{GB} the dislocation line energy, $[\rho]$ the difference in dislocation density across the boundary. The term $(\tau_{GB}\left[\rho\right])$ describes the difference in stored energy across the boundary.

Eq. 3.7 is solved using FEM for all the LS functions that describe the microstructure with a particular treatment of the convective part of the multiple junction [77]. After solving the equation vacuum regions might appear in FE mesh, thus it is necessary to correct them as was described in Eq. 3.3. Additionally, the minimal distance imposed between grains described by the same LS functions, is verified in order to avoid numerical coalescence thanks a swapping algorithm. Finally, after calculating the GBM, the LS functions lose their metric properties (no longer signed distance functions). Thus, before the next calculation it is necessary to perform a reinitialization procedure to restore their distance properties. In this work a direct geometrical reinitialization procedure is used [145].

3.3 Recrystallized grains

As described in chapter 1, mesoscale DDRX models usually represent nucleation as the appearance of recrystallized grains. The size, conditions and rate of appearance of recrystallized grains is defined according to phenomenological laws. In this work, the LS framework was coupled with phenomenological laws; this approach has been previously used in the literature to model both dynamic and static recrystallization [6, 79, 112], and it is further adapted to work in a CP framework.

3.3.1 Critical dislocation density

The critical dislocation density ρ_{cr}, defines when and where recrystallized grains can appear. Recrystallized grains can only appear on grains with a

dislocation density equal or higher than ρ_{cr}, defined as:

$$\rho_{cr} = \left[\frac{-2\gamma_{GB}\dot{\epsilon}\frac{K_2}{M_{GB}{\tau_{GB}}^2}}{ln\left(1-\frac{K_2}{K_1\rho_{cr}}\right)} \right]^{1/2} , \tag{3.8}$$

Eq. 3.8 is derived from the critical dislocation density equation introduced by Roberts and Ahlblom [51]. The parameters K_1 and K_2 are the same parameters as in the Yoshie-Laasroui-Jonas equation [45], described in chapter 2, that represent accumulation of dislocations due to hardening and the effect of dynamic recovery. When coupling the CP model, the Yoshie-Laasroui-Jonas equation is used as the hardening rule, to ensure compatibility between the models and to not introduce many additional parameters that need to be calibrated. Eq. 3.8 is solved using a fixed point algorithm.

3.3.2 Recrystallized grains Size

The size of the recrystallized grains that are introduced, described by their radius r^*, is calculated according to the Bailey-Hirsch criterion, Eq. 3.9. This criteria approximates the condition that the stored energy is high enough to overcome the capillarity forces, ensuring that the recrystallized grain will be able to grow.

This condition is approximated by assuming the recrystallized grains as perfect spheres. So, to compensate for errors in the description of the recrystallized grain topology, a numerical safety factor ω is generally introduced [6, 79]:

$$r^* = \omega\frac{2\gamma_{GB}}{\rho_{cr}\tau_{GB}} . \tag{3.9}$$

The errors in the description of the recrystallized grain topology can be reduced by reducing the mesh size, as illustrated in figure 3.1. This means, that the value of this factor will depend on the FE mesh used around the new ReX grains. Since this factor introduces an artificial increase in the recrystallized grains size that can affect the results of the model, ideally it should be kept as close as possible to a value of 1.

3.3.3 Recrystallized grains location

Following classical nucleation models, the criteria used to define sites for the appearance of recrystallized grains considers different rules: first, ReX grains can only appear in positions with a dislocation density higher than

the previously defined critical dislocation density. This combined, with the recrystallized grain size defined by Eq. 3.9 ensures that the recrystallized grains will growth. Second, it is initially assumed that recrystallized grains can only appear near the grain boundaries, this is done by defining a distance d from the grain boundary which is equal to the recrystallized grain diameter $2r^*$. The appearance of ReX grains near the boundaries ensures the presence of misorientation, and is in accordance to necklace nucleation which is quite classical in DDRX context [1]. However different criteria considering dislocation density gradients, misorientation, and misorientation gradients can also be defined.

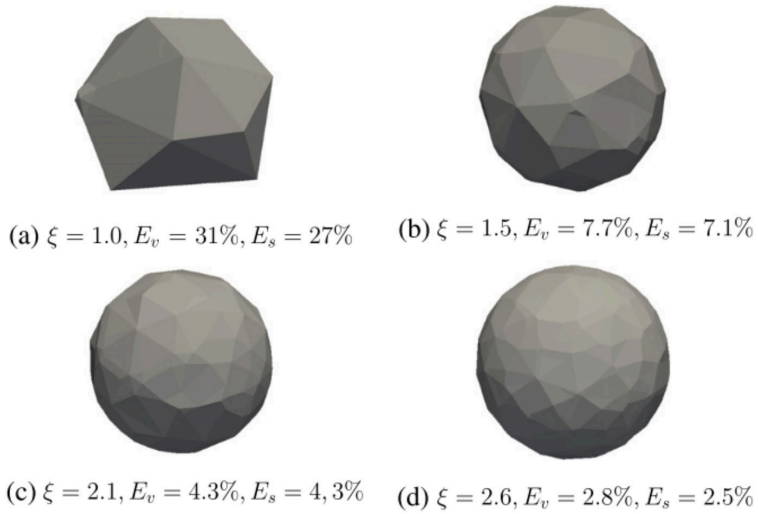

(a) $\xi = 1.0, E_v = 31\%, E_s = 27\%$ (b) $\xi = 1.5, E_v = 7.7\%, E_s = 7.1\%$

(c) $\xi = 2.1, E_v = 4.3\%, E_s = 4,3\%$ (d) $\xi = 2.6, E_v = 2.8\%, E_s = 2.5\%$

Figure 3.1: Recrystallized grains described using different FE mesh sizes. ξ is the ratio between the recrystallized grain radius and the mesh size, E_v is the error between the volume of the recrystallized grain and a sphere of the same radius, E_s is the error between the surface of the recrystallized grain and a sphere of the same radius. Image from [79].

3.3.4 Recrystallized grains appearance rate

The number of recrystallized grains that are going to be introduced is represented as a volume of recrystallized grains per unit of time $\dot{V}$, calculated with a variation of the proportional model of Peczak and Luton [52]:

$$dV = k_g \phi dt \ , \tag{3.10}$$

with k_g a probability coefficient that depends of the strain rate and temperature, and ϕ the total boundary surface area of grains with dislocation density

higher than the critical value, for the case of necklace nucleation.

3.4 Models coupling to model DDRX

The coupling of the models involves solving two FE problems, the mechanical, and the GBM migration. Both problems are solved on the same FEM mesh, which deforms according to the mechanical deformation, this prevent some of the problems described in chapter 1 associated with using multiple meshes. Fields corresponding to the variables considered in each FE problem are generated and associated to mesh nodes (P1 variables fields) or mesh elements (P0 variables fields). In the mechanical problem, the orientation and dislocation variables are defined as P0 variables, while for the GBM calculation the LS functions and the grains dislocation density are defined as P1 variables. So, in order to couple the models, it is necessary to define the initial values of the variables to be coherent for the two problems, plus during calculation the values need to be interpolated. Additionally the mesh size, time step, and remeshing operations need to be correctly adapted to ensure the correct solution of both problems and minimize the computational cost. Thus, sensibility analyses were performed for the models independently, and for the coupled model after the coupling algorithm was defined.

3.4.1 Grains generation and fields interpolation

The microstructure is immersed in a unstructured FE mesh as LS functions as illustrated in figure 3.2 for a Voronoi tessellation example. From the initial microstructure, the initial grain properties are generated. Most of the initial material properties can be defined as constants values for all elements and nodes inside the domain, except for cases of multi-phase materials. However some properties need to be defined according to the grain structure, one value defined per grain. These properties are the initial dislocation density and the initial grains orientation. In this framework both the orientation and the dislocation density can be defined by assigning specific values to each grain, or following a defined distribution.

Both the orientation and the dislocation density are generated initially as P1 variables following the grains description, with one value per grain. However, to perform the CP calculations they must be interpolated as P0 variables. This is done in the following way: for elements with all nodes belonging to the same grain, the value assigned to the element corresponds to the value of the grain. For elements with nodes belonging to different grains, the orientation value that represents the minimal rotation with respect to

the reference frame is assigned to the element (this definition constitutes a first approach, other definitions might be used). For the dislocation density, a weighted average is performed between the dislocation values of the grains that the nodes belong to, with the weights being the volume of the element belonging to each grain.

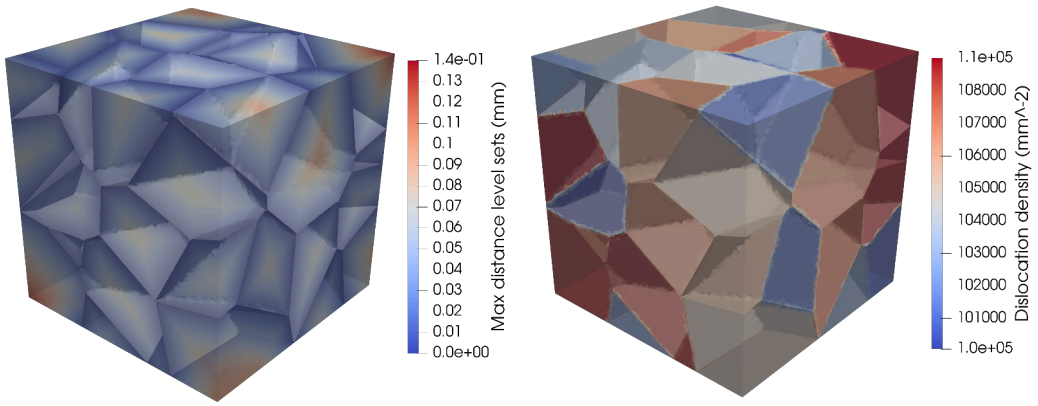

Figure 3.2: Max value of LS functions (left side) and initial dislocation density constant per grain (right side) in an unstructured finite element mesh representing 3D microstructure generated using Voronoi tessellation. Contours show the 0 value of the level set functions, i.e. the grain boundary network.

The P0 orientation and dislocation fields are used in the CP calculations. If CPFEM is used, their evolution will be heterogeneous even inside the grains. Next, in order to perform subsequent GBM calculations the dislocation density field must be interpolated back to a P1 field. However since this dislocation density field is an heterogeneous field, even inside the grains, the resulting velocity field due to energy gradients will also be highly heterogeneous.

In other to correctly solve the transport equation with a highly heterogeneous velocity field, a very refined mesh can be used, but it increases dramatically the computational cost, of the whole simulation [146]. To reduce the computational cost, the dislocation density field is averaged per grain in order to calculate the transport velocity as shown in figure 3.3. The averaging of the dislocation density field is an initial approach (classic in PF or LS frameworks) and it is further discussed in section 3.5.5.

To prevent numerical diffusion by the interpolation and the average procedure, the P0 fields from the CP calculation are kept and the effect of GBM are applied directly on them. The P1 dislocation density field used in the

GBM calculation is a temporal field that is always calculated from the P0 field and does not directly affect it.

GBM is driven by the reduction of the stored energy which implies a decrease of the dislocation density field inside the grains. Then, a minimal or annealed dislocation density ρ_0 which is material dependent is assigned to the swept areas. After the GBM calculation, the P0 dislocation density field is updated according to:

$$\rho_e = \rho_{e\,t-dt}\,(1 - f_{swept}) + \rho_0\,(f_{swept}) \ , \tag{3.11}$$

with ρ_e the dislocation density in the element after the GBM, $\rho_{e\,t-dt}$ the dislocation density in the element before GBM, and f_{swept} the swept volume fraction of the element.

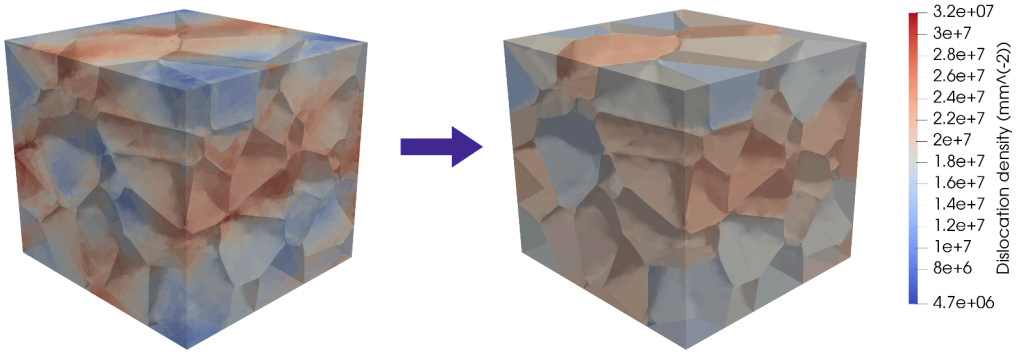

Figure 3.3: P0 dislocation density field from CP calculation (left side) and its corresponding averaged per grain P1 dislocation density field for the calculation of the GBM velocity (right side).

On the other hand, the P0 orientation field is only updated when an element is completely swept into another grain (all the element nodes are located inside another new grain). The orientation assigned is the orientation of its closest neighbour that was located in the new grain before the swept took place.

Post Nucleation treatment

After the introduction of a ReX grain, the P0 dislocation density and orientation fields must be updated in order to reflect the nucleation effect in the CP calculations. It is done in the following way: for the dislocation density field, the nucleated grains will have a dislocation density equal to the minimal dislocation density ρ_0. The update procedure for the elements in which

a recrystallized grain appears follows the one used for the GBM. The new dislocation field is calculated as:

$$\rho_e = \rho_{e\ t-dt}\,(1 - f_{nuc}) + \rho_0\,(f_{nuc}) \quad , \tag{3.12}$$

with f_{nuc} the volume fraction of the element occupied by the recrystallized grain. For the orientation field, the recrystallized grain orientation can be defined according to different criteria, in the same way as the initial orientations are generated. The criteria mostly used in this work are assigning a random orientation to the nucleated grain, or defining the recrystallized grain orientation as the orientation of the parent grain (grain in which the center of the recrystallized grain is located), plus a random misorientation of minimum 15° degrees. For the elements orientation field, only the elements with all their nodes inside the recrystallized grain are affected. The same orientation is assigned to all the elements.

The difference in the selection of affected elements, causes that some elements near the recrystallized grains boundaries will only have their dislocation density field updated. However the orientations field can not be treated in the same way as the dislocation density field. Figure 3.4 illustrates the update of the dislocation density field after the appearance of a recrystallized grains.

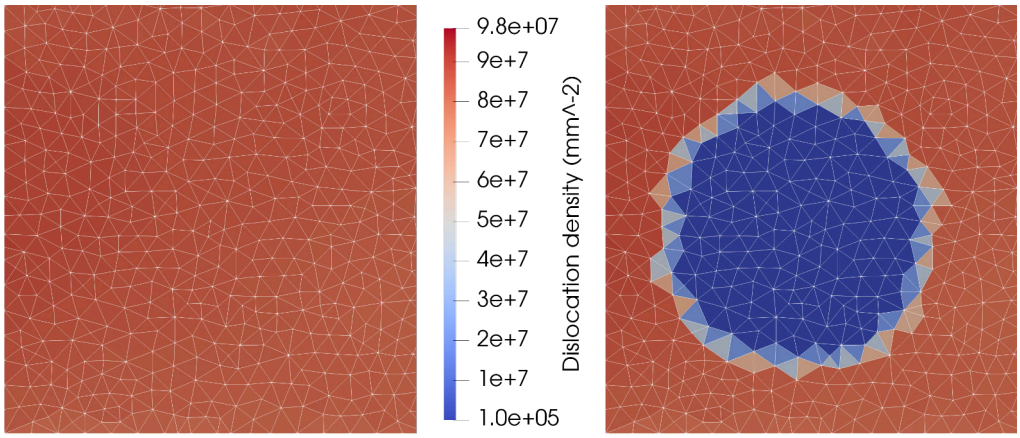

Figure 3.4: 2D view of the elements affected by the introduction of a recrystallized grain: dislocation density field.

Updating the dislocation density fields and orientation fields, creates additional localized gradients and breaks the equilibrium state of the CPFEM calculation. This can affect the convergence of the next CPFEM calculation.

3.4.2 CPFEM sensitivity analysis

A sensitivity analysis of the numerical parameters of the model was performed in order to ensure the convergence of the results and minimize the computational cost of the simulations. To perform this study, several simulations were performed by changing different numerical parameters (mesh size, time step, domain size) according to the studied cases. As described in chapter 2, an isotropic remeshing strategy with uniform size is used in the simulations.

The boundary conditions imposed for the simulations represent a channel die compression at a constant strain rate of $\dot{\epsilon} = 0.01(s^{-1})$. Figure 3.5 shows the schematic of the boundary conditions, the imposed velocity is calculated for the shown faces as the points coordinates multiplied by the strain rate. The remaining faces are forced to remain flat by imposing a velocity equal to 0, in the direction normal to the face.

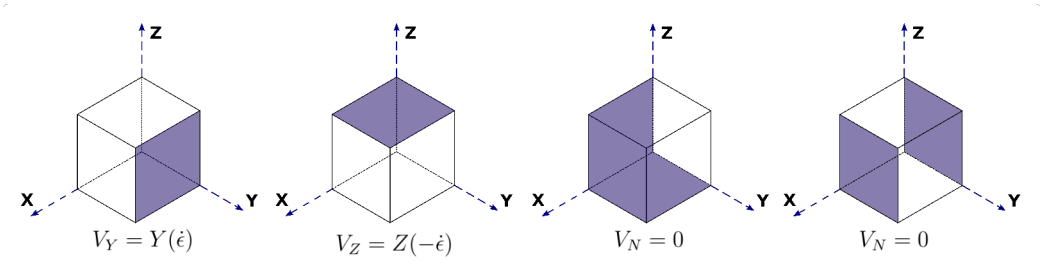

Figure 3.5: Schematic of the imposed boundary conditions.

The material parameters for the simulations were obtained from [6, 121], and the grains orientation follows a random distribution.

CPFEM mesh unstructured isotropic mesh size

For the CPFEM calculation, the number of elements required to ensure convergence in terms of stress (computed as the total force applied on the top Z face divided by the area) response and average dislocation density evolution was studied. The analysis is performed in terms of number of elements per grain (N_{elems}), calculated as the average equivalent grain diameter (D_{eq}) divided by the average mesh size (M_{size}):

$$N_{elems} = \frac{D_{eq}}{M_{size}} \tag{3.13}$$

For this analysis, CPFEM simulations on a domain of 200 grains, with a grain average size of 0.05 mm, with different mesh sizes were performed. The

simulations were performed up to a deformation of 25% without remeshing operations. The mesh size range considered was from 4.0 up to 8.0 elements per grain (The number of elements per grain refers to the relation between the equivalent grain diameter and the mesh size). The lower value of 4.0 elements per grain corresponds to the minimum value used in [79] as the number of elements required to ensure a correct representation of the recrystallized grains topology. The results in terms of stress and average dislocation density are presented in figure 3.6. The results showed that 4 elements per grain ensure a good average response in terms of convergence for the CPFEM simulations.

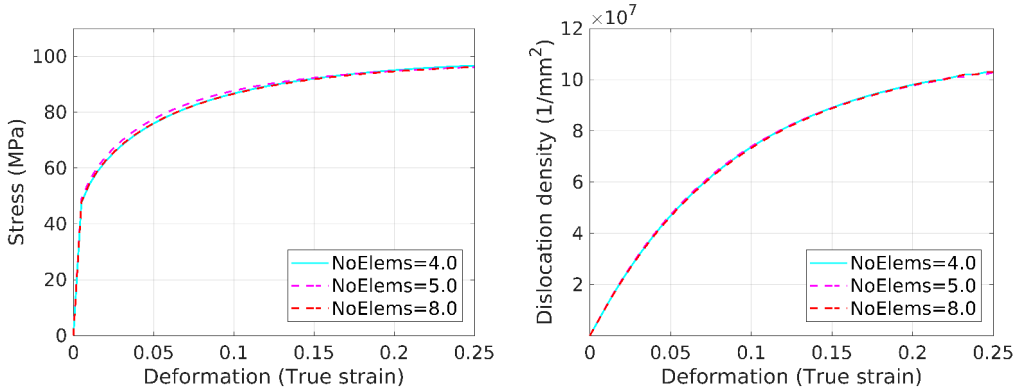

Figure 3.6: Stress vs strain curve (left side) and dislocation density vs strain curve (right side) for CPFEM simulations for different number of elements per grain. For a domain of 200 grains, with a grain average size of 0.05 mm.

To check the convergence in terms of local evolution, simulations of the deformation of a polycrystal with different mesh sizes were compared. To perform the comparison, the same sites were used in the Voronoi tessellation algorithm generate the microstructures, and the same initial orientations and dislocation density were assigned to each grain, ensuring that the initial polycrystals are equal for all the cases. The local dislocation density distribution weighted by the volume of the elements at different deformation levels, for the considered mesh sizes, are shown in figure 3.7. The mean L^2 difference (calculated by interpolating results of each simulation to a common mesh, Eq. 3.14) with respect to the case with the smaller mesh size were also calculated and are shown in figure 3.8.

$$L^2 = 100 * \sqrt{\frac{\sum_{i=1}^{N}(v_i - v'_i)^2}{\sum_{i=1}^{N}(v'_i)^2}} \quad , \tag{3.14}$$

with N the number of elements, v_i the variable value in the element i and $v_i^{'}$ the reference variable value in the element i.

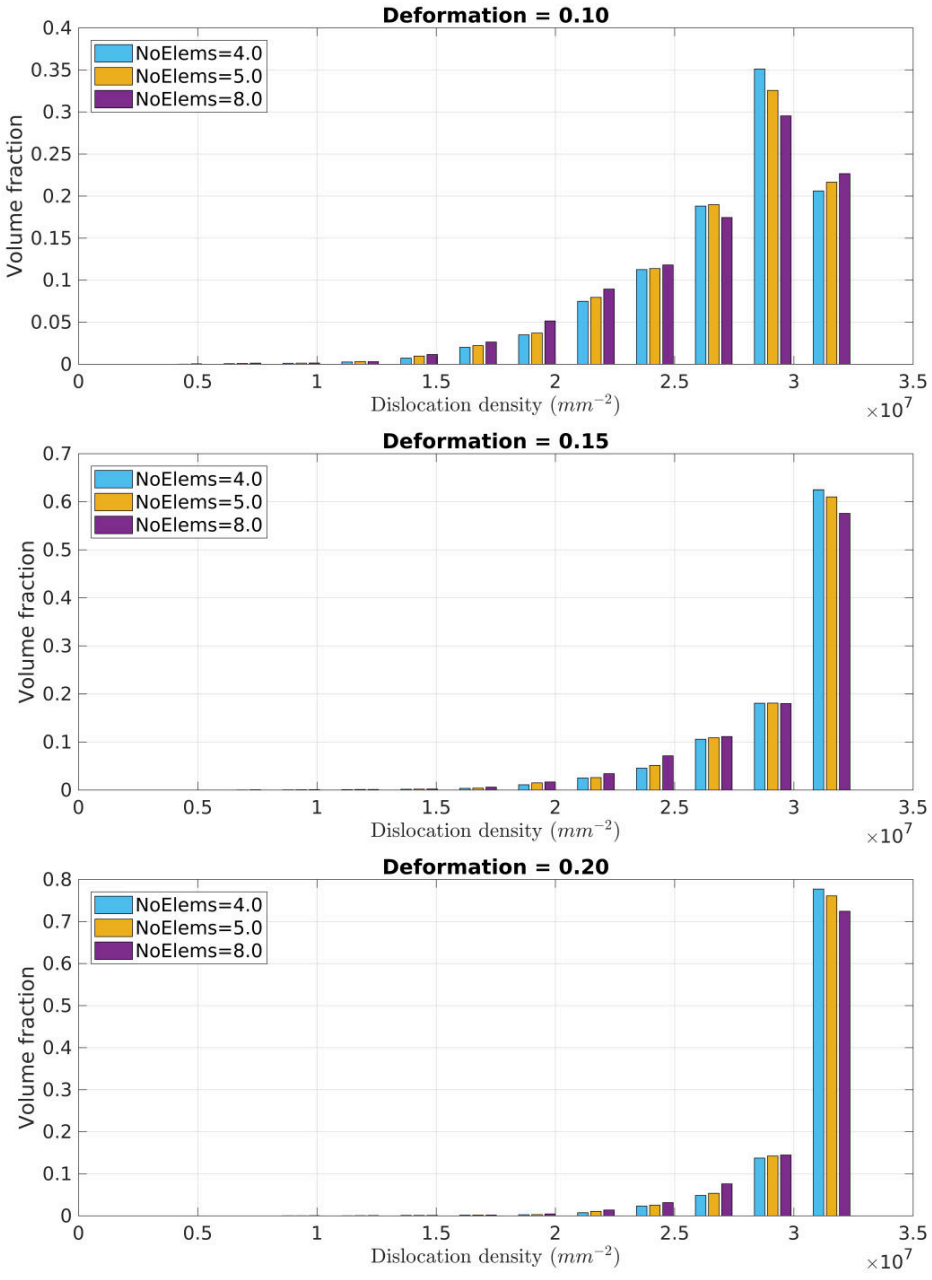

Figure 3.7: Comparison of the local dislocation density distribution in volume for the simulations of an identical polycrystal with different mesh sizes, for different deformation levels ($\epsilon = 0.10$ top, $\epsilon = 0.15$ middle, $\epsilon = 0.20$ bottom).

The results show moderate differences for the different mesh sizes. Bigger mesh sizes give a more stiff response of the polycrystal. With the increase in deformation more elements reach the maximum dislocation density, as determined by the used hardening law. This reduces the heterogeneity of the field and causes a reduction in the differences between the answers obtained for the different mesh sizes.

Since the reduction in the mesh size causes a significant increase in the computational cost, the choice in the mesh size will finally be a compromise between the required accuracy and the available computational resources. Here the initial value of four elements per initial grain will be used as the minimal value for the CPFEM simulations in which the average response is analyzed. For the DRX simulations, the mesh size required for the grain boundary migration calculation, the mesh size required for correct representation of the recrystallized grains, and the domain size i.e the number of grains, also needs to be considered. This is presented in the following sections.

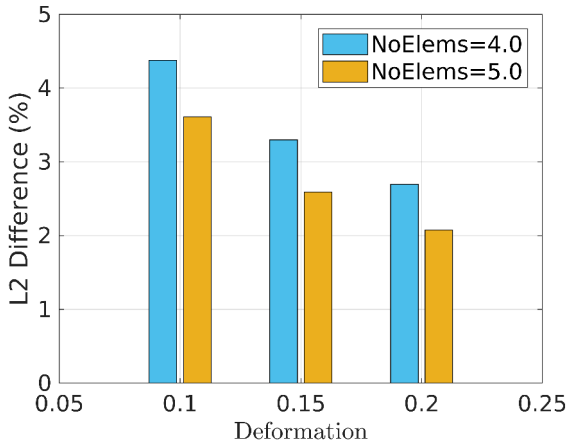

Figure 3.8: Mean L2 differences of the local dislocation density for the simulations of an identical polycrystal with different mesh sizes, calculated with respect to the case with the smaller mesh size, for different deformation levels.

Number of grains

The number of grains in the domain required to obtain convergence in the homogenized response of the polycrystal was analyzed. For this, simulations were performed for different domains size i.e. different number of grains, with an average grain size of 0.05 mm. Figure 3.9 shows the responses in terms

of stress and dislocation density.

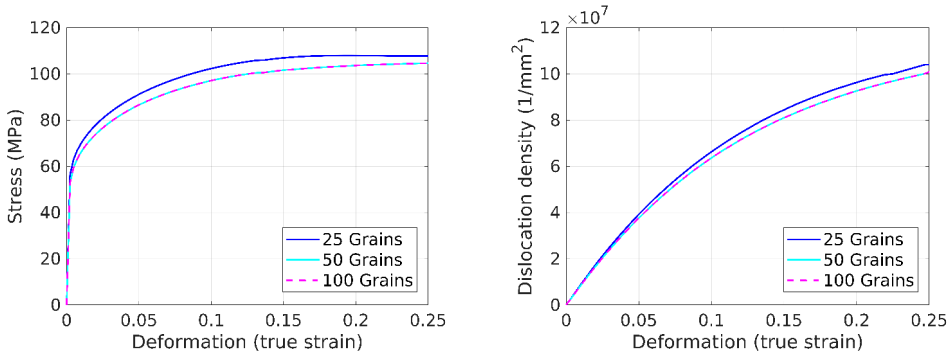

Figure 3.9: Stress vs strain (left side) and dislocation density vs strain (right side) response for simulations with different initial number of grains.

The results showed that 50 grains ensure convergence in the polycrystal response. Lower number of grains causes that the average polycrystal response depends on the orientations assigned to the initial microstructure.

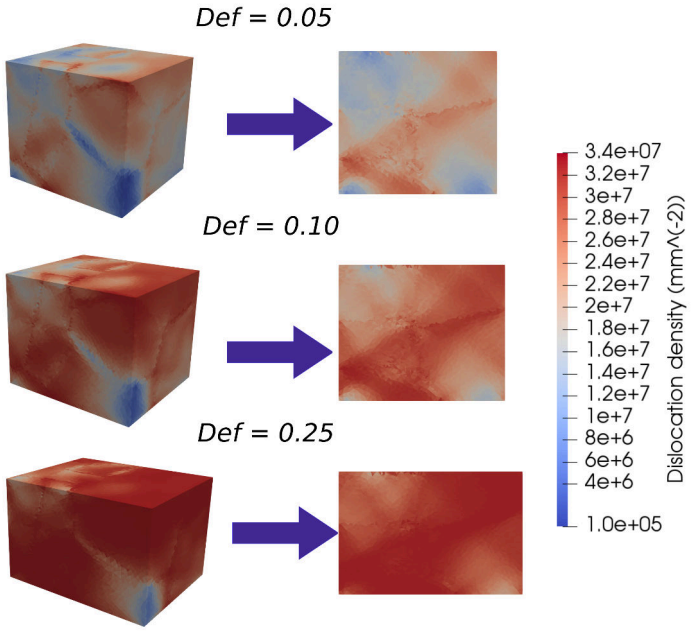

Figure 3.10: Local dislocation density evolution during CPFEM simulation. (Left side) Complete domain and (right side) middle plane cut of the domain.

The number of grains considered in the domain also defines the number of grains in contact with the boundary. Since the imposed boundary conditions can affect the evolution of the grains close to it, figure 3.10 shows the local density evolution of the dislocation density during the CPFEM calculation, for the case considering 25 grains in which the boundary effect should be greater. Additionally figure 3.11, shows the comparison of the dislocation density distributions by number between the elements near the boundary and the elements in the center of the domain, for the same simulation case.

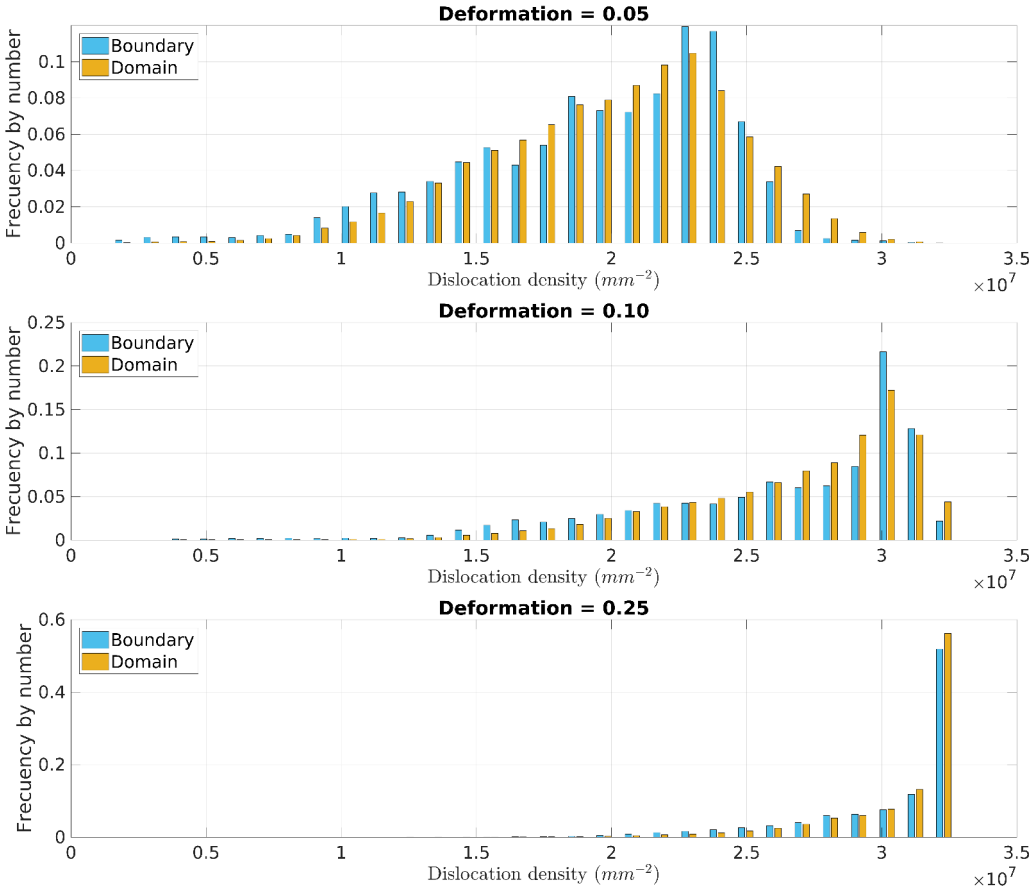

Figure 3.11: Local dislocation density evolution during CPFEM simulation. Distributions by number compared for elements in the center of the domain and elements near the boundary.

The results show that for the imposed boundary conditions, the elements near the boundary do not show a significant different behaviour than the rest of elements in the domain. The differences in the dislocation density evolution is determined by the orientation. Additionally since the used hardening

law (Yoshie-Laasroui-Jonas dislocation law, coupled with the Taylor hypothesis) sets a saturation value, after $\epsilon > 0.2$ most of the domain reaches the maximal dislocation density. When the maximal dislocation density value is reached the dislocation density does not evolve anymore. This effect contributes to the homogenization of the dislocation density in all the domain with the increase in deformation.

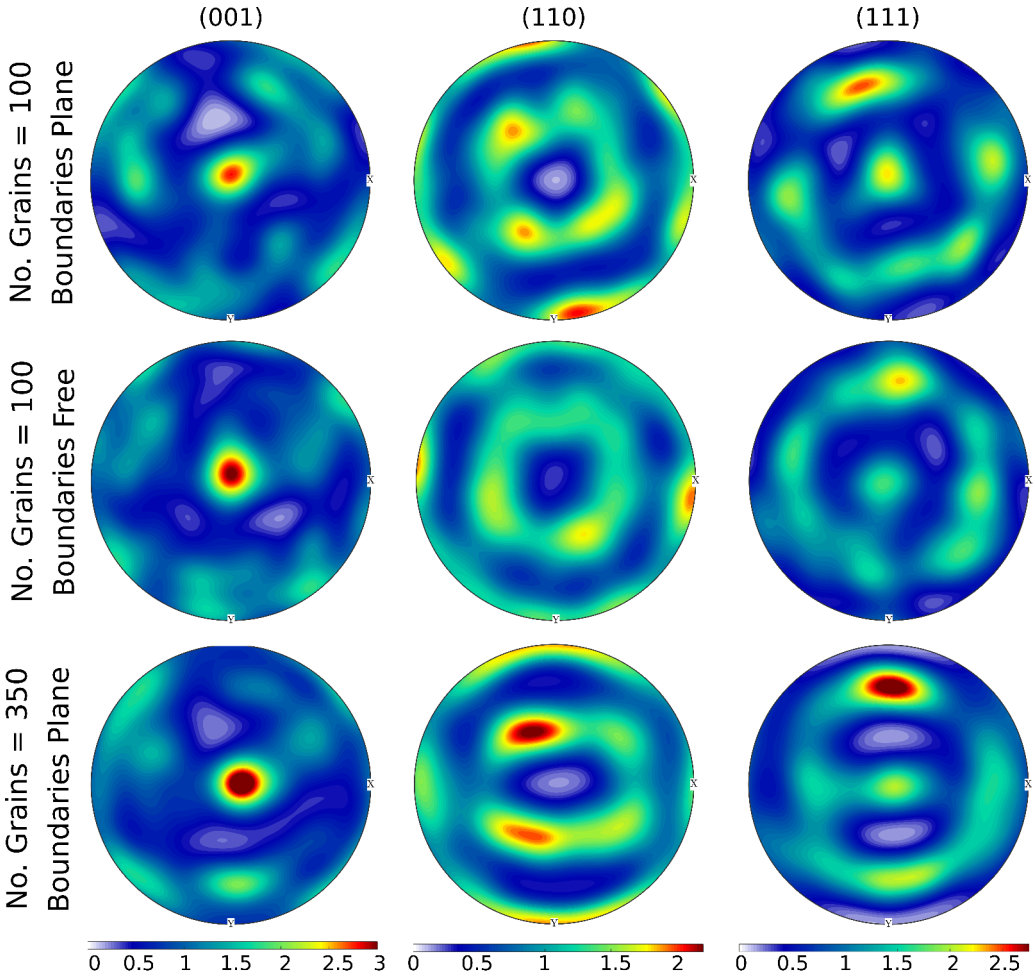

Figure 3.12: ODF pole figures in the (001) (110) (111) directions. CPFEM simulations up to $\epsilon = 0.60$: (Top) 100 grains with plane boundaries, (middle) 100 grains with free boundaries and (bottom) 350 grains with plane boundaries.

The effect of the number of grains and the boundaries on the texture evolution was also analyzed. Simulations were run with: an initial domain composed of 100 grains, considering the boundary conditions shown on fig-

ure 3.5; an initial domain composed of 100 grains, leaving the boundaries in direction of the axis x free; an initial domain composed of 350 grains, considering the boundary conditions shown on figure 3.5. The simulations were run up to $\epsilon = 0.60$, the maximal deformation level that can be reached without encountering numerical convergence problems, due to the distortion of the domain in the case with free boundaries. The ODF pole figures of the resulting final orientations are shown in figure 3.12

Comparing both cases with 100 grains shows that, the imposition of an additional plane boundary leads to the development of a stronger texture than the case with the free boundary. On the other hand, by comparing the cases with plane boundaries and different number grains, the results show that the case of 350 grains shows a stronger texture than the case that only consider 100 grains. From these results, it is clear than the texture development is affected by both the boundary conditions and the number of grains in the domain. However the final choice will be a compromise between the fact to be able to reach high deformation levels (boundary conditions) and to limit the computational cost (number of grains in the domain). So, for the next cases the domain will still be limited to 100 grains and plane boundary conditions will be used.

Time step

The final parameter studied was the time step, which considering a constant strain rate translates into a deformation step. Since CP is a highly non-linear problem, choosing an adequate mesoscopic deformation step is very important to ensure the convergence of the computation. However the non-linearity of the problem changes as the material evolves. The elasto-plastic transition (initial part of the stress-strain curve) being the more complex to resolve, followed by the plastic-hardening part (the material hardens as it is deformed), and the saturation part (material no longer hardens) being the less complex to resolve.

Additionally, in the coupled model, the GBM calculations and the appearance of recrystallized grains locally modify the dislocation density and orientation fields. This makes the following calculation more complex to resolve. So, a very small deformation step is required in order to ensure converge during all the states of the simulation. However keeping a very small deformation step during all simulation also increases drastically the total computational time.

The alternative proposed in this work in order to ensure convergence and minimize the computational cost, is to dynamically calculate the deformation time step during the simulation. The criteria used to calculate the deforma-

tion time step is based on the number of iterations required by the non-linear FE solver to reach convergence at each time step. This criteria is derived from the criteria used to adapt the time step in commercial FEM solvers like Abaqus.

An optimal interval for the number of iterations (I), defined by a minimal number of iterations $I_{min} = 7$ and a maximal number of iterations $I_{max} = 15$, was identified. This interval was identified by running several simulations with different intervals and comparing the simulations times along with the stability of the solution. So, during the simulation the time is updated according to:

$$\triangle t_{new} = \begin{cases} \triangle t_{old} * 1.5 & \text{if} \quad I < I_{min} \\ \triangle t_{old} & \text{if} \quad I \geq I_{min} \quad \text{and} \quad I \leq I_{max} \\ \triangle t_{old} * 0.5 & \text{if} \quad I > I_{max} \end{cases}, \tag{3.15}$$

with t_{new} the new time step and t_{old} the current time step. In case that convergence is not achieved, the time step is also reduced and the calculation is performed again. Figure 3.13 shows the stress vs strain curve and the deformation step vs strain curve, for a CPFEM simulation. This result shows that in this interval, the deformation step varies between 0.1% and 1%, and its value increases with deformation as the material hardens.

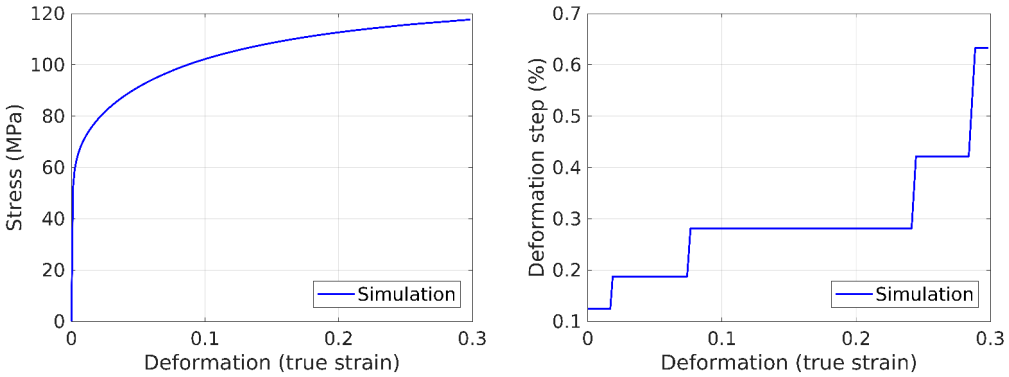

Figure 3.13: Stress vs strain curve (left side) and deformation step vs strain curve (right side) for CP simulation of 304L steel at a constant strain rate of $0.01s^{-1}$.

3.4.3 LS-FEM Sensitivity Analysis

In the previous section the numerical parameters for the CPFEM calculation were analyzed. Since the GBM requires the FE solution of a different

equation, the numerical parameters for the GBM calculation must also be analyzed. The parameters analyzed were time step and the mesh size relative to the grain size. Simulations of the GBM of a single spherical grain, immersed in an homogeneous matrix were performed. The grain dislocation density was initialized to ρ_0 and the matrix was initialized to the maximum dislocation density defined by $K1/K2$. Additionally the grain dislocation density follows the YLJ hardening equation for a constant macroscopic strain rate of $0.01(s^{-1})$. The material parameters were obtained from [79, 121].

The results were compared with the analytical solution available in [79]. Figure 3.14 shows the error of the simulated GBM in terms of calculated grain size for different mesh sizes and time steps, with respect to the analytical solution for the grain size evolution. The mesh sizes considered go from: 4 elements per grain, up to 8 elements per grain. The range of time steps considered goes from 1 s up to 10 s, for the cases considering different time steps the mesh size was set to 4 elements per grain.

The results for the different mesh sizes show that: for the case considering 4 elements per grain, the error starts at 20% at the beginning of simulation and goes down to 10% at the end of the simulation. For the case of 5 elements, the error remains relatively constant at levels around 10% during all the simulation. For the case of 7 elements, the error starts around 10% at the beginning of the simulation and goes down to 7% at the end of simulation. Finally for the case of 8 elements, the error remains constant around 5% during all the simulation.

For the different time steps the results show that: for the time step of 1 s the error starts at 60% at the beginning of the simulation and goes down to 40% at the end of simulation. The cases with time steps of 5 s and of 10 s show similar behaviours wit errors of 20% at the beginning of the simulation that go down to levels of 10% at the end of simulation.

The behaviour for the error for the different mesh sizes is consistent with the behaviour expected of a numerical solution. The error decreasing with the decrease in mesh size. In the previous section, when considering the effect of the mesh size in the CP simulations, the mesh size was set to 4 elements. However this results show that for the GBM calculation this mesh size leads to high errors (around 20%). So, to ensure the correct solution of the GBM migration calculation it is necessary to reduce the mesh size, i.e. consider 8 elements per grain. This mesh size leads to errors of 5% that are acceptable for this type of simulations.

To analyze the behaviour of the error for the different time steps it is necessary to consider that the total error in the calculation has multiple sources. Part of the error comes from the temporal discretization and part comes from the resolution methodology. The error related to the discretization can be

reduced by refining the time step. While, the error related to the numerical methodology comes from the numerical operations performed, that increase in number for smaller time steps.

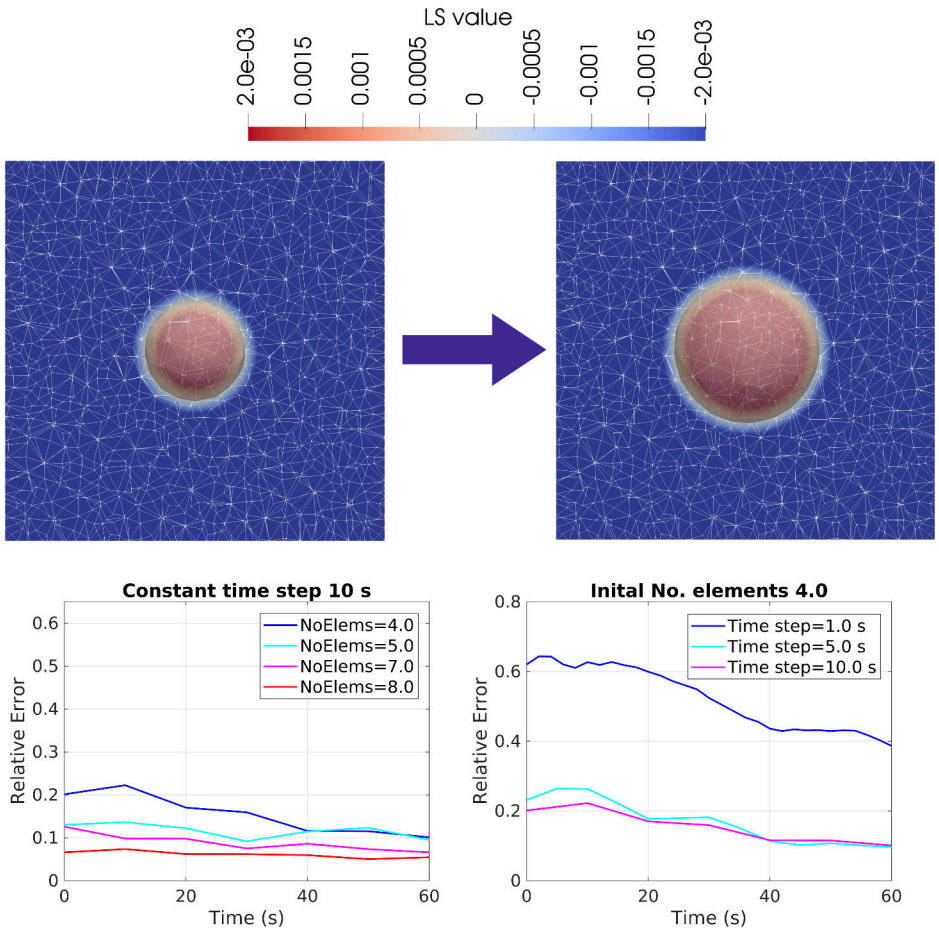

Figure 3.14: Error of the simulated GBM in terms of grain size for different mesh sizes (left side) and time steps (right side) (comparison with against analytical solution).

As it was previously described, the solution of the GBM with the current LS-FE framework requires the performance of several complementary numerical operations (removal of vacuum regions, transport of and reinitialization of the LS functions). Each numerical operation introduces errors that accumulate over recurrent iterations. The magnitudes of the introduced numerical errors are related to interpolation of the zero iso-value that defines the GB. Further details of these errors are precisely described and discussed in [147]. So, for the case considering a time step of 1 s the errors intro-

duced by the successive numerical operations (mainly the reinitialization) accumulate and lead to a very high total error in the simulation.

One alternative to reduce the errors introduced by the operations can be to use fitted meshes with nodes located along the zero iso-value of the LS functions. As described in chapter 2, this is one of the remeshing strategies available using the remesher FITZ. However, this alternative requires constant remeshing operations, as the position zero iso-value changes after each GBM calculation, that in 3D have currently a prohibitive computational cost. So, it is not viable option. As an alternative, in this work to minimize the number of operations performed and ensure the correct solution of the GBM, the time step range is set between 5 and 10 s.

3.4.4 Coupling Algorithm

The coupling of the models requires several considerations in order to reach an optimal solution in terms of numerical cost, convergence and accuracy:

- The CPFEM calculation requires a smaller time step for its resolution than the GBM calculation.

- In order to ensure convergence and minimize the computational cost of the CPFEM calculation, the time step needs to be adapted during the simulation.

- The elements quality deteriorates with each iteration as the nodes positions are updated after each CPFEM iteration (Updated Lagrangian approach). Therefore remeshing operations must be performed to ensure a good mesh quality.

- GBM calculations require several complementary operations making one time step iteration computational costly than one CPFEM time step iteration.

- Use of very small time steps in the GBM calculations can lead to numerical errors (mainly due to the reinitialization [147]).

- The insertion of recrystallized grains requires that the mesh size is small enough to correctly describe the recrystallized grains topology. Since recrystallized grains have a smaller size than the rest of the original microstructure, the mesh must be refined before recrystallized grains are inserted.

- As the dislocation density increases because of plastic deformation, the recrystallized grain size defined by Eq.3.9 decreases. Therefore the mesh size must be refined during deformation.

- Remeshing operations in 3D have a very high computational cost.

- After the insertion of ReX grains, the increase in dislocation density during just one CPFEM time step is not enough to cause the appearance of new ReX grains.

Taking the previous consideration into account. The implemented coupling algorithm utilizes two different time steps, one for the CPFEM iterations and one for the GBM iterations. Additionally the remeshing and nucleation operations are only performed when the GBM iteration is performed. For a clearer description the global coupling algorithm is summarized in figure 3.15.

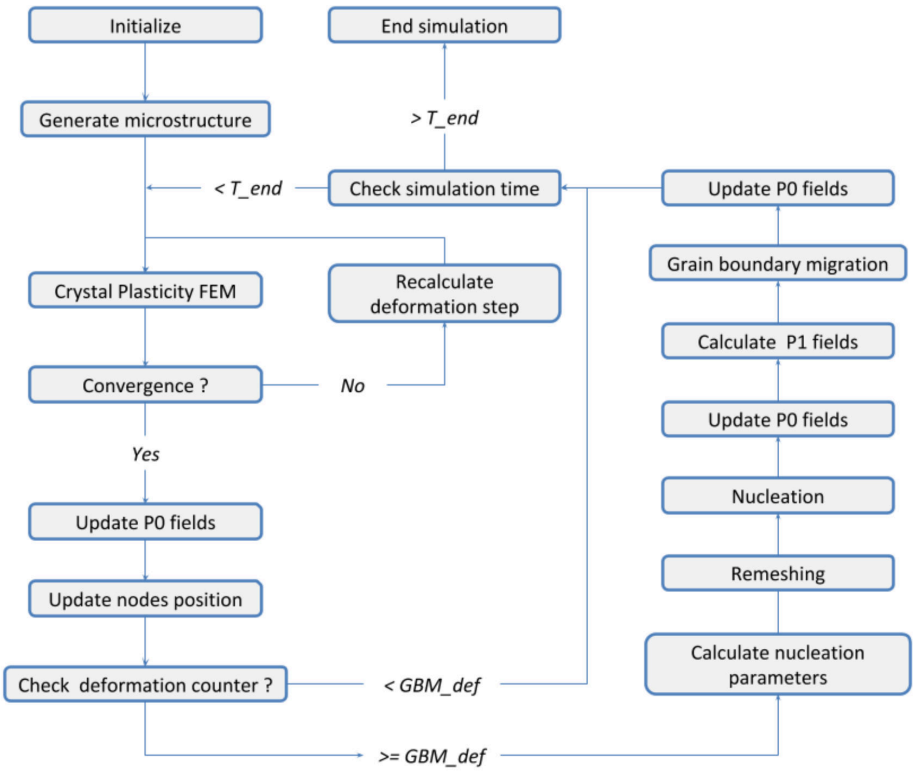

Figure 3.15: Coupling algorithm between the CPFEM and the dynamic recrystallization model.

3.5 Coupled model analysis

The sensitivity analysis presented in the previous section were performed considering each model independently. So, in this section further tests are performed for the coupled model.

3.5.1 Reference simulation

The presented coupling algorithm allows to perform full field 3D simulations of dynamic recrystallization. The simulations provide information of the average state of the microstructure and also describe the local evolution of the microstructure, including interactions between neighbours. Figure 3.16 shows an example of simulation concerning the compression of a domain composed of 400 initial grains. The simulation was ran on 4 processors of 24 cores each. The simulation time is shown to illustrate the computational cost.

The evolution of the microstructure is described in terms of: recrystallized fraction X (Eq. 3.16), volume-weighted mean grain size $\bar{R}$ (Eq.3.17), volume-weighted recrystallized mean grain size Eq. 3.18 and number of grains.

$$X = \frac{\sum_{i=1}^{n_{Rx}} S_i}{S_T} \,, \tag{3.16}$$

with n_{Rx} the number of recrystallized grains, S_i the volume of the corresponding grain, and S_T the total volume of the domain.

$$\bar{R} = \frac{\sum_{i=1}^{n} r_i S_i}{S_T} \,, \tag{3.17}$$

with n the total number of grains and r_i the equivalent spherical radius of each grain.

$$\bar{R}_X = \frac{\sum_{i=1}^{n_{Rx}} r_i S_i}{S_X} \,, \tag{3.18}$$

with S_X the total recrystallized volume.

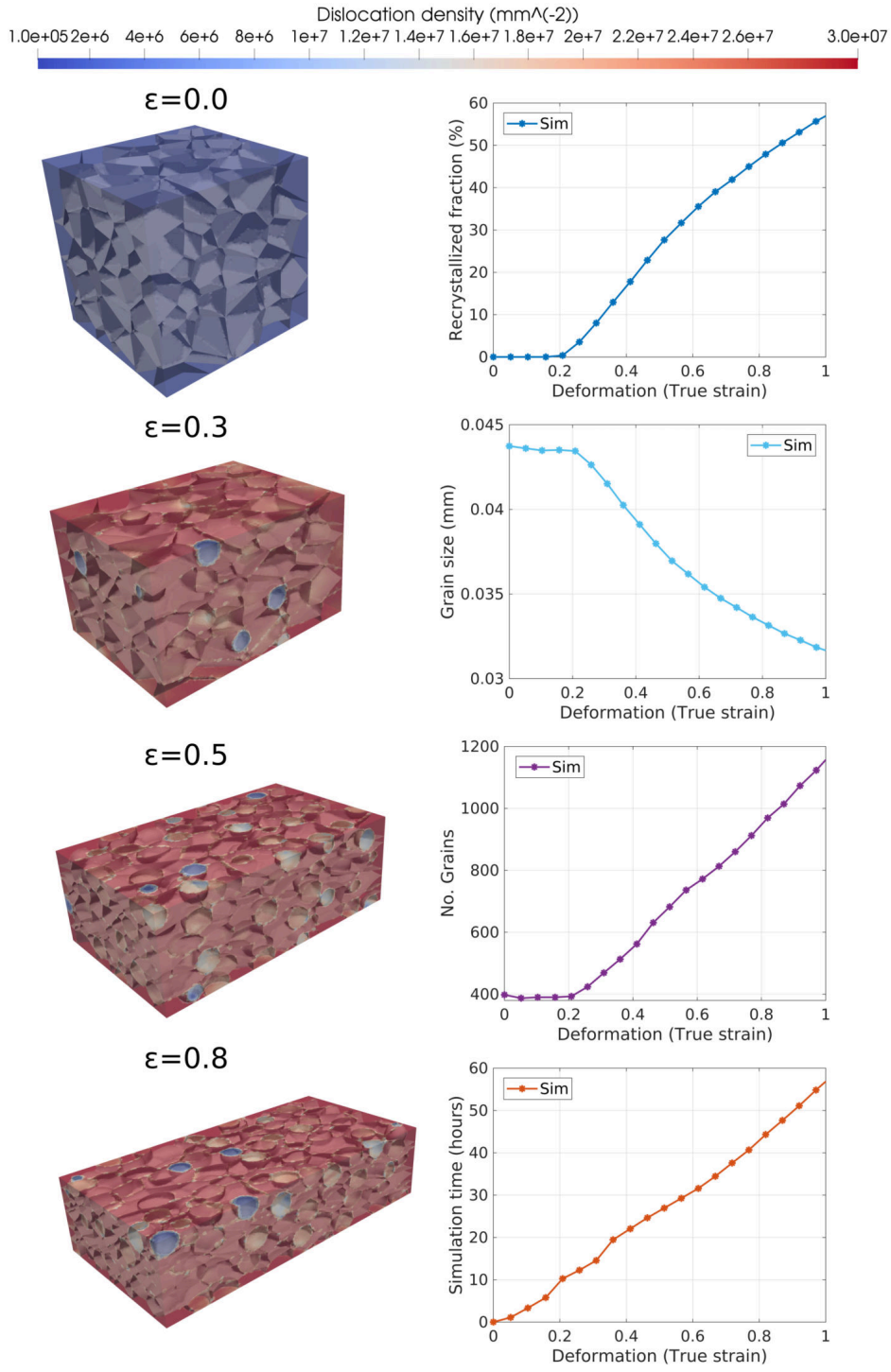

Figure 3.16: Compression test case of a domain composed of 400 initial grains.

3.5.2 Meshing/remeshing scheme for the coupled model

So far, an isotropic meshing/remeshing strategy with homogeneous mesh size has been used in this work, as described in chapter 2. In the context of DDRX simulations, Maire [6] used the same strategy to ensure that recrystallized grains are correctly described no matter where in the domain they are introduced. In this work, this strategy also ensures that intragranular gradients, that result from the CPFEM calculations, are correctly described.

However, as computational cost is one of the main limitations in the proposed coupled model, an isotropic meshing/remeshing strategy with heterogeneous element size, with smaller elements near the boundaries as detailed by Resk [140] and Fabiano [121], can help to limit the computational cost by reducing the total number of elements considered in the calculation. So, in order to define which strategy is more appropriate for the coupled DDRX model, tests between the two strategies were performed. Figure 3.17 illustrates the two meshing/remeshing strategies.

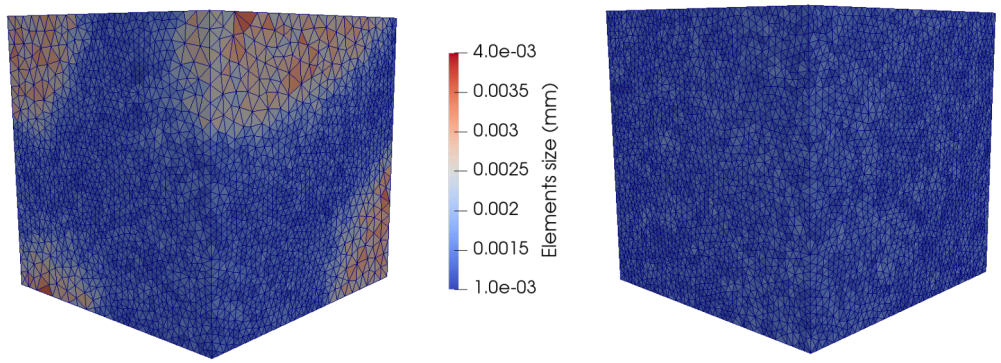

Figure 3.17: Example of remeshing strategies: (Left) isotropic mesh with heterogeneous element size and (right) isotropic mesh with homogeneous element size.

As previously described, in order to ensure a correct description of the ReX grains that are introduced, in the coupled model the minimal mesh size is defined as a function of the ReX grains size to ensure 8 elements per grain. Since the ReX grains size decreases along the simulation, the minimal mesh size is also reduced. This means that remeshing operations must be performed before the introduction of recrystallized grains, as described in the coupling algorithm. This criteria reduces the previously interval between remeshing operations, from the 25% value previously used for the CPFEM simulations, to a 5% value.

For the case of the isotropic mesh size with homogeneous value, the minimal mesh size corresponds to the mesh size in all the domain. While for the case of the isotropic mesh size with heterogeneous mesh size, the minimal mesh size is set in the zones near the boundaries where ReX grains can appear. The mesh size increases with the distance from the boundary to a maximal value of 4 elements per grain (defined according to the presented sensitivity analyses). In order to prevent convergence problems the increase in the mesh size is done gradually, as illustrated in figure 3.17. The tests performed considered an initial domain composed of 100 grains, subjected to hot compression up to 100% deformation. The results are shown in figure 3.18 in terms of simulation time.

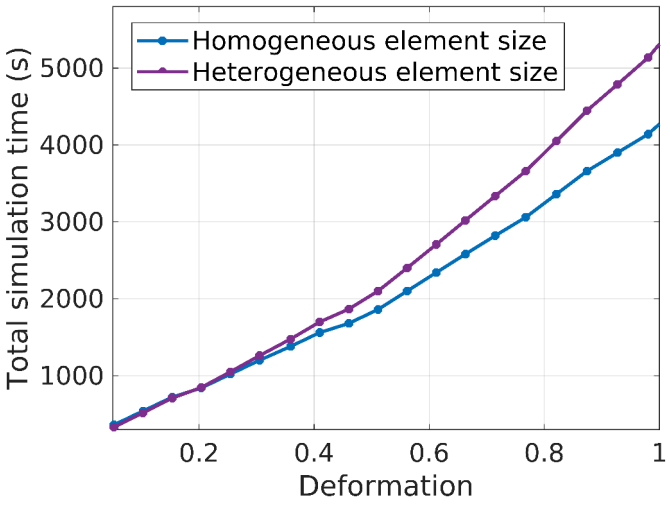

Figure 3.18: Comparison of computational time of DDRX simulations using different remeshing methodologies.

The results show that at low deformation levels the simulation time is similar for the two strategies. But, as strain increases and more recrystallized grains are introduced the isotropic mesh size with homogeneous size is more efficient. This behaviour can be explained considering that the number of topological operations required to create the mesh with heterogeneous size are higher, thus it is more computational costly. This usually can be compensated by the fact that the mesh with heterogeneous size contains fewer elements in total than the mesh with homogeneous size, since the mesh size is increased in zones far away from the boundaries. However, this is not applicable in this case, because the maximal mesh size inside the grains is also restricted to ensure a correct discretization for the CPFEM calculations. So,

the resulting total number of elements are similar in both cases. Furthermore, as the number of grains increases the zones in the domain where the minimal mesh size value is imposed also increases, reducing even more the difference in total number of elements between the two strategies. So, even if a more precise study concerning the impact of the thickness of the refining zone in the heterogeneous strategy could also be realized to enrich this discussion; for the simulations considered in this work, the homogeneous size strategy was definitively adopted. This conclusion is also in agreement with the detailed discussion concerning this topic described in [?].

3.5.3 Coupled model - Domain Size

Simulations were run to check the number of initial grains required to correctly describe the general behavior of the polycrystal. For this test, simulations of the coupled model were run considering different initial domains sizes, ranging from 20 to 200 initial grains. The results were analyzed considering the average behaviour in terms of X and $\bar{R}$, and are shown in figure 3.19.

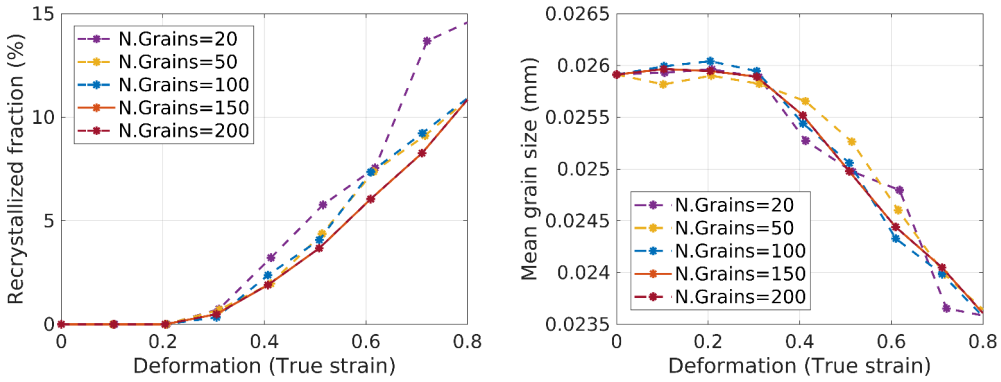

Figure 3.19: Results of simulations of dynamic recrystallization with different domains sizes, ranging from 20 to 100 initial grains, in terms of X (left) and $\bar{R}$ (right) .

The results show that the minimal number of grains required to ensure convergence in the simulation results in terms of both X and $\bar{R}$ is 150 grains. Simulations with lower number of grains, 50 and 100, are able to reproduce the same trends, but the results do not show a smooth behaviour. Simulations with lower number of initial grains, 25 grains, show divergence in the results at higher strain levels in terms of X, and more discontinuous behaviour in terms of $\bar{R}$.

3.5.4 Coupled model - Recrystallized grain safety factor

Since the safety factor w is a purely numerical parameter, it was necessary to analyze its effect on the model results. Simulations with the complete coupled model for a small domain, 10 grains, were performed for different values of w. The grains dislocation density was initialized to a value close to the ρ_{cr} in order to accelerate the appearance of recrystallized grains. A small domain was chosen in order to illustrate more clearly the effect of the nucleated grains in the general behaviour of the microstructure. Figure 3.20 illustrates the evolution the nucleated grains and figure 3.21 shows the evolution of $\bar{R}$ and $\bar{R}_X$.

From the tests, the first element that must be mentioned is that in the current coupled model, contrary to the model of [79], if the mesh is sufficient small to correctly describe the recrystallized grains topology, it is not necessary to include the parameter w. Even with a value set to 1, recrystallized grains are able to grow and do not disappear if the mesh size is set in order to include 8 elements per grain.

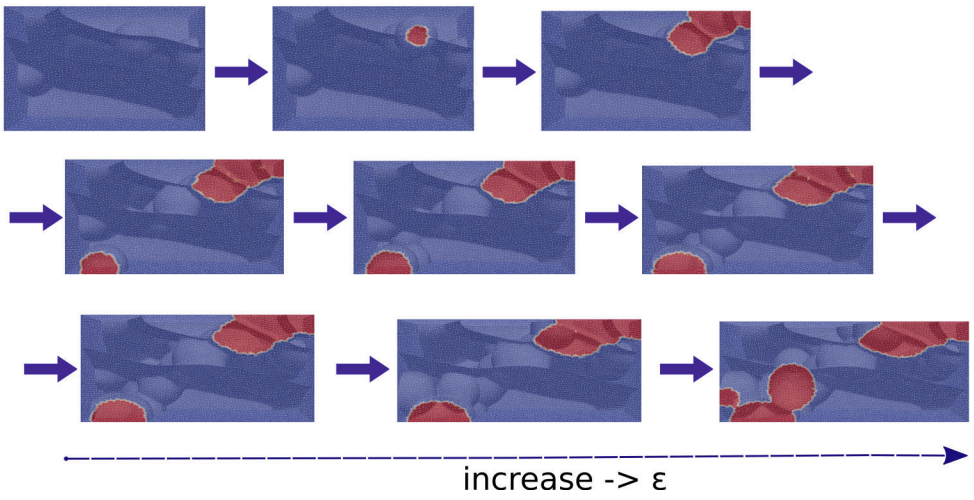

Figure 3.20: 2D view of the evolution of nucleated grains during DRX simulation of small domain composed of 10 initial grains.

The results also show that the value of w has significant effects on the simulation results and leads to overestimate $\bar{R}$ and $\bar{R}_X$. The introduction of bigger recrystallized grains facilitates their grow, leading to a faster increase in the recrystallized fraction. Additionally since the recrystallized grains introduced are bigger, the average grain size in the microstructure will converge toward a higher value.

In the end, the parameter w can be seen as a tool to reduce the computational cost, by increasing the mesh size (calculated as a function of the recrystallized grains size). However its use is not recommended since it has an significant impact in the simulation results. For the rest of this work it will be set to 1.

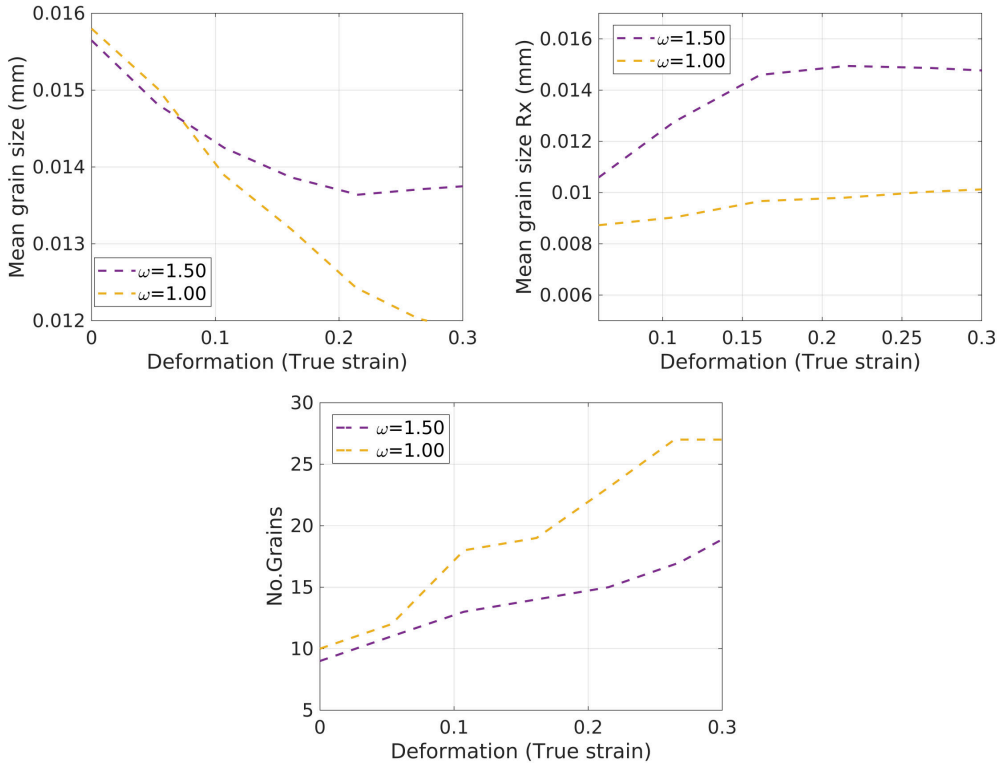

Figure 3.21: Results of simulations with different w values of 10 grains initialized with a dislocation density value close to ρ_{cr}.

3.5.5 Coupled model - recrystallized grains positions

As described in chapter 1, recrystallization originates from small-volumes that pre-exist in the deformed microstructure. The positions in which recrystallized grains are introduced in DDRX models is an open question. Different criteria exist in the literature in order to reproduce behaviours observed in experimental data, and are generally limited by the type of model used. For example, the criteria that restricts recrystallized grains appearance to only near the grain boundaries is valid for necklace type nucleation but does not correctly describe other nucleation types. So, in this coupled model, the additional information provided by the CPFEM model can be used to test

different criteria for the recrystallized grains position.

In the following several simulations were run, each considering different parameters to define the recrystallized grains position. The different criteria considered are based on the ρ field, orientations are not considered since at the polycrystal scale here, the formation of sub-grain boundaries can not be correctly predicted. All the criteria tested consider that the dislocation density must reach ρ_{cr} for the appearance of a recrystallized grain, to ensure that it will growth. In addition the following criteria were tested:

- First strategy, recrystallized grains can only appear near the boundary (necklace nucleation considered as a reference simulation).
- Second strategy, recrystallized grains can appear anywhere on the domain.
- Third strategy, recrystallized grains appear on sites with the highest value of ρ in the domain.
- Fourth strategy, recrystallized grains appear on sites with highest ρ gradient.

For, the third and fourth cases the ρ field is considered without averaging it over grains. The simulations are realized in a domain of 150 initial grains up to $\epsilon = 1.0$. The results are shown in: figure 3.22 in terms of X, $\bar{R}$ and $\bar{R}_X$. Figure 3.23 in terms of number of neighbours and recrystallized grains number of neighbours. Additionally figure 3.24 shows the nucleated grains positions at the end of the simulation.

The results show that, the average response in terms of recrystallized fraction evolution, mean grain size and average number of neighbours is very similar for all the considered cases. Differences between the results are only observed when considering only the behaviour of the recrystallized grains.

For the second case, when the deformation is lower than 0.6, recrystallized grains grow more than all the other cases, since they can appear in the interior of grains, their growth is not limited by other grains. But, at higher deformation levels the behaviour becomes equivalent to that of the reference case. In terms of number of neighbours since the recrystallized grains have more places to appear less clusters form, so they have a lower number of neighbours.

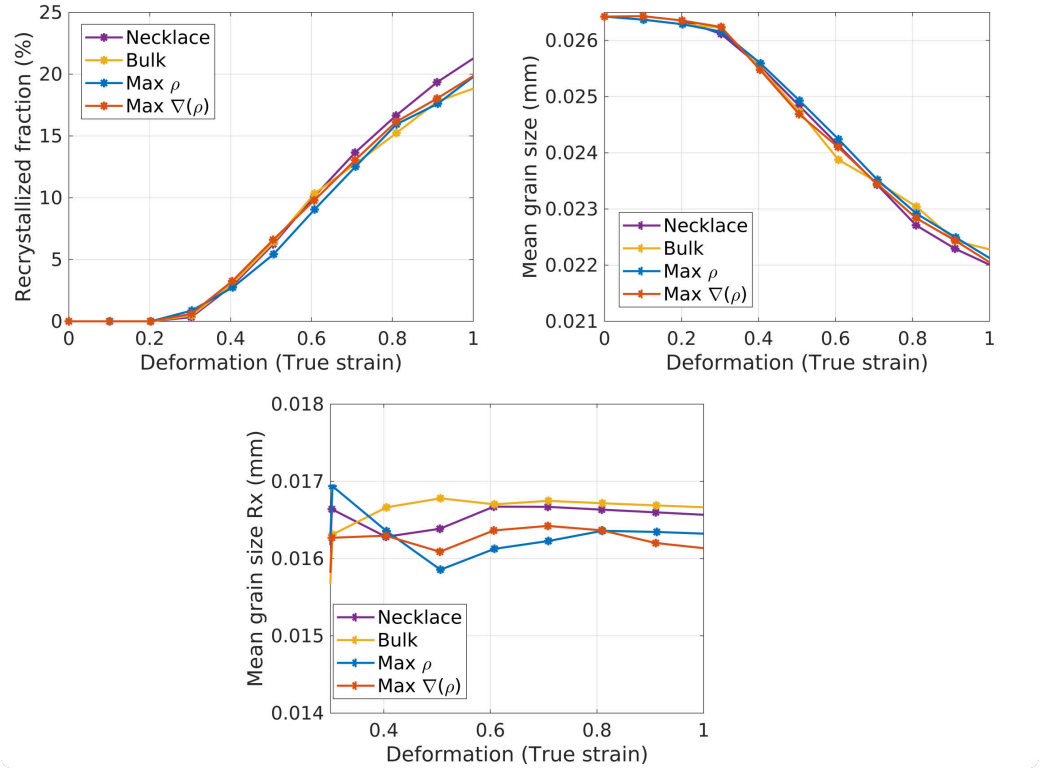

Figure 3.22: Results of simulations with different criteria for recrystallized grains position, in terms of X, $\bar{R}$ and $\bar{R}_X$.

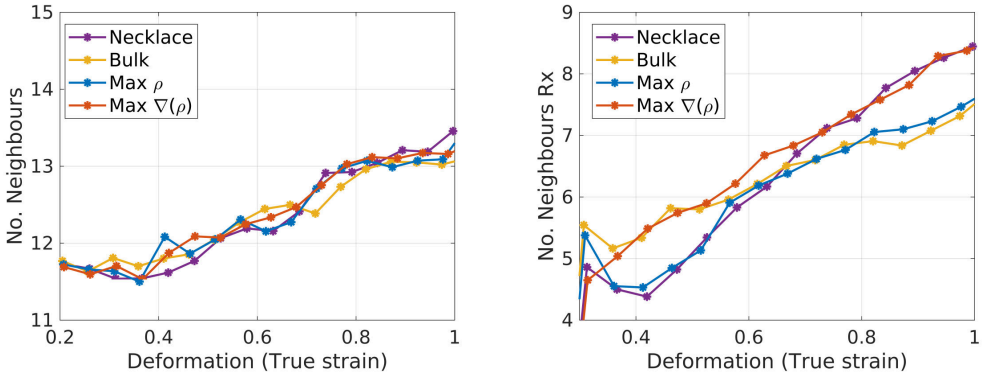

Figure 3.23: Results of the different simulations with different criteria for recrystallized grains position, in terms of grains number of neighbours and recrystallized grains number of neighbours.

For the third case, the recrystallized grains show lower sizes during all the

simulation. Local maximal ρ values appear first near multiple grain boundaries and near the domain boundaries, because the highest deformation incompatibilities are located in these positions. This causes that recrystallized grains tend to be near grains with lower ρ values than the grain they appear on, which limits their growth. In terms of neighbours, they show the lowest number of neighbours in all the cases during all the simulation. At high deformation, when most of the domain has reached the maximal ρ value, less localized maximal values are found so the behaviour becomes similar to case 2.

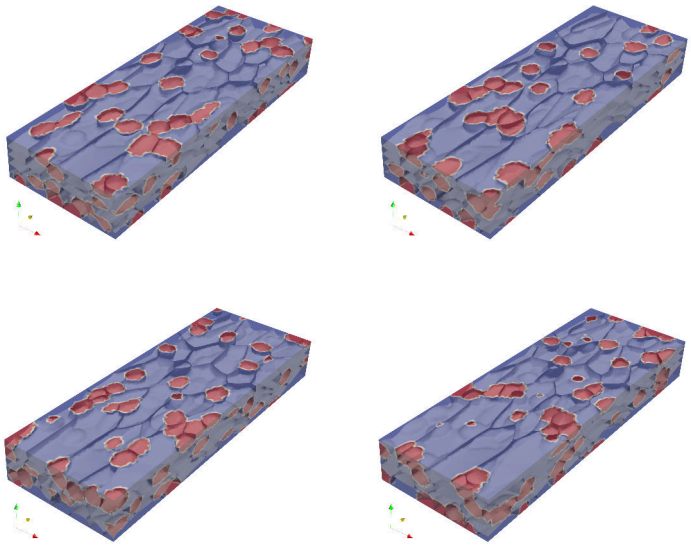

Figure 3.24: Recrystallized grains of the different simulations with different criteria for recrystallized grain position. (Top left) case 1, (top right) case 2, (bottom left) case 3 and (bottom right) case 4. Red color corresponds to the recrystallized grains.

The fourth case shows the highest clustering of recrystallized grains, with the highest number of neighbours during all the simulation, condition that also causes that clustered recrystallized grains limit each other growth. This behaviour is the result of the reinitialization of ρ to ρ_0 when a recrystallized grain is introduced, which creates very high gradients of ρ.

These results show that in all cases the general microstructural behaviour, remains globally the same. So, in theory each can be used to simulate the polycrystal evolution. It is necessary to compare the simulations results with experimental data in order to define which criteria fits better the actual physical phenomena. Additionally the criteria can be modified by defining

limit values instead of just maximal values.

Grain energy

Another approach that was tested relates to the calculation of the grain energy. So far, the grain energy has been calculated from the average dislocation density in the grain. However, as mentioned before it is possible to calculate an intragranular heterogeneous energy field from the heterogeneous dislocation density field that results from the crystal plasticity calculation. This type of calculation, will lead to a highly heterogeneous energy field, that requires a very small discretization and significantly increases the computational cost.

Following the methodology presented in [146] an intermediate approach, that considers the average energy per grain interface can be used. This means that instead of calculating an average stored energy per grain, the grain energy is averaged only around the grain interfaces. In this approach, the stored energy value is calculated for each interface as the average of all the nodes on the FE mesh that are closer to a given interface than to the others. To compare the approaches, simulations considering 100 initial grains in the microstructure, were run for cases with average homogeneous energy per grain and energy per grain interface. The results in terms on average behaviour are presented in figure 3.25 and grains distributions at $\epsilon = 0.70$ in figure 3.26.

The results considering the homogenized behaviour are very similar for the two cases. Small differences in behaviour are observed up to $\epsilon = 0.40$. The case with average energy per interface shows slightly higher recrystallized grains sizes and lower average non recrystallized grain sizes. However, at higher deformation levels, since most of the microstructure has reached the maximal dislocation density, the heterogeneity in the dislocation density field is greatly reduced, so the behaviour in the two cases is the same. Additionally, the grain size distributions also show very similar trends between the two methodologies.

In summary, the interface grain energy calculations does not show a significant change in the model results. This is caused in great part by the behaviour imposed by the chosen hardening law that sets a maximal dislocation density value. As deformation increases, most of the domain reaches the maximal dislocation density value, causing that the dislocation density field becomes almost homogeneous in all the domain (except recently introduced recrystallized grains and areas swept during GBM). Further tests should be performed considering a different hardening law. However, since in the current model, the hardening law is coupled with the phenomenological laws

describing the appearance of recrystallized grains, this change is not trivial. Additionally, using the interface methodology requires the performance of additional sensitivity test specially regarding the mesh size, so it will not be further considered in this work.

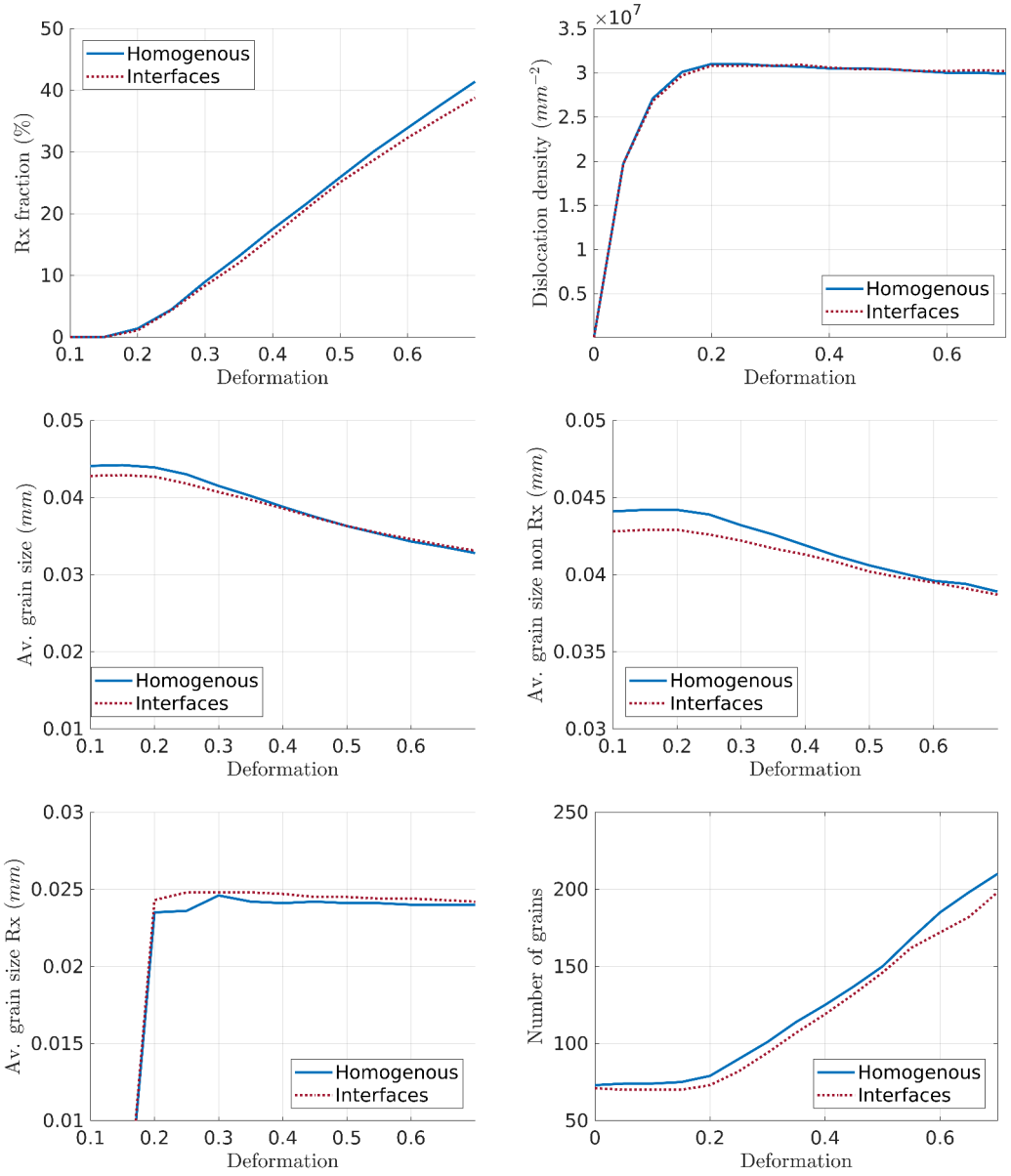

Figure 3.25: Comparison between simulations with homogeneous energy per grain and energy per grain interface. Homogenized results concerning the: recrystallized fraction, dislocation density, average grain sizes, number of grains.

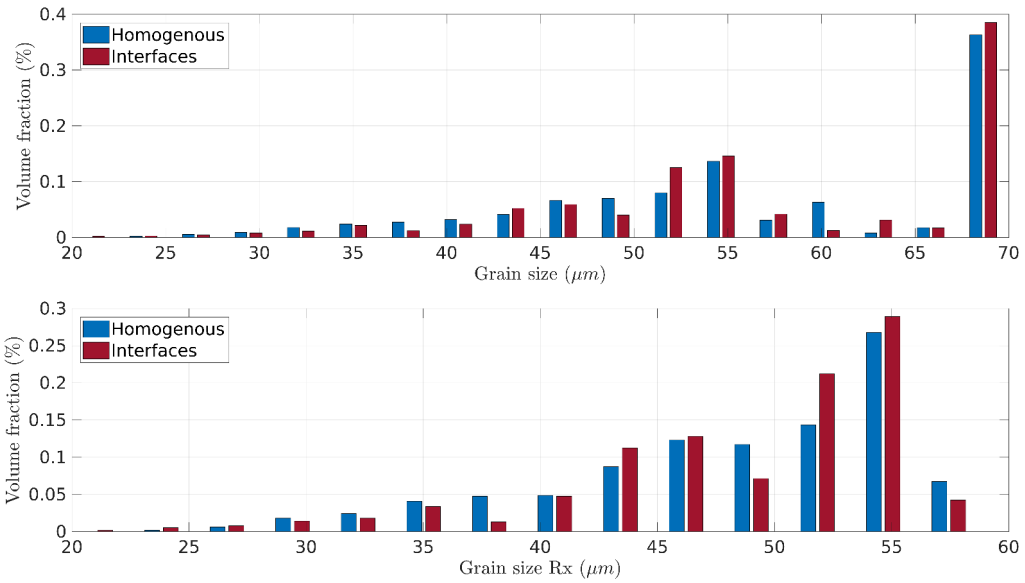

Figure 3.26: Comparison between simulations with homogeneous energy per grain and energy per grain interface. Grain size distributions at $\epsilon = 0.70$.

3.6 Summary and discussion

In this chapter the CPFEM model was coupled with a LS-FE formulation for GBM and phenomenological laws in order to perform 3D full field simulations of dynamic recrystallization up to high deformation in metals. The inclusion of the CPFEM model allows a much better representation of the plastic deformation phenomena than previous phenomenological approaches [79].

Sensitivity analysis of the different FE models numerical parameters were performed. The sensibility tests include discussions concerning the time step, mesh size and domain size. The results in terms of time step show that a multiple time step is required in order to ensure the convergence of the two FE problems. By considering the results, a coupling algorithm was developed, along with the interpolation scheme to take the $P0$ variables required in the CPFEM solution to $P1$ variables considered in the LS-FE problem. The proposed coupling algorithm minimizes the computational cost, which is one of the main limitations of the CPFEM model, and ensures the stability and convergence of both FE solutions.

The coupled model was also tested, for the nucleation parameters regarding the recrystallized grains safety factor and the nucleation positions. Results show that including the safety factor, even though it reduces the computational cost has significant effect in the model results. Additionally,

in the proposed model the results show that by ensuring a mesh size of 8 elements per grain, the numerical safety factor is not required in order to ensure that the nucleated recrystallized grains do not vanish. Considering its effect on the simulation results, it was not included ($w = 1$) in the model.

The additional information provided by the crystal plasticity model was used to define different criteria for the position of recrystallized grains, and the effect on the simulations results were compared. The results show that due to continuous deformation and continuous appearance of grains, the ReX grains position have limited influence on the results. However the necklace and bulk cases show to be the more favorable for recrystallized grains grow. This still remains an open question and the criteria chosen greatly depends on the data available in the model. In this work as considering materials that show classically necklace nucleation, the grain boundary criteria will be used.

Finally different approaches to calculated the grains stored energy were tested. The results show similar behaviour between the chosen methodologies. This is greatly influenced by the chosen hardening law. Further tests must be performed by considering different type of laws. The next step is the comparison of the model with experimental data, this will be presented in the next chapter.

3.7 Résumé en Français

Dans ce chapitre, le modèle CPFEM a été couplé à une formulation LS-FE pour la prise en compte de la migration des joints de grains. Des simulations champ complet 3D de recrystallisation dynamique sont considéres avec des niveaux de déformation potentiellement très élevés. L'inclusion du modèle CPFEM permet une bien meilleure représentation des phénomènes de déformation plastique que les précédentes approches à base phénoménologiques [79].

Une analyse de sensibilité des différents paramètres numériques des modèles EF a été réalisée. Le test de sensibilité inclut des discussions concernant le pas de temps, la taille de maille et la taille du domaine. Les résultats en termes de pas de temps ont montré qu'un pas de temps multiple est nécessaire pour assurer la convergence des deux problèmes EF. En considérant les résultats, un algorithme de couplage et un algorithme d'interpolation été développé. L'algorithme de couplage proposé minimise le coût de calcul, qui est l'une des principales limitations du modèle CPFEM, et assure la stabilité et la convergence des deux résolutions EF.

Le modèle couplé a également été testé pour les paramètres de nucléation concernant le facteur de sécurité sur la taille de grain recristallisé [6] et les positions des germes. Les résultats ont montré que l'inclusion du facteur de sécurité, même s'il réduit le coût de calcul, a un effet significatif sur les résultats du modèle. De plus, dans le modèle proposé, les résultats ont montré qu'en assurant une taille de maille de 8 éléments par grain, le facteur de sécurité numérique n'est pas nécessaire pour s'assurer que les grains recristallisés nucléés introduits ne disparaissent pas par diffusion numérique. Compte tenu de son effet sur les résultats de la simulation, il n'a pas été dans le modèle.

Les informations supplémentaires fournies par le modèle de plasticité cristalline ont été utilisées pour définir différents critères pour la position des grains recristallisés, et l'effet sur les résultats des simulations a été discuté. Les résultats ont montré qu'en raison de la déformation continue et de l'apparence continue des grains, la position des grains recristallisés a une influence limitée sur les résultats. Cette question reste ouverte et les critères choisis dépendent largement des données disponibles dans le modèle.

Enfin, différentes approches pour estimer le champ d'énergie stockée par déformation plastique ont été testées. Les résultats ont montré un comportement similaire entre les méthodologies choisies. Ceci est fortement influencé par la loi de durcissement choisie. D'autres tests doivent être effectués en considérant différents types de lois.

La prochaine étape est la discussion du modèle comparativement à données expérimentales, c'est le but du chapitre suivant.

Chapter 4

DDRX model calibration and validation

4.1 Introduction

In this chapter the full field model is compared with experimental measurements. First, the experimental tests and results are presented. The procedure to identify and validate the model parameters is detailed. A simplified model that uses the Taylor model is introduced to reduce the computational cost and improve the calibration procedure. Next the model results are discussed along with strategies to improve the model limitations. Finally the DDRX models using CPFEM, Taylor and phenomenological laws are compared. The experimental tests presented here were realized by Maire, L. in his Phd work [6]. In this work, only a re-analysis of the raw experimental data was performed.

4.2 Experimental Methods

Hot-compression tests were performed on 304L steel samples to reproduce industrial forging processes. The tests were performed for different sets of conditions in terms of strain rate and temperature.

The thermomechanical path is defined by the following steps: (A) The sample is put in the pre-heated oven. (B) The sample is kept at high temperature for 30 minutes to homogenize its temperature. (C) The sample is compressed at constant strain rate up to a given stain level. (D) The sample is water-quenched with the minimal possible delay (i.e. around 2 seconds) to stop post-dynamic microstructural evolutions.

The tests were performed in a MTS Landmark 370-25 compression machine equipped with a 2000 W oven. The lower and upper tools are made of superalloy Udimet 720, with a silicon nitride (Si_3N_4) ceramic insert, and molybdenum disulphide (MoS_2) as a lubricant. Two sample geometries (shown in figure 4.1) were tested, cylindrical samples to asses stress-strain curves and investigate the microstructure at low strain levels, and double-cone samples to investigate the microstructure at high strain levels.

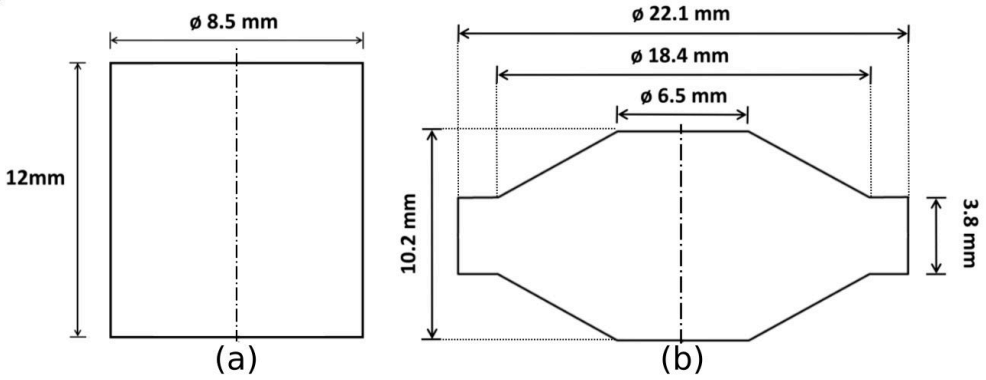

Figure 4.1: Sample geometries used in the thermomechanical tests, cylindrical samples (a) and double-cone samples (b). Dash-Dot lines indicate revolution axis.

After the compression tests, the samples were cut along the compression axis through the diameter, and polished in order to perform EBSD (Electron Back-Scatter Diffraction) measurements on specific points. On the cylindrical samples, EBSD measurements were taken at the center of the longitudinal section, and on the double-cone samples, the measurements were performed at the center and at distance of $R/3$ from the center of the longitudinal section, with R the radius of the deformed sample.

The local strain and strain rate level at the measurement points (given in table 4.1) were estimated from FEM simulations of the compression tests, performed using the software Forge®. The EBSD measurements were done using a Zeiss Supra 40 FEG SEM (Field Emission Gun Scanning Electron Microscope) equipped with a Bruker EBSD system. EBSD maps were acquired with a 0.47 μm step size, over an area of 250 μm by 330 μm, chosen to compromise between spatial resolution, measuring time and statistical representativity. The EBSD measurements were post-treated using the **MTEX** toolbox [148]. On the EBSD maps, a misorientation threshold of 10° was used to differentiate grains. Additionally, recrystallized grains were identified following the procedure described in [149]. Grains with size below 1.5

μm or with grain average misorientation GAM (Eq. 4.1) lower than 1 degree were considered as recrystallized.

A - Test conditions for stress-strain curves (Cylindrical samples)						
	Nominal Strain rate $\dot{\epsilon}(1/s)$					
$T(K)$	0.008	0.01	0.04	0.05	0.08	0.1
1273	$0-0.4$	$0-0.7^*$	$0-0.4^*$	$0-0.7$	$0-0.7^*$	$0-0.7$
1323	$0-0.4^*$	$0-0.7^*$				
1373	$0-0.4$	$0-0.7$				

B - Test conditions for EBSD measurements						
	Cylindrical samples			Double-cone samples		
	Local Strain rate $\dot{\epsilon}(1/s)$			Local Strain rate $\dot{\epsilon}(1/s)$		
$T(K)$	0.014	0.07	0.14	0.014	0.07	0.14
1273	0.65	0.65^*	0.65	$1.00, 1.35$	$1.00, 1.35^*$	$1.00, 1.35$
1323	0.65^*			$1.00, 1.35^*$		
1373	0.65			$1.00, 1.35$		

Table 4.1: Conditions considered for the experimental test, strain rate, temperatures, strain range (stress-strain curves - Table A) and strain level (EBSD measurements - Table B). $(*)$ Indicates data sets used for the model validation.

$$GAM = \frac{\sum_{i=1}^{n} KAM_i}{n} , \tag{4.1}$$

with n the total number of pixels belonging to the grain and KAM_i the kernel average misorientation of each pixel i of the grain defined as:

$$KAM_i = \frac{\sum_{j=1}^{m} \theta_{ij}}{m} , \tag{4.2}$$

with m the total number of neighbor pixels of a pixel i and θ_{ij} the misorientation between the pixel i and its neighbor j. Consistently with the misorientation threshold applied for grain detection, values of misorientation θ_{ij} higher than $10°$ are not considered.

EBSD data were also used to calculate: the recrystallized area fraction X, defined by Eq. 4.3; the mean grain size (2D) $\bar{D}_{N2D}$, defined by Eq. 4.4 and the mean grain size weighted by surface $\bar{D}_S$, defined by Eq. 4.5.

$$X = \frac{\sum_{i=1}^{N_X} S_{Xi}}{S_T} \ , \tag{4.3}$$

with N_X the number of recrystallized grains, S_{Xi} the surface (2D) of each recrystallized grain, and S_T the total area of the EBSD map.

$$\bar{D}_{N2D} = \frac{\sum_{i=1}^{N} d_i}{N} \ , \tag{4.4}$$

with N the total number of grains, d_i the equivalent circle diameter (2D) of each grain defined as $d_i = 2 * \sqrt{S_i/\pi}$.

$$\bar{D}_S = \frac{\sum_{i=1}^{N} d_i S_i}{S_T} \ , \tag{4.5}$$

with S_i the surface (2D) of each grain. Considering that the numerical model to be tested is a 3D model, 3D data was required in order to calibrate and validate it. So, 2D grain size distributions by number fraction and surface fraction were calculated and transformed into equivalent 3D grain size distributions by number fraction using the **inverse Saltykov** method [150]. The 3D grain size distributions by number fraction were used to calculate the 3D grain size distributions by volume fraction.

The mean 3D grain size weighted by number fraction $\bar{D}_{N3D}$, defined by Eq. 4.6 and the mean 3D grain size weighted by volume fraction $\bar{D}_V$, defined by Eq. 4.7, were also computed from both 3D distributions.

$$\bar{D}_{N3D} = \frac{\sum_{i=1}^{N} d_{3Di}}{N} \ , \tag{4.6}$$

with d_{3Di} the equivalent sphere diameter (3D) of each grain, defined as $d_{3Di} = 2 * (0.75(1/\pi)V_i)^{1/3}$.

$$\bar{D}_V = \frac{\sum_{i=1}^{N} d_{3Di} V_i}{V_T} \ , \tag{4.7}$$

with V_i the volume (3D) of each grain, and V_T the total volume. For the initial state of the microstructure $\bar{D}_{N3D} = 33.23$ (μm) and $\bar{D}_V = 86.53$ (μm). The X and the $\bar{D}_V$ values were used for the comparisons with the model results.

4.3 Experimental Results

4.3.1 Thermomechanical tests

The stress-strain curves obtained from the thermomechanical tests, were smoothed using high order polynomial interpolation, to reduce the experimental noise (Figure 4.2). In general terms, the curves show the expected behavior, with the stress increasing with increase in strain rate, and decreasing with the increase in temperature.

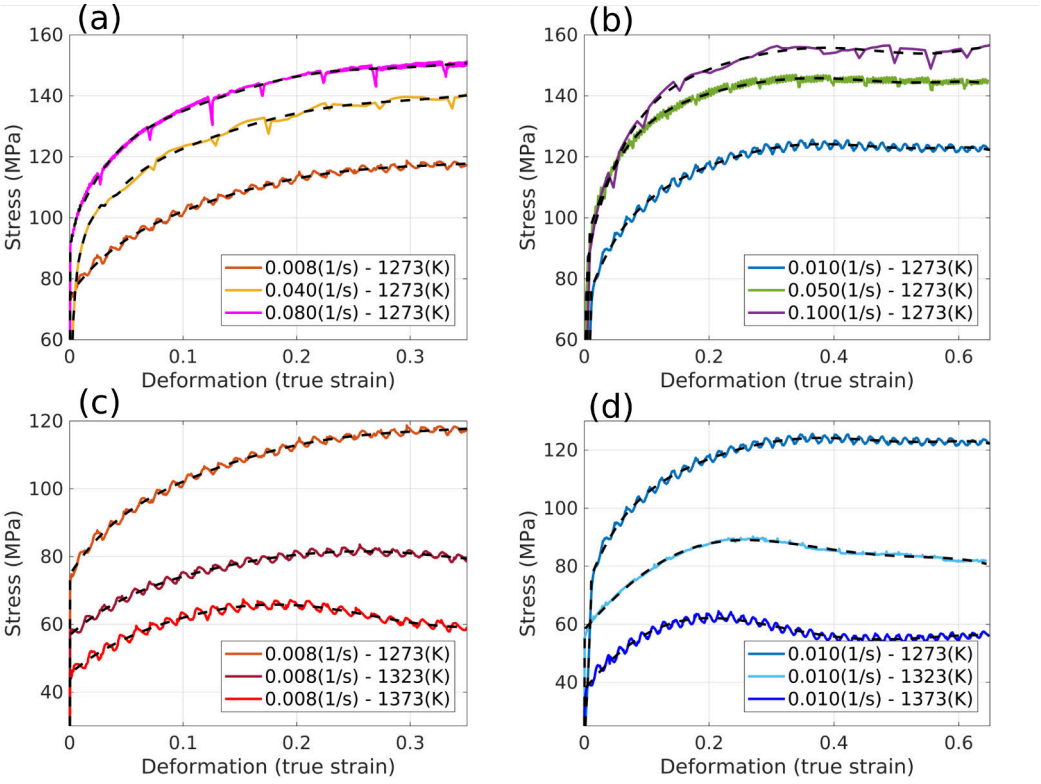

Figure 4.2: Measured (continuous lines) and interpolated (dashed lines) stress-strain curves for 304L steel cylindrical samples subjected to compression tests at high temperatures. Curves are grouped by temperature ((a) and (b)) and strain rate ((c) and (d)). Oscillations are artifacts due to periodic change in the tool velocity to follow imposed constant strain rate.

The results show that at $T = 1273°\ K$ for the considered strain rates, there is no significant difference between the peak stress (maximum stress value reached due to the strain hardening) and the steady state stress (stress value in the steady stress zone). However for the cases at higher tempera-

tures, specially at $T = 1373°\ K$, the differences between the peak stress and the steady steady state stress are clearly observed.

The used experimental set up does not allow to obtain accurate measurements at low strain levels. This makes difficult the identification of the macroscopic yield stress σ_0, so the values were taken from the literature [151]. The σ_0 values can also be obtained as: the intercept between the line defined by $\sigma = E*(\epsilon - 0.002)$ and the curve interpolated on the experimental measurements without considering the measurements at low strain levels.

The values obtained from both approaches are compared in figure 4.3. The results for the cases at $T = 1000°\ C$, show that the literature values have a clear tendency, σ_0 increasing with the increase in the strain rate. However, this tendency is not clear in the interpolated values. For the cases $\dot{\epsilon} = 0.008\ s^{-1}$, both the literature values and the interpolated values show an almost linear decrease with the increase in the temperature (figure 4.3-b). For all cases the interpolated values show higher σ_0 values than their corresponding literature values. Since there is clear difference between the two values, the effect on the model results of using each set of values were compared in section 4.4.

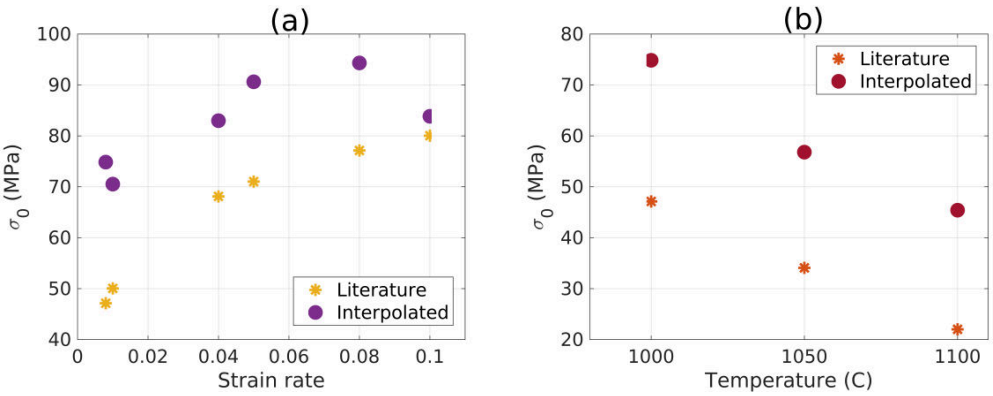

Figure 4.3: Comparison between the σ_0 values identified by extrapolation of experimental data procedure and values from the literature [151]. Constant temperature $T = 1000°\ C$ (a) and constant strain rate $\dot{\epsilon} = 0.008\ s^{-1}$ (b).

4.3.2 EBSD Measurements

In order to process the EBSD measurements, grains were detected as groups of neighbouring points with less than 10° misorientation angle. Twin boundaries, identified by 60° rotation around the $\langle 1, 1, 1 \rangle$ axis with a 5° tolerance, were ignored in the grain detection procedure as they are not considered in the model. Figure 4.4 shows the EBSD map of the initial microstructure with

and without twin boundaries, and the pole figures of the (001), (111) and (110) planes. The pole figures show that no preferred orientation is present in the initial microstructure.

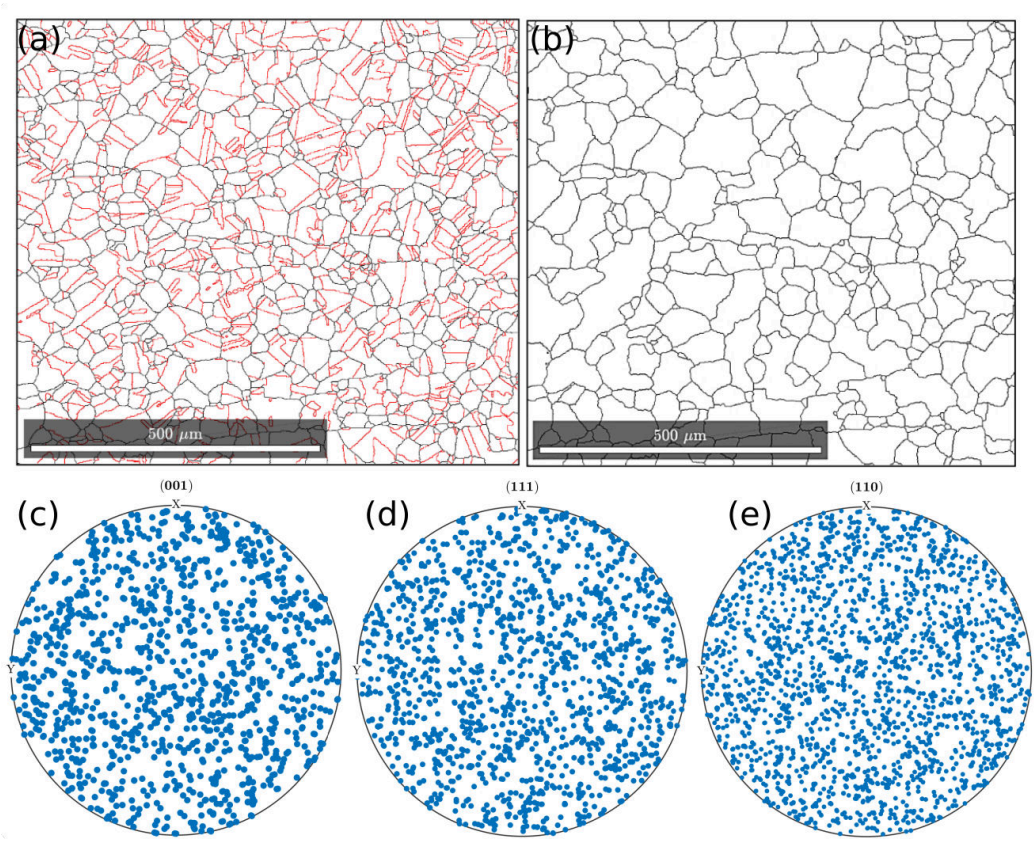

Figure 4.4: EBSD map of the sample before deformation with (a) and without twin boundaries (b). Twin boundaries plotted in red and grain boundaries excluding twins plotted in black. (001), (111) and (110) pole figures (c-e).

However, deformation causes that twin boundaries deviate from the 60° ⟨1 1 1⟩ ideal misorientation, so that some of them, or some parts of them, can get out of the tolerance of 5°. As a consequence, on highly deformed microstructures, it is not possible to correctly identify all the twin boundaries present in the microstructures. Figure 4.5 shows an EBSD map of a deformed sample with the twin boundaries plotted in red and grain boundaries excluding twins plotted in black. The EBSD maps show that twin boundaries are no longer identified as continuous lines and part of them is considered as a normal grain boundary, this can cause an artificial reduction in the measured grain size.

For the deformed samples figure 4.6 shows the evolution of the microstructure, with the increase in strain, in terms of GAM values and recrystallized grains for one set of deformation conditions. The evolution of the microstructure, from the initial state characterized by $\bar{D}_{N2D} = 43.1\ (\mu m)$ and $\bar{D}_S = 75.6\ (\mu m)$, in terms of recrystallized fraction, average grain size by number and by surface, are shown in figure 4.7 for the considered deformation conditions.

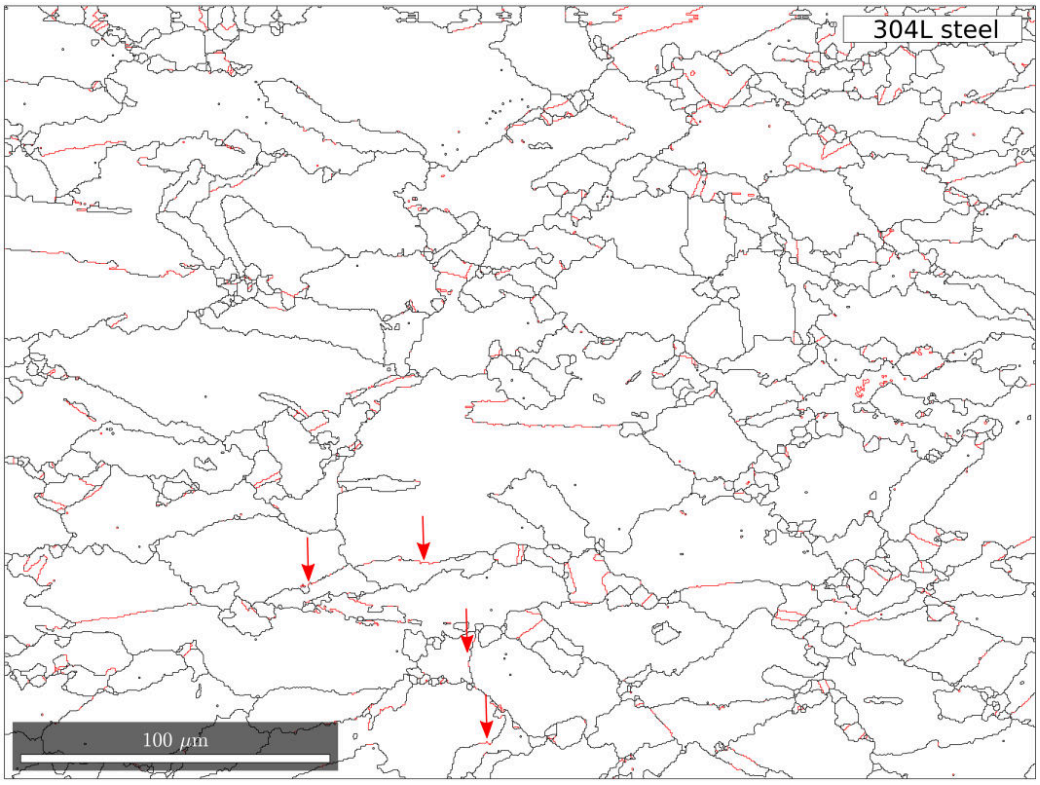

Figure 4.5: EBSD maps of the sample deformed at $T = 1273\ K\ -\dot{\epsilon} = 0.014\ s^{-1}\ -\epsilon = 0.65$. Twin boundaries plotted in red and grain boundaries excluding twins plotted in black.

The results show that the change in strain rate does not have significant effects in the evolution of the recrystallized fraction, while the increase in temperature causes an increase in the recrystallized fraction. In terms of grain size, the evolution of the grain sizes by surface shows that neither the changes in temperature or strain rates, causes a consistent change in the grain size evolution at all the considered deformation levels. $\bar{D}_S$, for the highest strain rate, shows an unexpected behaviour with significantly higher values at $\epsilon = 1.0$ than the other strain rates, this behaviour is likely to be due to

self-heating. In all cases even at low recrystallized fraction levels, there is a significant reduction of the initial grain sizes, this is caused in part by the twin identification issue described above.

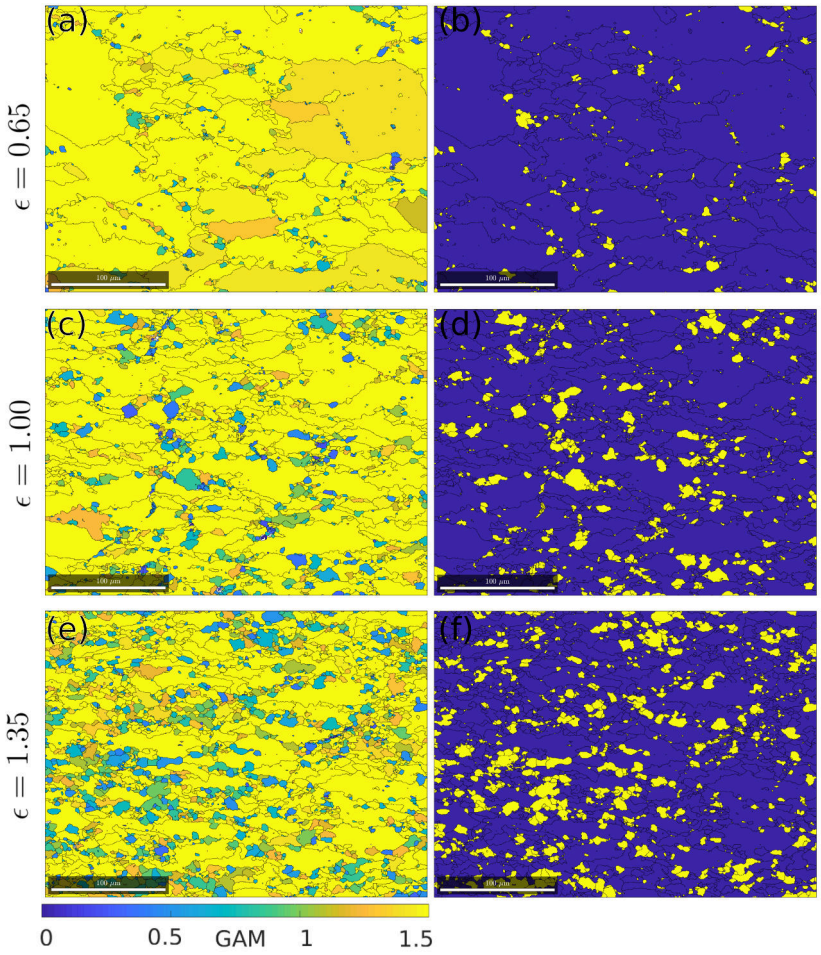

Figure 4.6: EBSD maps at different strain levels of the sample deformed at $T = 1000\ K\ -\ \dot{\epsilon} = 0.07\ s^{-1}$ with grain boundaries plotted in black. (a,c,e) Grains colored by GAM value. (b,d,f) Recrystallized grains (yellow) and non-recrystallized grains (blue).

For the 3D measurements, the evolution of the microstructure in terms of $\bar{D}_{N3D}$ and $\bar{D}_V$, from the initial state of $\bar{D}_{N3D} = 33.2\ \mu m$ and $\bar{D}_{N3D} = 86.5\ \mu m$, considering all the grains (the recrystallized grains and the non recrystallized ones), for the different deformation conditions are shown in figure 4.8.

The results show that the behaviour considering all the grains is consistent with the behaviour observed for the 2D data. With the increase in temperature the final grain size increases, while the different strain rates show very similar grain size values. For a given deformation condition, there is no significant change in the mean size of the recrystallized grains for the different strain levels. There is a small increase in size between the lower strain level and the middle strain level, but at the higher strain level, the size shows almost the same value that at the middle strain level. The increase in temperature also leads to higher mean recrystallized grain sizes, while the change in strain rate shows little influence. For the non recrystallized grains, the significant reduction in grain size between the non deformed state and the first measurement after deformation, is seen clearly.

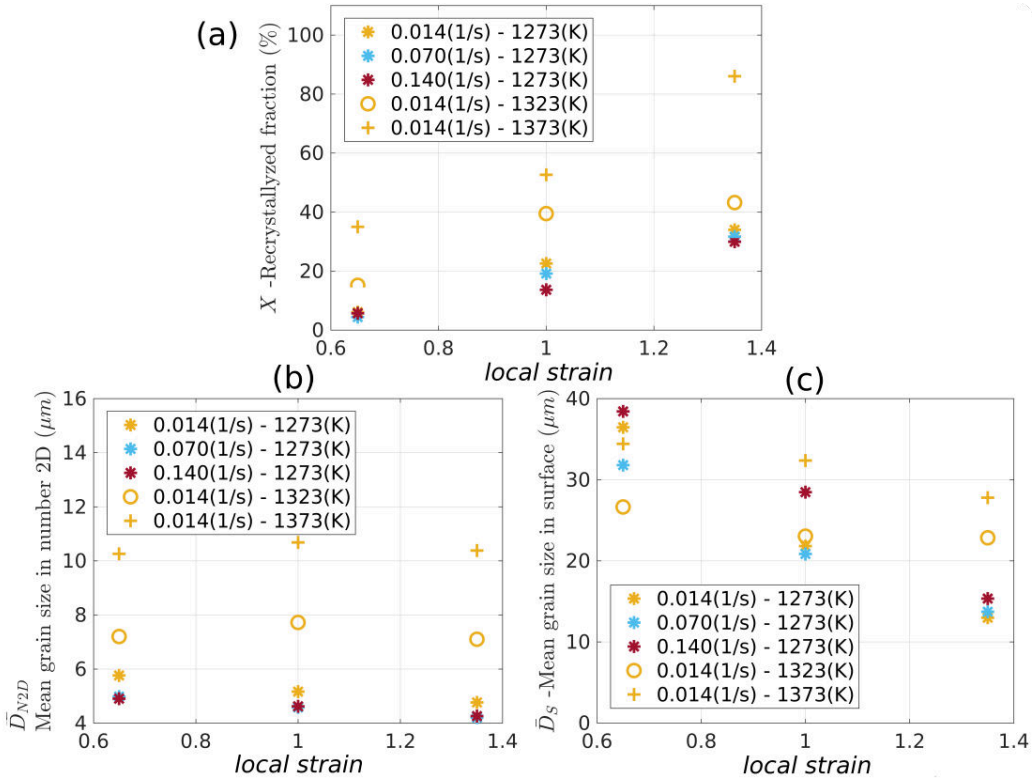

Figure 4.7: Evolution of recrystallized fraction X (a), average grain size by number $\bar{D}_{N2D}$ (b) and average grain size by surface $\bar{D}_S$ (c) as a function of strain for the different deformation conditions.

In terms of distributions, the results for one of the considered deformation conditions are shown in figure 4.9. Both the distributions by surface and volume show that the microstructure contains a significant fraction of

grains with sizes much smaller and much bigger than the mean value. The distributions do not present a regular shape that can be correctly fitted with the commonly used normal or log normal mathematical distributions.

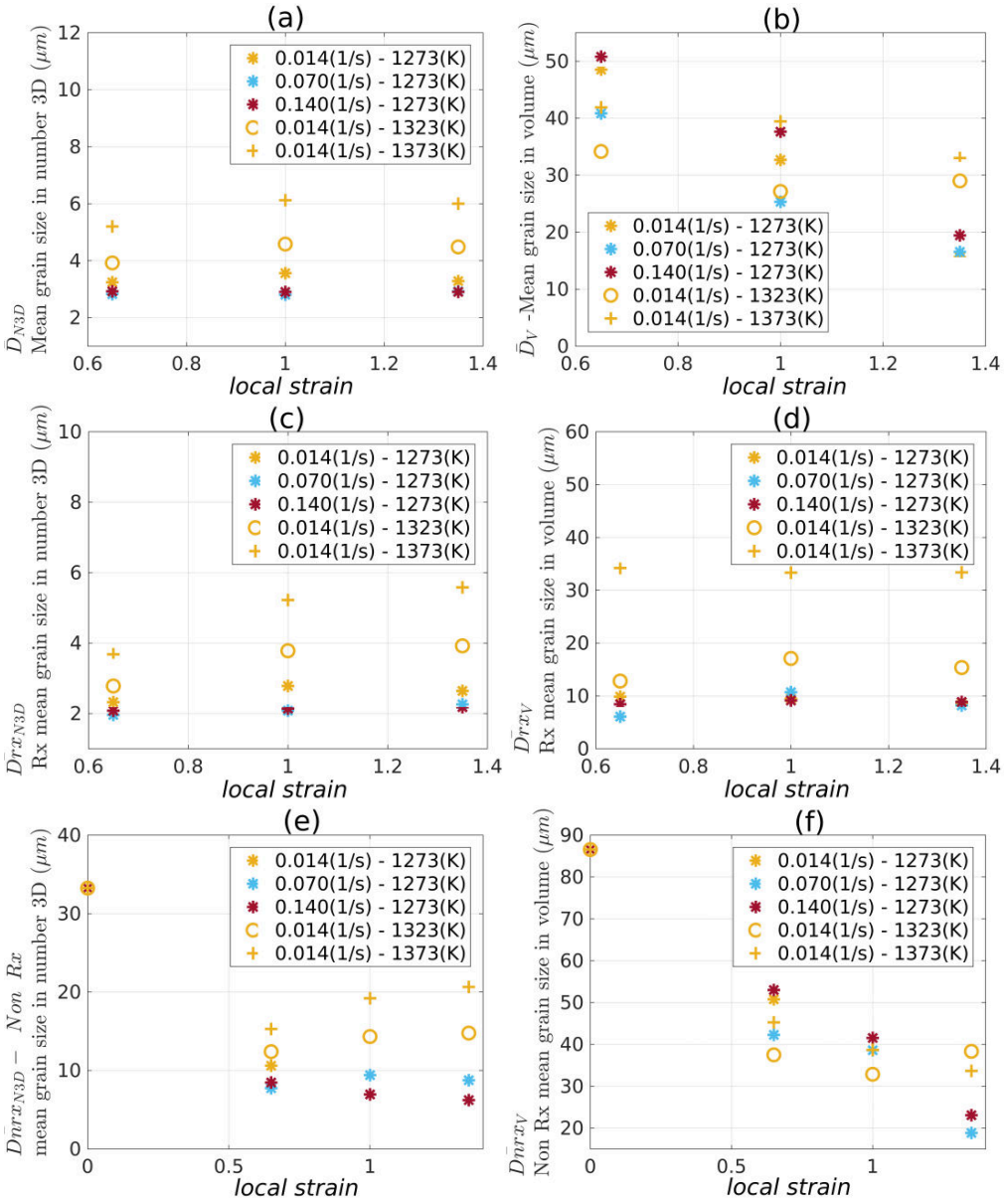

Figure 4.8: Evolution of $\bar{D}_{N3D}$ (a,c,e) and $\bar{D}_V$ (b,d,f) as a function of strain, considering all the grains (a,b), the recrystallized grains (c,d) and the non recrystallized grains (e,f) for the different deformation conditions.

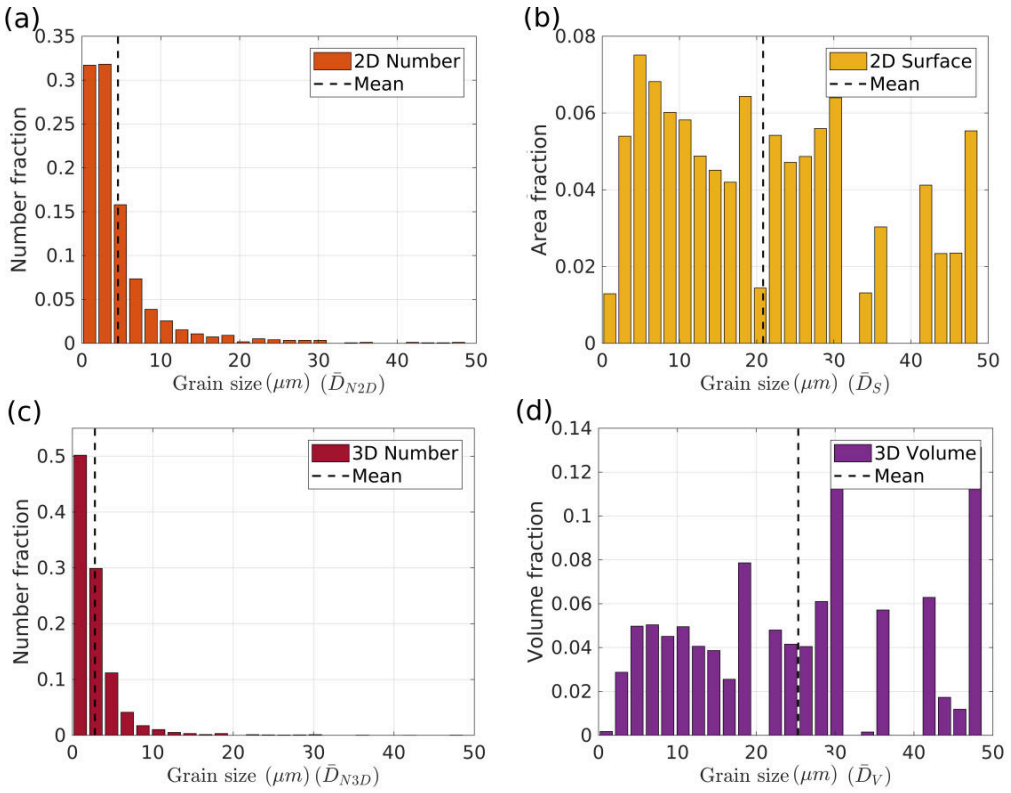

Figure 4.9: Grain size distributions by number fraction 2D (a), surface fraction(b), number fraction 3D (c) and volume fraction (d). Sample deformation conditions $T = 1273\ K - \dot{\epsilon} = 0.07\ s^{-1}\ - \epsilon = 1.0$.

4.4 Calibration and validation of CPFEM-LS model

4.4.1 Parameters identification procedure

The model was calibrated by performing inverse analysis, using the optimization tool Moopi [152]. The experimental data were divided into one set of data used for calibration and one other set used for validation, as depicted in table 4.1. The process was performed in two steps. First, only the crystal plasticity model parameters were calibrated and validated against the experimental stress-strain curves before DRX onset. Second, with the obtained parameters for the crystal plasticity part, the coupled model parameters were calibrated and validated against the recrystallization kinetics obtained from the EBSD maps.

For the first part, the parameters $K1$ and $K2$ were calibrated, these

parameters represent the generation of dislocations due to plastic deformation and their disappearance by dynamic recovery respectively, in the dislocation density (ρ) evolution law considered, i.e. the Yoshie-Laasroui-Jonas (see Eq. 2.29). The second part of the calibration procedure was done regarding the parameter k_g, which represents the probability of recrystallized grains appearance in the nucleation rate law (see Eq. 3.10). The remaining model parameters are summarized in table 4.2:

Symbol	Name	Value	Units	Source
E	Young's modulus	$[119 - 125]$	GPa	[151]
v	Poisson's ratio	0.34	$[-]$	[151]
μ	shear module	$[40 - 45]$	GPa	[151]
$\dot{\gamma}_0$	Ref. slip rate	0.001	$[s^{-1}]$	[121]
m	slip rate sensibility	0.05	$[-]$	[121]
M	Taylor factor	3	$[-]$	[153]
ψ	substructure type	0.15	$[-]$	[154]
b	Burgers vector	$2.5 * 10^{-10}$	m	[155]
σ_0	yield stress	$[20 - 80]$	MPa	[151]
M_b	GB mobility	$[0.51 - 3.47] * 10^{-12}$	m^4/Js	[156]
d_e	disl. line energy	$1.47 * 10^{-9}$	J/m	[6]
γ_b	GB energy	0.6	J/m	[7]
ρ_0	min disl. density	$1 * 10^{11}$	m^{-2}	[157]

Table 4.2: Values of the model parameters for the considered thermo-mechanical conditions.

For the simulations, the imposed boundary conditions represent a channel die compression with a constant strain rate, as ilustrated in figure 2.11. As previously mentioned, this type of boundary conditions, without free surfaces, are imposed to prevent the polycrystal from collapsing onto itself due to the rotation of some grains caused by the plastic deformation. For $304L$ steel, the deformation resulting from the imposed boundary conditions is an acceptable representation of the experimental compression tests.

4.4.2 Calibration and validation of the CPFEM model

For the calibration and validation of the CPFEM computations, the data considered was: up to $\epsilon = 0.25$ for $T = 1273(K)$, and up to $\epsilon = 0.20$ for $T = 1323(K)$ and $T = 1373(K)$. This is done in order to minimize the effect of recrystallization in the stress response. Only the effects of strain hardening and dynamic recovery are considered, which are the two phenomena

related to the parameters K_1 and K_2. Figure 4.10 (a,b) shows the results of the calibration procedure. In general terms, the model results show good agreement with the experimental results. The largest differences are seen in the initial part of the curves, specially for higher temperatures. They are related to the chosen σ_0 value.

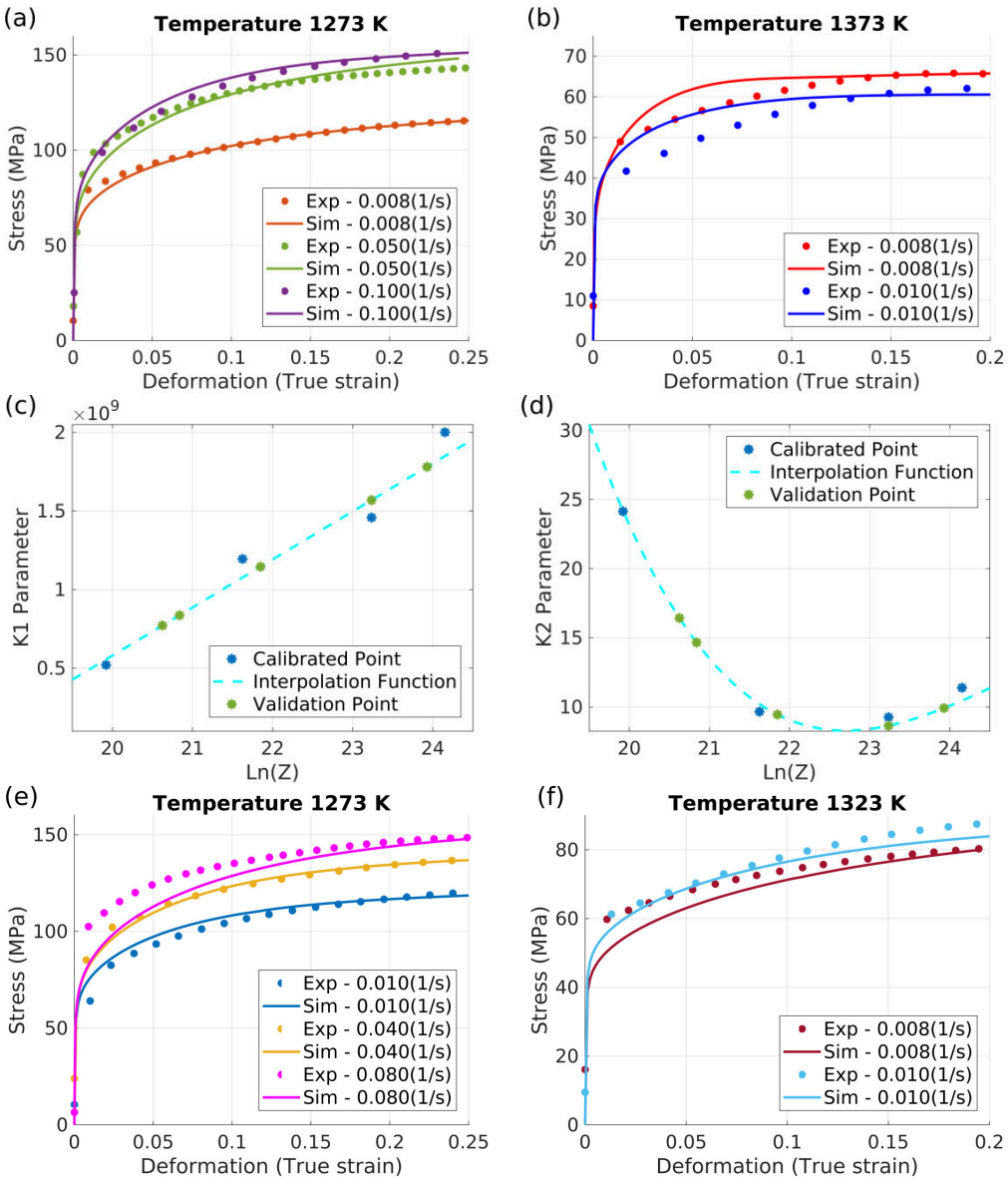

Figure 4.10: Comparisons between the CPFEM model results and the experimental results for the stress-strain curves. Calibration (a,b), Parameters evolution (c,d) and Validation(e,f).

The identified parameter values were used to construct functions that describe the evolution of model parameters as a function of the Zener Hollomon parameter, defined as:

$$Z = \dot{\epsilon}\ exp(Q/RT)\ . \tag{4.8}$$

with $\dot{\epsilon}$ the strain rate, Q an apparent activation energy, R the gas constant and T the absolute the temperature. The identified values and their corresponding functions are also shown in figure 4.10 (c,d). With the constructed functions, the parameters value for the thermomechanical conditions set for validation of the model were calculated and simulations were run for these thermomechanical conditions. The simulated results compared to experimental measurements are presented in figure 4.10 (e,f). The results are consistent with the results observed in the calibration procedure, showing that the model predictions are in good agreement with the experimental measurements. The largest differences are also observed in the initial part of the curves, this can be again partially explained by the uncertainty in the identification of σ_0 in the experimental curves.

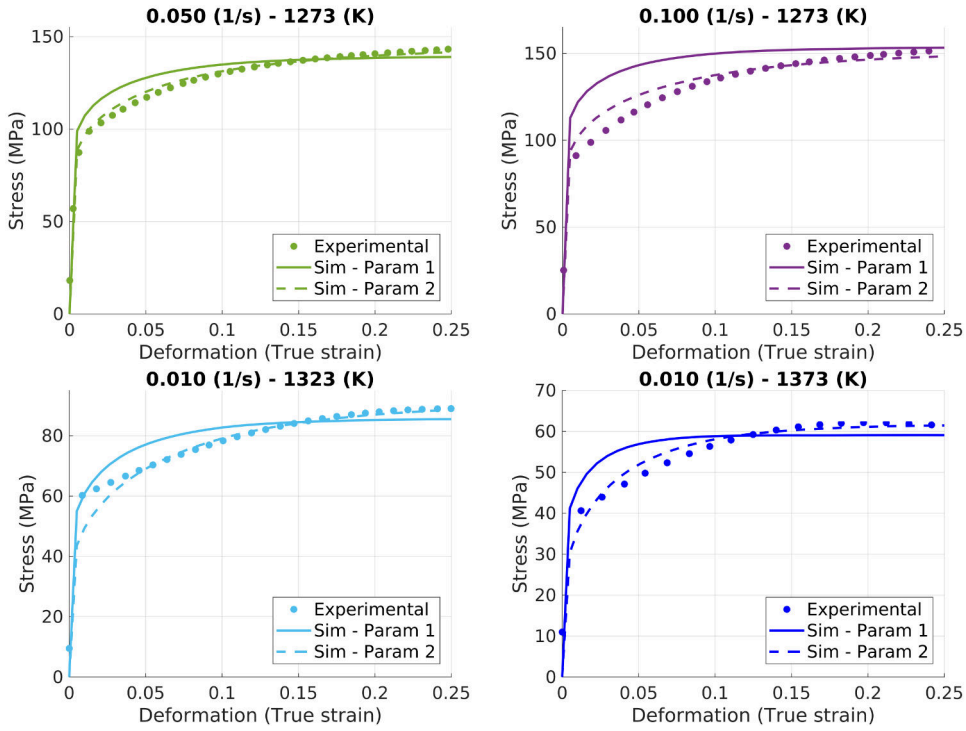

Figure 4.11: Comparison between the CPFEM model results with the initially identified parameters, the model results with the identified parameters including the $k_0$value, and experimental measurements.

Since the biggest errors in the model are related to the identification of σ_0, a second calibration was performed using the σ_0 values identified by interpolation. However, no significant improvements were observed in the model results. A third alternative, considering that $k_0 = \sigma_0/M$, was to consider the parameter k_0 as one of the parameters to be identified in the calibration procedure and the model was re-calibrated. This was done for the thermomechanical conditions with the largest errors between the simulated results and the experimental data. Figure 4.11, shows the simulated results obtained for both the original calibrated parameters and the new calibrated parameters plotted along with the experimental measurements.

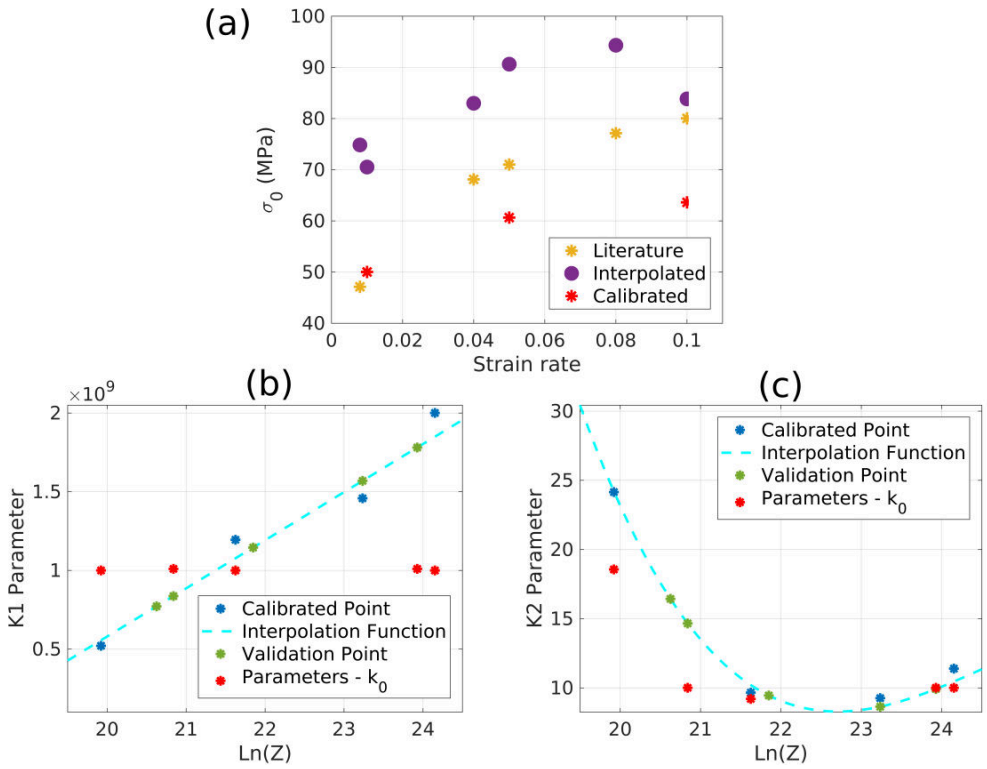

Figure 4.12: Comparison of the σ_0 (a), K_1 (b) and K_2 (c) values identified with the different approaches.

The results show that by also calibrating the k_0 value, it is possible to obtain a better fit to the experimental results. The differences previously observed at low deformation level are reduced. The new identified k_0 values show significant differences with the values obtained from the literature and the values identified from the extrapolation of the experimental curves. Additionally the inclusion of the k_0 value in the calibration procedure has

an influence on the values of K_1 and K_2. Figure 4.12 shows the comparison between σ_0, K_1 and K_2 values identified with the different approaches.

All the identified parameters values fit the ranges previously reported in the literature [121, 6]. However the general trend of the K_1 values identified in the second set, constant for different thermomechanical conditions, does not agree with the trends observed in the literature (the value of K_1 changing for different thermomechanical conditions).

Therefore, considering that the parameters K_1 and K_2 are also present in other model equations (they are used to defined the critical dislocation density Eq. 3.8, which is used to define the start of nucleation and the recrystallized grains size Eq. 3.9), for this work the first set of identified parameter values were finally initially used.

4.4.3 Calibration and validation of the coupled model

Using the identified values K_1 and K_2, the parameter k_g was identified following the same methodology previously described. The coupled model results were compared with the experimental data of the EBSD measurements in terms of recrystallized fraction and average grain size ($\bar{D}_V$). Figure 4.13 (a,b) shows the results of the calibration procedure for the coupled model. The results show good agreement in terms of recrystallized fraction. For the average grain size ($\bar{D}_V$), there is an important difference between the model results and the experimental data at higher strains.

The identified parameter values were used to construct a piece-wise linear function that describes the evolution of the parameter k_g in terms of the thermomechanical conditions described by the Z parameter. This type of function was used due to the limited number of experimental points. The identified values and the interpolated function are shown in figure 4.13 (c).

Following the previously described procedure the interpolated function is used to calculate the parameter value (figure 4.13 (c)) for the thermomechanical conditions chosen to validate the model. The results are shown in figure 4.13 (e,f). The results show the same trend as the results observed in the calibration phase. The model correctly predicts the recrystallized fraction, but shows some errors in average grain size value predicted at higher strains.

The disagreement between the model results and the experimental data, in terms of mean grain size ($\bar{D}_V$), can be explained by several factors related mainly to the twin boundaries and the size of inserted recrystallized grains. These limitations of the proposed model and the calibration procedure are discussed in section 4.5.

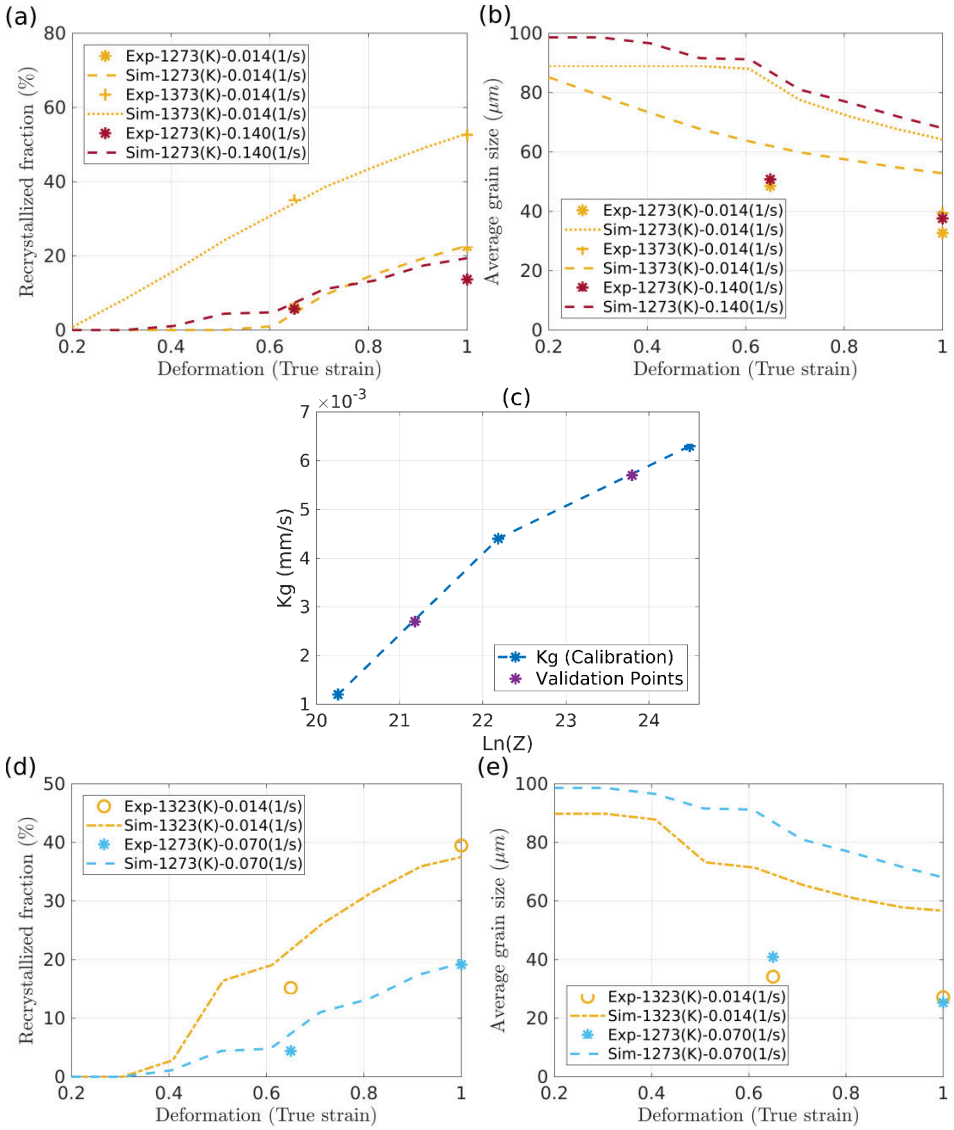

Figure 4.13: Comparison between the coupled model results and the experimental results, recrystallized fraction (a,d) and average grain size ($\bar{D}_V$) (b,e). Calibration (a,b), Parameters evolution (c) and Validation(d,e).

4.5 Model discussion

4.5.1 Dislocation density evolution

The main advantage of including CPFEM is to obtain a better description of the evolution of the dislocation density and the orientations of the grains

during DRX. However the current framework does not consider yet the grains orientation in the GB migration calculations, they only influence the deformation in the CPFEM model, so the most relevant variable remains the dislocation density evolution.

In the current framework, the evolution of dislocation density is defined by a saturation type hardening law, the Yoshie-Laasroui-Jonas law (Eq. 2.29). This law is a simplified model that was used due to the limited experimental data available to identify the material parameters. It defines a maximal value for the dislocation density, thus, at high deformation levels, when a significant part of the microstructure has reached the saturation value, the heterogeneity in the microstructure is significantly reduced as illustrated in figure 4.14. The exceptions are recrystallized grains as they are inserted with a minimal dislocation density and zones swept during GB migration. Since these zones are also subjected to deformation, they also harden and later reach the saturation value.

However, considering that the energy gradient is the dominant force in GB migration during DDRX, even if the percentage of these grains is low their effect is significant in the microstructure. So, to better describe the dislocation density evolution, distributions by volume fraction are presented in figure 4.15, for one simulation case. Figures 4.14 and 4.15 show that: at low deformation levels, before nucleation has started $\epsilon < 0.20$, there is significant heterogeneity in the distribution of the dislocation density in the microstructure. The effect of the grain orientation is clear with zones in the microstructure showing low and high dislocation density levels.

At higher deformation levels most of the grains present in the microstructure ($\approx 80\%$) have a dislocation density equal to the maximal value. On these grains that have already reached the maximal dislocation density value, only zones near boundaries that have been swept due to grain boundary migration show different dislocation density levels (figure 4.14). Considering only the case of recrystallized grains, the results show a similar behaviour with the majority of the grains ($\approx 75\%$) having the maximal dislocation density. These are the recrystallized grains, that have already hardened and can also serve as nucleation sites.

However the remaining recrystallized grains show dislocation density levels among a wide spectrum. Figure 4.15 (d) shows dislocation density distribution considering only recrystallized grains with dislocation density lower than the maximal value. These results show that, of these remaining grains, only ($\approx 5\%$) show the minimal dislocation value, these are the grains that just appeared in the microstructure and have not deformed yet. The other recrystallized grains show several dislocation levels which result from the different hardening rates caused by the differences in orientations.

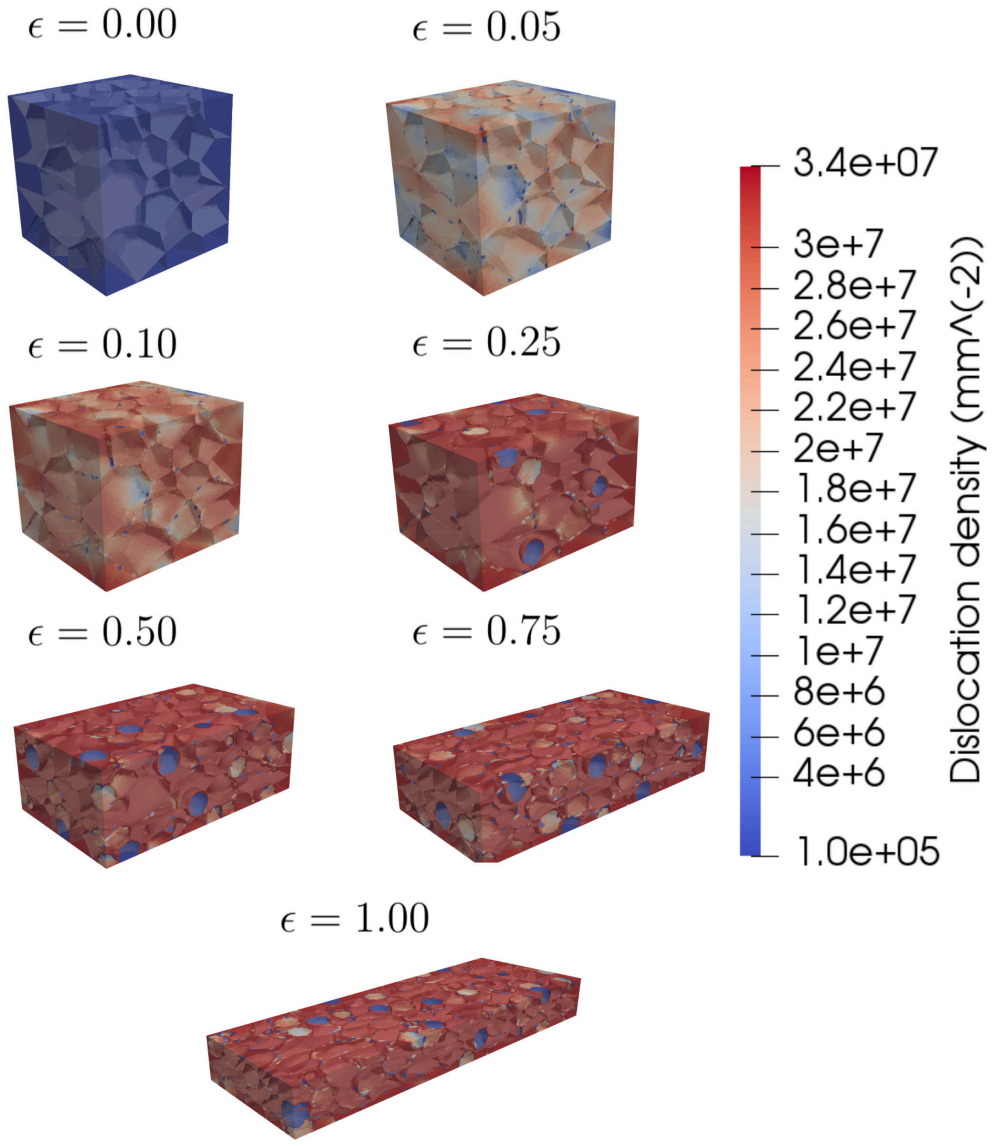

Figure 4.14: Example of the simulation framework.

These results illustrate that with the current hardening law, which is an important simplification of the dislocation density evolution, and with the current framework which does not consider the misorientation effect on the grain boundary energy, replacing CPFEM with a simplified Taylor models could provide similar results with a reduction in the computational cost. This alternative is explored and presented next.

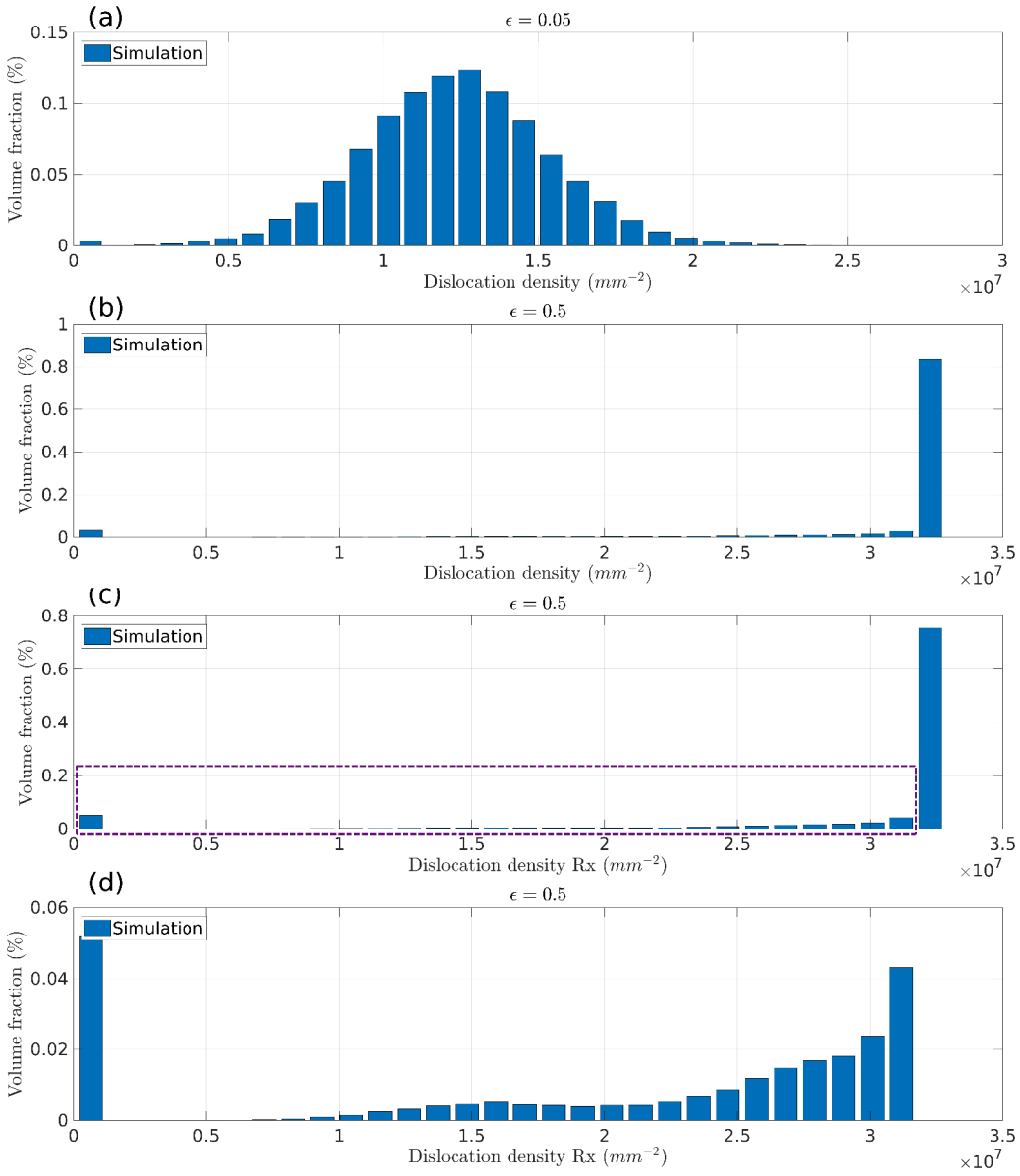

Figure 4.15: Evolution of the dislocation density in terms of volume distribution during DRX simulation. (a) All grains $\epsilon = 0.05$, (b) All grains $\epsilon = 0.50$, (c) Recrystallized grains at $\epsilon = 0.50$,(d) Zoom to recrystallized grains at $\epsilon = 0.50$.

4.5.2 Comparison with simplified models

To evaluate the effect of including the CPFEM in our recrystallization model, the proposed coupled model was compared with simplified full field models:

- The phenomenological model proposed by Maire [79]: the macroscopic deformation rate is imposed on all grains. The evolution of the dislocation density on each grain is calculated according to Eq. 2.29 (Yoshie-Laasroui-Jonas law). In this approach, the mechanical equilibrium problem is not solved nor satisfied, no grain interactions are considered, and the crystal structure nor the initial grains orientations are considered. The evolution of all grains is equal.

- The CP-Taylor model: The macroscopic deformation rate is also imposed on all grains. However, instead using Eq. 2.29 to calculate the evolution of the dislocation density directly, the CP library is used. Meaning, the evolution of the dislocation density on each grain is calculated according to the algorithm described in chapter 2, section 2.4, using Eq. 2.29 as the hardening law. In this approach, the mechanical equilibrium problem is not solved nor satisfied, and no grain interactions are considered. However, the crystal structure and the grains orientations are considered. Each grain will evolve differently according to its orientation.

The three models use the same LS framework and phenomenological laws to model grain boundary migration and recrystallization, the difference between then is the way that plastic deformation is considered. The same material and numerical parameters, calibrated for the coupled CPFEM-LS DDRX model, were used in the three cases.

The simulation case considered consists on 304L steel subjected to compression at a constant strain rate $\dot{\epsilon} = 0.014\ s^{-1}$, a temperature of $T = 1323\ (K)$, up to a deformation level of $\epsilon = 1.0$, then hold at the same temperature during 50 (s). The simulation results are shown in figure 4.16 in terms of average behaviour, in figure 4.17 in terms of dislocation density distributions by volume and in figure 4.18 in terms of grain size distributions by volume. The results show that there are clear differences in the behaviour observed between the three models, the difference in the formulations are directly related to the evolution of the dislocation density, however since the evolution dislocation density drives the other mechanisms these differences are extended to the other variables.

The dislocation density in average increases more quickly in the phenomenological model. This approach shows the higher hardening rate, followed by the Taylor model as shown in figure 4.16 (a). However figure 4.17 (a) shows that even if the average dislocation density is higher for the phenomenological model, some specific grain orientations have higher hardening rates, this phenomena is not seen in the phenomenological model since the

grains orientations are not considered. This causes that the critical dislocation density is reached quicker in the Taylor model and subsequently recrystallized grains appear more quickly.

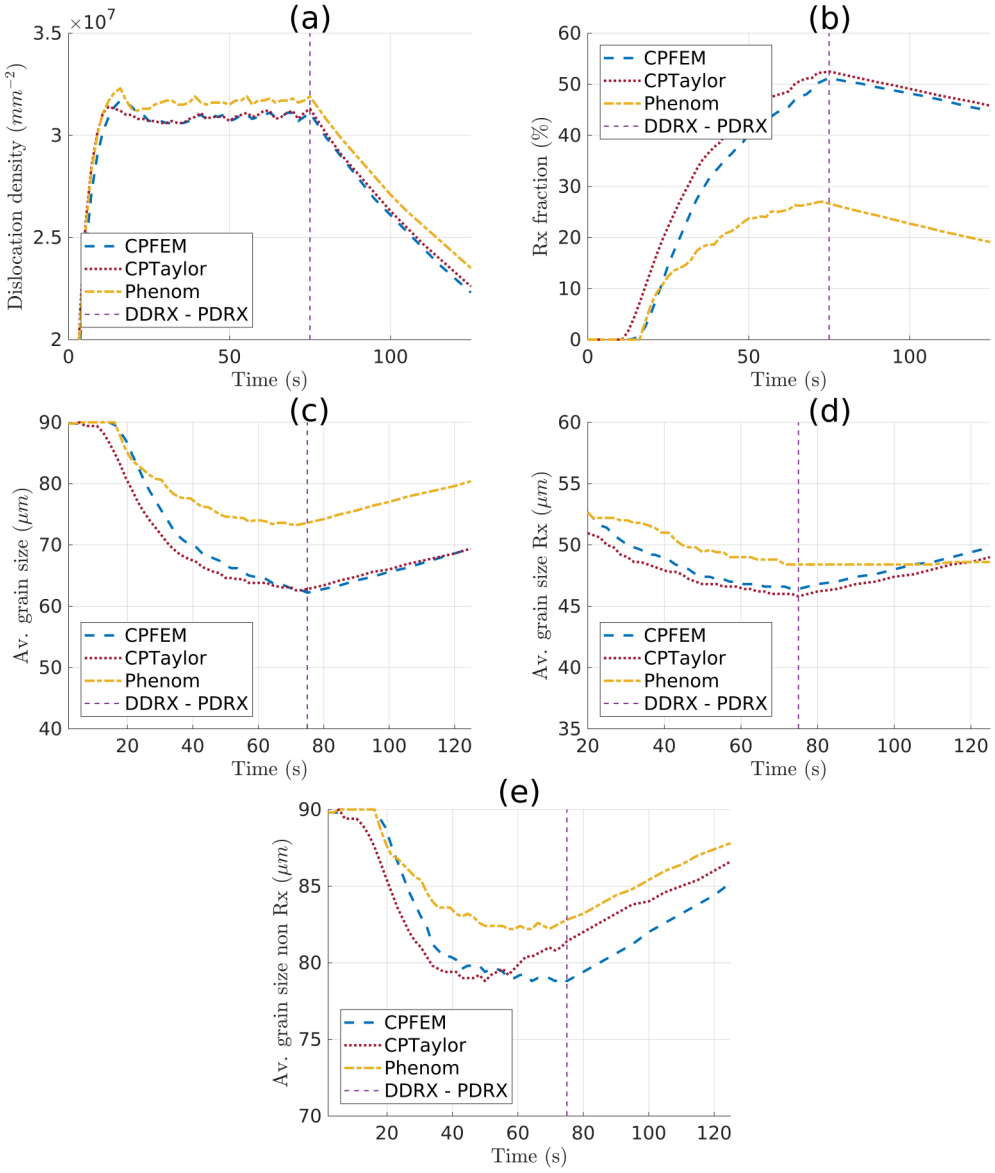

Figure 4.16: Comparison between the models results. (a) Average dislocation density, (b) recrystallized fraction and average grain sizes by volume considering all grains (c), recrystallized grains (d) and non recrystallized grains (e).

At high deformation levels, the differences are lower since most of the

microstructure reaches the critical dislocation density. However as seen in figures 4.17 (b,c), the phenomenological model shows the highest percentage of completely recrystallized grains. Even if these differences seem small, they have a significant effect in the evolution of the microstructure, specially for the recrystallized grains.

The dislocation density gradient between recrystallized grains and their hardened neighbours is the driving force for recrystallized grain grow. Therefore, new recrystallized grains will harden much faster and thus have less time to grow and consume their neighbours. This directly translates in a lower increase in the recrystallized fraction as shown in figure 4.16 (b), and smaller decreases in the average grain size of non recrystallized grains as shown in figure 4.16 (c,e).

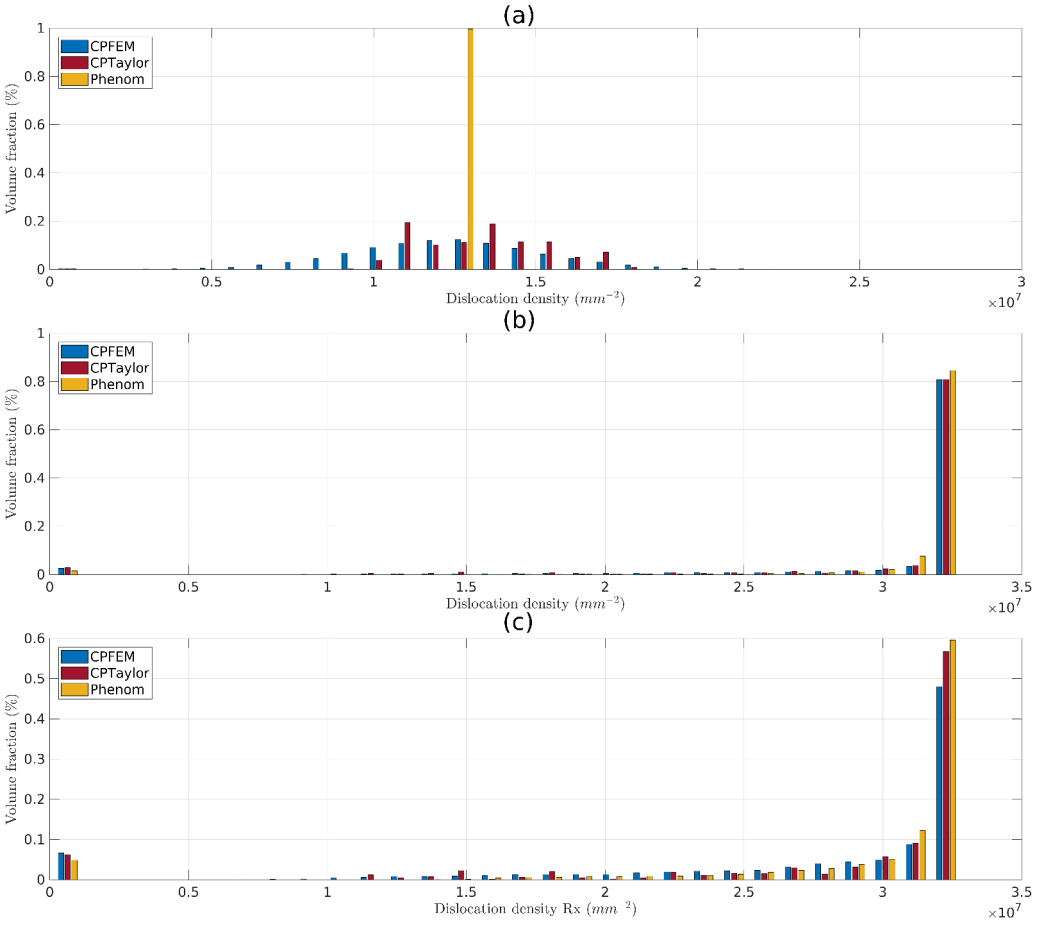

Figure 4.17: Comparison between the models results. Dislocation density distributions by volume, all grains $\epsilon = 0.05$ (a), all grains $\epsilon = 0.50$ (b) and recrystallized grains $\epsilon = 0.50$ (c).

This aspect can also be seen in the grain size distributions (figures 4.18 b,c). At both deformation levels, the phenomenological model has a higher percentage of bigger grains than the other models. The Taylor and CPFEM models on the other hand show a very similar behaviour, the main differences being caused by the quicker start in recrystallization in the Taylor model. Regarding the PDRX phase, the main differences between the behaviours observed between the phenomenological model and the Taylor and CPFEM models is caused by the higher number of recrystallized grains with low dislocation density at the end of deformation phase. Since no additional hardening is happening, the recrystallized grains with low dislocation density have the more favorable conditions to grow.

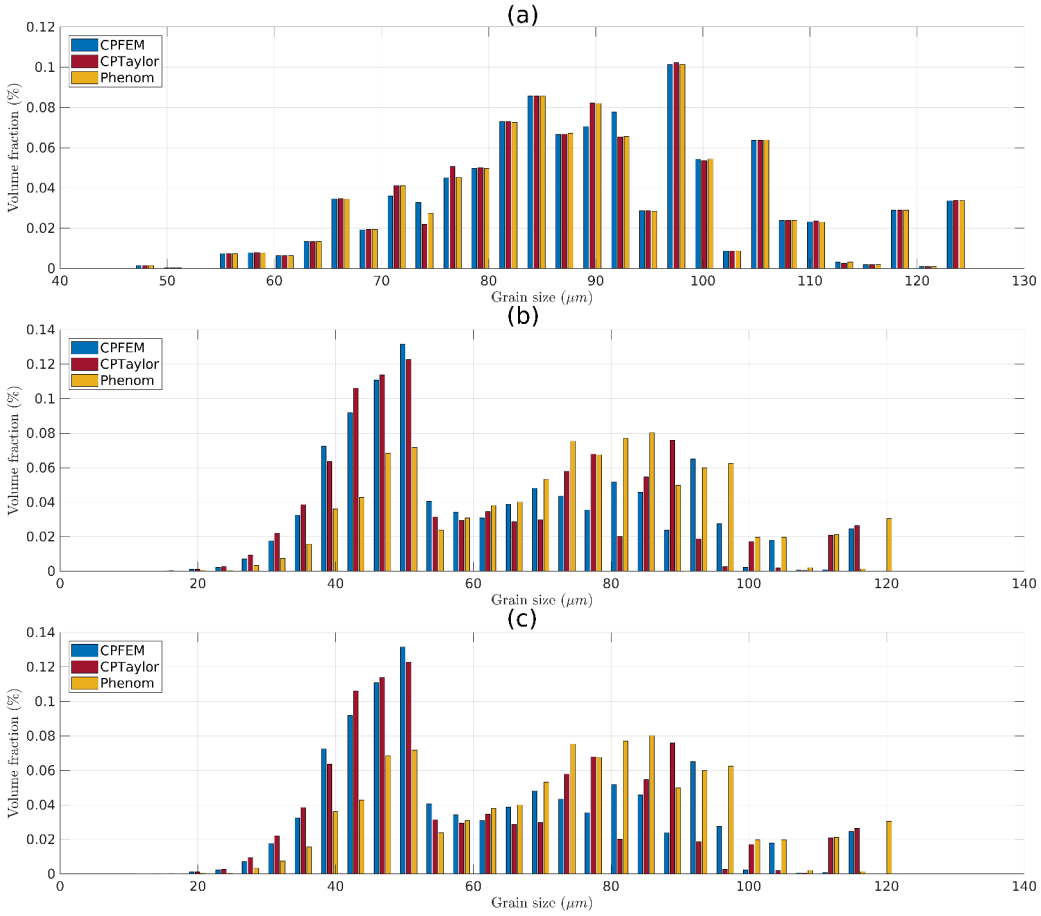

Figure 4.18: Comparison between the models results. Grain size distributions by volume considering all grains $\epsilon = 0.05$ (a), $\epsilon = 0.50$ (b) and $\epsilon = 0.10$ (c).

The model texture prediction was also compared. Since the phenomeno-

logical model does not consider orientations, it was not included in this comparison. Figure 4.19 shows the final texture predicted by the CPFEM model and the Taylor model. The results show a clear difference between the model results, even if some similar pattern can be observed. The texture predicted by the Taylor model shows very few different orientation points, caused by the homogeneous rotation imposed by the model formulation. Since all elements inside a grain have the same initial orientation and deform in the same way, their final orientation will be the same. This is not the case in the CPFEM model in which each element can deform differently.

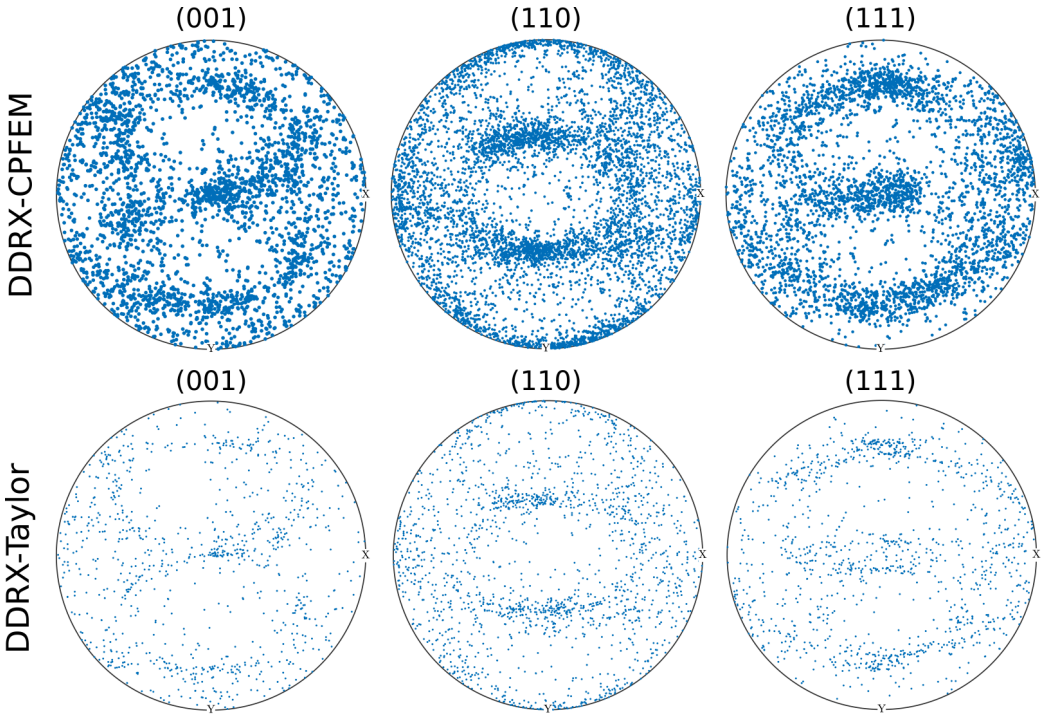

Figure 4.19: Comparison between the CPFEM model and Taylor model texture prediction.

Comparisons were also performed imposing different orientations for the introduced recrystallized grains: First, assigning a random orientation to recrystallized grain; Second assigning an orientation derived from the orientation of the parent grain. The results showed no significant differences between the two cases, the final texture pattern obtained is almost the same. This shows that in the current framework the final orientation is mostly defined by the deformation (crystal plasticity). Since recrystallized grains are also subjected to plastic deformation, their orientation evolution is also determined by the deformation conditions and their evolution is similar to the

non recrystallized grains.

The models computational cost was also compared, the results are presented in figure 4.20. The computational cost was normalized by dividing the total run time of each simulation by the lowest run time (0.50 (h) for the phenomenological model with the lower number of elements). The initial number of elements was also normalized by dividing the number of elements in each case by minimal number of elements of the considered cases (270294 elements).

The computational cost comparison shows that the increase in computational cost between the phenomenological model and the Taylor model are not significant, while the differences in the results is. However the increase in computational cost caused by the inclusion of the CPFEM model is quite large. So it could be affirm that in order to fully take advantage of the inclusion of CPFEM it is necessary to further improve the model to consider a more complex hardening law and consider heterogeneous grain boundary energy.

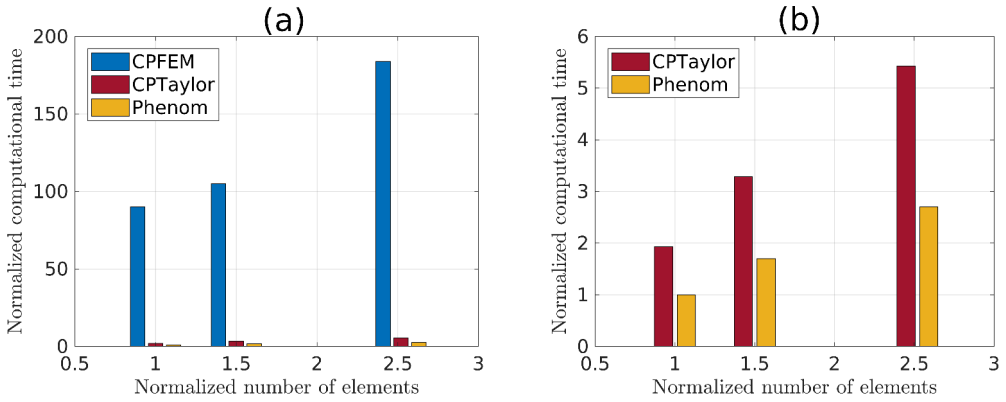

Figure 4.20: Comparison between the models computational cost for different initial number of elements. All models (a) and zoom showing only phenomenological and Taylor models.

4.5.3 Recrystallized grains size and twin grain boundaries

Two limitations were identified when comparing the model with experimental data. First, the size of inserted recrystallized grains calculated according to Eq. 3.9, that depends on the values of the parameters K_1 and K_2, defines a size over the measured recrystallized grains size. Figure 4.21 shows the modeled recrystallized grains size compared to measured experimental

recrystallized grain size at $\epsilon = 0.65$ for the different thermomechanical conditions. This over prediction of the recrystallized grains size introduces errors in the model predictions.

Second, as mentioned in section 4.2 and illustrated in figure 4.5, the difficulties to identify twin boundaries on deformed microstructures introduce an artificial reduction in the experimental grain sizes as strain increases. This effect is illustrated by the evolution of the mean grain size of the non recrystallized grains presented in figure 4.8. The results show a higher reduction in the grain size between the non deformed state and the first deformed state, which can not be explained only by the effects of recrystallization at such low strain.

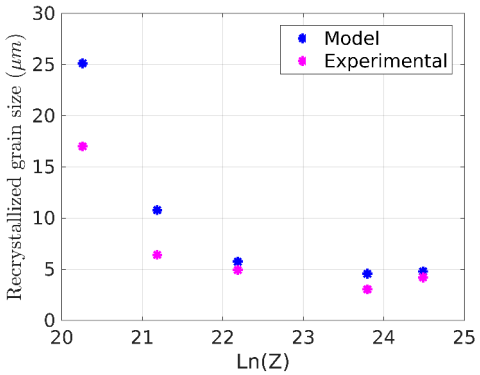

Figure 4.21: Model recrystallized grains (r^*) size compared with measured experimental recrystallized grain size at $\epsilon = 0.65$ for the different thermomechanical conditions.

To circumvent these two limitations: First a re-calibration of the parameters K_1 and K_2 was performed, the objective was to define K_1 and K_2 values that give the same mechanical behaviour but define a smaller recrystallized grain size. To do this, the parameter $k_0 = \sigma_0/M$ that defines the initial microscopic yield stress of the material, and the parameter m that represents the flow rule sensitivity in the crystal plasticity model, were also introduced into the calibration parameters.

The initial procedure calibrated the parameters K_1 and K_2, by considering only the mechanical behaviour without taking into into account their effect in the other mechanisms included in DDRX. As showed before this can introduce significant errors in the model. To minimize this error, the additional calibration step considers the effect of the parameters on all the mechanisms involved. This means that instead of calibrating the parameters by separating the mechanical behaviour from the grain size, recrystallized

grain size and recrystallized grain size, they are considered together.

By re-calibrating the parameters, for the deformation conditions $\dot{\epsilon} = 0.014(s^{-1})$ $T = 1273(K)$, the model recrystallized grain size was reduced from $r^* = 24.87\ \mu m$ with the initial parameters to $r^* = 11.45\ \mu m$ with the new parameters. This reduction in the model recrystallized grain size, involves a significant increase in the computational cost as the mesh size is defined according to the r^* value. Second, to address the twin boundaries identification issue, a second initial digital microstructure was generated. This microstructure follows the experimental grain size distribution but considers twin boundary as general grain boundary in the grain detection procedure. Figure 4.22 shows the grain size distributions for the two cases. However, the current framework does not consider heterogeneous grain boundary energy, so the effect is only related to the initial grain size. One of the perspectives of this work is then to enhance the current framework to consider heterogeneous (misorientation dependence) and anisotropic (+ inclination dependence) grain boundary energy following the works of [38].

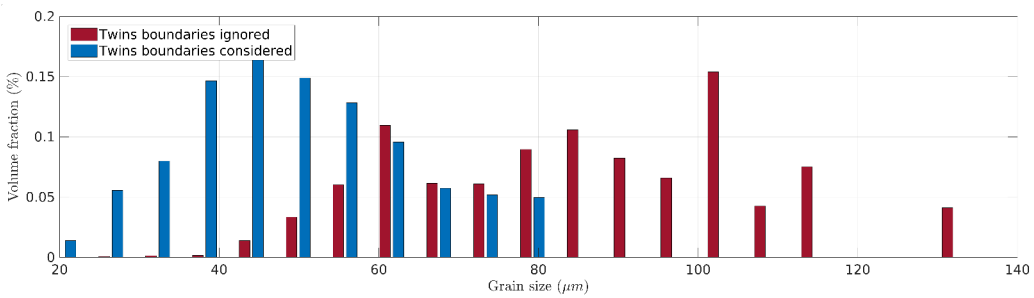

Figure 4.22: Grain size (d_{3D}) distributions by volume of the initial digital microstructures considering and without considering twin boundaries in the grain detection procedure.

Simulations were run with the new parameters and with the two initial microstructures, the simulation with the initial microstructure generated ignoring twin boundaries is further mentioned as case 1, and the simulation with the initial microstructure generated considering twin boundaries as regular grain boundaries is further mentioned as case 2. The results are shown in terms of average behaviour in figure 4.23, and in terms of grain size distributions by volume at $\epsilon = 1.0$ in figure 4.24.

The results show that by improving the parameters to define a smaller recrystallized grain, consistent with the experimental data, the numerical predictions better fit the experimental data. The average dislocation shows a very similar behaviour in both cases, meaning that the number of initial

grains and their sizes do not have significant effect in how the average dislocation density evolves. This will be further discussed in the next section.

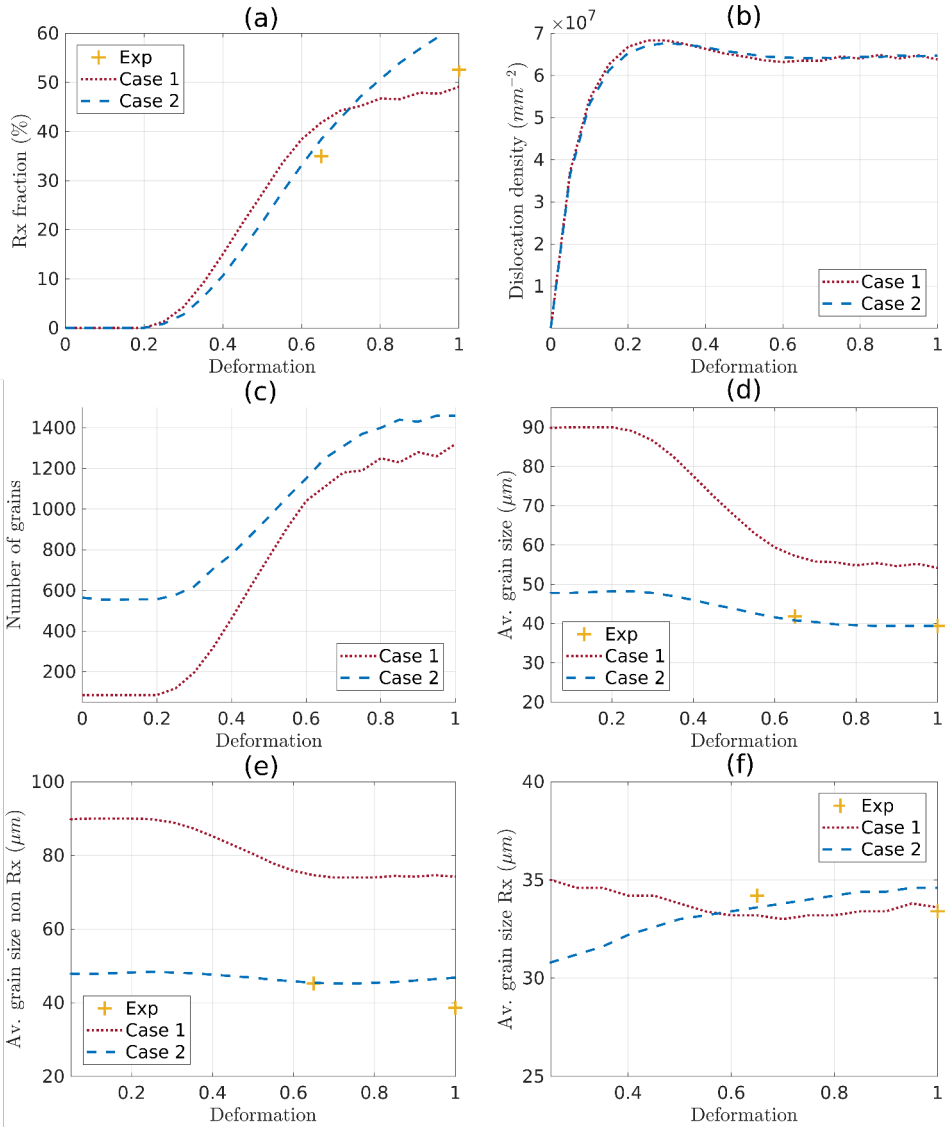

Figure 4.23: Simulation results considering different initial mean grain sizes compared against experimental data in terms of average behaviour. (a) Recrystallized fraction, (b) dislocation density, (c) number of grains, (d) average grain size ($\bar{D}_V$), (e) average non recrystallized grain size ($\bar{D}_{NRxV}$), (f) average recrystallized grain size ($\bar{D}_{RxV}$).

However there are differences in the evolution of microstructure. The evolution of the average grain size ($\bar{D}_V$) shows that: the reduction of the

average grain size is dependent to the difference between the initial grain size and inserted recrystallized grains size. A bigger difference translates in a bigger reduction in the average grain size. This is also observed for the non recrystallized grain size evolution.

For both cases the model correctly reproduces the evolution of the recrystallized fraction. The simulation with the smaller initial microstructure shows a higher recrystallized fraction at high deformation levels, while the simulation with a bigger initial mean grain size shows a higher recrystallized fraction at the lower deformation levels. The observed behaviour is consistent with the evolution of the average recrystallized grains size ($\bar{D}_{RxV}$), which at lower deformation levels shows higher values, but with the increase in deformation, this behaviour inverses.

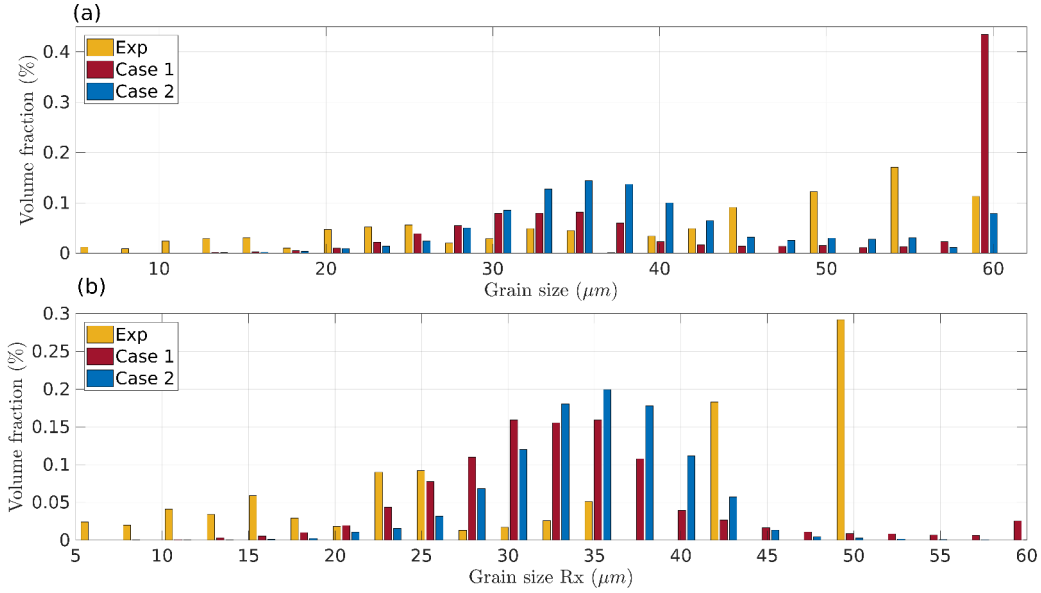

Figure 4.24: Comparisons of simulation results for both cases with different initial microstructure with experimental data. Grain size (d_{3D}) distributions by volume. All grains (a) and recrystallized grains (b)/

This difference of behaviour is caused by: First, the higher number of grains boundaries that allow recrystallized grains to appear on more places, causing less clustering between them, this effect was already discussed. Second, the smaller differences in size between the recrystallized grains and non recrystallized grains, which translates in similar capillarity effects. Thus, when the recrystallized grains harden, the capillarity effect become the main driving force in the GB migration. Therefore, the simulation results show that having bigger grains can favor recrystallization at lower deformation lev-

els when the recrystallized fraction is lower. But at higher deformation levels, when there is a higher number of recrystallized grains in the microstructure, having smaller grains translates in less clustering between them and smaller differences in the capillarity effect. This aspect allows the recrystallized grains to grow more quickly.

In terms of grain size distributions (figure 4.24), one can summarize the results as: in case 1, the microstructure shows a higher percentage of big grains than case 2 and experimental data, even though the sizes and the percentages of the bigger grains in the microstructure has been significantly reduced with respect to the initial state. This behaviour is a clear indicator of the limitations of not including twins in the microstructures, as these big grains are not consumed in the simulation by the effects of recrystallization.

Regarding the recrystallized grains distributions, which at this deformation level ($\epsilon = 1.0$) are the majority of grains in the microstructure, the results show that in both simulations cases the recrystallized grains grow less than in experimental data. From the initial insertion diameter of $2 * r^* = 22.90\ \mu m$, most of the simulation recrystallized grains grow to sizes between 30 μm and 40 μm while in the experimental data the recrystallized grain sizes reach values around 50 μm. Due to the model formulation, recrystallized grain sizes smaller than the insertion size are very difficult to capture as recrystallized grains are inserted with a size that ensures their growth. One alternative to improve this behaviour is to use a size distribution based on the experimental data instead of using a constant size for the ReX grains.The simulation results compared with experimental data in terms of grain size distribution at $\epsilon = 1.0$ deformation level are shown in figure 4.25.

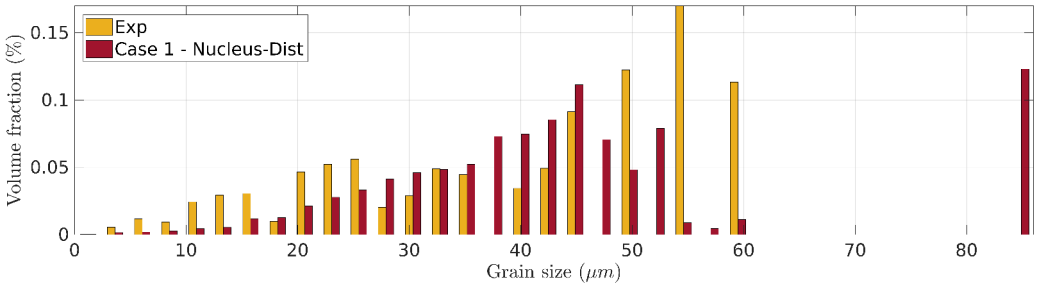

Figure 4.25: Comparisons of simulation results for case 1, defining r^* as a size distribution, with experimental data. Grain size (d_{3D}) distribution by volume.

The results show that with this alternative, the simulation results fit more closely the experimental data, specially for the smaller grains, however this

approach is restrictive since it requires additional data to define the grain size distribution. Additionally, differences in microstructure growth rates are still observed similar to the other cases. The results show a significant improvement with respect to the initial calibration procedure, however the model still present limitations related to GBM. Further works in the definition of the GB mobility and energy must be performed in order to improve the model capability.

4.5.4 Models comparison - Optimized parameters

With the optimized parameters, simulations were run for the recrystallization model coupled with CPFEM, CP Taylor and the phenomenological model. The simulations were run using the same parameters in all the models. The results were compared between the models and with the experimental data and are summarized in figure 4.26 in terms of average behaviour and in figures 4.27 and 4.28 as grain size distributions by volume for $\epsilon = 0.65$ and $\epsilon = 1.00$ respectively.

The results show: For the phenomenological model, most of the recrystallized grains that are introduced disappear. Since the new parameters define a smaller insertion size, the energy gradient intensity decreases in time and thus recrystallized grains do not have enough time to reach the required size to overcome capillarity forces. This causes that the recrystallized fraction does not continue to increase, but keeps a very low value during all the simulation. This value is kept by the constant introduction of new recrystallized grains, as the dislocation density remains at levels above the critical value. This behaviour can also bee seen in the grain size distributions, which show very small changes between them for the different deformation levels. This result shows that the need for safety factor introduced by [79] does not comes only from the errors in the geometrical description of the grains due to the mesh size, but also from the accelerated hardening rate caused using the phenomenological model.

Regarding the CPFEM and the CP Taylor models, similarly to the previous comparison, the results show that the quicker hardening rate in the CP Taylor model causes recrystallization to start first. This leads to a higher increase in the number of grains and recrystallized fraction compared with the CPFEM model. The CPFEM model shows the closest fit to the experimental data, this is expected since the parameters value used were calibrated for the CPFEM model. On the other hand, the grain size evolution shows that, even if the the reduction in size caused by recrystallization starts more quickly in the CP Taylor model, the values of the two models converge to a similar value at the highest deformation levels. This result agrees with

the behaviour previously observed when comparing simulations with different initial sizes, showing that the reduction in average grain size depends on the difference between the initial grain size and the size of the introduced recrystallized grains.

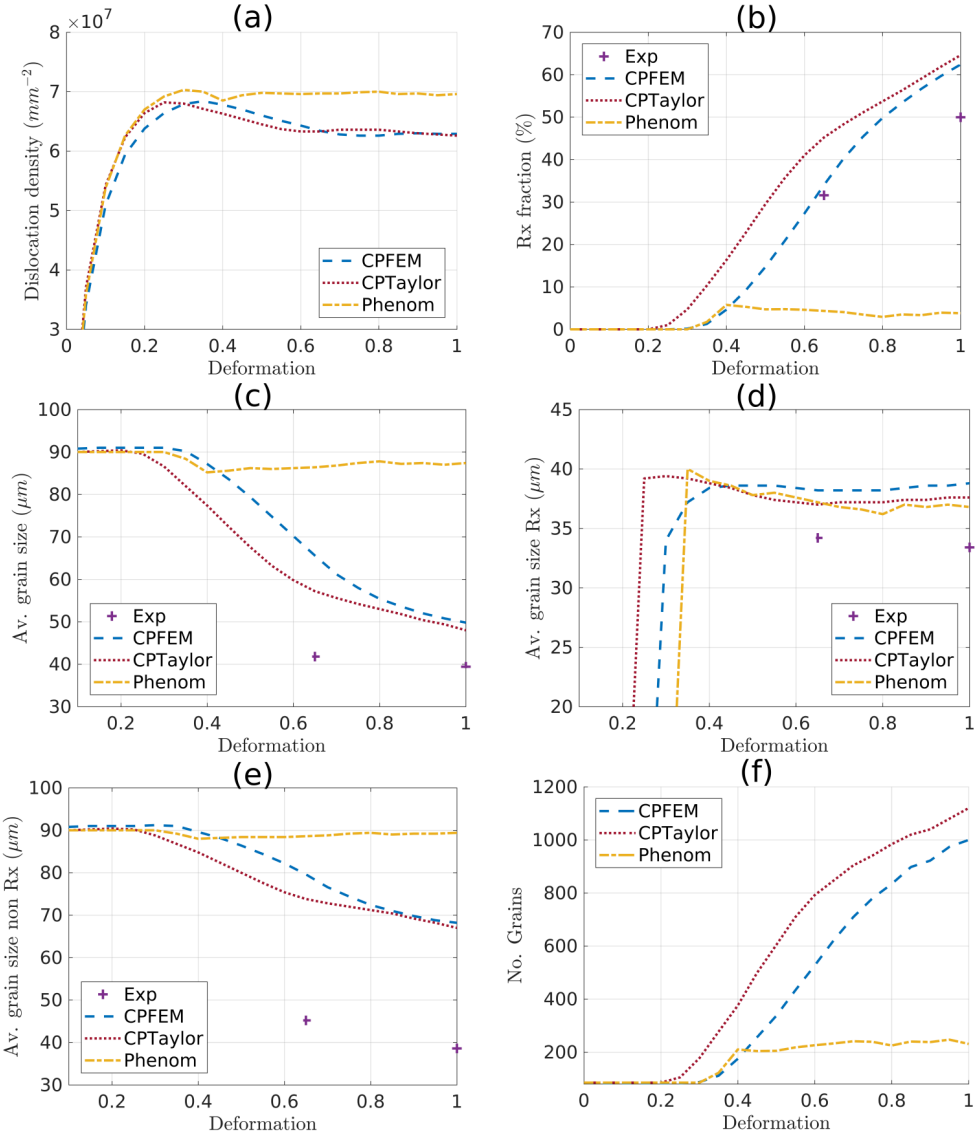

Figure 4.26: Comparisons between the models results (optimized parameters) and experimental data. (a) Average dislocation density, (b) recrystallized fraction, average grain sizes by volume considering all grains (c), recrystallized grains (d) and non recrystallized grains (e), and number of grains (f).

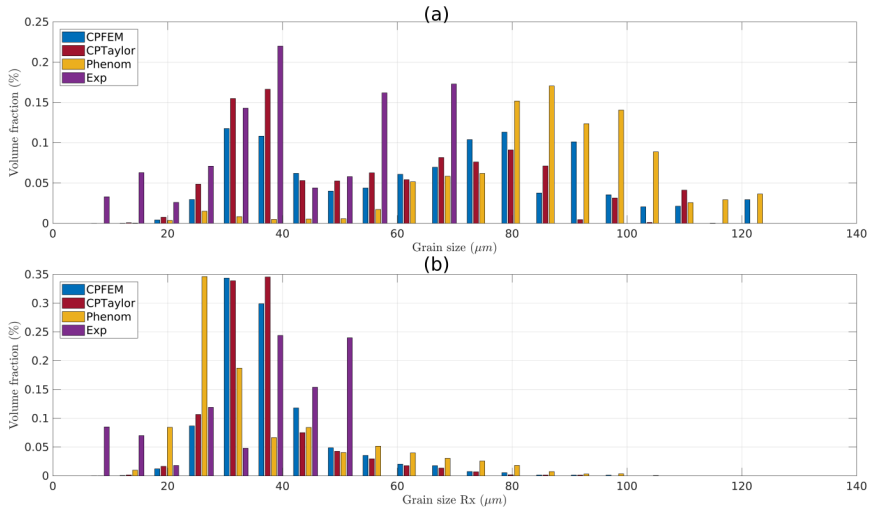

Figure 4.27: Comparison between the models results (optimized parameters) and experimental data. Grain size distributions by volume $\epsilon = 0.65$ considering all grains (a), considering only recrystallized grains (b).

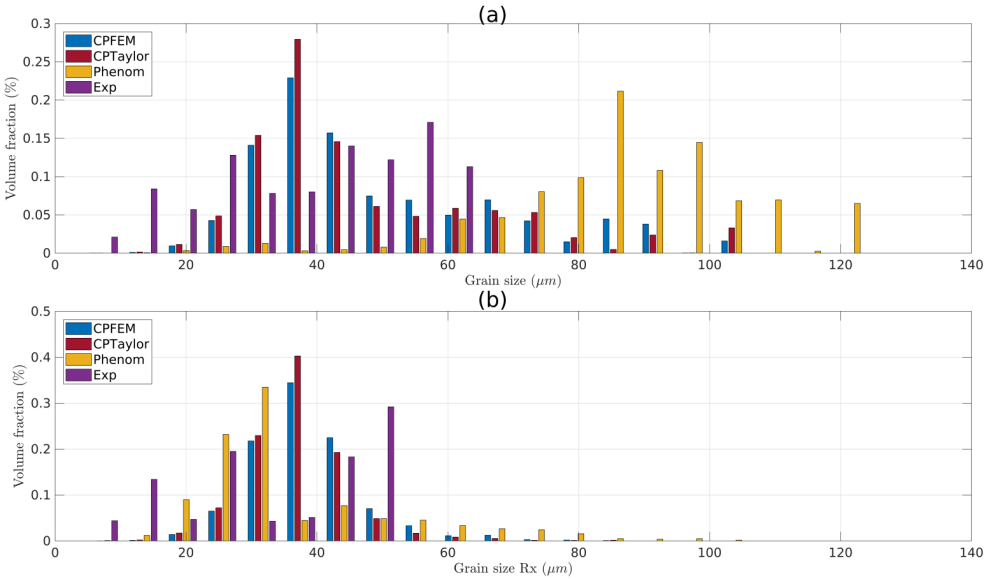

Figure 4.28: Comparison between the models results (optimized parameters) and experimental data. Grain size distributions by volume $\epsilon = 1.00$ considering all grains (a), considering only recrystallized grains (b).

The grain size distributions show that either model is able to completely reproduce the experimental distribution. Even if the models average recrys-

tallized grain size shows a higher average value than the experimental data, the volume distributions shows that the experimental data has a higher percentage of bigger recrystallized grains than the simulations, and a higher percentage of smaller recrystallized grains. As mentioned before, further investigations and improvements need to be performed on the mobility and GB energy definitions in order to better describe the evolution of the microstructure.

4.6 Recrystallized grains identification

Comparing simulation data with experimental data for recrystallization mechanisms is also limited by the difficulty in identifying recrystallized grains on experimental samples, specially for full field models that aim to provide a spatial reproduction of the microstructure evolution. On simulation models, the recrystallized grains can be clearly tracked and identified, since they appear following an imposed algorithm. However, this is much more complex to discuss this aspect on experimental samples. The procedure used in this work to identify recrystallized grains uses the GAM criteria, following the work of [149], it corresponds to a commonly used procedure in the literature.

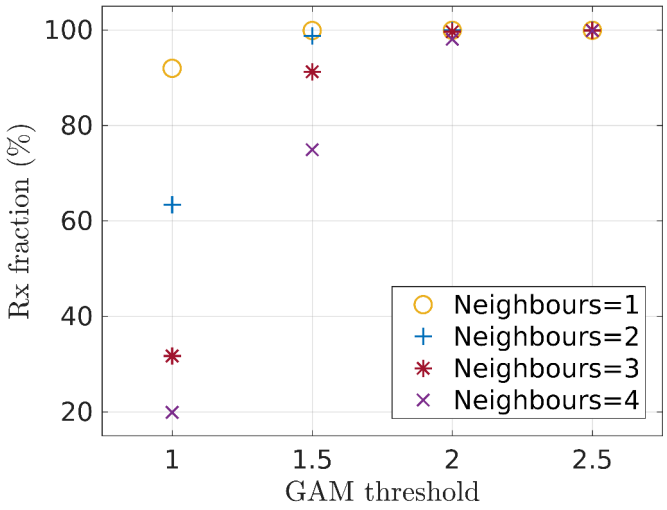

Figure 4.29: Changes in the recrystallization fraction, for the sample deformed at $\dot{\epsilon} = 0.014\ s^{-1}$ $T = 1323(K)$ $\epsilon = 1.0$, for different GAM thresholds and different order of neighbours considered for the calculation of the KAM value, used in the identification of recrystallized grains.

This procedure relies on establishing a GAM threshold, and the calculation of the GAM value depends on the KAM value, whose calculation depends on the spatial resolution of the measurement and of the order of neighbours considered. Figure 4.29 shows the changes in the recrystallization fraction value, for the sample deformed at $\dot{\epsilon} = 0.014\ s^{-1}$ $T = 1323\ K$ and $\epsilon = 1.0$, for different GAM thresholds and different order of neighbours, considered in the identification of recrystallized grains. These results show the sensitivity derived from the difficulties in the identification of recrystallized grains on experimental samples. This aspect is also a future topic of discussion concerning the comparisons of full-field computations of DRX phenomenon and experimental data.

4.7 Summary and discussion

In this chapter the recrystallization model results were compared with experimental data for the case of 304L steel subjected to compression at high temperatures. The raw data from the experimental tests performed during the PhD of Maire, L. [6] were processed and analyzed.

The experimental data were used to calibrate and validate the model. The model parameters K_1, K_2 and K_g, related to the strain hardening, dynamic recovery, and nucleation probability were identified, for a range of strain rates between $0.008 - 0.1\ (1/s)$ and temperatures between $1273 - 1373\ K$. The results show that the calibration of the parameters K_1, K_2 considering only the stress-strain behaviour can lead to the definition of recrystallized grains sizes that do not agree with the experimental data. Since this calibration procedure considers only the effect of these two parameters on the mechanical behaviour, additional calibration steps, that consider also the effect of the parameters in the recrystallized grain size definition were included in order to minimize these errors.

The results show that, for the considered deformation conditions, the model correctly predicts the average behavior of several of the main variables of interest during dynamic recrystallization. However the grain size distributions illustrate that the rate of growth of recrystallized grains is still not correctly modeled.

The evolution of the dislocation density in the current framework was also analyzed. The results show that, during most of the DRX mechanism, the dislocation density of the microstructure is not that heterogeneous, as most of the grains reach the maximal dislocation density value. The grains that are constantly evolving are only the recrystallized grains, from the time that they are introduced until they completely hardened. This time window depends

on the hardening rate, which can change according to the grain orientation and location. This behaviour is the result of the chosen hardening law, which is an important simplification concerning the dislocation density evolution.

Additionally not being able to model the behaviour of twin grains boundary presents an important limitation. Since in the current framework the only alternatives available are ignoring them completely or treat them as regular grain boundaries. This translates into considering different initial grain size distributions.

Simulations were run for both cases and the effects were analyzed. the results show that, smaller grain sizes in the initial microstructures favors recrystallized grains growth. As having smaller grains translates into higher number of grain boundaries that serve as nucleation sites. This reduces clustering between the recrystallized grains which can limit their growth. Also, when recrystallized grains harden, since the main driving force in their growth is the capillarity effect, having a similar size than non recrystallized grains increases the probability that they will not be consumed.

The model was also compared with simplified formulations, that use a phenomenological law or crystal plasticity with the Taylor hypothesis, to model plastic deformation. The results show significant differences in the microstructure evolution between the CPFEM and CP Taylor models when compared with the phenomenological model, which derives mostly form the accelerated hardening rate of the grains caused by not considering the grains orientations.

The models were also compared in terms of computational cost and showed that using CP Taylor model does not cause a significant increase in the computational cost comparatively to the phenomenological model. Its is then an interesting alternative in the current framework. Due to the complexity of the DRX mechanism and the limitations of the current framework, several perspective improvements can sill be made, in the next chapter some of them will be presented.

4.8 Résumé en Français

Dans ce chapitre, les résultats du modèle de recristallisation ont été comparés aux données expérimentales pour une acier austénitique de type 304L soumis à compression à haute température. Les données brutes issues des tests expérimentaux réalisés lors de la thèse de L.Maire [6] ont été traitées et analysées dans ce sens.

Les données expérimentales ont été utilisées pour calibrer et valider le modèle. Les paramètres du modèle K_1, K_2 et K_g, liés à l'écrouissage, à la restauration dynamique et à la probabilité de germination ont été identifiés, pour une plage de taux de déformation entre $0.008 - 0.1$ $(1/s)$ et des températures entre $1273 - 1373$ K. Les résultats montrent que la calibration des paramètres K_1, K_2 en considérant uniquement le comportement contrainte-déformation peut conduire à la définition de tailles de grains recristallisés qui ne sont pas en accord avec les données expérimentales. Étant donné que cette procédure d'étalonnage ne considère que l'effet de ces deux paramètres sur le comportement mécanique, des étapes d'étalonnage supplémentaires, qui prennent également en compte l'effet des paramètres dans la définition de la taille des germes, ont été incluses afin de minimiser ces erreurs.

Les résultats montrent que, pour les conditions de déformation considérées, le modèle prédit correctement le comportement moyen de plusieurs des principales variables d'intérêt lors de la recristallisation dynamique. Cependant, les distributions de taille de grains montrent que le taux de croissance des grains recristallisés n'est pas toujours correctement modélisé.

L'évolution de la densité de dislocation a également été analysée. Les résultats montrent que, pendant la majeure partie du mécanisme de DRX, la densité de dislocation de la microstructure n'est pas réellement hétérogène, car la plupart des grains atteignent la valeur de densité de dislocation maximale. Les grains en constante évolution ne sont que les grains recristallisés, depuis leur introduction jusqu'à leur durcissement complet. Cette fenêtre de temps dépend de la vitesse de durcissement, qui peut évoluer en fonction de l'orientation et de l'emplacement du grain. Ce comportement est le résultat de la loi d'écrouissage choisie, qui correspond à une simplification importante de l'évolution de la densité réelle de dislocation.

De plus, le fait de ne pas pouvoir prendre en compte les macles est une limitation importante. En effet, de manière communément répandue, les macles sont ignoreés ou considéreés comme des joints de grains normaux. Il est montré que cela a un impact fort sur la discussion concernant la prédiction des distributions de taille de grains.

Le modèle a également été comparé à des formulations simplifiées, qui utilisent une loi phénoménologique ou une plasticité cristalline avec l'hypothèse

de Taylor, pour modéliser la déformation plastique. Les résultats montrent des différences significatives dans l'évolution de la microstructure entre les modèles CPFEM et CP Taylor et le modèle phénoménologique [6], ces différences dérivent principalement de l'accelération de la vitesse de durcissement accéléré des grains provoquée par la non-prise en compte des orientations des grains.

Les modèles ont également été comparés en termes de coût de calcul. L'utilisation du modèle CP Taylor n'entraîne pas d'augmentation significative du coût de calcul par rapport au modèle phénoménologique. C'est ainsi une alternative intéressante dans le cadre actuel. En raison de la complexité du mécanisme de DRX et des limites actuelles du modele propose, plusieurs perspectives sont envisagées, certaines d'entre elles sont introduites au chapitre suivant.

Chapter 5

Perspectives

5.1 Introduction

In this chapter some perspectives concerning applications and improvements of the model, that could not be completed due to time limitations, are proposed and explored.

5.2 Particle stimulated nucleation

The phenomenological laws describing the appearance of recrystallized grains used in this work and in most of the models described in chapter 1, consider only dislocation density as the criteria for nucleation occurrence and disregard the effect of orientation gradients which are also required for nucleation to occur. In cases of necklace nucleation, when nucleation is observed mostly near the grain boundaries, the presence of orientation gradients is ensured by the presence of the grain boundary.

However, this does not apply for other nucleation events like intra granular nucleation or particle stimulated nucleation (PSN). Further study is required to derive more general nucleation criteria, to do this one interesting alternative is to study the conditions for PSN occurrence, since compared to other nucleation mechanisms the nucleation sites can be more easily identified.

PSN occurs on material containing coarse hard particles with sizes larger than $1\mu m$. The presence of the hard particles, when the material is plastically deformed, creates differentiated deformation zones (Particle deformation zones PDZ) as shown in figure 5.1, that serve as potential nucleation sites. The PDZ are characterized by the presence of high stored energy and high misorientation gradients. Their presence accelerates the recrystal-

lization mechanism, leading to grain refinement and texture randomization. Several experimental studies on this subject are present in the literature [158, 159, 160, 161, 162].

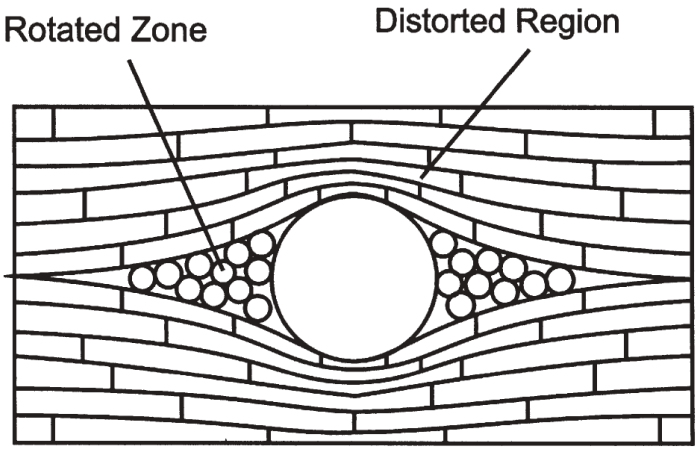

Figure 5.1: Schematic representation of the deformation zone around the hard particle. Image from [1].

However, there is not enough insight about the preferred nucleation site inside the deformation zone, because of the difficulties to perform experimental measurements. Numerical simulation studies, have also been proposed [31, 163, 164, 165, 166, 162], but most of them rely on simplified crystal plasticity models, are limited to 2D or only reach low deformation levels. Since our CPFEM framework can overcome these limitations, simulations of the PDZ were performed. An initial approximation was done using macroscopic visco-plasticity FEM, then CPFEM was used with the aim to reproduce experimental results observed in the literature.

5.2.1 PSN-PDZ visco-plasticity simulations

Initial simulations of the deformation around the hard particles were performed using the Von Mises macroscopic deformation model with a multiplicative hardening law [17]:

$$\sigma_y = \sigma_{y0} + K\bar{\epsilon}^m\dot{\bar{\epsilon}}^n \quad , \tag{5.1}$$

The dislocation density, which translates to stored energy, is represented at the macro level by the equivalent plastic deformation. Since the model does not consider grain orientations, the misorientation field was estimated form the infinitesimal spin tensor $\mathbf{w}$, which can be decomposed into a rotation

angle and a rotation vector. The misorientation is then calculated as the maximal difference in the rotation of an element and its neighbours.

The simulations were performed for a domain of $10\mu m$, containing one hard particle and composed roughly of 300.000 tetrahedral elements. The elements size is non-uniform but isotropic, with smaller elements in the zone near the particle, 0.05 μm, and larger elements near the boundaries of the domain, 0.75 μm.

In order to simulate the hard particle behaviour, the mechanical properties were increased so that the particle is almost rigid and no plastic deformation occurred. The materials properties are shown in table 5.1 for the domain and the particle. The coefficients for the multiplicative hardening law were obtained from [167]. The simulations were performed up to 75% strain level, and global remeshing was performed every 25% strain level.

Property	Domain	Particle
$E\,(MPa)$	$70e3$	$140e3$
ν	0.33	0.43
$K\,(MPa)$	$68.62 * 10^3$	$333.33 * 10^3$
$\sigma_{y0}\,(MPa)$	275	27500

Table 5.1: Material properties for the domain and the particle

Simulations were performed for different loading conditions, shear, compression and tension, and for different particles sizes $1\mu m$, $1.5\mu m$, and $2\mu m$. The most significant results are detailed next.

Figure 5.2 presents the equivalent plastic deformation and the equivalent deviatoric stress for a compression case, for a particle size of $1\mu m$. It is seen that the presence of the hard particle creates a specific distribution of the plastic deformation. Characterized by the appearance of dead zones, zones with no plastic deformation near the particle located at the top, bottom, left and right sides. Passing the dead zones, zones with high plastic deformation are located, creating a cross like pattern. The maximal plastic deformations are located near the hard particle in a diagonal pattern. The general pattern of the results obtained, presence of dead zones and localized zones of max plastic deformation agree with the results found in other simulation studies.

Figure 5.3 shows, for the same case described before, the rotation angle and the mean misorientation angle. It is seen that only the diagonal zones around the particle present a significant rotation. The zones located to the right, left, top and bottom of the particle, in which plastic deformation is localized, present no rotation. The rotation angles present an homogeneous behavior with very delimited zones with high rotation or no rotation at all.

This behavior translates into very small zones with high misorientation located in the diagonals of the hard particle, but separated from the vicinity of the particle.

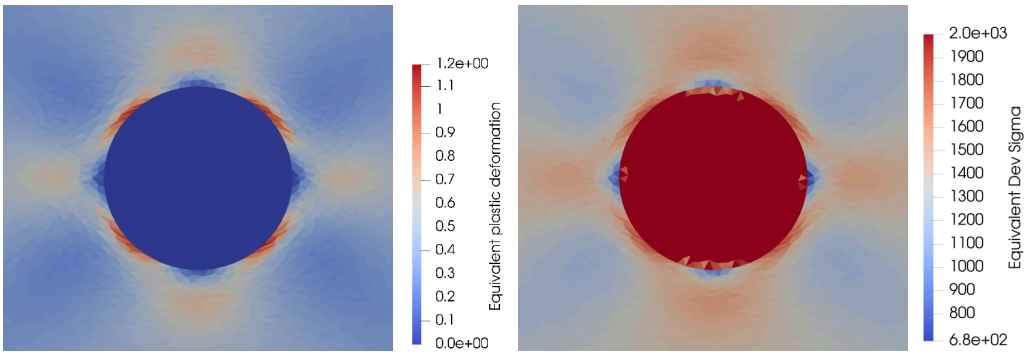

Figure 5.2: Equivalent plastic deformation left and equivalent deviatoric sigma right - Compression case.

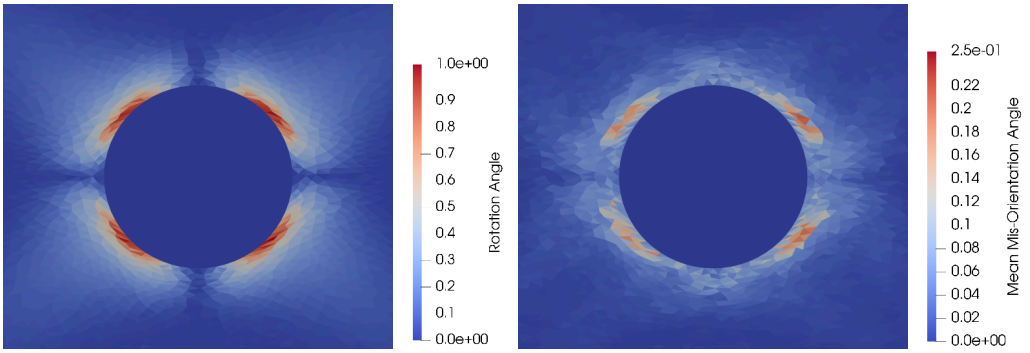

Figure 5.3: Rotation angle left and mean misorientation angle right - Compression case.

When looking at the equivalent plastic deformation and the misorientation, it is seen that only specific zones present both high plastic deformation and high misorientation, the zones along the diagonals near the surface of the particle. Next, the equivalent plastic deformation and mean misorientation were analyzed for different loading cases and different particles sizes. Figures 5.4 and 5.5 show the equivalent plastic deformation and mean misorientation respectively, for compression, tension, and shear cases.

The results show no significant differences between loading cases, the same patterns and behavior described previously for the compression case, are seen for the other two loading conditions. Finally, the results for different particles sizes, in context of compression case, were compared. However

since the macroscopic model used does not consider size dependent effects, no significant changes were observed. The results show the same distribution pattern for both particles sizes, with an increase in the equivalent plastic deformation magnitude with increase in particle size. While the misorientation magnitudes keep very similar values for the different particle sizes considered.

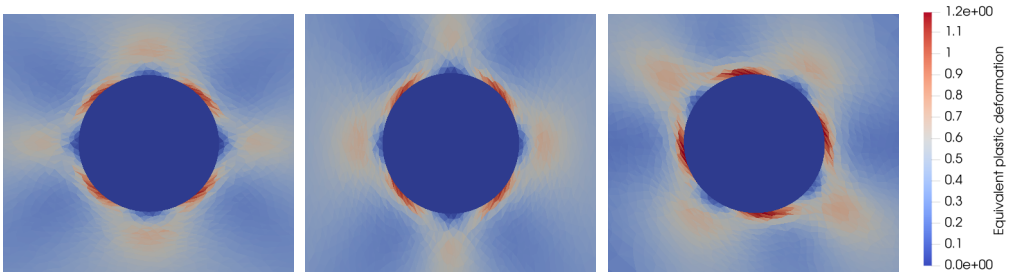

Figure 5.4: Equivalent plastic deformation for different loading cases. Compression (left), tension (center) and shear (right).

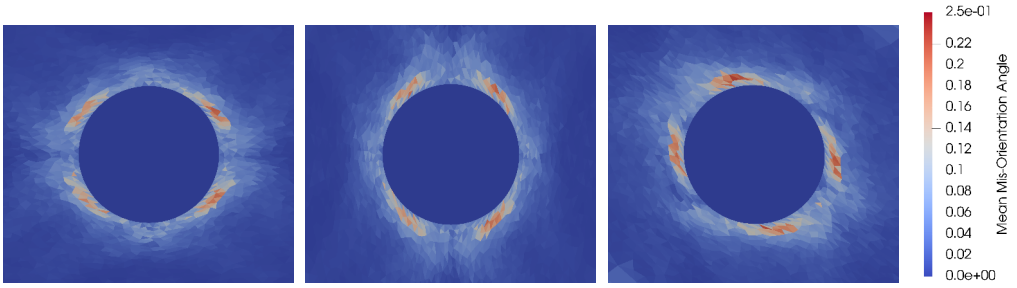

Figure 5.5: Mean misorientation for different loading cases. ompression (left), tension (center) and shear (right).

The simulations performed only give an initial approximation due to the simplicity of the model used. Our CPFEM model is then used in order to propose a more realistic description of the phenomena, especially for the orientation and mean misorientation. However this first simple analysis corroborates that the numerical framework can simulate the PDZ up to high deformation levels.

5.2.2 PSN-PDZ CPFEM simulations

CPFEM simulations were used to simulate a PDZ following the experimental test performed by Fonseca et al. [162]. This case was selected as detailed

experimental measurements of the deformation pattern around a hard particle were available to be compared against the simulation results. In this work high resolution digital image correlation was used to map the deformation around particles of different sizes in a model Al-Si alloy, and the deformation maps were compared concerning the local lattice rotation obtained using EBSD. In the experimental set up the samples are deformed in channel die, the normal direction (ND) corresponds to the loading direction and the rolling direction (RD) corresponds to the free surface on the channel die set. An schematic of the experimental set up is presented in [162]. The deformation maps and rotation maps in the transversal direction (TD), for the cases of a isolated big particle and a isolated small particle are shown in figure 5.6. The rotation are calculated with respects to an undeformed point.

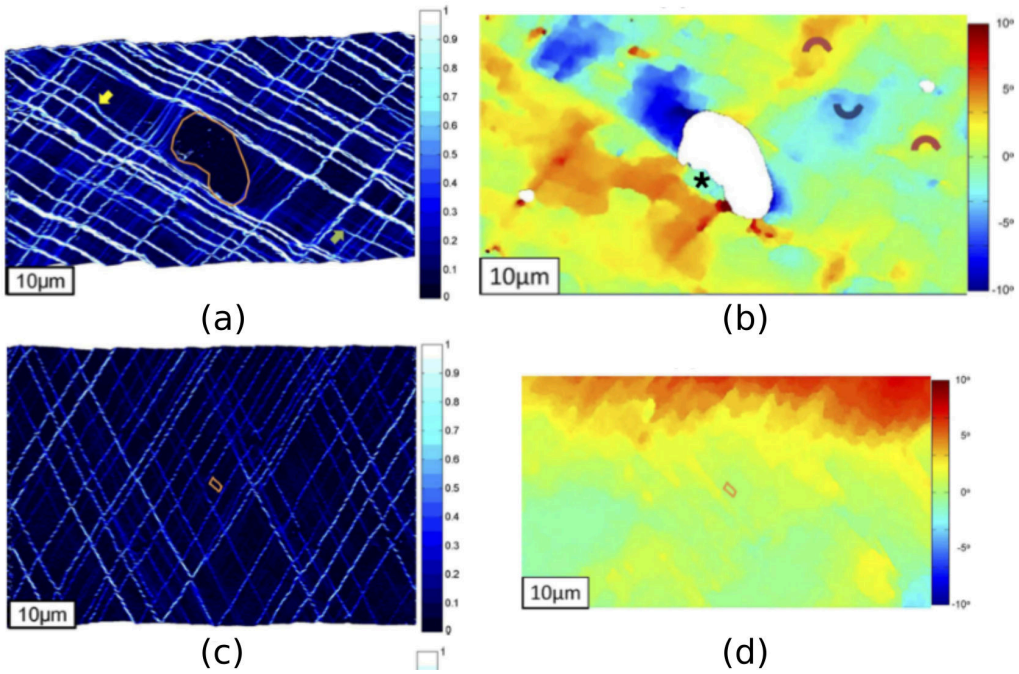

Figure 5.6: Deformation maps (a,c) and TD rotation maps (b,d) for the cases of a isolated big particle (a,b) and a isolated small particle (c,d) from the work of Fonseca et al. [162]. Figures modified from [162].

The results show that the presence of the large particle interrupts the formation of deformation bands around the particle. The presence of the big particle also reduces the spacing between the deformation bands around it, compared to the distance between the further away form the particle. The small particle on the other hand does not seem to have any effect on the deformation bands observed. Additionally, the rotation maps show that the

presence of the small particle does not cause any effect, with layers of gradual increasing rotation from bottom to top. While, the presence of big particle clearly disrupts the rotation field and creates zones with a high rotation gradient around the particle.

In an attempt to reproduce the observed behaviour, CPFEM simulations were run. The simulation domains were set with a particle mimicking the shape of the particle seen in the experimental measurements. The hardening law used is the Yoshie-Laasroui-Jonas dislocation law, coupled with the Taylor hypothesis (presented in chapter 2). To simulate the behaviour of the hard particle, the same approach used in the macroscopic simulations was used, the K_0 in the CP hardening law for the particle was set to be significantly higher than the rest of the domain. The mesh was generated with a variable size, with smaller elements around the particle. The mesh was also generated with nodes located along the surface of the particle. Since only the 2D profile of the particle is known, the 3D shape of the particle was assumed to be a revolution of the known 2D profile along its middle axis. The general simulation domain is shown in figure 5.7.

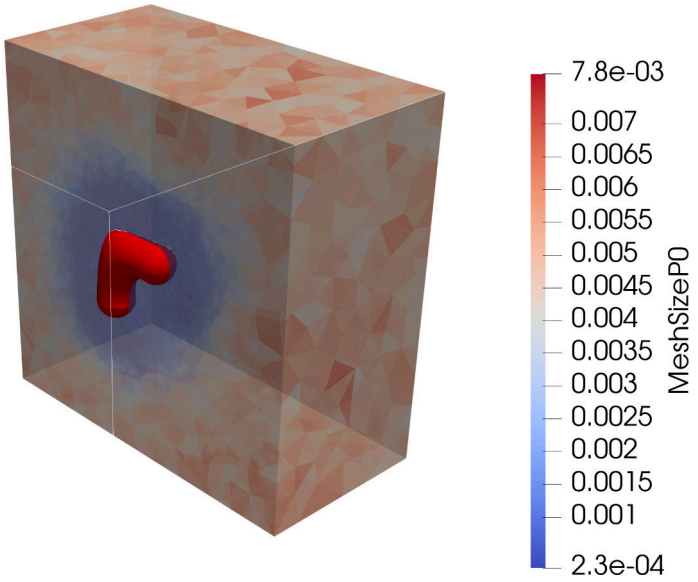

Figure 5.7: PDZ-CPFEM simulation domain.

From the simulation results presented in [162], it is clear that the CPFEM simulation setup used in their work was not able to reproduce the formation of the deformation bands around the particle. To improve this results, differ-

ent simulations setups were considered that attempt to facilitate the simulation of the deformation bands formation by considering different boundary conditions, domain shapes and material properties. The simulation set ups considered are: first, a complete domain with the top and bottom boundaries as plane faces. Second, half the domain restricting the deformation in the normal direction on the particle surface with the top and bottom boundaries as plane faces. Third, half the domain restricting the deformation in the normal direction on the particle surface with the top and bottom boundaries as serrated faces; fourth, half the domain restricting the deformation in the normal direction on the particle surface with the top and bottom boundaries as plane faces, plus diagonal planes with lower $K0$ values in the domain. In all the cases the loading corresponds to a channel die compression. The different simulations set ups are shown in figure 5.8.

The simulations correspond to a single crystal configuration, the same initial orientation was assigned to the domain including the particle, the orientation corresponds to the crystal orientation reported in [162]. The simulations results were compared in terms of plastic deformation, dislocation density and rotation in the TD direction. The rotation was calculated using the same procedure as in the experimental test, as the rotation from the initial orientation. The results for the considered simulations set ups are shown in figures 5.9, 5.10, and 5.11 (The second case results are not shown as the results are quite similar to the third case).

In all cases the plastic deformation shows patterns with zones around the particle with very high deformation levels along with undeformed zones. The first case shows the lower deformation levels around the particle with only 2 very localized high deformation zones. The third case on the other hand shows the highest deformation levels, with zones with high deformation around all the particle. The fourth case shows a similar pattern around the particle as the first case, plus planes with high deformation that correspond to the weakened zones (planes with lower $K0$ values). It is interesting that in the fourth case the amount of plastic deformation in the the weakened zones is not homogeneous. The weakened bands that cross the particle show a concentration of plastic deformation on the lower right zone of the domain while on the upper left zone the amount of plastic deformation is reduced.

Additionally, we can see that restricting the deformation in the normal direction on the particle surface blocks the possibility of the domain to deform and rotate in one direction. This increases the magnitude of plastic deformation, a similar effect was described in [162] caused by using 2D simulations. In the fourth case this effect is reduced since the zones with lower K_0 values help to distribute the plastic deformation. When comparing with the experimental deformation maps, the results show that the deformation lines

observed are not reproduced by CPFEM, even in the fourth case in which attempts are made to artificially introduce this behaviour. The simulation does not show the same behaviour as in experimental data in terms of locations and spacing. However there is a clear effect in terms of the magnitude of the plastic deformation in the weakened zones that cross the particle, this effect is similar to the interruption of the deformation bands observed in the experimental data.

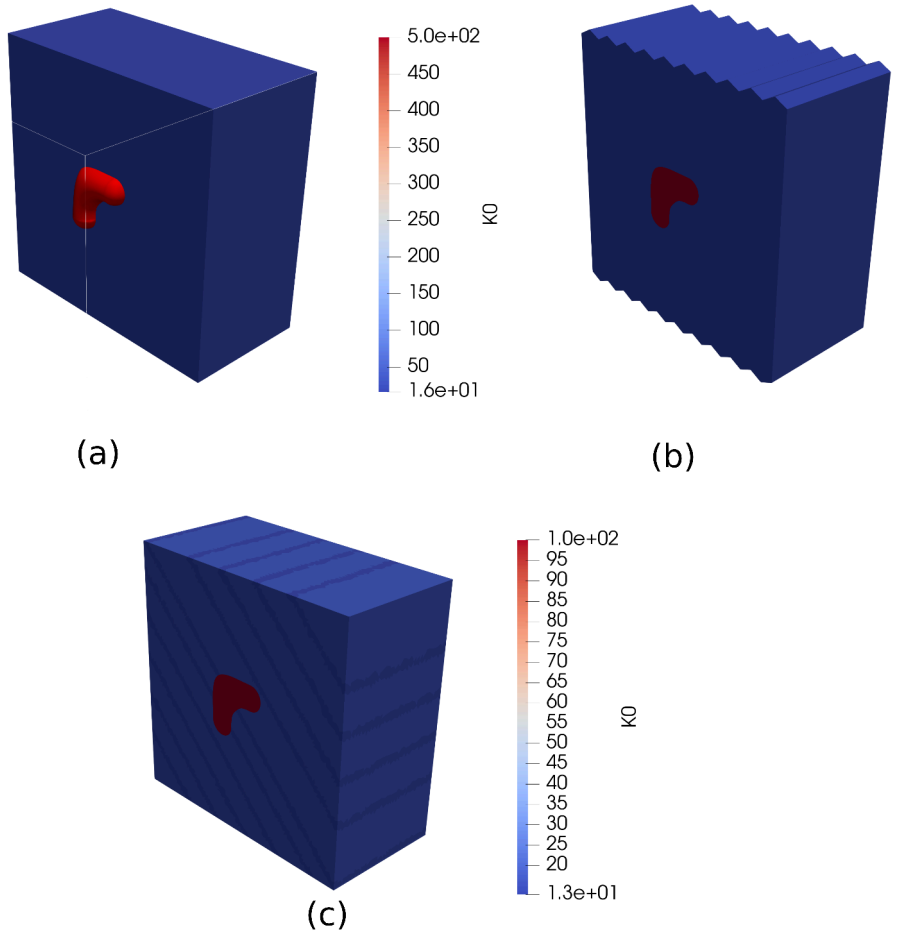

Figure 5.8: PDZ-CPFEM simulations set ups. (a) complete domain with the top and bottom boundaries as plane faces, (b) half domain restricting the deformation in the normal direction on the particle surface with the top and bottom boundaries as serrated faces and (c) half domain restricting the deformation in the normal direction on the particle surface with the top and bottom boundaries as plane faces, plus diagonal planes with lower $K0$ values in the domain.

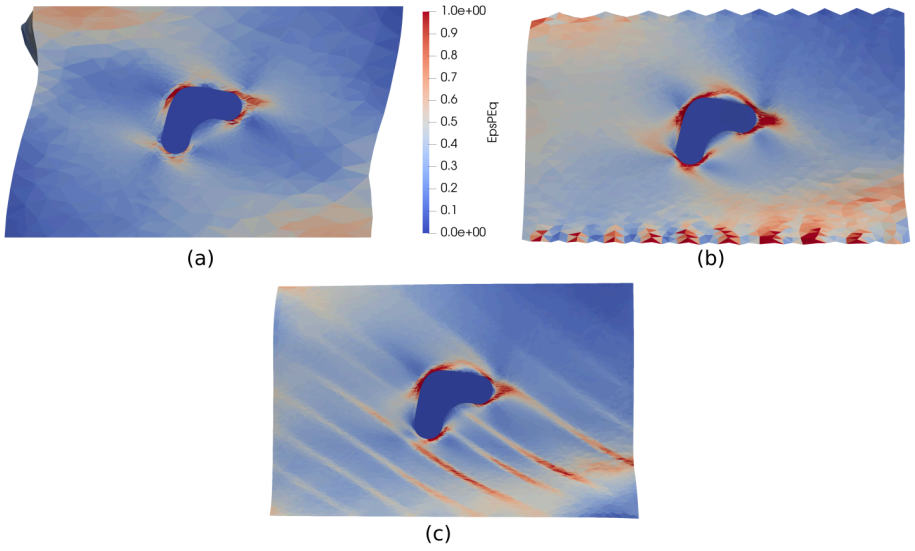

Figure 5.9: PDZ-CPFEM simulations results in terms of plastic deformation. (a) First set up, (b) third set and (c) fourth set up up.

The dislocation density comparison shows that: In all cases the dislocation density in most of the domain has reached the saturation value, preventing it to evolve any more. Comparing with the previous results the observed patterns are not exactly the same as the plastic deformation patterns since zones with deformation levels with $\epsilon_p >= 0.4$ show the dislocation saturation value, so the dislocation density maps are more homogeneous. However there are still zones around the particle low dislocation levels corresponding to the zones with the lower deformation levels. Thus the first case shows more zones with low dislocation density than the third case. While the fourth case, the zones with lower K_0 values also present high values of dislocation density.

The rotation maps show that: In all cases there are zones around the particle with positive rotation and negative rotations. The negative rotations are localized around the top and bottom zones the particle, while the positive rotations are localized in the front and back of the particle. When comparing with the experimental rotation maps the simulation patterns show a qualitative agreement with the experimental data, the differences observed are related to the differences in shape in the particle. Comparing the simulations cases, the results show that the first case show the lower rotation than the other two cases. Also, the fourth case shows that the zones with low $K0$ values distort the rotation patterns introducing behaviours that are not observed in the experimental data.

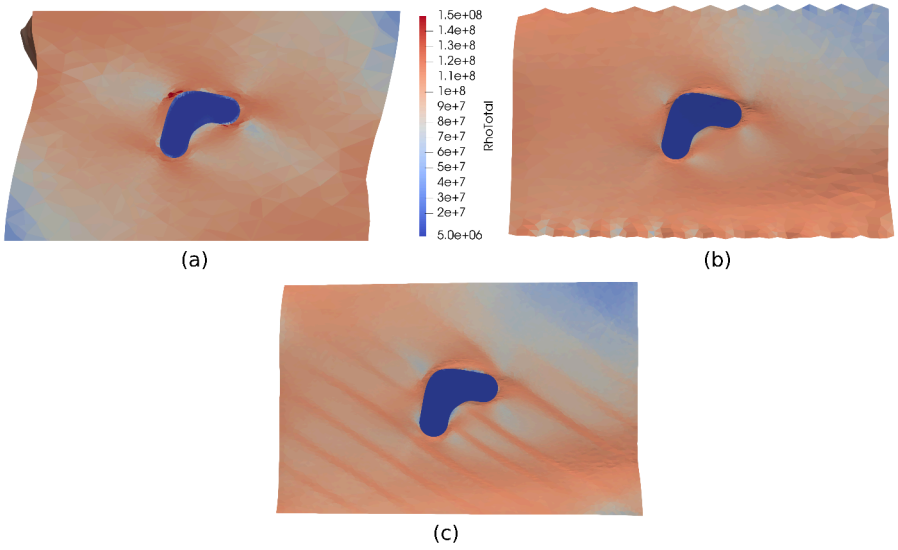

Figure 5.10: PDZ-CPFEM simulations results in terms of dislocation density. (a) First set up, (b) third set and (c) fourth set up up.

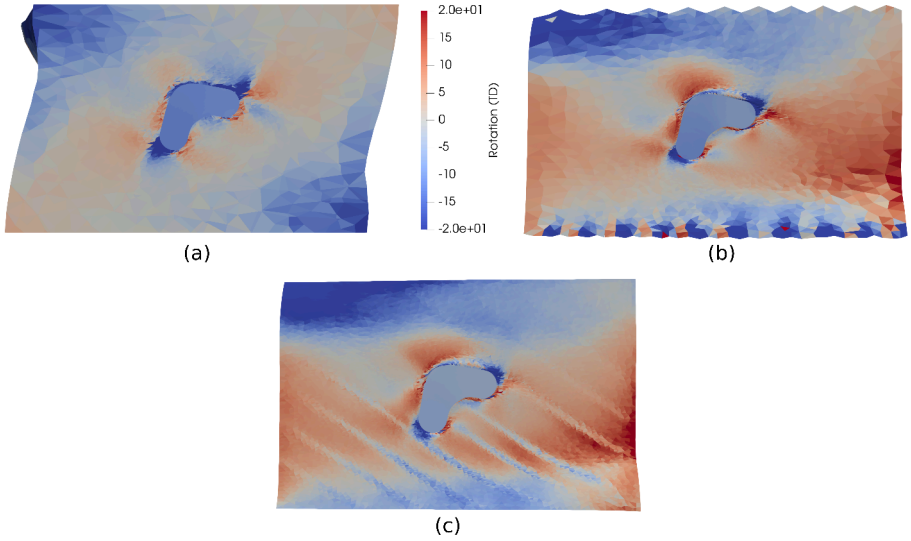

Figure 5.11: PDZ-CPFEM simulations results in terms of rotation (TD). (a) First set up, (b) third set and (c) fourth set up up.

The results show that the CPFEM framework is not able to completely

reproduce the PDZ observed in the experimental data, however some of the features are correctly reproduced. So, further improvements can be made: first, the flow rules and hardening rules used rely on important simplifications, one directly related to the deformation bands formation is the latent hardening due to slip system interaction that is not considered in the used hardening law. Second, the available experimental data is very limited, additional data is required to obtain a better representation of the particle shape in 3D, and enough tests to be able to calibrate and validate the CPFEM model. Such works are planned as perspectives of these works.

5.3 CDRX

In the proposed developments, so far only discontinuous dynamic recrystallization has been considered. Since in DDRX, clear stages of appearance and growth of recrystallized grains can be identified, it can be modeled by introducing recrystallized grains in the microstructure, as it has been done in this work. However this is not the case for continuous dynamic recrystallization (CDRX) mechanism. CDRX is a strain induced phenomena, that occurs by progressive rotations of subgrains with small grain boundary migration [1].

So, to model CDRX, it is necessary to considered how subgrain boundaries evolve as plastic deformation occurs. To incorporate subgrain boundary evolution in our LS framework, an initial approach is proposed in which subgrain boundaries are also represented by level set functions. The initial level sets functions that describe high angle grain boundaries (HAGB) are further subdivided using additional level set functions. Since both HAGB and low angle grain boundaries (LAGB) boundaries are described as LS functions, the difference in their behaviour will be determined by the grain boundary energy. To consider anisotropic grain boundary energy in the GBM calculation, the level set framework proposed by Fausty [38] is used. The grain boundary energy is calculated as function of misorientation using a Read–Shockley equation (described in chapter 1).

The main objective of the test is to observe how LAGB behave and if during deformation the increase in misorientation will lead to LAGB naturally evolving in HAGB. The initial test proposed considers a single crystal with subgrain boundaries described by level set functions, compressed at high temperature. Figure 5.12 shows the considered crystal with its subgrain boundaries, the color scale shows the KAM value, used to quantify the misorientation. For this initial test the material properties considered are the same of 304L steel, described in previous chapters. For the simulations only the CPFEM and subgrain boundary migration calculations are considered,

no recrystallized grains are introduced.

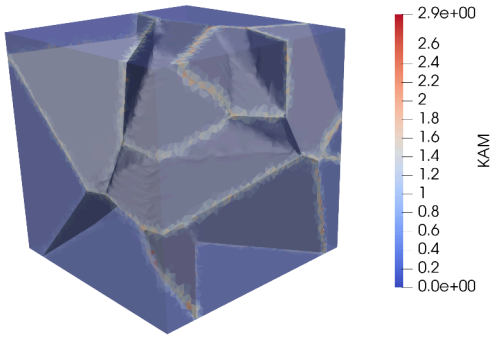

Figure 5.12: Single crystal with LS functions used to represent subgrain boundaries.

The crystal was deformed up to $\epsilon = 50\%$. Simulations were run considering heterogeneous grain boundary energy (misorientation dependence but not inclination one) and constant grain boundary energy. Figure 5.13 shows a side view of the deformed crystal for both cases. The color scales correspond to the subgrain sizes, which are calculated as function of the grain volume and the KAM values.

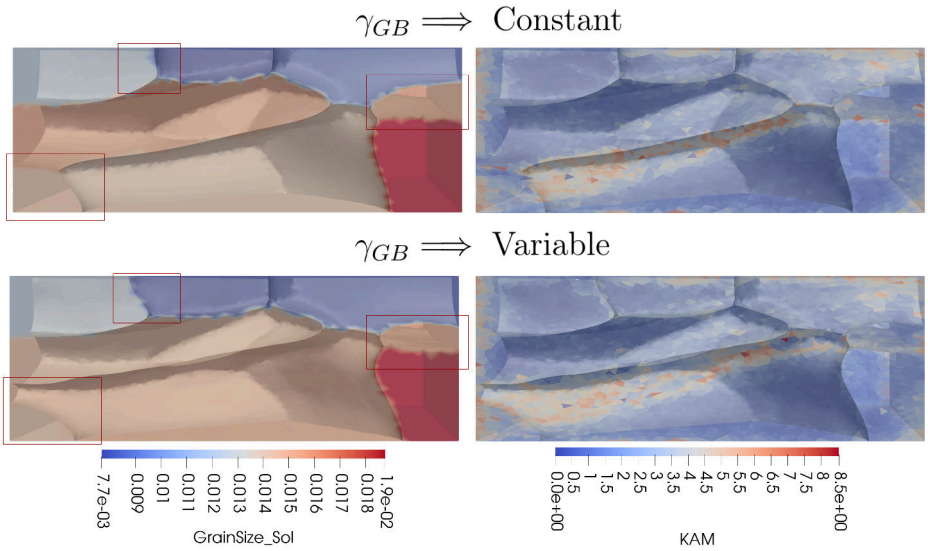

Figure 5.13: Side view of single crystal deformed at high temperature with LS functions representing subgrain boundaries. GBM calculated considering constant (top) and variable (bottom) subgrain boundary energy. Color bars indicate subgrain size (left) and KAM (right).

The results shows that in both cases the final grain sizes and KAM values are almost the same. However we can see clear differences in the curvatures of the subgrain boundaries between the two cases. Additionally the evolution of the KAM values clearly show a significant increase in misorientation along the subgrain boundaries. However, the increase in misorientation is not big enough to consider a new high angle grain boundary, but for this case the deformation level considered was not very high.

A second test was performed considering a bi-crystal with each grain subdivided into five LAGB. The initial properties of the bi-crystal were generated as: First the dislocation fields and orientation fields are generated considering only the HAGB, the orientations are generated to ensure a misorientation higher than 15° between them. Then a small variation between the subgrains is introduced, the variation is set to be smaller than the variation between different grains. Figure 5.14 shows the dislocation density field and the KAM field for the bi-crystal case.

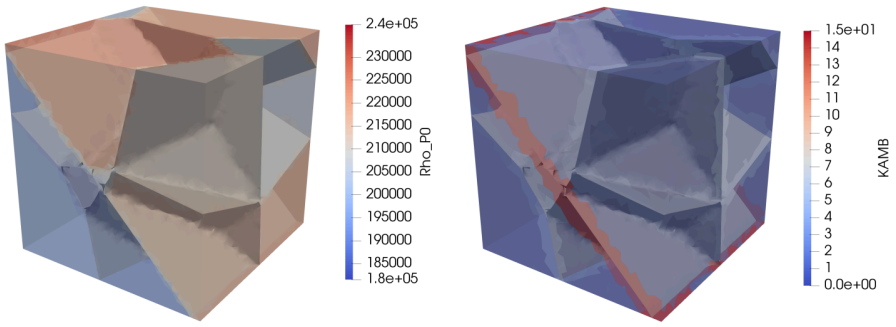

Figure 5.14: Dislocation density and KAM fields generated considering the LAGB subdivision.

The bi-crystal was subjected to compression at high temperature. As in the previous case, we only considered CPFEM and subgrains and grain boundary migration calculations, recrystallized grains are not introduced. The evolution of the KAM field is shown in figure 5.15. The results showed that the motion of the grain boundary is driven by the difference in size between the subgrain boundaries, leading to a fast disappearance of the smaller ones. Additionally, as in the previous, case the KAM value shows a clear increase in misorientation. However in this case the zone with the highest misorientation does not completely overlap with the locations of the zero-isovalues of the LS functions. This is an important limitation, as there is no

guarantee that the LS functions describing the subgrain boundaries will be located on the zones in the highest misorientation increases due to plastic deformation.

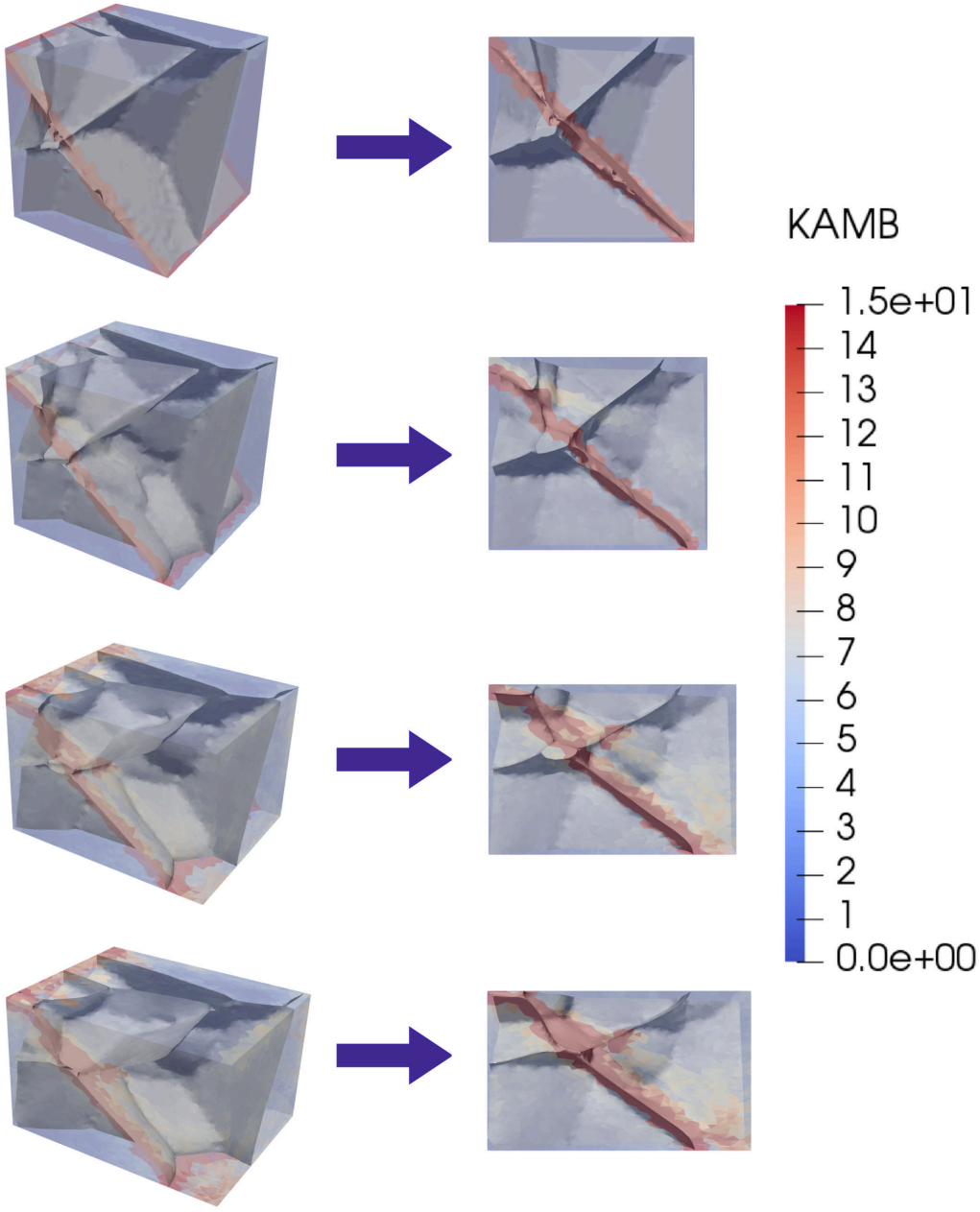

Figure 5.15: Evolution of the KAM field with the deformation of the domain. 3D view (left) and frontal view (right).

One alternative to overcome this is to include more subgrain boundaries, however this will also lead to a significant increase of the computational cost. A more efficient approach can be to not subdivide a grain from the beginning of the simulation but to do it only when the misorientation has reached a certain threshold, considering grain fragmentation. Further work must be performed to determine the best alternative, this initial test were only intended to illustrate a method proposed to describe CDRX by using CPFEM and LS-FEM.

5.4 VPSC

One of the main limitations of the proposed model remains the high computational cost of the simulation due to the CPFEM simulations, as discussed in chapter 4. As an alternative, a CP-Taylor approach was proposed. However, this approach consists in a strong simplification that does not consider grain interaction at all. An intermediate approach is the VPSC model [14, 26, 27, 28]. The VPSC model considers a visco-plastic approach in which the strain rate in an individual grain (r) is defined as:

$$\dot{\boldsymbol{\epsilon}}(r) = \sum_{\alpha} \boldsymbol{P}^{\alpha} \dot{\gamma}^{\alpha} \quad , \tag{5.2}$$

$$\dot{\gamma}^{\alpha} = \dot{\gamma}_0^{\alpha} \left(\frac{\boldsymbol{P}^{\alpha} : \boldsymbol{\sigma}(r)}{\tau_{\alpha}^{cr}} \right)^{n} \quad , \tag{5.3}$$

with $\boldsymbol{P}^{\alpha}$ the Schmidt tensor on the slip system α, $\dot{\gamma}^{\alpha}$ the slip rate on the slip system, $\dot{\gamma}_0^{\alpha}$ a reference slip rate, τ_{α}^{cr} the CCRS and $\boldsymbol{\sigma}(r)$ the Cauchy stress on the grain. In the VPSC formulation the relation between the stress and the strain inside the domain of a grain can be linearized as:

$$\dot{\boldsymbol{\epsilon}}(r) = \mathscr{M}(r) : \boldsymbol{\sigma}(r) + \dot{\boldsymbol{\epsilon}}_0(r) \quad , \tag{5.4}$$

with $\mathscr{M}(r)$ the viscoplastic compliance fourth order tensor with its inverse $\mathscr{L}(r) = \mathscr{M}^{-1}(r)$ and $\dot{\boldsymbol{\epsilon}}_0(r)$ the back-extrapolated term of the grain. In the VPSC formulation $\mathscr{M}(r)$ is defined from equations 5.2 and 5.3 as:

$$\mathscr{M}(r) = n\dot{\gamma}_0^{\alpha} \sum_{\alpha} \frac{\boldsymbol{P}^{\alpha} \otimes \boldsymbol{P}^{\alpha}}{\tau_{\alpha}^{cr}} \left(\frac{\boldsymbol{P}^{\alpha} : \boldsymbol{\sigma}(r)}{\tau_{\alpha}^{cr}} \right)^{n-1} \quad . \tag{5.5}$$

The same linearization is extended to the polycrystal medium level as:

$$\dot{\boldsymbol{E}} = \overline{\mathscr{M}} : \boldsymbol{\Sigma} + \dot{\boldsymbol{E}}_0 \quad , \tag{5.6}$$

with $\dot{\boldsymbol{E}}$ the macroscopic strain rate, $\boldsymbol{\Sigma}$ the macroscopic stress, $\overline{\mathscr{M}}$ the macroscopic viscoplastic compliance tensor and $\dot{\boldsymbol{E}}_0$ the macroscopic back-extrapolated term. Each grain is considered as an elliptical inclusion embedded inside the domain which causes distortions in the macroscopic strain rate $\tilde{\dot{\boldsymbol{\epsilon}}}(r)$ and stress fields $\tilde{\boldsymbol{\sigma}}(r)$:

$$\tilde{\dot{\boldsymbol{\epsilon}}}(r) = \dot{\boldsymbol{\epsilon}}(r) - \dot{\boldsymbol{E}} \ , \tag{5.7}$$

$$\tilde{\boldsymbol{\sigma}}(r) = \boldsymbol{\sigma}(r) - \boldsymbol{\Sigma} \ . \tag{5.8}$$

The distortions are related through the interaction tensor $\tilde{\mathscr{M}}$ as:

$$\tilde{\dot{\boldsymbol{\epsilon}}}(r) = -\tilde{\mathscr{M}} : \tilde{\boldsymbol{\sigma}}(r) \ , \tag{5.9}$$

$\tilde{\mathscr{M}}$ is calculated as function of the symmetric Eshelby tensor $\mathscr{S}$ as:

$$\tilde{\mathscr{M}} = (I - \mathscr{S})^{-1} : \mathscr{S} : \overline{\mathscr{M}} \ , \tag{5.10}$$

$$\mathscr{S} = sym\,(\mathscr{T}) : \overline{\mathscr{L}} \ , \tag{5.11}$$

with I the fourth order identity tensor, $\mathscr{T}$ the result of the green functions integration, that solve the mechanical equilibrium equations, over the domain of ellipsoidal grain (the derivation and integration procedure will be not be presented here) as (written in index notation for clarity):

$$\mathscr{T}_{klij} = \frac{abc}{4\pi} \int_0^{2\pi} \int_0^{\pi} \frac{\alpha_j \alpha_l A^{-1}_{ki}}{\left[[(a\alpha_1)^2 + (b\alpha_2)^2 + (c\alpha_3)^2]^{1/2} \right]^3} \sin\theta d\theta d\phi \ , \tag{5.12}$$

with θ and ϕ the spherical coordinates of the Fourier unit vector α; a, b and c the axis of the grain ellipsoid; $A_{ik} = \alpha_j \alpha_l \overline{\mathscr{L}}_{ijkl}$. From the interaction tensor $\tilde{\mathscr{M}}$ the localization tensors are defined as:

$$\mathscr{B}(r) = \left(\mathscr{M}(r) + \tilde{\mathscr{M}} \right)^{-1} : \left(\overline{\mathscr{M}} + \tilde{\mathscr{M}} \right) \ , \tag{5.13}$$

$$\boldsymbol{b}(r) = \left(\mathscr{M}(r) + \tilde{\mathscr{M}} \right)^{-1} \left(\dot{\boldsymbol{E}}_0 - \dot{\boldsymbol{\epsilon}}_0(r) \right) \ . \tag{5.14}$$

The interaction tensors define the localization equations that relate the macroscopic stress to the stress in the grain:

$$\boldsymbol{\sigma}(r) = \mathscr{B}(r) : \boldsymbol{\Sigma} + \boldsymbol{b}(r) \ . \tag{5.15}$$

The polycrystal model imposes the condition that the weighted average (represented by the symbols $\langle\ \rangle$) of the grains strain rates has to coincide with the macroscopic behaviour:

$$\dot{\boldsymbol{E}} = \langle \dot{\boldsymbol{\epsilon}}(r) \rangle \quad . \tag{5.16}$$

With this condition the macroscopic viscoplastic compliance tensor and the macroscopic back-extrapolated term are defined as, considering that all grains have the same shape:

$$\overline{\mathscr{M}} = \langle \mathscr{M}(r) : \mathscr{B}(r) \rangle \quad , \tag{5.17}$$

$$\dot{\boldsymbol{E}}_0 = \langle \mathscr{M}(r) : \boldsymbol{b}(r) + \dot{\boldsymbol{\epsilon}}_0(r) \rangle \quad , \tag{5.18}$$

and if the grains have different shapes, meaning that their corresponding Eshleby tensors are different:

$$\overline{\mathscr{M}} = \langle \mathscr{M}(r) : \mathscr{B}(r) \rangle : \langle \mathscr{B}(r) \rangle^{-1} \quad , \tag{5.19}$$

$$\dot{\boldsymbol{E}}_0 = \langle \mathscr{M}(r) : \boldsymbol{b}(r) + \dot{\boldsymbol{\epsilon}}_0(r) \rangle - \langle \mathscr{M}(r) : \mathscr{B}(r) \rangle : \langle \mathscr{B}(r) \rangle^{-1} : \langle \boldsymbol{b}(r) \rangle \quad . \tag{5.20}$$

The classical VPSC formulation does not consider elastic effects, the grain rotations and hardening are not considered in the calculation of stress, they are calculated only after the stress iteration is finished. To obtain an intermediate approach between the CP-Taylor and CPFEM approaches, we have tried to couple the CP library presented in chapter 2, with the VPSC approach. Since the CP library considers elastic effects and the effect of grain rotations and hardening in the stress calculation, the limitations previously mentioned can be overcome. Also, since the CP library has a modular structure the resulting code will be more versatile without a specific flow rule embedded in the formulation.

The proposed approach is described in the following algorithm. The stress calculation on each grain is calculated using the CP library described in chapter 2 and $\mathscr{M}(r) = \mathscr{L}^{-1}(r)$, with $\mathscr{L}(r) = \tilde{\mathscr{C}}_P$.

1. Assume Taylor approximation $\longrightarrow \dot{\boldsymbol{\epsilon}}(r) = \dot{\boldsymbol{E}}$

2. For all grains using the CP library calculate:

   - $\boldsymbol{\sigma}(r)$ and $\mathscr{M}(r)$

- The calculation also gives the new orientation and CRSS of the grains, however this values are not updated yet.

3. Approximate:

   - $\overline{\mathscr{M}} = \langle \mathscr{M}(r) \rangle$
   - $\dot{\boldsymbol{E}}_0 = \langle \dot{\boldsymbol{\epsilon}}_0(r) \rangle$

   (a) Calculate Eshelby tensor for all considered grain shapes

   - $\mathscr{T} \longrightarrow$ numerically integrate Eq. 5.12
   - $\mathscr{S} \longrightarrow$ compute Eq. 5.11

   (b) Compute $\tilde{\mathscr{M}} \longrightarrow$ Eq. 5.10

   (c) Compute $\mathscr{B}(r)$ and $\boldsymbol{b}(r) \longrightarrow$ Eq. 5.13 and 5.14

   (d) Recalculate $\overline{\mathscr{M}}$ and $\dot{\boldsymbol{E}}_0 \longrightarrow$ Eq. 5.17 and 5.18

   (e) Calculate change $\overline{\mathscr{M}}$ value $\triangle\overline{\mathscr{M}}$:

   - if $\triangle\overline{\mathscr{M}} < tol \longrightarrow$ continue
   - if $\triangle\overline{\mathscr{M}} > tol \longrightarrow$ return to step (a)

4. Compute $\boldsymbol{\Sigma} \longrightarrow$ Eq. 5.6

5. For all grains solve Eq. 5.9 for $\dot{\boldsymbol{\epsilon}}(r) \longrightarrow$ NR algorithm

   - Each NR iteration requires a calculation of the CP library

6. Calculate $\triangle\boldsymbol{\sigma}(r)$

7. Check conditions $\triangle\boldsymbol{\sigma}(r) < tol$ and $\boldsymbol{\Sigma} = \langle \boldsymbol{\sigma}(r) \rangle$

   - If conditions are full-filled, finish calculation and update state variables
   - If conditions are not full-filled return to step (3).

The code is currently in development and testing. The initial implementation is done however some convergence problems have not been solved yet, it constitutes another perspective of theses works.

5.5 Summary and Discussion

In this chapter, perspective works aimed to address some of the limitations of the current model were presented and explored:

First, the current nucleation criteria only describes necklace type nucleation and relies on criteria that only considers dislocation density. To discuss a more robust nucleation criteria, FEM plasticity models (including CPFEM) to study the PDZ present in PSN nucleation has been considered. Initial simulations were performed using a macroscopic visco-plasticity model to evaluate the capability of the FEM framework and the proposed approach, that represents the particle as a part of the domain with very high mechanical resistance. The macroscopic model results showed a qualitative reproduction of the PDZ zone with differentiate zones with high and low deformation levels, and zones with differentiate degrees of rotation. This initial approximation showed agreement with PDZ descriptions found in the literature, and served as an initial validation test of the used approach.

Further simulations were performed by using a CPFEM model, to try and reproduce experimental measurements of a PDZ found in the literature. The simulation results showed good agreement in reproducing the experimental rotation pattern around the particle. However, the simulations were not able to reproduce the deformation bands observed in experimental measurements, and the effect on them caused by the presence of the hard particle. The plastic deformation patterns along with the dislocation density distributions observed in the simulation results indicate that a more complex hardening law is required to better reproduce this behaviour and to consider particle size effect. Also further experimental information is required to better characterize the particle shape and to calibrate and validate the CPFEM model.

Second, the current framework only considers DDRX by introducing recrystallized grains according to discontinuous nucleation rate laws, but does not consider recrystallization by continuous subgrain rotation due to plastic deformation. To consider this phenomenom an initial approach was proposed that uses level set functions to describe not only HAGB but also LAGB. In this approach the grain boundary energy is defined according to the Read–Shockley equation and the formulation proposed by [38] is used, since it can consider heterogeneous grain boundary energy.

An initial test was performed considering the deformation of a bi-crystal. The results showed that the LAGB boundaries migration is mostly dependent on the initial size, leading to a quick reduction of the smaller LAGB. This behaviour is related to the material parameters and can be calibrated. The results also showed that, during the simulation the LAGB location does not correspond with zones were higher misorientation is developed. This is highly

dependant on the LAGB initial locations and increasing the number of LAGB can lead to better results, further tests must be performed.

Third, one of the main limitations of using CPFEM is the computational cost. On chapter 4 a simplified approach was proposed using the Taylor simplification along with crystal plasticity, however this is a strong simplification. An alternative is the VPSC formulation. Traditional VPSC formulations does not consider elasticity, and the hardening and rotation calculations are uncoupled from the stress evolution, they are only considered after the stress calculation is finished.

Thus, to propose an approach that does not include these limitations, a VPSC formulation based on the crystal plasticity formulation used in this work was implemented. Instead of using the traditional linearizations proposed in the VPSC formulation, the strain rate - stress relation is defined according to the tangent module described in chapter 2. Additionally the stress calculation for each grain is performed according to the CP algorithm described in chapter 2. However initial tests performed show convergence problems that need to be solved.

5.6 Résumé en Français

Dans ce chapitre, des perspectives visant à aborder certaines des limites du modèle actuel ont été présentées et explorées:

Premièrement, les critères de germination actuels ne décrivent que des modes de germination en collier et reposent sur des lois qui ne prennent en compte que la densité de dislocation. Pour proposer un critère de germination plus robuste, des modèles de plasticité FEM (dont CPFEM) pour étudier la germination aux bords des particules pourrait être investiguée. Des simulations initiales ont ainsi été réalisées à l'aide d'un modèle de viscoplastique macroscopique, pour évaluer la capacité du cadre FEM et l'approche proposée, qui représente la particule comme une partie du domaine à très haute résistance mécanique, à reproduire des modes de germination réalistes. Les résultats du modèle macroscopique ont montré une reproduction qualitative avec des zones différenciées avec des niveaux de déformation élevés et faibles et des zones avec des degrés de rotation différenciés. Cette première approximation a montré une concordance avec les descriptions trouvées dans la littérature, et a servi de test de validation initiale de l'approche utilisée.

D'autres simulations ont été effectuées en utilisant un modèle CPFEM, pour essayer de reproduire des mesures expérimentales d'une PDZ trouvée dans la littérature. Les résultats de la simulation ont montré un bon accord dans la reproduction du mode de rotation autour de la particule. Cependant, les simulations n'ont pas pu reproduire les bandes de déformation observées dans les mesures expérimentales, et l'effet sur celles-ci provoqué par la présence de la particule dure. Les modèles de déformation plastique ainsi que les distributions de densité de dislocation observées dans les résultats de la simulation, indiquent qu'une loi d'écrouissage plus complexe est nécessaire pour mieux reproduire ce comportement. Des informations expérimentales supplémentaires sont également nécessaires pour mieux caractériser la forme des particules et pour calibrer et valider le modèle CPFEM.

Deuxièmement, le cadre actuel ne considère la DRX qu'en introduisant des grains recristallisés selon les lois de la vitesse de germination, mais ne considère pas la recristallisation par rotation continue des grains due à la déformation plastique. Pour considérer ce phénomène, une première approche a été proposée qui utilise des fonctions LS pour décrire non seulement les interfaces fortement désorientés (HAGB) mais également les faiblement désorientés (LAGB). Dans cette approche, l'énergie des joints de grains est définie selon l 'équation de Read - Shockley et la formulation proposée par [38] est utilisées. L'idée étant finalement de pouvoir à l'avenir considérer les mécanismes de germination continue.

Un premier test a ete realise en considérant la déformation d'un bicristal

constitué de sous-grains. Les résultats initiaux montrent que l'emplacement des LAGB ne correspond pas aux zones ou une plus forte désorientation s'installe lors de la déformation. Ce sujet doit clairement être investigué plus avant afin d'améliorer la représentativité des critères de germination de notre modèle.

Troisièmement, l'une des principales limites des calculs CPFEM reste leur coût de calcul. Au chapitre 4, une approche simplifiée a été proposée en utilisant la simplification de Taylor dans la plasticité cristalline, il s'agit évidemment d'une simplification forte. Une alternative est la formulation VPSC. Les formulations VPSC traditionnelles ne prennent pas en compte l'élasticité, et les calculs d'écrouissage et de rotation sont découplés de l'évolution des contraintes, ils ne sont pris en compte qu'une fois le calcul des contraintes terminé. Ainsi, pour proposer une approche qui n'inclut pas ces limitations, une formulation VPSC basée sur la formulation en plasticité cristalline utilisée dans ce travail a été mise en œuvre. Au lieu d'utiliser les linéarisations traditionnelles proposées dans la formulation VPSC, la relation vitesse de déformation - contrainte est définie selon le module tangent décrit au chapitre 2. De plus, le calcul des contraintes pour chaque grain est effectué selon l'algorithme CP décrit au chapitre 2. Cependant les premiers tests effectués montrent des problèmes de convergence qui doivent encore être résolus.

Chapter 6

Conclusions

Context

The main objective of this work was the development of a new DDRX model that provides a better description of the local anisotropic behaviour and evolution of materials subjected to hot forming operations, than the ones provided by the models currently found in the literature.

Among the different type of DRX models found in the literature, only full field models are able to describe local behaviour since they explicitly represent the microstructure. However most full field models present important limitations when dealing with high deformation levels as most of them require uniform structure grids. Additionally, due to the computational cost and difficulties to represent 3D grains evolution, several models rely on 2D simplifications.

In the context of the DIGIMU project developed at CEMEF, in the PhD work of [6] a 3D DRX model was proposed. This model is based on the Level-Set method in a finite element context. The main advantages of the LS framework are: Its versatility to include several microstructural mechanisms in a robust numerical framework; the implicit representation of grain boundaries that allows it to represent complex 3D shapes and their evolution even at high deformation levels. By coupling the LS framework with a remeshing framework, also developed in CEMEF, the developed model is capable to simulate DDRX up to high deformation levels.

This DDRX model includes important simplifications. One of them is the description of plastic deformation. Plastic deformation is modeled according to a phenomenological law, that does not consider the grains orientations nor their crystal structure. Thus, all grains in the model deform equally so no anisotropy is considered. To propose a more accurate model, in this work we

coupled the LS-FEM model with a compatible CPFEM model, to perform 3D full field DRX simulations up to high deformation levels.

Conclusions and achievements

In the first chapter the DDRX models proposed in the literature were reviewed, focusing on models that propose improved descriptions of plastic deformation. This review showed that CP formulations are the best available alternative to describe the plastic behaviour in the context of DDRX mechanisms and several models that incorporate CP formulations in the context of DDRX have been proposed in the literature. However, these models present several limitations in describing high deformation levels. This aspect explains the interest and relevance of the model proposed in this work.

The first step considered in order to build the new DDRX model was the development of a crystal plasticity library. The library was developed as a versatile tool. The code facilitates the inclusion of different behaviour laws, can be used by itself or with a FEM solver. The developed library has been used in this work to model the behaviour of an Al alloy and 304L steel, both as material points simulations and coupled with FEM. It has also been used in the work of [168] to model the behaviour of olivine crystals.

In the library, an alternative method to the commonly used Voigt notation for handling tensorial quantities was implemented. This method, which derived from a particular tensorial base, simplifies and reduces the computational cost of the tensorial operations required in CP calculation. From this work, a modification to the classical mixed velocity pressure finite element formulation was proposed, that allows to account for the non isotropic compressiblity [169].

After the CP library was developed and validated, the CPFEM model was coupled with the LS-FEM method for GBM and phenomenological laws. By including the CP model, not only a better description of the plastic deformation phenomena is obtained, but the input data for the GBM and nucleation models are also improved. To couple the models, a coupling algorithm was developed. The coupling algorithm includes an appropriate interpolation scheme to transfer the information from the P0 fields considered in the CPFEM model to the P1 fields considered in the LS-FEM model and back. This strategy ensures a coupling of the models in which the effect of all different phenomena are considered in all the models. This aspect is indeed a limitation found in several of the DDRX-CP models available in the literature where the effect of nucleation and GBM process are generally not considered in CP calculations. Another advantage of the proposed coupled model with

respect to the models found in the literature is the use of a single mesh that deforms according to the CP calculations. This facilitates the interpolation process, reduces the computational cost and memory requirements, and does not present problems of coherence between the calculations' domains due to the differences in the way that each mesh is deformed.

The development of coupling algorithm included a detailed sensibility analysis to determine the numerical parameters that ensure convergence of the results and minimize the computational cost. The results showed that: In order to ensure convergence and minimize the computational error, different time steps were required. Thus, the CPFEM iterations are subdivided into smaller time steps. Similar strategies are reported in the literature. In addition, the time step for the CPFEM calculations is adapted dynamically during the simulation. This prevents convergence problems in the CPFEM calculations after nucleation events, this problem is also reported in the models found in the literature. The analysis also showed that with the inclusion of the CPFEM model and the use of mesh size adaptation, it is not necessary to include an artificial increase in nucleus size to prevent the collapse of recrystallized grains, as considered in the model of [6].

Once the numerical parameters were defined, additional test were performed regarding the position of recrystallized grains and the calculation of the grains energy by the accumulation of dislocations. The tests regarding the recrystallized grains position showed that: Due to the continuous deformation and continuous appearance of grains, the nucleated grains position has limited influence on final results. However the necklace and bulk cases showed to be the more favorable for recrystallized grains grow, when compared with criteria that consider maximal dislocation density and/or its gradient. The main factor affecting the evolution of the recrystallized grains is how clustered they are. The tests regarding the calculation of the grains accumulated energy showed that: the difference in the results does not justify the increase in computational cost required by the heterogeneous energy and energy per interface approaches.

The proposed new CPFEM-LS DDRX model was compared with experimental data. First the material parameters K_1, K_2 and K_g, were calibrated for a range of strain rates between $0.008-0.1$ $(1/s)$ and temperatures between $1273-1373$ K. The calibration procedure proposed by [6] was modified to consider the effect of the parameters K_1, K_2 on the microstructural evolution. This modification was necessary as considering only the mechanical behaviour can lead to errors in the definition of recrystallized size, that lead to non-physical results.

The model results compared to experimental showed good agreement for the average behaviour in the range of temperatures and strain rates consid-

ered. However the grain size distribution showed that the rate of growth of recrystallized grains is underestimated. Experimental measurements show percentages of recrystallized grains with bigger sizes than the ones seen in the simulation results. Since this behaviour is related to several factors like the dislocation density evolution, the grain boundary mobility and grain boundary energy, more detailed studies into these factors must be performed specially considering that these variables are defined according to simple phenomenological laws.

The model results also showed that even with CPFEM calculations, the dislocation density field is not that heterogeneous, as when recrystallization starts, most of the domain has reached the maximal dislocation density value. Only zones affected by recrystallization in which the recrystallization density is reinitialized are constantly evolving. The rate at which this zones hardens depends on their orientation and neighbours. This behaviour is of course dependent of the chosen hardening law, which is an important simplification. By considering these aspects, a possible simplification of the model was proposed, by replacing the CPFEM model with a CP Taylor model. With the CP Taylor model, the interactions between grains are not considered, however the effect of the crystal structure and orientation are still taken into account. Comparisons of DRX simulations results were performed using the phenomenological law, the CP Taylor model and the CPFEM model.

The results showed significant difference in the recrystallization dynamics when using the phenomenological law due to the accelerated hardening, while the CPFEM and CP Taylor showed similar results. In terms of computational cost the increase in computational time from the phenomenological model to CP Taylor model is small. The CPFEM model model on the other hand implies a significant increase in computational cost. The similarity of the results between the CPFEM model and the CP Taylor model is caused in part that much of the information provided by the CPFEM model, the orientations evolution, is not considered, and due to the behaviour of dislocation density field that depends on the chosen hardening law.

The presented coupled model constitutes a good first approach to improve dynamic recrystallization modeling and can serve as a reference to evaluate simplifications and assumptions. For example, with the current formulation for an industrial context, the CP-Taylor model is a viable alternative to improve the plastic deformation definition in the DIGIMU software framework that would not cause a significant increase in the computational cost.

Additional perspectives

The current framework still includes significant simplifications, some of them derived from the phenomenological laws used. These simplifications cause that several of the additional data obtained by using CPFEM, are not considered. Improvements are required to fully account for the additional information obtained by incorporating CPFEM. These simplifications are:

- The CP hardening rule currently used that was adopted from previous work [6]. This law defines the evolution of the dislocation density considering only two terms, does not consider interaction between slip systems, and considers a single critical resolved shear stress for all slip systems. In chapter 2 several alternatives were described, the main difficulty with the implementation of a new law is the determination of the different parameters, specially for complex laws.

- The grain boundary energy defined as homogeneous and independent of the misorientation. This simplification does not allow the consideration of twin boundaries, limitation that was discussed in chapter 4. Integrating the work of [38, 170] to improve the grain boundary energy definition is an interesting perspective that has been initially explored in chapter 5.

- The grain boundary mobility is also defined as homogeneous, does not consider anisotropic behaviour and is calculated according to an Arrhenius law. The PhD work of [171] constitutes a interesting perspective in improving this definition.

Bibliography

[1] A. D. Rollett, G. S. Rohrer, F. J. Humphreys, Recrystallization and related annealing phenomena, 3rd Edition, Elsevier, 2017.

[2] R. D. Doherty, D. A. Hughes, F. J. Humphreys, J. J. Jonas, D. Juul Jensen, M. E. Kassner, W. E. King, T. R. McNelley, H. J. McQueen, A. D. Rollett, Current issues in recrystallization: A review, Materials Science and Engineering A 238 (1997) 219–274. doi:10.1016/S0921-5093(97)00424-3.

[3] T. Sakai, A. Belyakov, R. Kaibyshev, H. Miura, J. J. Jonas, Dynamic and post-dynamic recrystallization under hot, cold and severe plastic deformation conditions, Progress in Materials Science 60 (2014) 130–207. doi:10.1016/j.pmatsci.2013.09.002.

[4] Mines ParisTech, Cemef - Centre de mise en forme des matériaux (2020).
URL `https://www.cemef.mines-paristech.fr/`

[5] Mines ParisTech, The Digimu ANR Industrial Chair (2020).
URL `https://chaire-digimu.cemef.mines-paristech.fr/`

[6] L. Maire, Full field and mean field modeling of dynamic and post-dynamic recrystallization in 3D. Application to 304L steel, Ph.D. thesis, MINES ParisTech (2018).

[7] K. Huang, R. E. Logé, A review of dynamic recrystallization phenomena in metallic materials, Materials and Design 111 (2016) 548–574. doi:10.1016/j.matdes.2016.09.012.

[8] L. Madej, M. Sitko, M. Pietrzyk, Perceptive comparison of mean and full field dynamic recrystallization models, Archives of Civil and Mechanical Engineering 16 (4) (2016) 569–589. doi:10.1016/j.acme.2016.03.010.

[9] H. Hallberg, Approaches to modeling of recrystallization, Metals 1 (2011) 16–48. doi:10.3390/met1010016.

[10] D. Hull, D. Bacon, Introduction to Dislocations, 4th Edition, Butterworth-Heinemann, 2001.

[11] H. Resk, Finite element modelling of grain-scale heterogeneities in polycrystalline aggregates, Ph.D. thesis, MINES ParisTech (2010).

[12] M. Ohring, Engineering Materials Science, Academic Press, 1995. doi:10.1016/B978-012524995-9/50031-3.

[13] T. Sakai, J. J. Jonas, Overview no. 35 Dynamic recrystallization: Mechanical and microstructural considerations, Acta Metallurgica 32 (1984) 189–209. doi:10.1016/0001-6160(84)90049-X.

[14] U. Kocks, C. Tome, H. Wenk, Texture and Anisotropy, Cambridge University Press, 2000.

[15] E. Schmid, W. Boas, Kristallplastizität, Springer Verlag, 1935.

[16] F. Roters, P. Eisenlohr, L. Hantcherli, D. Tjahjanto, T. Bieler, D. Raabe, Overview of constitutive laws, kinematics, homogenization and multiscale methods in crystal plasticity finite-element modeling: Theory, experiments, applications, Acta Materialia 58 (4) (2010) 1152–1211. doi:10.1016/J.ACTAMAT.2009.10.058.

[17] A. M. Habraken, Modelling the plastic anisotropy of metals, Archives of Computational Methods in Engineering 11 (1) (2004) 3–96. doi:10.1007/BF02736210.

[18] G. Sachs, Zur ableitung einer fliessbedingung, Zeitschrift des Vereins deutscher Ingenieure 72 (1928) 734–736.

[19] G. Taylor, Plastic Strain in Metals, Journal of the Institute of Metals 62 (1938) 307–324.

[20] H. Honeff, H. Mecking, A method for determination of active slip systems and orientation changes during single crystal deformation, Proceedings of the 5th meeting, Textures of Materials, Aachen 8 (1998) 265–275.

[21] U. Kocks, G. Canova, How Many Slip Systems and Which? Deformation of Polycrystals, Tech. rep., Riso National Laboratory (1981).

[22] J. Hirsch, K. Lücke, Overview no. 76: Mechanism of deformation and development of rolling textures in polycrystalline f.c.c. metals—II. Simulation and interpretation of experiments on the basis of Taylor-type theories, Acta Metallurgica 36 (1988) 2883–2904. doi:10.1016/0001-6160(88)90173-3.

[23] P. Van Houtte, L. Delannay, I. Samajdar, Quantitative Prediction of Cold Rolling Textures in Low-Carbon Steel by Means of the Lamel Model, Textures and Microstructures 31 (1999) 109–149. doi:10.1155/tsm.31.109.

[24] P. Van Houtte, L. Delannay, S. Kalidindi, Comparison of two grain interaction models for polycrystal plasticity and deformation texture prediction, International Journal of Plasticity 18 (3) (2002) 359–377. doi:10.1016/S0749-6419(00)00102-9.

[25] P. Van Houtte, S. Li, M. Seefeldt, L. Delannay, Deformation texture prediction: from the Taylor model to the advanced Lamel model, International Journal of Plasticity 21 (2005) 589–624. doi:10.1016/j.ijplas.2004.04.011.

[26] A. Molinari, G. Canova, S. Ahzi, A self consistent approach of the large deformation polycrystal viscoplasticity, Acta Metallurgica 35 (12) (1987) 2983–2994. doi:10.1016/0001-6160(87)90297-5.

[27] R. Lebensohn, C. Tomé, A self-consistent anisotropic approach for the simulation of plastic deformation and texture development of polycrystals: Application to zirconium alloys, Acta Metallurgica et Materialia 41 (9) (1993) 2611–2624. doi:10.1016/0956-7151(93)90130-K.

[28] S.-B. Lee, R. A. Lebensohn, A. D. Rollett, Modeling the viscoplastic micromechanical response of two-phase materials using Fast Fourier Transforms, International Journal of Plasticity 27 (5) (2011) 707–727. doi:10.1016/J.IJPLAS.2010.09.002.

[29] J. Eshelby, The determination of the elastic field of an ellipsoidal inclusion, and related problems, In Proceedings - Royal Society of London A. Mathematical and physical sciences 241 (1957) 376–396.

[30] S. Kalidindi, C. Bronkhorst, L. Anand, Crystallographic texture evolution in bulk deformation processing of FCC metals, Journal of the Mechanics and Physics of Solids 40 (1992) 537–569. doi:10.1016/0022-5096(92)80003-9.

[31] P. Bate, Modelling deformation microstructure with the crystal plasticity finite element method, Philosophical Transactions of the Royal Society A: Mathematical, Physical and Engineering Sciences 357 (1999) 1589–1601. doi:10.1098/rsta.1999.0391.

[32] A. Arsenlis, D. Parks, Modeling the evolution of crystallographic dislocation density in crystal plasticity, Journal of the Mechanics and Physics of Solids 50 (9) (2002) 1979–2009. doi:10.1016/S0022-5096(01)00134-X.

[33] L. Delannay, P. Jacques, S. Kalidindi, Finite element modeling of crystal plasticity with grains shaped as truncated octahedrons, International Journal of Plasticity 22 (10) (2006) 1879–1898. doi:10.1016/J.IJPLAS.2006.01.008.

[34] R. Lebensohn, N-site modeling of a 3D viscoplastic polycrystal using Fast Fourier Transform, Acta Materialia 49 (14) (2001) 2723–2737. doi:10.1016/S1359-6454(01)00172-0.

[35] R. Lebensohn, R. Brenner, O. Castelnau, A. D. Rollett, Orientation image-based micromechanical modelling of subgrain texture evolution in polycrystalline copper, Acta Materialia 56 (15) (2008) 3914–3926. doi:10.1016/J.ACTAMAT.2008.04.016.

[36] P. Eisenlohr, M. Diehl, R. Lebensohn, F. Roters, A spectral method solution to crystal elasto viscoplasticity at finite strains, International Journal of Plasticity 46 (2013) 37–53. doi:10.1016/j.ijplas.2012.09.012.

[37] T. Read, W. Shockley, Dislocation models of crystal grain boundaries, Physical Review 78 (1950) 275 – 289.

[38] J. Fausty, N. Bozzolo, D. Pino Muñoz, M. Bernacki, A novel level-set finite element formulation for grain growth with heterogeneous grain boundary energies, Materials and Design 160 (2018) 578–590. doi:10.1016/j.matdes.2018.09.050.

[39] J. Fausty, N. Bozzolo, M. Bernacki, A 2D level set finite element grain coarsening study with heterogeneous grain boundary energies, Applied Mathematical Modelling 78 (2020) 505–518. doi:10.1016/j.apm.2019.10.008.

[40] J. Zhang, W. Ludwig, Y. Zhang, H. H. B. Sørensen, D. J. Rowenhorst, A. Yamanaka, P. W. Voorhees, H. F. Poulsen, Grain boundary mobilities in polycrystals, Acta Materialia 191 (2020) 211 – 220. doi:10.1016/j.actamat.2020.03.044.

[41] A. Bhattacharya, Y.-F. Shen, C. M. Hefferan, S. F. Li, J. Lind, R. M. Suter, G. S. Rohrer, Three-dimensional observations of grain volume changes during annealing of polycrystalline ni, Acta Materialia 167 (2019) 40 – 50. doi:10.1016/j.actamat.2019.01.022.

[42] J. Han, S. L. Thomas, D. J. Srolovitz, Grain-boundary kinetics: A unified approach, Progress in Materials Science 98 (2018) 386 – 476. doi:10.1016/j.pmatsci.2018.05.004.

[43] K. Chen, J. Han, D. Pan, J. Srolovitz, The grain boundary mobility tensor, Proceedings of the National Academy of Sciences 117 (2020) 4533–4538. doi:10.1073/pnas.1920504117.

[44] F. Montheillet, O. Lurdos, G. Damamme, A grain scale approach for modeling steady-state discontinuous dynamic recrystallization, Acta Materialia 57 (2009) 1602–1612. doi:10.1016/j.actamat.2008.11.044.

[45] A. Yoshie, H. Morikawa, Y. Onoe, K. Itoh, Formulation of static recrystallization of austenite in hot rolling process of steel plate, Transactions of the Iron and Steel Institute of Japan 27 (1987) 425–431. doi:10.2355/isijinternational1966.27.425.

[46] U. F. Kocks, Laws for Work-Hardening and Low-Temperature Creep, ASME Journal of Engineering Materials and Technology 98 (1976) 76–85.

[47] H. Mecking, U. F. Kocks, Kinetics of flow and strain-hardening, Acta Metallurgica 29 (1981) 1865–1875. doi:10.1016/0001-6160(81)90112-7.

[48] G. Gottstein, L. Schvindlerman, Grain Boundary Migration in Metals, 2nd Edition, CRC Press: Boca Raton, 2010.

[49] J. Burke, D. Turnbull, Recrystallization and grain growth, Progress in Metal Physics 3 (1952) 220 – 292. doi:10.1016/0502-8205(52)90009-9.

[50] J. Christian, The Theory of Transformations in Metals and Alloys, Pergamon, 2002.

[51] W. Roberts, B. Ahlblom, A nucleation criterion for dynamic recrystallization during hot working, Acta Metallurgica 26 (5) (1978) 801–813. doi:10.1016/0001-6160(78)90030-5.

[52] P. Peczak, M. J. Luton, The effect of nucleation models on dynamic recrystallization: I. Homogeneous stored energy distribution, Philosophical Magazine B 68 (1) (1993) 115–144. doi:10.1080/13642819308215285.

[53] P. Peczak, M. J. Luton, The effect of nucleation models on dynamic recrystallization ii. heterogeneous stored-energy distribution, Philosophical Magazine B 70 (4) (1993) 817–849. doi:10.1080/01418639408240254.

[54] C. Roucoules, M. Pietrzyk, P. Hodgson, Analysis of work hardening and recrystallization during the hot working of steel using a statistically based internal variable model, Materials Science and Engineering: A 339 (2003) 1 – 9. doi:10.1016/S0921-5093(02)00120-X.

[55] P. Bernard, S. Bag, K. Huang, R. Logé, A two-site mean field model of discontinuous dynamic recrystallization, Materials Science and Engineering A 528 (2011) 7357–7367. doi:https://doi.org/10.1016/J.MSEA.2011.06.023.

[56] H. Li, X. Sun, H. Yang, A three-dimensional cellular automata-crystal plasticity finite element model for predicting the multiscale interaction among heterogeneous deformation, DRX microstructural evolution and mechanical responses in titanium alloys, International Journal of Plasticity 87 (2016) 154–180. doi:10.1016/j.ijplas.2016.09.008.

[57] T. O. Saetre, O. Hunderi, E. Nes, Computer simulation of primary recrystallisation microstructures: The effects of nucleation and growth kinetics, Acta Metallurgica 34 (6) (1986) 981–987. doi:10.1016/0001-6160(86)90207-5.

[58] K. Marthinsen, O. Lohne, E. Nes, The development of recrystallization microstructures studied experimentally and by computer simulation, Acta Metallurgica 37 (1) (1989) 135–145. doi:10.1016/0001-6160(89)90273-3.

[59] T. Furu, K. Marthinsen, E. Nes, Modelling recrystallisation, Materials Science and Technology 6 (11) (1990) 1093–1102. doi:10.1179/mst.1990.6.11.1093.

[60] A. Kolmogorov, On the Statistical Theory of Crystallization of Metals, Izv. Akad. Nauk SSSR, Ser. Mat. 3 (1937) 355–359.

[61] M. Avrami, Kinetics of Phase Change. I General Theory, The Journal of Chemical Physics 12 (1939) 1103–1112. doi:10.1063/1.1750380.

[62] W. Johnson, R. Mehl, Reaction Kinetics in Processes of Nucleation and Growth, Transactions of the American Institute of Mining and Metallurgical Engineers 135 (1939) 416–442.

[63] D. G. Cram, H. S. Zurob, Y. J. Brechet, C. R. Hutchinson, Modelling discontinuous dynamic recrystallization using a physically based model for nucleation, Acta Materialia 57 (2009) 5218–5228. doi:10.1016/j.actamat.2009.07.024.

[64] D. G. Cram, X. Y. Fang, H. S. Zurob, Y. J. Bréchet, C. R. Hutchinson, The effect of solute on discontinuous dynamic recrystallization, Acta Materialia 60 (2012) 6390–6404. doi:10.1016/j.actamat.2012.08.021.

[65] O. Beltran, K. Huang, R. Logé, R. Loge, A mean field model of dynamic and post-dynamic recrystallization predicting kinetics, grain size and flow stress, Computational Materials Science 102 (2015) 293–303. doi:10.1016/J.COMMATSCI.2015.02.043.

[66] L. Maire, J. Fausty, M. Bernacki, N. Bozzolo, P. De Micheli, C. Moussa, A new topological approach for the mean field modeling of dynamic recrystallization, Materials and Design 146 (2018) 194–207. doi:10.1016/j.matdes.2018.03.011.

[67] R. B. Potts, C. Domb, Some generalized order-disorder transformations, Mathematical Proceedings of the Cambridge Philosophical Society 48 3 (1952) 106. doi:10.1017/S0305004100027419.

[68] J. Li, H. Xu, T. T. Mattila, J. K. Kivilahti, T. Laurila, M. Paulasto-Kröckel, Simulation of dynamic recrystallization in solder interconnections during thermal cycling, Computational Materials Science 50 (2010) 690–697. doi:10.1016/j.commatsci.2010.09.035.

[69] A. D. Tutcuoglu, A. Vidyasagar, K. Bhattacharya, D. M. Kochmann, Stochastic modeling of discontinuous dynamic recrystallization at finite strains in hcp metals, Journal of the Mechanics and Physics of Solids 122 (2019) 590–612. doi:10.1016/j.jmps.2018.09.032.

[70] F. Chen, K. Qi, Z. Cui, X. Lai, Modeling the dynamic recrystallization in austenitic stainless steel using cellular automaton method, Computational Materials Science 83 (2014) 331–340. doi:10.1016/j.commatsci.2013.11.029.

[71] W. Chuan, Y. He, L. H. Wei, Modeling of discontinuous dynamic recrystallization of a near-α titanium alloy IMI834 during isothermal hot compression by combining a cellular automaton model with a crystal plasticity finite element method, Computational Materials Science 79 (2013) 944–959. doi:10.1016/j.commatsci.2013.08.004.

[72] E. Popova, Y. Staraselski, A. Brahme, R. K. Mishra, K. Inal, Coupled crystal plasticity - Probabilistic cellular automata approach to model dynamic recrystallization in magnesium alloys, International Journal of Plasticity 66 (2015) 85–102. doi:10.1016/j.ijplas.2014.04.008.

[73] L. Madej, M. Sitko, A. Legwand, K. Perzynski, K. Michalik, Development and evaluation of data transfer protocols in the fully coupled random cellular automata finite element model of dynamic recrystallization, Journal of Computational Science 26 (2018) 66–77. doi:10.1016/j.jocs.2018.03.007.

[74] L. A. Barrales Mora, 2D vertex modeling for the simulation of grain growth and related phenomena, Mathematics and Computers in Simulation 80 (2010) 1411–1427. doi:10.1016/j.matcom.2009.08.005.

[75] Y. Mellbin, H. Hallberg, M. Ristinmaa, An extended vertex and crystal plasticity framework for efficient multiscale modeling of polycrystalline materials, International Journal of Solids and Structures 125 (2017) 150–160. doi:10.1016/j.ijsolstr.2017.07.009.

[76] B. Merriman, J. K. Bence, O. S. J., Motion of Multiple Junctions: A Level Set Approach, Journal of Computational Physics 112 (1994) 334–363. doi:10.1006/jcph.1994.1105.

[77] M. Bernacki, Y. Chastel, T. Coupez, R. Logé, Level set framework for the numerical modelling of primary recrystallization in polycrystalline materials, Scripta Materialia 58 (2008) 1129–1132. doi:10.1016/J.SCRIPTAMAT.2008.02.016.

[78] M. Bernacki, R. Logé, T. Coupez, Level set framework for the finite-element modelling of recrystallization and grain growth in polycrystalline materials, Scripta Materialia 64 (2011) 525–528. doi:10.1016/J.SCRIPTAMAT.2010.11.032.

[79] L. Maire, B. Scholtes, C. Moussa, N. Bozzolo, D. Pino Muñoz, A. Settefrati, M. Bernacki, Modeling of dynamic and post-dynamic recrystallization by coupling a full field approach to phe-

nomenological laws, Materials and Design 133 (2017) 498–519. doi:10.1016/j.matdes.2017.08.015.

[80] C. Krill III, L.-Q. Chen, Computer simulation of 3D grain growth using a phase field model, Acta Materialia 50 (2002) 3059–3075. doi:10.1016/s1359-6454(02)00084-8.

[81] I. Steinbach, O. Shchyglo, Phase-field modelling of microstructure evolution in solids: Perspectives and challenges, Current Opinion in Solid State and Materials Science 15 (2011) 87–92. doi:10.1016/j.cossms.2011.01.001.

[82] P. Zhao, Y. Wang, S. R. Niezgoda, Microstructural and micromechanical evolution during dynamic recrystallization, International Journal of Plasticity 100 (2018) 52–68. doi:10.1016/j.ijplas.2017.09.009.

[83] S. Kurijai, K. Shizawa, Modelling and simulation of dynamic recrystallisation based on multi-phase-field and dislocation-based crystal plasticity models, Philosophical Magazine (2020). doi:10.1299/transjsme.19-00341.

[84] O. Bouaziz, P. Buessler, Iso-work increment assumption for heterogeneous material behavior modelling, Advanced Engineering Materials 6 (2004) 79–83. doi:10.1002/adem.200300524.

[85] G. Zhou, Z. Li, D. Li, Y. Peng, H. Wang, P. Wu, Misorientation development in continuous dynamic recrystallization of AZ31B alloy sheet and polycrystal plasticity simulation, Materials Science and Engineering A 730 (2018) 438–456. doi:10.1016/j.msea.2018.05.095.

[86] G. Zhou, Z. Li, D. Li, Y. Peng, H. S. Zurob, P. Wu, A polycrystal plasticity based discontinuous dynamic recrystallization simulation method and its application to copper, International Journal of Plasticity 91 (2017) 48–76. doi:10.1016/j.ijplas.2017.01.001.

[87] T. Tang, G. Zhou, Z. Li, D. Li, L. Peng, Y. Peng, P. Wu, H. Wang, M. G. Lee, A polycrystal plasticity based thermo-mechanical-dynamic recrystallization coupled modeling method and its application to light weight alloys, International Journal of Plasticity 116 (2019) 159–191. doi:10.1016/j.ijplas.2019.01.001.

[88] J. A. Glazier, M. P. Anderson, G. S. Grest, Coarsening in the two-dimensional soap froth and the large- Q potts model: A detailed comparison, Philosophical Magazine B: Physics of Condensed Matter;

Statistical Mechanics, Electronic, Optical and Magnetic Properties 62 (1990) 615–647. doi:10.1080/13642819008215259.

[89] D. Raabe, Scaling Monte Carlo kinetics of the potts model using rate theory, Acta Materialia 48 (2000) 1617–1628. doi:10.1016/S1359-6454(99)00451-6.

[90] A. Rollett, M. Luton, J. Srolovits, Microstructural simulation of dynamic recrystallization, Acta Metallurgica et Materialia 40 (1992) 43–55.

[91] P. Peczak, A Monte Carlo study of influence of deformation temperature on dynamic recrystallization, Acta Metallurgica Et Materialia 43 (1995) 1279–1291. doi:10.1016/0956-7151(94)00280-U.

[92] D. Raabe, Cellular automata in materials science with particular reference to recrystallization simulation, Annual Review of Materials Research 32 (2002) 53–76. doi:10.1146/annurev.matsci.32.090601.152855.

[93] F. Chen, Z. Cui, J. Liu, W. Chen, S. Chen, Mesoscale simulation of the high-temperature austenitizing and dynamic recrystallization by coupling a cellular automaton with a topology deformation technique, Materials Science and Engineering A 527 (2010) 5539–5549. doi:10.1016/j.msea.2010.05.021.

[94] M. Sitko, Ł. Madej, Modelling of the cellular automata space deformation within the RCAFE framework, AIP Conference Proceedings 1769 (2016). doi:10.1063/1.4963547.

[95] A. Legwand, M. Sitko, K. Perzynski, L. Madej, RCAFE Based numerical model of dynamic recrystalization, Journal of Machine Engineering 16 (2016) 52–60.

[96] A. Soares, A. Ferro, M. Fortes, Computer simulation of grain growth in a bidimensional polycrystal, Scripta Metallurgica 19 (1985) 1491 – 1496. doi:10.1016/0036-9748(85)90157-7.

[97] H. Frost, C. Thompson, C. Howe, J. Whang, A two-dimensional computer simulation of capillarity-driven grain growth: Preliminary results, Scripta Metallurgica 22 (1988) 65 – 70. doi:10.1016/S0036-9748(88)80307-7.

[98] K. Kawasak, T. Naga, K. Nakashima, Vertex models for two-dimensional grain growth, Philosophical Magazine B 60 (1989) 399–421. doi:10.1080/13642818908205916.

[99] E. A. Lazar, J. K. Mason, R. D. MacPherson, D. J. Srolovitz, A more accurate three-dimensional grain growth algorithm, Acta Materialia 59 (2011) 6837–6847. doi:10.1016/j.actamat.2011.07.052.

[100] L. A. Barrales Mora, G. Gottstein, L. S. Shvindlerman, Three-dimensional grain growth: Analytical approaches and computer simulations, Acta Materialia 56 (2008) 5915–5926. doi:10.1016/j.actamat.2008.08.006.

[101] D. Weygand, Y. Bréchet, J. Lépinoux, A vertex dynamics simulation of grain growth in two dimensions, Philosophical Magazine B 78 (1998) 329–352. doi:10.1080/13642819808206731.

[102] Y. Mellbin, H. Hallberg, M. Ristinmaa, A combined crystal plasticity and graph-based vertex model of dynamic recrystallization at large deformations, Modelling and Simulation in Materials Science and Engineering 23 (2015). doi:10.1088/0965-0393/23/4/045011.

[103] Y. Mellbin, H. Hallberg, M. Ristinmaa, Recrystallization and texture evolution during hot rolling of copper, studied by a multiscale model combining crystal plasticity and vertex models, Modelling and Simulation in Materials Science and Engineering 24 (2016). doi:10.1088/0965-0393/24/7/075004.

[104] I. Steinbach, F. Pezzolla, B. Nestler, M. Seeßelberg, R. Prieler, G. Schmitz, J. Rezende, A phase field concept for multiphase systems, Physica D: Nonlinear Phenomena 94 (3) (1996) 135 – 147. doi:10.1016/0167-2789(95)00298-7.

[105] B. Nestler, A. A. Wheeler, Phase-field modeling of multi-phase solidification, Computer Physics Communications 147 (1) (2002) 230 – 233, proceedings of the Europhysics Conference on Computational Physics Computational Modeling and Simulation of Complex Systems. doi:10.1016/S0010-4655(02)00252-7.

[106] L.-Q. Chen, Phase-field models for microstructure evolution, Annual Review of Materials Research 32 (2002) 113–140. doi:10.1146/annurev.matsci.32.112001.132041.

[107] P. Zhao, T. Song En Low, Y. Wang, S. R. Niezgoda, An integrated full-field model of concurrent plastic deformation and microstructure evolution: Application to 3D simulation of dynamic recrystallization in polycrystalline copper, International Journal of Plasticity 80 (2016) 38–55. doi:10.1016/j.ijplas.2015.12.010.

[108] R. A. Lebensohn, A. K. Kanjarla, P. Eisenlohr, An elasto-viscoplastic formulation based on fast Fourier transforms for the prediction of micromechanical fields in polycrystalline materials, International Journal of Plasticity 32-33 (2012) 59–69. doi:10.1016/j.ijplas.2011.12.005.

[109] N. Moelans, A. Godfrey, Y. Zhang, D. Juul Jensen, Phase-field simulation study of the migration of recrystallization boundaries, Physical Review B - Condensed Matter and Materials Physics 88 (2013). doi:10.1103/PhysRevB.88.054103.

[110] Y. Aoyagi, K. Shizawa, Multiscale crystal plasticity modeling based on geometrically necessary crystal defects and simulation on fine-graining for polycrystal, International Journal of Plasticity 23 (2007) 1022–1040. doi:10.1016/j.ijplas.2006.10.009.

[111] T. Takaki, A. Yamanaka, Y. Higa, Y. Tomita, Phase-field model during static recrystallization based on crystal-plasticity theory, Journal of Computer-Aided Materials Design 14 (2007) 75–84. doi:10.1007/s10820-007-9083-8.

[112] B. Scholtes, R. Boulais-Sinou, A. Settefrati, D. Pino Muñoz, I. Poitrault, A. Montouchet, N. Bozzolo, M. Bernacki, 3D level set modeling of static recrystallization considering stored energy fields, Computational Materials Science 122 (2016) 57–71. doi:10.1016/J.COMMATSCI.2016.04.045.

[113] E. B. Marin, On the formulation of a crystal plasticity model., Tech. rep., Sandia National Laboratories (SNL) (2006). doi:10.2172/890604.

[114] J. Bishop, R. Hill, A theory of the plastic distortion of a polycrystalline aggregate under combined stresses, Philosophical Magazine 42 (1951) 414–417.

[115] J. Hutchinson, Creep and plasticity of hexagonal polycrystals as related to single crystal slip, Metallurgical Transactions A 8 (1977) 1465–1469.

[116] R. Asaro, A. Needleman, Overview no. 42 Texture development and strain hardening in rate dependent polycrystals, Acta Metallurgica 33 (6) (1985) 923–953. doi:10.1016/0001-6160(85)90188-9.

[117] R. Becker, Analysis of texture evolution in channel die compression—I. Effects of grain interaction, Acta Metallurgica et Materialia 39 (6) (1991) 1211–1230. doi:10.1016/0956-7151(91)90209-J.

[118] D. K. Kim, J. M. Kim, W. W. Park, H. W. Lee, Y. T. Im, Y. S. Lee, Three-dimensional crystal plasticity finite element analysis of microstructure and texture evolution during channel die compression of if steel, Computational Materials Science 100 (2015) 52–60. doi:10.1016/j.commatsci.2014.09.032.

[119] G. Sarma, B. Radhakrishnan, T. Zacharia, Finite element simulations of cold deformation at the mesoscale, Computational Materials Science 12 (2) (1998) 105–123. doi:10.1016/S0927-0256(98)00036-6.

[120] R. K. Abu Al-Rub, G. Z. Voyiadjis, A physically based gradient plasticity theory, International Journal of Plasticity 22 (2006) 654–684. doi:10.1016/j.ijplas.2005.04.010.

[121] A. L. Fabiano, Modelling of Crystal Plasticity and Grain Boundary Migration of 304L Steel at the Mesoscopic Scale, Ph.D. thesis, MINES ParisTech (2013).

[122] A. Arsenlis, D. M. Parks, R. Becker, V. V. Bulatov, On the evolution of crystallographic dislocation density in non-homogeneously deforming crystals, Journal of the Mechanics and Physics of Solids 52 (2004) 1213–1246. doi:10.1016/J.JMPS.2003.12.007.

[123] K. Cheong, E. P. Busso, Discrete dislocation density modelling of single phase FCC polycrystal aggregates, Acta Materialia 52 (2004) 5665–5675. doi:10.1016/j.actamat.2004.08.044.

[124] A. Ma, F. Roters, A constitutive model for fcc single crystals based on dislocation densities and its application to uniaxial compression of aluminium single crystals, Acta Materialia 52 (12) (2004) 3603–3612. doi:10.1016/j.actamat.2004.04.012.

[125] A. Ma, F. Roters, D. Raabe, On the consideration of interactions between dislocations and grain boundaries in crystal plasticity finite element modeling. Theory, experiments, and simulations, Acta Materialia 54 (8) (2006) 2181–2194. doi:10.1016/j.actamat.2006.01.004.

[126] A. Ma, F. Roters, D. Raabe, A dislocation density based constitutive model for crystal plasticity FEM including geometrically necessary dislocations, Acta Materialia 54 (8) (2006) 2169–2179. doi:10.1016/j.actamat.2006.01.005.

[127] E. B. Marin, P. R. Dawson, On modelling the elasto-viscoplastic response of metals using polycrystal plasticity, Computer Methods in Applied Mechanics and Engineering 165 (1998) 1–21. doi:10.1016/S0045-7825(98)00034-6.

[128] J. C. Simo, T. J. Hughes, Computational Inelasticity, Springer, 1998.

[129] J. Mandel, Generalisation de la theorie de plasticite de W. T. Koiter, International Journal of Solids and structures 1 (1965) 273–295. doi:10.1016/0020-7683(65)90034-x.

[130] S. Matthies, M. Humbert, On the Principle of a Geometric Mean of Even-Rank Symmetric Tensors for Textured Polycrystals, Journal of Applied Crystallography 28 (1995) 254–266. doi:10.1107/S0021889894009623.

[131] G. Leibfried, N. Breuer, Point Defects in Metals I, Springer, 1978.

[132] F. Roters, P. Eisenlohr, T. R. Bieler, D. Raabe, Crystal Plasticity Finite Element Methods: In Materials Science and Engineering, Wiley-VCH, 2010.

[133] D. Arnold, F. Brezzi, M. Fortin, A stable finite element for the stokes equations, Calcolo 21 (1984) 337–344. doi:10.1007/BF02576171.

[134] T. Coupez, H. Digonnet, R. Ducloux, Parallel meshing and remeshing, Applied Mathematical Modelling 25 (2) (2000) 153 – 175, dynamic load balancing of mesh-based applications on parallel. doi:10.1016/S0307-904X(00)00045-7.

[135] M. Shakoor, M. Bernacki, P.-O. Bouchard, A new body-fitted immersed volume method for the modeling of ductile fracture at the microscale: Analysis of void clusters and stress state effects on coalescence, Engineering Fracture Mechanics 147 (2015) 398 – 417. doi:10.1016/j.engfracmech.2015.06.057.

[136] J. Nye, Some geometrical relations in dislocated crystals, Acta Metallurgica 1 (1953) 153–132. doi:10.1016/0001-6160(53)90054-6.

[137] S. Osher, J. Sethian, Fronts propagating with curvature dependent speed: Algorithms based on hamilton-jacobi formulations, Journal of Computational Physics 79 (1988) 12–49. doi:10.1016/0021-9991(88)90002-2.

[138] H.-K. Zhao, T. Chan, B. Merriman, S. Osher, A variational level set approach to multiphase motion, Journal of Computational Physics 127 (1) (1996) 179 – 195. doi:10.1006/jcph.1996.0167.

[139] R. Loge, M. Bernacki, H. Resk, L. Delannay, H. Digonnet, Y. Chastel, T. Coupez, Linking plastic deformation to recrystallization in metals using digital microstructures, Philosophical Magazine 88 (2008) 3691–3712. doi:10.1080/14786430802502575.

[140] H. Resk, L. Delannay, M. Bernacki, T. Coupez, R. Logé, Adaptive mesh refinement and automatic remeshing in crystal plasticity finite element simulations, Modelling and Simulation in Materials Science and Engineering 17 (7) (2009) 075012. doi:10.1088/0965-0393/17/7/075012.

[141] M. Bernacki, H. Resk, T. Coupez, R. E. Logé, Finite element model of primary recrystallization in polycrystalline aggregates using a level set framework, Modelling and Simulation in Materials Science and Engineering 17 (6) (2009) 064006. doi:10.1088/0965-0393/17/6/064006.

[142] K. Hitti, P. Laure, T. Coupez, L. Silva, M. Bernacki, Precise generation of complex statistical Representative Volume Elements (RVEs) in a finite element context, Computational Materials Science 61 (2012) 224–238. doi:10.1016/J.COMMATSCI.2012.04.011.

[143] B. Merriman, J. K. Bence, S. J. Osher, Motion of multiple junctions: A level set approach, Journal of Computational Physics 112 (1994) 334 – 363. doi:10.1006/jcph.1994.1105.

[144] M. Bernacki, N. Bozzolo, P. De Micheli, B. Flipon, J. Fausty, L. Maire, S. Florez, Numerical Modeling of Recrystallization in a Level Set Finite Element Framework for Application to Industrial Processes, in: Recrystallization: Types, Techniques and Applications, Nova, 2019, p. 350.

[145] M. Shakoor, B. Scholtes, P. O. Bouchard, M. Bernacki, An efficient and parallel level set reinitialization method. Application to micromechanics and microstructural evolutions, Applied Mathematical Modelling 39 (23-24) (2014) 7291–7302. doi:10.1016/j.apm.2015.03.014.

[146] D. N. Ilin, N. Bozzolo, T. Toulorge, M. Bernacki, Full field modeling of recrystallization: Effect of intragranular strain gradients on grain boundary shape and kinetics, Computational Materials Science 150 (2018) 149–161. doi:10.1016/j.commatsci.2018.03.063.

[147] S. Florez, M. Shakoor, T. Toulorge, M. Bernacki, A new finite element strategy to simulate microstructural evolutions, Computational Materials Science 172 (2020) 109335. doi:10.1016/j.commatsci.2019.109335.

[148] F. Bachmann, R. Hielscher, H. Schaeben, Grain detection from 2d and 3d EBSD data-Specification of the MTEX algorithm, Ultramicroscopy 111 (2011) 1720–1733. doi:10.1016/j.ultramic.2011.08.002.

[149] A. Nicolay, J. M. Franchet, J. Cormier, H. Mansour, M. de Graef, A. Seret, N. Bozzolo, Discrimination of dynamically and post-dynamically recrystallized grains based on EBSD data: application to Inconel 718, Journal of Microscopy 273 (2019) 135–147. doi:10.1111/jmi.12769.

[150] E. Underwood, Quantitative Stereology, 2nd Edition, Addison-Wesley, 1970.

[151] L. Gavard, Recristallisation dynamique de aciers inoxydables austenitiques de haute purete, Ph.D. thesis, Ecole Nationale Superieure des Mines de Saint Etienne (2001).

[152] E. Roux, Assemblage mecanique : strategies de optimisation des procedes et de identification des comportements mecaniques des materiaux, Ph.D. thesis, MINES ParisTech (2011).

[153] E. V. Kozlov, N. A. Koneva, Internal fields and other contributions to flow stress, Mater Science and Engineering: A 234-236 (1997) 982–985. doi:10.1016/S0921-5093(97)00381-X.

[154] L. Bäcke, Modeling the Microstructural Evolution during Hot Deformation of Microalloyed Steels, Ph.D. thesis, Royal Institute of Technology Sweden (2009).

[155] N. Yazdipour, C. H. Davies, P. D. Hodgson, Microstructural modeling of dynamic recrystallization using irregular cellular automata, Computational Materials Science 44 (2008) 566–576. doi:10.1016/j.commatsci.2008.04.027.

[156] M. El Wahabi, J. M. Cabrera, J. M. Prado, Hot working of two AISI 304 steels: A comparative study, Materials Science and Engineering A 343 (2003) 116–125. doi:10.1016/S0921-5093(02)00357-X.

[157] K. Huang, R. E. Logé, Microstructure and flow stress evolution during hot deformation of 304L austenitic stainless steel in variable thermo-mechanical conditions, Materials Science and Engineering A 711 (2018) 600–610. doi:10.1016/j.msea.2017.11.042.

[158] M. Ardakani, F. Humphreys, The annealing behaviour of deformed particle containing aluminium single crystals, Acta Metallurgica et Materialia 42 (1994) 763–780. doi:10.1016/0956-7151(94)90273-9.

[159] H. Chan, F. Humphreys, The recrystallisation of aluminium-silicon alloys containing a bimodal particle distribution, Acta Metallurgica 32 (1984) 235–243. doi:10.1016/0001-6160(84)90052-X.

[160] M. Ferry, F. Humphreys, The deformation and recrystallization of particle- containing aluminium crystals, Acta Materialia 44 (1996) 3089–3103. doi:10.1016/1359-6454(95)00432-7.

[161] M. Ferry, N. Hamilton, F. Humphreys, Continuous and discontinuous grain coarsening in a fine grained particle containin g Al Sc alloys., Acta Materialia 53 (2005) 1097–1109. doi:10.1016/J.ACTAMAT.2004.11.006.

[162] J. Q. Da Fonseca, L. Ko, The kinematics of deformation and the development of substructure in the particle deformation zone, IOP Conference Series: Materials Science and Engineering 89 (2015). doi:10.1088/1757-899X/89/1/012012.

[163] B. Radhakrishnan, G. Sarma, H. Weiland, P. Baggethun, Simulations of deformation and recrystallization of single crystals of aluminium containing hard particles, Modelling and Simulation in Materials Science and Engineering 8 (2000) 737–750. doi:10.1088/0965-0393/8/5/307.

[164] J. Humphreys, P. Bate, Gradient plasticity and deformation structures around inclusions, Scripta Materialia 48 (2003) 173–178. doi:10.1016/S1359-6462(02)00359-7.

[165] J. F. Humphreys, P. S. Bate, A. Gholinia, I. Brough, Measuring and Modelling the Microstructures of Two-Phase Aluminium Alloys after Deformation, Materials Science Forum 715-716 (2012) 23–32. doi:10.4028/www.scientific.net/msf.715-716.23.

[166] C. Schafer, J. Song, G. Gottstein, Modeling of texture evolution in the deformation zone of second phase particles, Acta Materialia 57 (2009) 1026–1034. doi:10.1016/J.ACTAMAT.2008.10.052.

[167] Z.-C. Lin, C.-C. Chen, H.-H. Wang, The determination of material strength coefficient and strain hardening constant by inverse method, Journal of Materials Processing Technology 209 (5) (2009) 2393 – 2401. doi:10.1016/j.jmatprotec.2008.05.039.

[168] J. Furstoss, From crystal to plate boundaries : numerical modeling of mantle rocks microstructural evolution, Ph.D. thesis, MINES ParisTech (2020).

[169] J. Furstoss, D. Ruiz Sarrazola, M. Bernacki, D. Pino Muñoz, Handling tensors using tensorial kelvin bases : application to olivine polycrystal deformation modeling using elastically anisotropic cpfem., Submitted to Computational Mechanics (2020).

[170] J. Fausty, Towards the full field modeling and simulation of annealing twins using a Finite Element Level Set method, Ph.D. thesis, MINES ParisTech (2020).

[171] B. Murgas, Towards a precise description of the mobility and its numerical integration in finite element modeling of recrystallization mechanisms, Ph.D. thesis, MINES ParisTech (2021).

ABSTRACT

Dynamic recrystallization (DRX) is one of the main metallurgical phenomena responsible for the evolution of the microstructure of metallic materials subjected to hot metal forming processes. Understanding and predicting the subsequent physical mechanisms is of prime importance as the resulting microstructure will be directly responsible of the final in-use material properties.
Thus, numerous phenomenological models (JMAK type for example) aiming to describe DRX have been developed in the state of the art. However, because of the complexity of the mechanisms involved in DRX and their interactions, phenomenological or mean field models are not able to fully account for the local evolution of the microstructure and full field approaches are required generally when precise calculations are aimed.
Most DRX full field models have limitations in their ability to model high deformation (which limits their applicability for real industrial thermomechanical treatments) and in their description of plastic deformation (which is often grossly simplified).
In this PhD, a new full field discontinuous DRX (DDRX) model is proposed by coupling a crystal plasticity finite element method (CPFEM) with a level-set finite element (LS-FE) framework to describe the grain boundary network motion. The proposed model considers anisotropic plastic deformation and its impact on grain boundary motion. Combined with a remeshing methodology, the proposed numerical framework is capable of describing DDRX up to very large deformation levels. The model is calibrated and compared against experimental measurements of 304L steel. Moreover, the interest of this strategy (ratio precision/numerical cost) is also discussed comparatively to a simpler approach (CP Taylor approximation). All these developments are realized in a generic CPFEM module easily usable in any FE code.

KEYWORDS

Dynamic recrystallization, Full field model, Crystal plasticity, Level-set, Finite element method, 304L Steel.

RÉSUMÉ

La recristallisation dynamique (DRX) est l'un des principaux phénomènes métallurgiques responsable de l'évolution de la microstructure des matériaux métalliques survenant lors de luer mise en forme à chaud. Comprendre et prévoir ce phénomène physique est d'une importance primordiale car la microstructure résultante est en général directement responsable des propriétés finales du matériau.
Ainsi, de nombreux modèles phénoménologiques (de type JMAK par exemple) visant à décrire la DRX ont été développés dans l'état de l'art. Cependant, en raison de la complexité des mécanismes impliqués et de leurs interactions, les modèles phénoménologiques ou de champ moyen ne sont pas en mesure de rendre pleinement compte de l'évolution locale de la microstructure et des approches de type champ complet sont nécessaires.
La plupart des modèles DRX en champ complet ont des limites dans leur capacité à modéliser une déformation élevée (ce qui les rend en général inutilisable pour des chemins thermomécaniques industriels) et dans la description de la déformation plastique (souvent très simplifié).
Dans cette thèse, un nouveau modèle à champ complet pour la recristallisation dynamique discontinue (DDRX) est proposé en couplant une méthode éléments finis de plasticité cristalline (CPFEM) avec un cadre élément finis - level set (LS-FE) pour décrire le mouvement des joints de grains. Le modèle proposé prend en compte la déformation plastique anisotrope et son impact sur le mouvement des joints de grains. Combiné à une méthodologie de remaillage, le cadre numérique proposé est capable de décrire la DDRX jusqu'à des niveaux de déformation très importants. Le modèle est calibré et comparé aux mesures expérimentales de l'acier 304L. De plus, l'intérêt de cette stratégie (ratio précision / coût numérique) est également discuté comparativement à une approche simplifie (approximation CP Taylor). Tous ces développements sont réalisés dans un module CPFEM générique facilement utilisable dans n'importe quel code EF.

MOTS CLÉS

Recristallisation Dynamique, Modèle en champ complet, Plasticité Cristalline, Level-set, Méthode des éléments finis, Acier 304L.